High–Entropy Prussian Blue Analogues for Sodium-Ion Batteries and Memristor Applications

Zur Erlangung des akademischen Grades einer

DOKTORIN DER INGENIEURWISSENSCHAFTEN (Dr.-Ing.)

von der KIT-Fakultät für Elektrotechnik und Informationstechnik des

Karlsruher Instituts für Technologie (KIT)

angenommene

DISSERTATION

von

M.Eng. Yueyue He

geb. in Sichuan, China

Tag der mündlichen Prüfung: 17.01.2025

Hauptreferent: Prof. Dr. rer. nat. Jasmin Aghassi-Hagmann, KIT

Korreferent: Prof. Dr. Christian Kübel, Technical University Darmstadt

Abstract

High-entropy materials (HEMs) are emerging as promising single-phase multi-component materials, offering remarkable compositional and functional tunability. Elements can be systematically replaced, added, or removed, with these modifications inherently altering interactions and thus influencing the material's overall properties. Prussian blue analogues (PBAs), part of metal-organic frameworks (MOFs) family, have attracted considerable interest as insertion materials due to their open 3D framework structure, favorable redox activity, and tunable physicochemical properties. In this dissertation, high-entropy approach is applied to PBAs to synthesize a series of functional materials. These materials have been notably utilized in sodium-ion batteries (SIBs) and printed memristors, helping to overcome critical issues in the development of long-life SIBs and advanced resistive switching devices. This dissertation is structured into three main sections, outlined as follows:

The first scientific part of this thesis deals with single-metal monoclinic structured Prussian White (PW, $Na_xMn[Fe(CN)_6]_y$) cathodes, belonging to PBAs, which are known for a relatively low stability and corresponding capacity decay. The high-entropy approach is first applied to monoclinic PW sodium-ion cathodes to tackle the issue of unfavorable multilevel phase transitions during electrochemical cycling. A series of Mn-based PW compounds, including high-, medium-, and low-entropy variants with up to six metal species, were synthesized. The high-entropy PW with the composition $Na_{1.65}Mn_{0.4}Fe_{0.12}Ni_{0.12}Cu_{0.12}Co_{0.12}Cd_{0.12}[Fe(CN)_6]_{0.92}\square_{0.08}\cdot 1.09H_2O$ demonstrated enhanced cyclability compared to medium/low-entropy and conventional single-metal PWs. Drawing on data from complementary characterization techniques, an intrinsic mechanism for the improved stability of the disordered PW structure during Na^+ insertion/extraction is proposed. This mechanism is attributed to the dual effect of suppressing phase transitions and mitigating gas evolution.

The second scientific part deals with the application of high-entropy concept to PBAs to facilitate the engineering of crystal structures with varied configurations through precise control of reaction temperatures. The strategic integration of five metal species (Mn, Co, Fe, Ni, and Cu) results in two variants: cubic high-entropy PBA (referred to as HEPBA) and monoclinic HEPBA. Despite similar composition and configurational entropy, their electrochemical behavior in SIBs varies significantly.

The cubic HEPBA cell shows high reversibility, favorable thermal stability and enables extended cycle life (15000 cycles), characterized by unprecedented endurance for high-voltage/temperature operation. The superior performance of cubic HEPBA can be attributed to inhibited structural distortions. By contrast, the prevailing monoclinic structure of PBA exacerbates lattice distortions, leading to compromised transport kinetics and increased degradation during cycling. Therefore, this thesis emphasizes the preference for highly symmetrical, high-entropy battery materials and underscores the complex connection between structure and performance.

The third part utilizes high-entropy approach in PBAs to design a non-volatile, bipolar printed memristor. The device is composed of a microplotted HE-PBA active layer, specifically $Na_{1.38}Mn_{0.3}Fe_{0.3}Co_{0.133}Ni_{0.133}Cu_{0.133}[Fe(CN)_6]_{0.84}\square_{0.16}\cdot 0.92H_2O$, with a laser-ablated indium tin oxide (ITO) bottom electrode and an inkjet-printed Ag top electrode. The printed memristor offers several advantages, including low power consumption, non-volatility, self-compliance, and forming-free behavior in memory applications. Also, the Ag/HE-PBA/ITO device exhibits metallic behavior in the low resistive state and insulating behavior in the high resistive state. Through comprehensive experiments and simulation studies, this thesis elucidates that the insulating-metallic transition results from the extraction/insertion of Na^+ ions, rather than the formation/rupture of Ag conducting filaments. The HE-PBA-based memristor operates using a low-energy process closely associated with the Na-ion extraction/insertion reaction, similar to the principle of Na-ion batteries. As a result, the printed memristor exhibits low operation voltage ($V_{SET} = -0.26$ V, $V_{RESET} = 0.36$ V), low power consumption ($P_{SET} = 26$ μW, $P_{RESET} = 8.0$ μW), and a high R_{OFF}/R_{ON} ratio of 10^4. The ion-driven resistive switching strategy presented in this dissertation may offer valuable insights into mitigating high power consumption and addressing volatility issues in other memristors.

Zusammenfassung der Arbeit

Hochentropiematerialien (HEMs) sind vielversprechende, einphasige und komplexe Mehrkomponentenmaterialien, die eine außergewöhnliche Flexibilität in chemischer Zusammensetzung und Funktion bieten. Durch systematisches Ersetzen, Hinzufügen oder Entfernen von Elementen lassen sich die Wechselwirkungen in der Kristallstruktur gezielt beeinflussen, was die Eigenschaften des Materials steuert. Preußisch-Blau-Analoga (PBAs), eine Untergruppe der Metall-organischen Gerüstverbindungen (MOFs), haben aufgrund ihrer offenen 3D-Struktur, hohen Redoxaktivität und anpassbaren physikochemischen Eigenschaften großes Potenzial als Insertionsmaterialien für Batterieelektroden. Diese Dissertation überträgt den Hochentropieansatz auf PBAs, um eine Reihe von Funktionsmaterialien zu synthetisieren, die für Natrium-Ionen-Batterien (SIBs) und gedruckte Memristoren verwendet werden, und so wesentliche Herausforderungen bei der Entwicklung langlebiger SIBs und moderner elektrischer Bauelemente zu bewältigen. Die Arbeit gliedert sich in drei experimentelle Kapitel:

Im ersten Kapitel werden monokline Preußischweiß-Kathoden (PW, $Na_xMn[Fe(CN)_6]_y$), eine Unterklasse der PBAs mit eingeschränkter Stabilität und Kapazitätsabnahme, untersucht. Der Hochentropieansatz wird erstmals auf monokline PW-Natriumionenkathoden angewandt, um die durch mehrstufige Phasenübergänge bedingte Kapazitätsminderung beim Zyklieren zu reduzieren. Eine Reihe von Mn-basierten PW-Varianten mit hoher, mittlerer und niedriger Konfigurationsentropie und bis zu sechs Metallarten wurden synthetisiert. Das Hochentropie-PW mit der Zusammensetzung $Na_{1.65}Mn_{0.4}Fe_{0.12}Ni_{0.12}Cu_{0.12}Co_{0.12}Cd_{0.12}[Fe(CN)_6]_{0.92}\square_{0.08}\cdot 1.09H_2O$ zeigte im Vergleich zu PW mit niedriger Entropie und herkömmlichen Einzelmetall-PWs eine verbesserte Zyklisierbarkeit. Analysen mithilfe komplementärer Charakterisierungstechniken legen nahe, dass die Stabilitätssteigerung der ungeordneten PW-Struktur durch eine Phasenübergangsunterdrückung und Gasentwicklungsreduktion hervorgerufen wird.

Das zweite Kapitel befasst sich mit der strukturellen Vielfalt von PBAs, die sich aus präziser Reaktionstemperatursteuerung und der Anwendung des Hochentropieansatzes ergibt, wobei fünf Metallarten (Mn, Co, Fe, Ni und Cu) integriert werden. Dies resultiert in zwei Varianten: einem

kubischen und einem monoklinen Hochentropie-PBA (HEPBA). Trotz ähnlicher Zusammensetzung und Entropie zeigen die beiden Varianten unterschiedliche elektrochemische Eigenschaften in SIBs. Die kubische HEPBA-Zelle zeichnet sich durch hohe Reversibilität, gute thermische Stabilität und verlängerte Zyklenlebensdauer (15.000 Zyklen) aus, die auf eine verringerte Strukturverzerrung zurückzuführen ist. Im Gegensatz dazu verstärken monokline Strukturen Gitterverzerrungen, was die Transportkinetik hemmt und zu erhöhter Degradation führt. Die Ergebnisse verdeutlichen, dass hochsymmetrische Strukturen für Hochentropie-Batteriematerialien vorteilhaft sind und die komplexe Beziehung zwischen Struktur und elektrochemischen Eigenschaften prägen.

Im dritten Kapitel wird der Hochentropieansatz zur Entwicklung eines beständigen, bipolaren gedruckten Memristors verwendet. Das Bauelement besteht aus einer gedruckten aktiven HE-PBA-Schicht ($Na_{1.38}Mn_{0.3}Fe_{0.3}Co_{0.133}Ni_{0.133}Cu_{0.133}[Fe(CN)_6]_{0.84}\square_{0.16}\cdot 0.92H_2O$) zwischen einer laserstrukturierten Indiumzinnoxid (ITO)-Elektrode und einer tintenstrahlgedruckten Silberelektrode. Der gedruckte Memristor zeichnet sich durch geringen Stromverbrauch, Beständigkeit, Selbstanpassung und Formfreiheit aus. Im niederohmigen Zustand zeigt das Ag/HE-PBA/ITO-Bauteil metallisches Verhalten, im hochohmigen Zustand hingegen isolierendes Verhalten. Experimentelle und simulationsgestützte Untersuchungen zeigen, dass der Übergang von isolierend zu metallisch durch Na^+-Ioneneinlagerung ausgelöst wird. Dieser HE-PBA-basierte Memristor bietet eine niedrige Betriebsspannung (V_{SET} = −0,26 V, V_{RESET} = 0,36 V), geringen Stromverbrauch (P_{SET} = 26 µW, P_{RESET} = 8,0 µW) und ein hohes R_{OFF}/R_{ON}-Verhältnis von 10^4. Die vorgestellte ionengetriebene Schaltstrategie könnte zur Reduktion des hohen Stromverbrauchs und zur Lösung von Volatilitätsproblemen bei anderen Memristoren beitragen.

Table of Contents

Part I. Introduction

1. Motivation

High-entropy materials (HEMs), which integrate multiple components into a single-phase structure, represent a new class of advanced materials characterized by flexible properties that can be readily tailored through the selection of specific elements and the alteration of stoichiometry. Specifically, these materials are composed of at least five distinct chemical elements, each present in atomic ratios ranging from 5% to 35%, and exhibit a configurational entropy surpassing 1.5*R*, where *R* is the ideal gas constant. The high-entropy concept is founded on the idea to maximize configurational entropy to promote manifold interactions among multiple elements, often referred to as cocktail effects. This endows HEMs with unexpected and often unprecedented properties. Thereby, HEMs provide extensive opportunities for adjusting their composition and functionality, facilitating tailored material properties to meet specific application needs. This versatility makes HEMs valuable in various research fields, including environmental protections, thermoelectric devices, catalysts, sensing devices and electrochemical energy storage.

Prussian blue analogue materials (PBAs), belonging to the class of metal-organic frameworks (MOFs), have sparked tremendous interest as insertion materials due to their unique advantages, such as open framework structure, high redox activity, large porosity as well as tunable physicochemical properties. PBAs offer a flexible composition that allows tailoring of a position, and consequently their properties, through the high-entropy approach. The 3D open framework of PBAs, with large interstitial sites, facilitates the diffusion of large ions, such as Na^+ and K^+. With this structure, PBAs have been demonstrated to be suitable host materials for facile Na^+ insertion/extraction in sodium-ion batteries (SIBs). SIBs are being considered as an ideal low-cost and high-efficiency supplement, or even an alternative, to lithium-ion batteries (LIBs) for large-scale energy storage, which is essential for advancing a low-carbon economy. Despite their potential, PBAs used as cathodes in SIBs still require material optimization to boost their electrochemical performance, specifically their specific energy density. Major challenges plague practical application of PBAs, which are closely associated with complicated structural changes during Na^+-ions extraction/insertion, leading to capacity fading and poor cyclability. The high-entropy approach facilitates the incorporation of multiple elements in equimolar or near-equimolar proportions within the PBA framework, enhancing structural

adaptability. This strategy is expected to reduce defect formation and improve the mechanical stability of PBA cathodes, thereby extending cycle life under high-demand operating conditions. Given the promising characteristics of HEMs, the high-entropy approach is applied to PBAs as cathodes for SIBs to mitigate a series of unfavourable multilevel phase transitions during cycling and improve electrochemical performance in this dissertation.

Furthermore, high-entropy PBAs (HEPBAs) offer notable potential as insertion materials for the development of advanced memristive devices, attributed to their favorable Na^+ diffusion coefficients, robust structural stability, and superior ionic conductivity. These properties provide flexibility in fine-tuning device performance to meet stringent demands. Memristors, as a distinct class of resistive switching devices, can alternate between high and low resistive states in response to applied electrical stimuli, enabling information storage and processing through resistance modulation. This capability renders them highly advantageous for applications such as memory storage, neuromorphic computing, and artificial intelligence. Key attributes of memristors—including non-volatile memory retention, high data density, low power consumption, rapid switching speeds, and scalability—position them as promising candidates for advanced electronic technologies. Incorporating high-entropy configurations within PBAs presents a significant advancement in memristor design, expected to improve essential properties, such as ion mobility, tunable physicochemical characteristics, and increased structural durability. These advancements are expected to play a crucial role in the development of advanced memristors capable of achieving faster switching speeds, greater scalability, and enhanced reliability compared to traditional devices. Integrating PBAs with the high-entropy approach opens up new possibilities for achieving high-performance memristive technologies. However, the utilization of HEPBAs as insertion materials in memristors remains largely unexplored, and the resistive switching mechanism of HEPBA-based memristors is not yet well-understood. Therefore, this thesis aims to investigate two promising domains—SIBs and memristors—by employing the high-entropy method in PBAs to develop long-life SIBs and innovative memristive switching devices.

2. Aim of the Dissertation

The aim of this dissertation is the preparation of HEPBAs and the utilization of these compounds in SIBs and printed memristors. The dissertation focuses on the introduction of high-entropy approach into PBAs to design a series of promising long-life sodium-ion cathode active materials with robust structure. In addition, the HEPBAs were printed as memristors to further expand the practical applications. This thesis comprises three main sections, as follows:

In the first section, synthesis of a series of Mn-based Prussian White (PWs) materials, i.e., high-, medium- and low-entropy PWs with up to six metal species was conducted. PWs refer specifically to the white coloured powder form of PBAs, which forms when the PBA structure is based on a majority of Mn ions. This section focuses on the electrochemical characterization, energy-storage mechanism and entropy-mediated effects in order to explore and expand the structural and compositional diversity of PWs and to elucidate the role of configurational entropy and compositional disorder within this system.

In the second section, two HEPBAs with similar composition but varying structure, namely cubic vs. monoclinic, were synthesized and compared. Specifically, the electrochemical behavior of HEPBAs as cathodes for SIBs application is investigated in a wider electrochemical window (1.5–4.5 V) and harsh conditions (high specific current and temperature). A comprehensive analysis of the structure, electrochemical properties, and energy-storage mechanism of cubic and monoclinic HEPBAs is conducted to explore the influence of high-entropy configurations on structure-property relationships. With the optimized HEPBAs, the full-cell and high-temperature performance are evaluated to further investigate the applicability of HEPBAs in SIBs.

In the third section, the fabrication of HEPBA-based printed memristors was developed. This section involves fabricating memristors using printing technologies such as inkjet printing and microplotting, with a focus on evaluating their electrical performance. Given the absence of prior applications of HEPBAs in memristors, a crucial aspect of the research is to understand their conduction mechanisms.

3. Introduction to Sodium-Ion Batteries and Memristors

3.1. Sodium-Ion Batteries (SIBs)

Rechargeable batteries have generated significant interest as a reliable means of supporting the future low-carbon economy, offering practical strategies for efficiently supplying electric energy to power various electronics.[1] The development of rechargeable batteries, originally spurred by the demand for portable smart electronic devices, has expanded substantially over the years. This expansion now includes significant applications in large-scale stationary grid storage and electric vehicles (EVs). Lithium-ion batteries (LIBs) have been commercialized in the early 1990s, due to their high energy density. Later on, LIBs quickly dominated the market for consumer electronics and have a significant impact on our modern society. The rapid societal progress observed has largely been fueled by non-sustainable resources, which are expected to reach a consumption rate of 28 terawatts (TW) by 2050, roughly equal to 20 billion tons of oil annually.[2] The growth in rechargeable battery technology offers a promising solution to curbing this excessive use of non-sustainable resources. Not surprisingly, fabrication of large-scare electronics has given rise to the significant consumption of lithium resources. The geographical uneven distribution (mainly in South America) and scarcity of lithium lead to high costs.[3] The high risk of explosion in LIBs under high-rate conditions is considered the most significant challenge. Therefore, developing low-cost and highly safe rechargeable batteries has become a more urgent need.

SIBs are considered the most promising long-life energy storage devices in the development of "beyond lithium-ion" batteries due to their similar chemical properties to LIBs. Sodium is more than 1000 times abundant than lithium and geographically evenly distributed,[4,5] which reduces concerns about resource availability and cost (see **Figure 3.1a**). The abundance of sodium is a major driver for the development of SIBs. Sodium is less reactive than lithium, which can contribute to improved safety characteristics, including reduced risk of thermal runaway and fire hazards. Besides, the working principle and manufacturing technology of LIBs and SIBs are similar, i.e., a lot of "know-how" could be directly transferred from LIBs to SIBs.[4] This substantially reduces the technological barrier for large-scale production of SIBs. Hence, SIBs are regarded as ideal candidates for LIBs in energy storage systems (see **Figure 3.1b**). At present, the SIBs have gradually been studied from the academic to the industries globally. The industrial research are mainly in EU, China, Japan, and United States,[4] as shown in **Figure 3.1c**. Investigating SIBs with a focus on achieving high safety, efficiency, and longevity is crucial for advancing their practical applications.

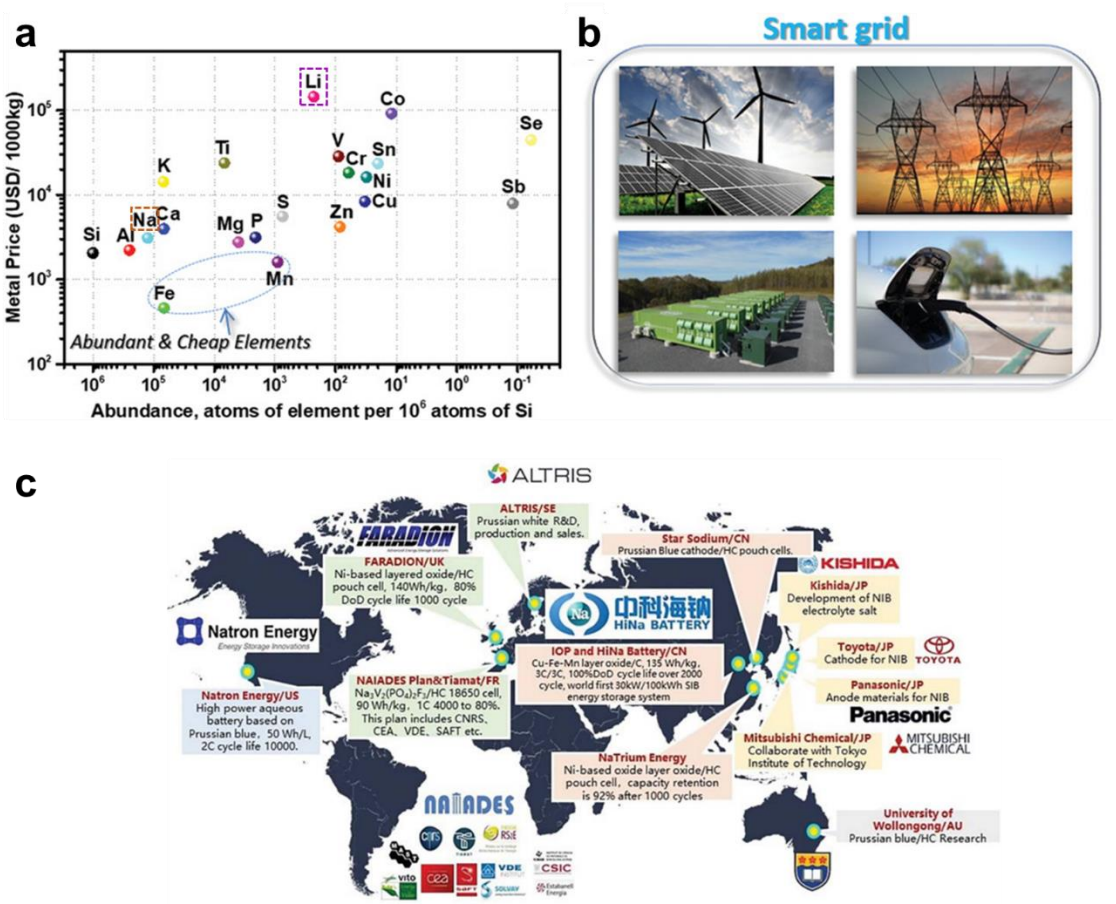

Figure 3.1. (a) Relationship between the elements' abundance in the Earth's crust (continental) and metal prices, from ref[5]. (b) Representative smart grid constituents: wind/solar energy, power transmission, energy storage devices, and power usage, from ref[5]. (c) Global companies in the SIBs industry, from ref[4].

3.1.1. SIBs Architectures

SIBs are composed of a cathode, an anode and a separator soaked in an electrolyte.[4] The cathode material is typically deposited on an aluminum current collector, however, for the current collector on the anode site, an alloying reaction with sodium at low potentials should be prevented, therefore either aluminum or copper current collectors are used. Cathode materials can be categorized into layered oxides (Na_xMO_2,$0<x\leq1$, M = Cr, V, Ni, Co, Fe, Mn), polyanionic phosphate-based compounds, Prussian blue analogues materials (PBAs, $Na_xM[Fe(CN)_6]\cdot nH_2O$, M stands for transition metal ions) and organic compounds (see **Figure 3.2**).[4,6] Carbon (hard carbon), insertion materials (oxides and polyanion materials), alloy-type (metals), and conversion-type (oxides and sulfides) materials can be used as anode materials.[4] Among the alkali metals, sodium is the only one showing incapability in intercalating to graphite, so natural graphite couldn't be used as anode in SIBs. Since hard carbons have disordered structures with randomly oriented graphene layers and larger interlayer spacing, they

can provide more sodium diffusion pathways and sodium storage sites, therefore they are considered as the most promising anode intercalation materials for SIBs.[4] Alloying-type materials such as tin (Sn), antimony (Sb), bismuth (Bi), silicon (Si), germanium (Ge), and phosphorus (P) and others enable the storage of sodium through alloying reactions, represented as follows: $x\mathrm{Na}^{+} + xe^{-} + \mathrm{M} \leftrightarrow \mathrm{Na}_x\,\mathrm{M}$.

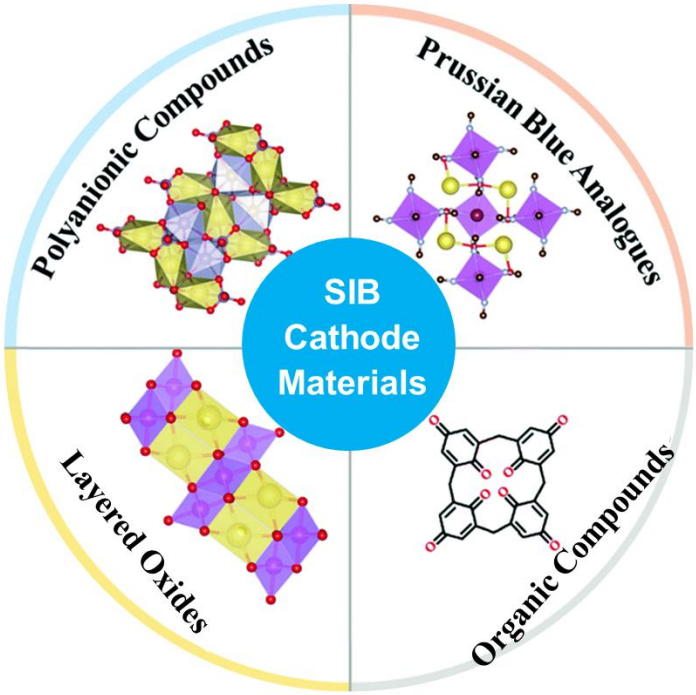

Figure 3.2. Cathode materials of SIBs.

The separator is a membrane typically made of electrically insulating material, such as polypropylene, whose role is the prevention of an electrical short circuit caused by direct contact between the electrodes while allowing for sodium-ion diffusion. The membrane is immersed in a specific electrolyte. The electrolyte consists of a sodium-salt (e.g., sodium perchlorate ($NaClO_4$) dissolved in an organic solvent mixture (e.g., ethylene carbonate (EC), dimethyl carbonate (DMC), propylene carbonate (PC) and fluoroethylene carbonate (FEC)). **Figure 3.3** illustrates four typical types of shape for rechargeable batteries, that is, coin, cylindrical, prismatic, and pouch cells.[1] Coin cell (**Figure 3.3a**) is a very common type of batteries in the lab, due to their low-cost, small volume and easy fabrication.

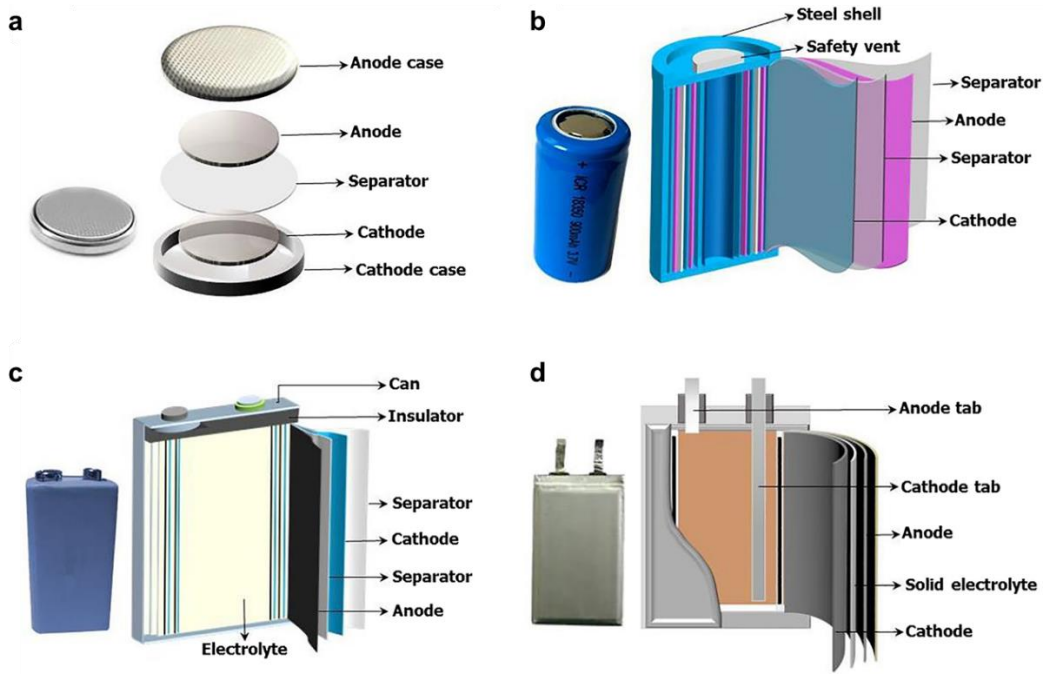

Figure 3.3. Schematic illustration of typical rechargeable battery configurations: (a) coin, (b) cylindrical, (c) prismatic and (d) pouch shapes, from ref[1].

3.1.2. Working Principles of SIBs

A battery is a device, that converts chemical energy into electric energy and vice versa, in the case of secondary batteries based on (reversible) redox reactions. During the discharge of the battery, energy is released, and during charge, energy is stored. **Figure 3.4** shows a typical SIB consisting of a hard carbon anode on a copper current collector and a Prussian blue cathode material (e.g., $Na_2Fe[Fe(CN)_6]$) on an aluminum current collector separated by a membrane soaked in electrolyte. When immersed in the electrolyte, the two electrodes create a potential difference E, also known as the electromotive force, which is responsible for the redox reaction occurring at each electrode and releasing electrons passing through an external circuit. More specifically, during charge, the cathode material (e.g., $Na_2Fe[Fe(CN)_6]$) is oxidized, which means that electrons are released from the electrode and travel through an external circuit towards the anode by the electric force provided to charge the battery. In order to compensate for this process and maintain charge neutrality within the electrode, sodium ions are extracted from the $Na_2Fe[Fe(CN)_6]$ and enter the electrolyte across the electrode-electrolyte interface (**Equation 3.1**). At the same time, the anode material (hard carbon) is reduced, meaning that the externally provided electrons are compensated by the insertion of sodium ions from the electrolyte into the hosting structure (**Equation 3.2**). In the discharging process, the $Na_2Fe[Fe(CN)_6]$ particles are reduced, and Na^+ intercalate back to the positive electrode. This reversible extraction and insertion of sodium-ion into the electrodes is referred to as rocking-chair mechanism discovered by Goodenough

in 1980.[7] The overall cell reaction is stated in **Equation 3.3**.

$$\text{Cathode: } Na_2Fe[Fe(CN)_6] \rightleftharpoons Na_{2-x}Fe[Fe(CN)_6] + xNa^+ + xe- \quad \textbf{(Equation 3.1)}$$

$$\text{Anode: } C + xNa^+ + xe- \rightleftharpoons Na_xC \quad \textbf{(Equation 3.2)}$$

$$\text{Overall: } Na_2Fe[Fe(CN)_6] + C \rightleftharpoons Na_{2-x}Fe[Fe(CN)_6] + Na_xC \quad \textbf{(Equation 3.3)}$$

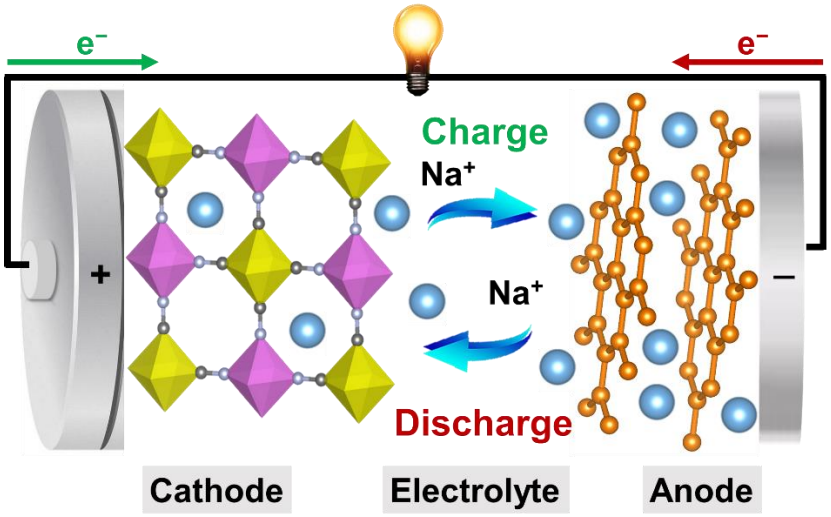

Figure 3.4. Simple schematic of the $Na_2Fe[Fe(CN)_6]$/hard carbon battery in the charge and discharge mode. The external circuit allows to drive an electric current through a load in order to counterbalance the ionic current.

Although SIBs are regarded as low-cost secondary batteries, their development has been less successful due to the lack of suitable host materials capable of facilitating reversible Na^+ insertion reactions. Unlike lithium ions, which have a smaller radius of 0.76 Å, sodium ions are larger with a radius of 1.02 Å. This size disparity leads to substantial volume changes in the host materials during the process of sodiation (Na^+ insertion) and desodiation (Na^+ extraction). These volume changes diminish the overall volumetric energy density of the battery, making it less efficient compared to LIBs. Additionally, sodium has a significantly higher atomic weight of 23 g/mol, more than three times that of lithium at 6.9 g/mol. This higher molar mass results in lower gravimetric capacities for active sodium materials, further impacting the overall energy storage capabilities of SIBs. Therefore, the critical challenge lies in identifying and developing suitable host materials that can mitigate these issues and enable SIBs to achieve high-performance. The search for such host materials is crucial for advancing the practical application and widespread adoption of SIBs in various energy storage systems.

3.2. Memristors (Resistive Switching Devices)

The concept of a "memristor" device was initially proposed by L. Chua in 1971,[8] as the fourth basic circuit element. Memristors, abbreviated from "memory resistors", are electronic devices with two terminals that exhibit a unique property known as resistive switching (RS).[9] They are characterized by their ability to change resistance in response to the amount and direction of current passing through them. This resistance can be switched between high resistance state (HRS, denoted as OFF state) and low resistance state (LRS, referred to as ON state). This characteristic endows them with information processing abilities, for applications like computation, information storage and detectors.[10,11] They are promising for various applications such as non-volatile memory storage (like flash memory replacements), neuromorphic computing (mimicking biological neural networks), and even in logic circuits for unconventional computing paradigms. More specifically, these resistive states can be used to represent different logic states. For example, the HRS can be determined to logic "0" of the binary code, while the LRS corresponds to logic "1" state. Hickmott discovered for the first time the RS phenomena in oxide materials (e.g., SiO_x, TiO_2, Al_2O_3) more than 60 years ago.[12] In the past decade, plenty of academic and giant industries, like SanDisk/Toshiba, IMECAS, Unity, and Micron/Sony have made notable progress on RS memories. The remarkable progress of memristors is largely attributed to their distinctive properties, including low power requirements, high-speed switching, and extensive scalability. These characteristics make them highly suitable for advanced computing architectures, paving the way for extensive applications, particularly in neuromorphic and in-memory computing systems,[13] as illustrated in **Figure 3.5**. In neuromorphic computing, memristors mimic the synaptic behavior of biological neurons, enabling efficient learning and pattern recognition tasks. They offer the potential for building artificial neural networks that can process information in a manner similar to the human brain. In-memory computing utilizes the ability of memristors to store and process data in the same location, reducing the need for data transfer between storage and processing units. This approach can significantly enhance the speed and efficiency of computation tasks, particularly for large-scale data analytics and machine learning application.

In the current Big Data era, driven by artificial intelligence (AI) and the Internet of Things (IoT), there is a substantial demand for processing vast amounts of data.[13–15] However, traditional computing systems face a significant challenge known as the "von Neumann bottleneck," where memory and processing units are separate in digital hardware. This bottleneck restricts the efficiency and speed of data processing. To overcome these limitations, advanced computing architectures are being developed. These architectures aim to integrate memory and processing units, enabling faster and more efficient data processing. Memristors play a crucial role in these advancements by offering the ability

to store and process data in the same location, which can significantly reduce latency and energy consumption compared to traditional systems.[16] Overall, memristors represent a promising advancement in electronic devices, offering new capabilities for memory storage and computing that could revolutionize future technologies.

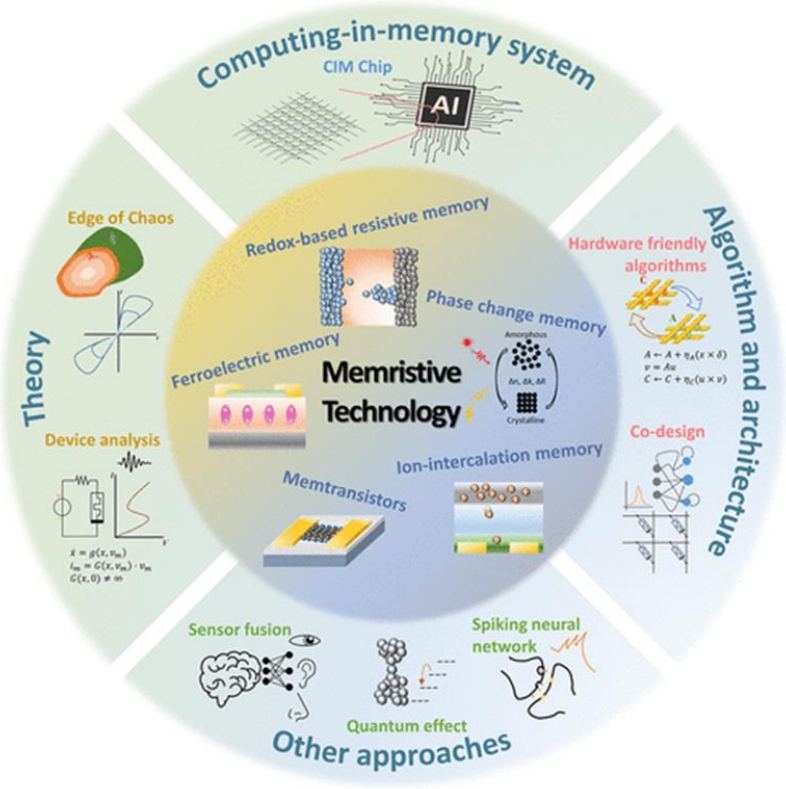

Figure 3.5. Development of memristive technology, from ref[13].

3.2.1. Memristors Architectures

Memristor typically consists of a simple sandwich structure, in which the middle active layer is sandwiched between two electrodes, as depicted in **Figure 3.6**. The active layers have insulating or semiconducting properties. Most common metals e.g., Pt, Au, Ag, Ti, Ni, ITO (indium tin oxide) and Cu, are used as top or bottom electrodes,[17] while TaN and TiN are popular in the industry.[18] To date, a diverse range of materials can be used as active layer, including metal oxides,[9,19,20] chalcogenides,[21] 2D-materials,[22,23] molecular materials,[24] hybrid perovskites,[25,26] organic materials,[27] silicon,[28,29] nitrides,[30,31] insertion materials,[32] and carbon materials.[33]

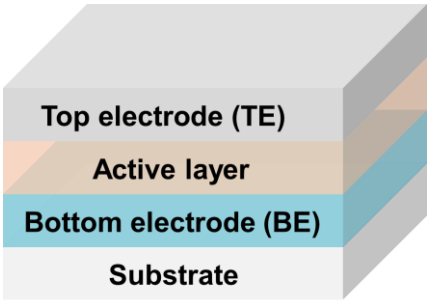

Figure 3.6. Schematics of memristor with sandwich structure.

3.2.2. Working Principles of Memristors

The RS process in memristors involves transitioning between HRS and LRS. The SET process typically describes the transition from HRS to LRS, while the RESET process describes the transition from LRS to HRS. These transitions can be characterized using current-voltage (*I*-*V*) measurements. As shown in **Figure 3.7**, *I*–*V* curve presents switching characteristics of memristors obtained by manipulating applied electric field and compliance current (CC) during testing. CC is essential in managing the SET process for memristors. Implementing a CC limit is crucial to safeguard the device against permanent breakdown. The RS behavior of memristors can generally be classified into unipolar and bipolar RS modes. In a unipolar mode (**Figure 3.7 a**), the change in the resistance state only depends on the magnitude of applied voltage and not the polarity.[34] Bipolar RS behavior refers to the switching direction being dependent on the polarity of the applied voltage.[35] Consequently, the SET process occurs only at one polarity, while the RESET process occurs only at the opposite polarity, as illustrated in **Figure 3.7b**. In some circumstances, if unipolar and bipolar RS appear in a single device, this phenomenon is called nonpolar RS. Furthermore, for unipolar memristors, the devices typically feature a symmetric structure, using the same material for both top and bottom electrode.[36] In contrast, bipolar switching devices usually have an asymmetric structure, employing different materials for top and bottom electrode.[37]

Memory can be divided into two primary categories: volatile memory and nonvolatile memory. Volatile memory requires a continuous power supply to maintain the stored information. When the power is turned off, all stored data is lost. Nonvolatile memory retains data even when the power supply is turned off, making it ideal for long-term storage of information. One of the promising uses of memristor devices is “non-volatile memory” for computing. Their ability to retain data without power, combined with potential advantages in speed, endurance, and density, positions them as a key component in advancing memory technologies for future computing systems.

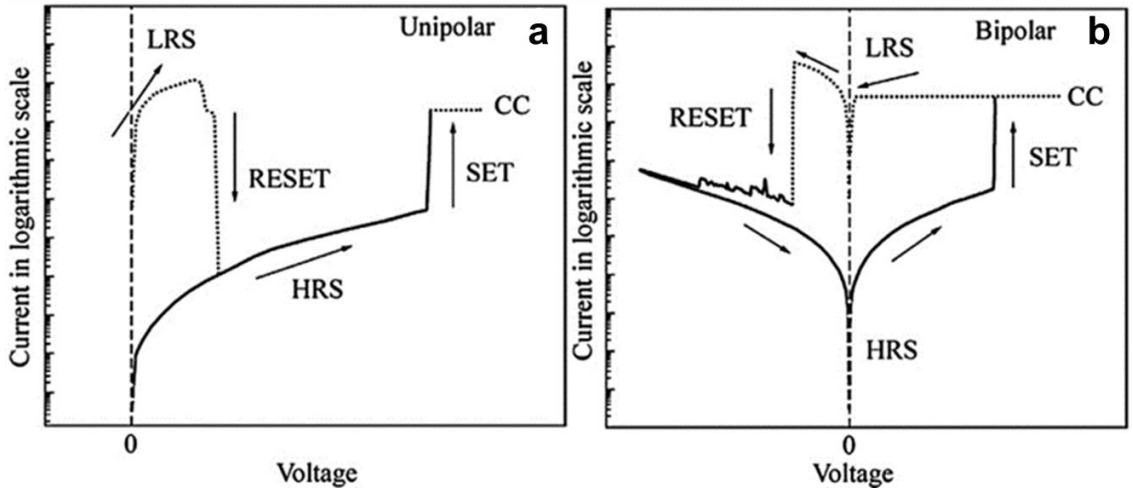

Figure 3.7. Schematics of *I–V* curve switching characteristics of memristors. (a) unipolar mode, (b) bipolar mode. CC stands for compliance current, from ref[37].

Currently, the main redox-based resistive switching mechanisms studied in memristive devices include electrochemical metallization mechanism, valence change mechanism, thermochemical mechanism and ion-insertion mechanism.[9,38,39]

In the regime of the electrochemical metallization mechanism (ECM), the electrodes are typically composed of an electrochemically active electrode (e.g., Ag, Cu or Ni) and an inert electrode (e.g., Pt, Pd, or Au).[34] Under an electric field pointing from the active electrode to inert electrode, the active metal (Ag, Cu or Ni) can be oxidized to generate metal cations (Ag^{+}, Cu^{2+} or Ni^{2+}) in the active electrode. Then the ions migrate towards the inert electrode under the influence of chemical and electric potential gradient. From classical electrochemistry, the ions should be reduced at the inert electrode and the conductive filaments composed of the active metals grow from the inert electrode to the active electrode. Long conductive filaments connecting both of the electrodes are formed and result in an LRS. In the subsequent RESET process, the rupture of the conductive filaments occurs locally due to electrochemical dissolution or Joule heating driven by a reverse voltage or a larger voltage. Hence, the RS process involves the formation (LRS state) and disruption (HRS state) of conductive filaments.[9]

The valence change mechanism (VCM), prevalent in metal oxides, involves key redox reactions comprising the transport of oxygen anions and subsequent valence changes in the cation sublattice to create conducting mixed valence states.[40] The mechanism is triggered by the migration of oxygen anion species, which involves the movement of corresponding oxygen vacancies within the active or resistive switching layer under the influence of an external electric field.[9]

The thermochemical mechanism (TCM) occurs when the thermochemical redox process predominates

over the electrochemical process. In this mechanism, thermally induced stoichiometry variations and redox reactions cause changes in local conductivity. Due to the thermal nature of these elementary processes, the switching between different resistive states is inherently unipolar.[40]

Ion-insertion materials have recently gained attention as innovative resistive switching materials, enabling reversible ion migration within their lattice structure.[41] These materials allow ions (e.g., lithium, sodium, or hydrogen ions) to reversibly insert and extract from their structure without causing significant changes to the crystalline framework. This process affects the material's electronic conductivity by altering the ion concentration, which in turn influences the number of free electrons or holes in the conduction or valence bands. Several insertion materials, such as $Li_{4+3x}Ti_5O_{12}$,[39] Li_xFePO_4 or $LiCoO_2$ have been reported as RS materials arising from Li^+ migration.[42,43] Exploring additional ion-insertion materials is crucial for advancing development of new memristors.

3.3. Prussian Blue Analogues (PBAs)

Metal-organic frameworks (MOFs) have attracted tremendous attention in materials science, due to their inherent advantages, such as high surface areas, high porosity and large framework flexibility. MOFs are notable examples of insertion materials for secondary batteries and memristor applications due to their porous structure, which facilitates ionic and gas penetration and reactions over a large surface area. In this thesis, the addressed secondary batteries are SIBs, as SIBs are considered as cost-effective alternatives to LIBs. However, their development has faced challenges due to the scarcity of suitable host materials capable of facilitating reversible Na^+ insertion reactions. Among the various existing candidates, certain PBAs appear to be attractive materials by virtue of the unique advantages, such as their MOFs structure as well as other functional properties.

3.3.1. Structure of PBAs

PBAs emerging as MOFs materials assembled by metal ions and organic linkers have the general formula $A_xM[Fe(CN)_6]_y\square_{1-y}\cdot nH_2O$ ($0\leqslant x \leqslant 2$; $0\leqslant y<1$), where A represents mobile cations Li^+, Na^+, K^+, etc.; M is the nitrogen-coordinated transition metal ion (e.g., Mn, Fe, Cu, Co, Zn, etc.) and Fe is coordinated with carbon (see **Figure 3.8**).[44,45] PBAs lattices with large interstitial "A" sites (≈4.6 Å) allow for Li^+, Na^+, K^+, Mg^{2+}, Al^{3+}, Zn^{2+} and Ca^{2+} accommodation.[46] Large amount of interstitial water molecules and vacancies of $[Fe(CN)_6]$ (□ stands for the vacancies) exist in the crystal framework. For example, the chemical formula of Na^+-based PBAs can be expressed as $Na_xM[Fe(CN)_6]_y\square_{1-y}\cdot nH_2O$. There are three types of crystal structure of PBAs obtained by tunning different synthesis condition: cubic, monoclinic and rhombohedral.[44] The latter two show reduced symmetry compared to the cubic state.[47]

3.3.2. Advantages of PBAs as SIB and Memristor Active Materials

PBAs can be synthesized through various facile methods, including co-precipitation, hydrothermal synthesis, and electrodeposition,[48] as illustrated in **Figure 3.9**. Co-precipitation involves mixing solutions containing the desired metal ions and a precipitating agent to form a solid product. It's a straightforward and effective method for producing PBAs with controlled composition and morphology. Hydrothermal synthesis uses high temperature and pressure in a sealed vessel to crystallize materials from aqueous solutions, allowing the growth of high-purity and well-defined crystals. Electrodeposition involves the reduction of metal ions on an electrode surface to form a solid material, allowing precise control over the thickness and composition of the PBA films.

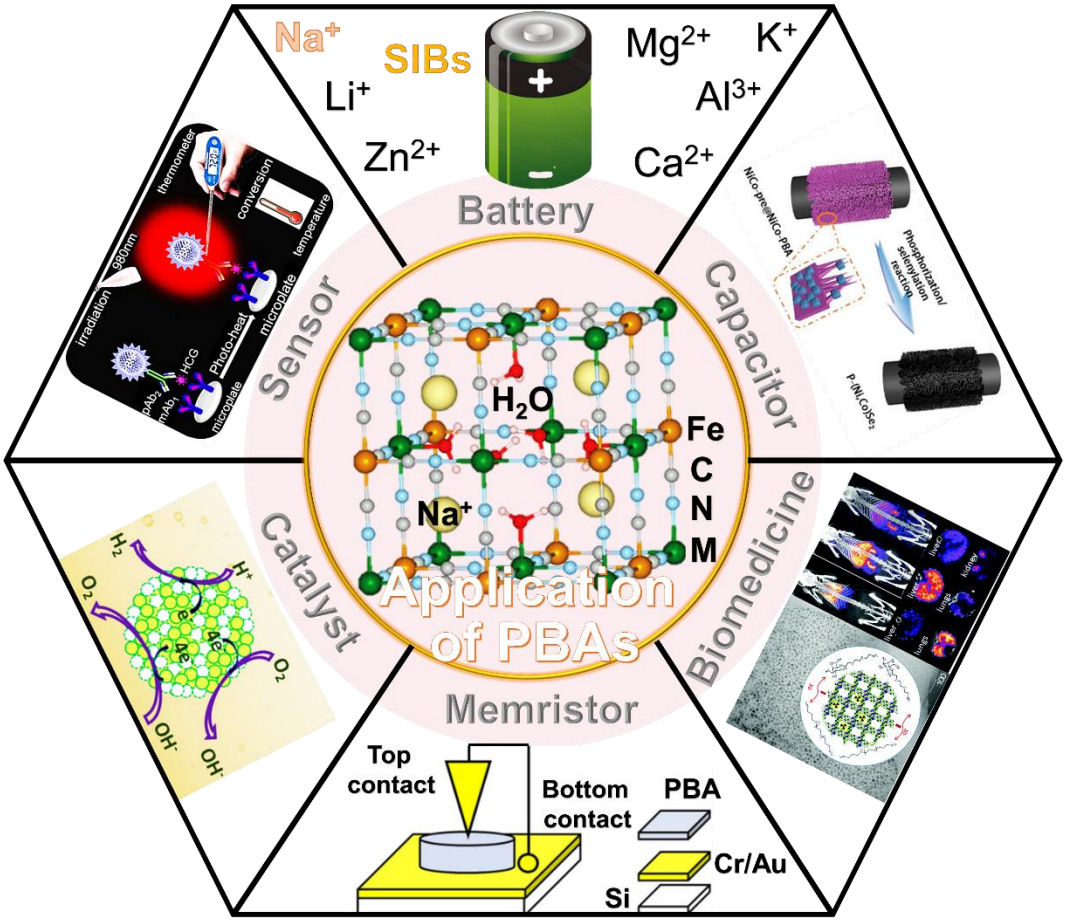

Figure 3.8. Structure of PBAs and their application schematic.

The open framework structure of PBAs provides abundant three-dimensional (3D) diffusion channels, making them well-suited for accommodating large alkali cations such as Na^+ and K^+. This structure facilitates high mobility and allows for reversible insertion and extraction reactions. PBAs possess two redox-active sites ($M^{2+/4+}$ and $Fe^{2+/4+}$), contributing to their high electrochemical activity and enabling a theoretical capacity of approximately 170 mAh g^{-1} for sodium storage. This is particularly evident in compounds like $Na_2Fe[Fe(CN)_6]$, where both the transition metal and the iron sites participate in the redox process.[46] PBAs exhibit high porosity characteristic of MOFs, which contributes to their high surface area and accessibility for ion insertion. This porosity enhances their performance in energy storage and other applications by providing ample active sites for reactions. PBAs demonstrate a high Na^+ diffusion coefficient (~10^{-9} cm^2 s^{-1}),[49,50] which indicates rapid ion transport within the material. This high diffusion rate is crucial for achieving fast charge/discharge cycles in SIBs and other energy storage devices. The composition of PBAs can be tailored by introducing different transition metals at the M sites, allowing for customization of their properties. By selecting appropriate metal precursors, it is possible to modify the electronic, magnetic, and electrochemical characteristics of PBAs to suit

specific applications. Owe to their appealing characteristics, PBAs offer extensive possibilities for applications, including catalyst,[51–53] sensor,[54–56] capacitor,[57–60] biomedicine,[61,62] and beyond, [45,46,63] as shown in **Figure 3.8**. PBAs have shown significant progress in secondary batteries as well,[64,65] especially excelling in SIBs with performance advantages that surpass those of other battery systems such as lithium-ion, zinc-ion, aluminum-ion, potassium-ion, and magnesium-ion batteries.[64]

In short, PBAs offer a range of advantages including facile synthesis methods, an open framework structure conducive to ion mobility, high redox activity, notable porosity, rapid ion diffusion, and customizable composition. These features make them promising materials for applications in energy storage and other advanced technologies.

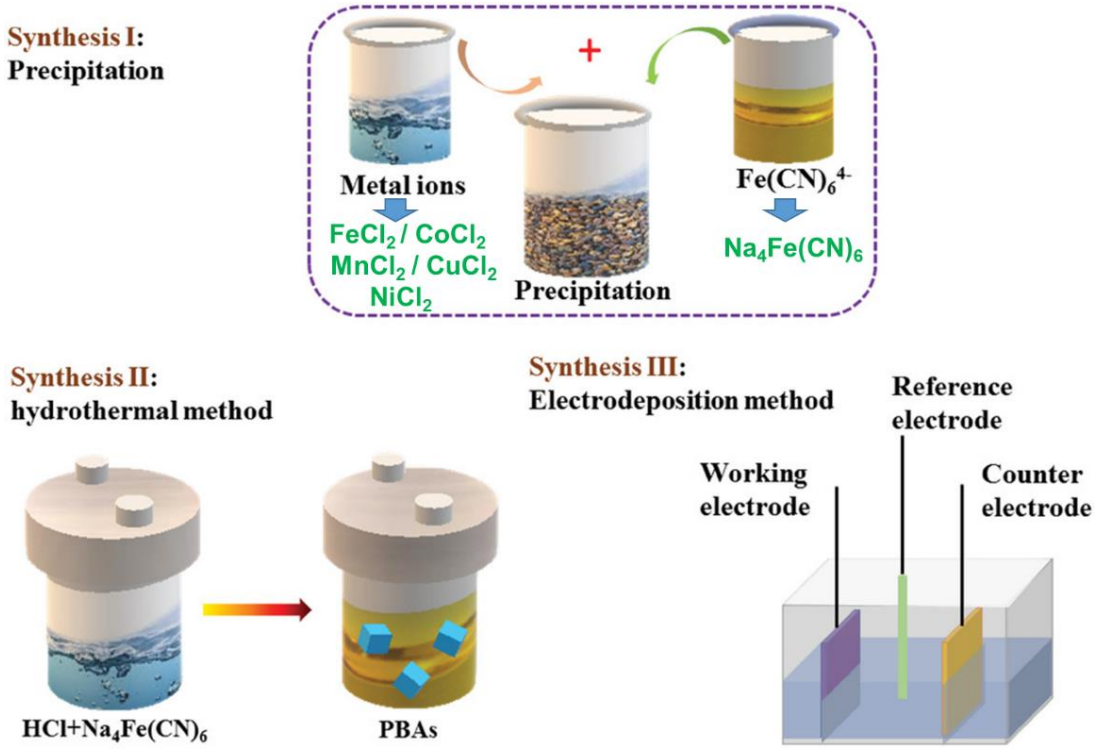

Figure 3.9. Different synthesis methods of PBAs, from ref[48].

3.3.3. Challenges for the Application of PBAs in SIBs and Memristors

Despite their promising features, PBAs as cathode materials for SIBs application encounter several challenges that impede their commercial viability.[44,65] **Figure 3.10** summarizes the challenges of PBAs as cathode materials. During electrochemical cycling, PBAs often undergo phase transitions that are not fully reversible. This can degrade the structural integrity of the material, leading to capacity fade and reduced cycle life. The insertion and extraction of Na^+ ions cause significant volume changes due to the larger ionic radius of Na^+ compared to Li^+. This volume expansion and contraction induce mechanical strain within the PBA lattice, which can lead to cracking of the active material over time. PBAs are prone to side reactions with electrolytes and other cell components. These reactions can produce unwanted by-products that deposit on the electrode surface, increasing internal resistance and further reducing the battery's efficiency and lifespan. The $[Fe(CN)_6]$ vacancies represent the primary structural defect in PBAs. However, a significant drawback of high vacancy content within the framework is its propensity to destabilize the crystal structure, leading to potential collapse during cycling.[65] Additionally, these vacancies can be occupied by water molecules. However, the presence of coordinated water in the lattice cause a variety of adverse effects. Specifically, crystal water molecules exhibit a strong tendency to reside within or compete with Na^+ ions for interstitial spaces, potentially obstructing the transport of Na^+ ions into the lattice interior and thereby severely deteriorating the electrochemical performance of PBAs in SIBs application.[46] Ensuring structural stability is crucial for achieving improved performance.

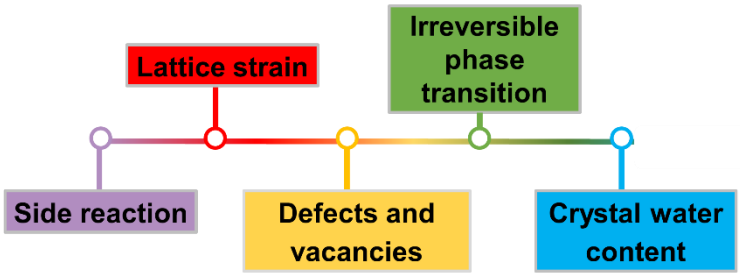

Figure 3.10. Challenges of PBAs as cathode materials.

On the other hand, research on using PBAs in resistive switching devices is notably limited. Only few studies have investigated simple $K_xFe[Fe(CN)_6]_y$ materials in these applications, and the underlying switching mechanisms remain poorly understood.[66,67] This highlights the need for thorough exploration to uncover the potential of PBAs in resistive switching technology.

Preliminary studies aimed mitigating the structural evolution of PBAs mainly focused on partial atom

replacement,[68–70] removal of interstitial water and vacancies,[57,71] introducing complexing agents[47,72,73] or constructing cation vacancies.[74] Recently, the integration of high-entropy concept into PBAs has led to the development of a series of novel compounds known as high-entropy PBAs (HEPBAs), highlighted in Chapters 5 and 6 for their potential as cathodes in SIBs.[75] Additionally, significant success was achieved in the application of HEPBAs to memristors for the first time, as documented in Chapter 7. The introduction of high-entropy as a strategy to optimize the structure and performance of materials has proven highly effective in this dissertation. Therefore, the following section provides a summary description of high-entropy materials (HEMs) and offers a detailed explanation of the employment of the high-entropy approach as an optimization strategy for PBAs.

3.4. High–Entropy Materials (HEMs)

Entropy is used to describe the chaos or disorder in a given system, which has a certain natural tendency to increase in spontaneous processes. In 2004, high-entropy concept is first developed in high entropy alloys (HEAs) reported by Yeh *et al*.[76] and Cantor *et al*.[77] independently. This concept expanded to high-entropy ceramics, and the first examples in powder form, known as high-entropy oxides (HEOs),[78] were pioneered by Rost *et al*. Since then, the high-entropy concept has drawn increasing interest in materials science and promoted the rapid development of a series of single-phase multi-component materials called HEMs.[79,80]

HEMs represent a paradigm shift in materials science where the traditional approach of using one or two primary elements is expanded to include five or more elements in roughly equal proportions, as shown in **Figure 3.11a**. Notably, HEMs, compared to materials with relatively simple compositions (i.e., one to three elements), exhibit two distinct features: a vast compositional space due to multielemental combinations and complex atomic configurations resulting from the random mixing of these multiple elements.[81] This vast compositional space allows for a broad range of elemental combinations, enhancing the potential for diverse functionalities, while the complex atomic configurations contribute to unique material properties not typically observed in simple compositions. Therefore, the utilization of the high-entropy concept to single-phase material promises an introduced great versatility and further the possibility to tailor properties,[82,83] which enables the design of compounds to meet specific needs and applications.

Furthermore, the unique properties of HEMs have motivated a broad range of active research for potential applications in environmental protections, thermoelectric devices, catalysts, sensing devices and electrochemical energy storage.[81–87] The evolution of HEMs, originating from alloys[88–90] and subsequently extending to ceramics,[80,91,92] oxides,[78,93,94] oxyfluorides,[87,95] borides,[91] carbides,[96,97] nitrides,[98] sulfides,[99] silicides,[100] MOFs[75,101] and phosphides[102] over the past decade (see **Figure 3.11**), underscores their versatile applicability.

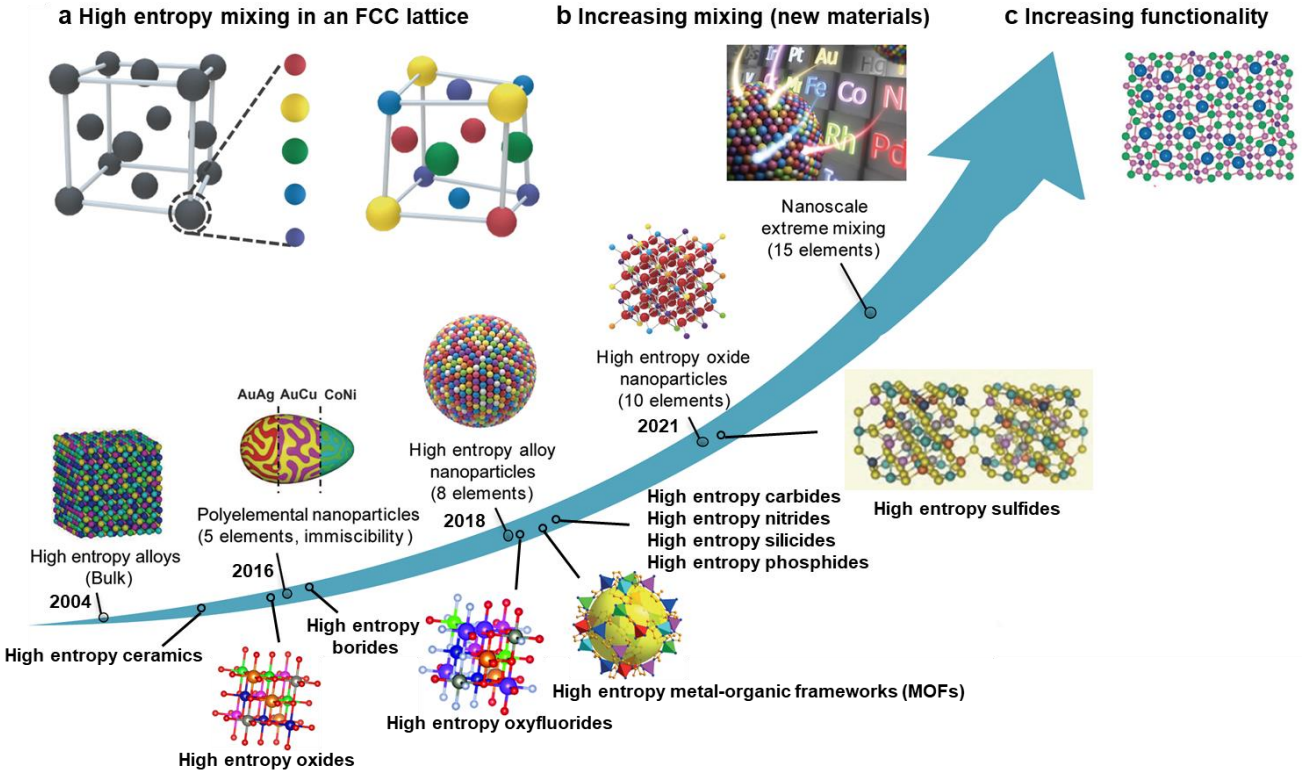

Figure 3.11. (a) Schematic showing high-entropy mixing in a face-centered cubic lattice. (b, c) Development of HEMs with multielemental composition and enhanced functionality.

3.4.1. High–Entropy Concept

Because the earliest HEMs were alloys, their definition is primarily based on HEAs principles. HEAs are characterized in two main ways: by their compositional structure, which includes multiple principal elements, and by their configurational entropy, which represents the degree of atomic disorder resulting from these elements. The former involves a composition of at least five dominant elements within a single-phase crystal structure, each being between 5% and 35% of the atomic percentage.[76] The later defines HEAs with the configurational entropy (ΔS_{conf}) greater than $1.5R$, where the ideal ΔS_{conf} for a random solid solution can be generally expressed as an **Equation 3.4** derived from the Boltzmann and Gibbs interpretation of entropy.[89]

$$\Delta S_{\mathrm{conf}} = -R\left(\sum_{\mathrm{i}=1}^{\mathrm{n}} x_{\mathrm{i}} \ln x_{\mathrm{i}}\right) \qquad \textbf{(Equation 3.4)}$$

In this equation, the R is the ideal gas constant, the molar fraction of the i^{th} component is represented by x_{i}. For a number of components n, the configurational entropy reaches the largest value when the atomic fraction is the same for all components ($x_1 = x_2 = x_3$ and so on). In this case, the configurational entropy per mole is:[103]

$$\Delta S_{\mathrm{conf}} = -R\left(\tfrac{1}{n}\ln\tfrac{1}{n} + \tfrac{1}{n}\ln\tfrac{1}{n} + \cdots \tfrac{1}{n}\ln\tfrac{1}{n}\right) = -R\ln\tfrac{1}{n} = R\ln n. \qquad \textbf{(Equation 3.5)}$$

In this equation, the $^1/_n \ln {}^1/_n$ terms correspond to the number of incorporated elements.

The concept of high-entropy was later extended to oxides and other systems. Therefore, the configurational entropy of HEMs can be obtained from **Equation 3.6**:

$$\Delta S_{\mathrm{conf}} = -R[(\sum_{\mathrm{i}=1}^{\mathrm{n}} x_{\mathrm{i}} \ln x_{\mathrm{i}}) + (\sum_{\mathrm{j}=1}^{\mathrm{m}} x_{\mathrm{j}} \ln x_{\mathrm{j}})] \quad \textbf{(Equation 3.6)}$$

In this equation, x_{i} and x_{j} correspond to the molar fraction of the i^{th} and j^{th} component of the respective sublattice, respectively. The n and m represent the number of elements in the sublattices.

For equiatomic materials containing 4, 5 and 6 elements, the ΔS_{conf} value is $1.39R$, $1.61R$ and $1.79R$, respectively. As a result, materials are generally classified as high-entropy ($\Delta S_{\mathrm{conf}} > 1.5R$), medium-entropy ($1.0R < \Delta S_{\mathrm{conf}} < 1.5R$) and low-entropy materials ($\Delta S_{\mathrm{conf}} < 1.0R$).[104] Hence, HEMs must contain more than 4 elements in a single-phase crystal structure with a resultant configurational entropy exceeding $1.5R$.

In HEMs, the change in Gibbs free energy resulting from the introduction of individual elements (ΔG_{mix}) is influenced by alterations in enthalpy (ΔH_{mix}), representing the energy required to mix elements in a single-phase structure and entropy (ΔS_{mix}). This relationship is described by the equation:[105]

$$\Delta G_{\mathrm{mix}} = \Delta H_{\mathrm{mix}} - T\Delta S_{\mathrm{mix}} \quad \textbf{(Equation 3.7)}$$

In this equation, T represents temperature. The interaction between ΔH_{mix} (typically positive) and $-T\Delta S_{\mathrm{mix}}$ (typically negative, reflecting the entropy change) can occasionally result in $-T\Delta S_{\mathrm{mix}}$ counterbalancing ΔH_{mix}, leading to a more negative ΔG. This phenomenon, known as "entropy stabilization", favors the dominance of a single-phase structure at higher temperatures.[105] Entropy stabilization, however, occurs only under specific energetic conditions and is often challenging to demonstrate.

To calculate the total entropy of a solid, in addition to configurational entropy, it is essential to account for other contributions such as vibrational, electronic, and magnetic entropy.[105] While vibrational entropy can significantly impact a material's properties, its absolute value alone does not determine the relative phase stabilities.[106] Further investigations have also revealed cases where vibrational entropy decreases as the number or diversity of elements increases, complicating its role in predicting phase stabilities.[107,108] Thus, considering these findings, configurational entropy remains the key factor when adding elements, though other entropy types are also important.

3.4.2. The Impacts of High–Entropy Approach

Yeh proposed a set of four core effects for HEMs: the high entropy effect, sluggish diffusion effect, lattice distortion effect, and cocktail effects,[109,110] as displayed in **Figure 3.12**. The high-entropy effect plays a role in thermodynamics by promoting the formation of multi-element solid solutions in the equilibrium state, particularly at high temperatures. The number of phases is far lower than the maximum number predicted by the Gibbs phase rule.[109] This implies that high mixing entropy enhances the mutual solubility among elements and prevents phase separation into terminal solution phases or intermetallic compounds. The high entropy effect promotes a random distribution of atoms within the crystal lattice. The random distribution of atoms leads to local deviations from the ideal atomic positions that would be occupied if the material were composed of a single or a few primary elements. The constituent elements often have different atomic sizes and chemical properties. When these elements are randomly distributed across the lattice sites, it can lead to mismatches in atomic sizes and local coordination environments.[109] For example, a smaller atom may find itself surrounded by larger atoms, leading to strained or distorted lattice configurations. Lattice distortions play a crucial role in determining the mechanical, thermal, and chemical properties of HEMs. Local distortions can hinder dislocation movement and enhance the material's resistance to deformation, thereby improving its strength and hardness. However, excessive lattice distortions in HEMs can indeed have negative effects on ductility and toughness. The sluggish diffusion effect profoundly influences the rate of phase transformations. In materials such as HEAs, these transformations rely on cooperative atomic diffusion to achieve equilibrium partitioning among phases. However, lattice distortion within HEAs can impede atomic movement, thereby restricting the overall diffusion rate.[110] HEMs exhibit not only the fundamental characteristics of their constituent elements but also synergistic interactions between these elements, often referred to as "cocktail effects". The cocktail effects were firstly proposed by Ranganthan,[111] which often exhibit tailorable versatility as well as unprecedented properties of HEMs.

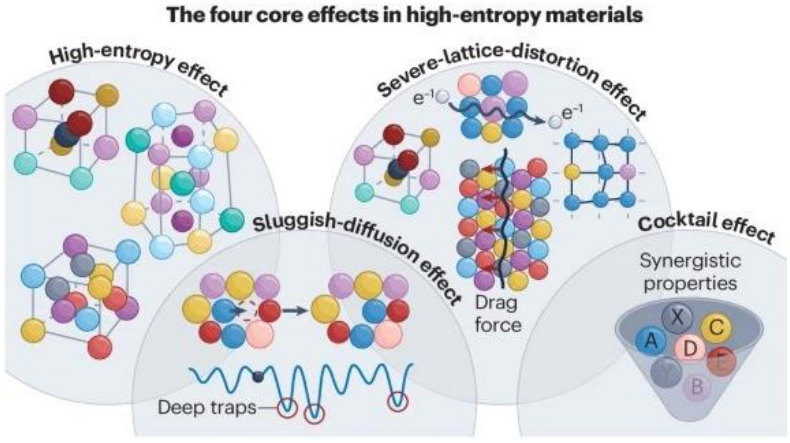

Figure 3.12. Schematic of four core effects of high-entropy materials, from ref[110].

3.4.3. High–Entropy PBAs (HEPBAs)

In this dissertation, the high-entropy approach is applied to a series of PBA compounds, which are subsequently utilized in both SIBs and printed memristors. Both fields of issues can be properly addressed with HEPBAs, since the structure is suitable for both applications and the properties can be fine-tuned by a careful change of stoichiometry and elemental composition using high-entropy means. More specifically, the chemical composition of PBAs is generally expressed with $Na_xM[Fe(CN)_6]_y$, where the M position could be tailored by high-entropy approach. The strategy of introducing the high-entropy approach can be achieved by substituting M ions with Fe, Mn, Co, Ni, Cu, Zn etc. The entropy site can only be formed on the M site (i.e. N-coordinated site), as the chosen synthesis based on $Na_4Fe(CN)_6$ as starting material does not allow a variation of the C-coordinated site, and the C-coordinated site is quite challenging to substitute under room and low temperature synthesis condition. When the M positions are exclusively occupied by Mn, resulting in compounds, i.e., $Na_xMn[Fe(CN)_6]_y$, they are referred to as Prussian white materials (PWs), owing to their characteristic white powder appearance. **Figure 3.13a** shows cubic structural HEPBAs obtained by introducing equimolar Fe, Mn, Cu, Ni and Co to the same lattice site of M in the $Na_xM[Fe(CN)_6]_y$. Configurational entropy values depend on the number of elements, as illustrated in **Figure 3.13b**. The high-entropy environment in PBAs introduces cocktail effects, which induce mixing and can yield elemental states that are not achievable with binary or ternary materials.

In short, the ability to tailor properties through high-entropy design endows PBAs with flexible compositions and diverse functionalities, thereby broadening their scope of applications. Due to the compositional change, cocktail effects and lattice distortions, the application of the high-entropy approach results in various improvements with regards to the electrochemical properties and structural stability, as further described in Chapter 5, 6 and 7.

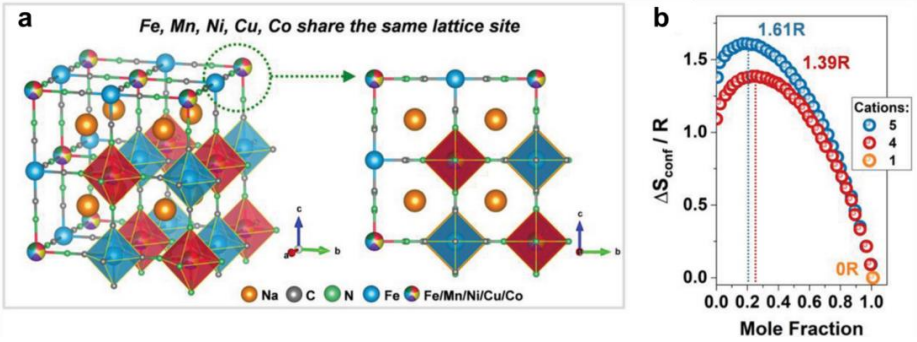

Figure 3.13. (a) Schematic illustration of the crystal structure of HEPBAs with 5 equimolar metals. (b) Dependence of configurational entropy on the number of elements.

Part II. Theory and Background

4. Experimental Methods

4.1. Fundamentals and Measurement Techniques

This section provides an overview of the primary characterization techniques employed for material analysis in this dissertation. These techniques include： X-ray diffraction (XRD), thermogravimetric analysis (TGA), differential scanning calorimetry (DSC), scanning electron microscopy (SEM), transmission electron microscopy (TEM), X-ray photoelectron spectroscopy (XPS), transmission X-ray absorption spectroscopy (XAS), X-ray emission spectroscopy (XES) and inductively coupled plasma optical emission spectroscopy (ICP-OES).

4.1.1. Powder X–Ray Diffraction (XRD)

Powder XRD is a useful technique for determining the crystal structure of bulk materials by analysing the diffraction patterns of X-rays passing through powdered samples.[112] **Figure 4.1** illustrates the basic principles of diffraction. It uses electromagnetic radiation of wavelength in the same order of magnitude as the interatomic distances in the crystal lattice. Given that X-rays typically have wavelengths around 1 Å, they effectively produce diffraction patterns that reflect the arrangement of atoms in the material. X-rays are generated when an electron beam hits a target material (such as Cu, Mo, Ag, Ga and so on): electrons are emitted from a hot cathode (e.g., fine tungsten filament) due to thermionic emission and accelerated in an electric field to collide with the water-cooled target (anode). The X-rays are elastically scattered at each atom. As it encounters multiple sets of crystalline planes within the material, the radiation scattered by each plane interacts with that from other planes. This interaction leads to constructive and destructive interference patterns, which are fundamental in determining the crystal structure through diffraction analysis. At some particular angles, the scattering follow Bragg's law:[113,114]

$$n\lambda = 2d\sin\theta \qquad \textbf{(Equation 4.1)}$$

(n is an integer, λ is the wavelength of the incident radiation and d is the interatomic distance, and θ is the incident angle).

As shown in **Figure 4.1**, the two X-ray beams having identical wavelength are scattered by two successive crystal lattice planes. The distance of the two crystal lattice planes is *d*. If beam II travels an extra length of $2d\sin\theta$ (i.e., path difference between the X-rays is $2d\sin\theta$) compared to beam I, and this path difference is an integer number of wavelengths. These mean that the two waves will interact constructively once they meet, which results in strengthened signal and makes it possible to detect the diffracted radiation by X-ray detector. However, if the extra distance is not an integer multiple of the

wavelength, it will lead destructive interaction, i.e., the electromagnetic waves cancel each other out, and no radiation can be detected.[114,115] In this dissertation, the XRD patterns of samples were collected using a STOE STADI P diffractometer (Mo source, λ = 0.70932 Å) in the range of 5° < 2θ < 35° in transmission geometry or a STOE STADI P diffractometer with a Ga-jet X-ray source (Ga-K_β radiation, λ = 1.20793 Å) in the range of 10° < 2θ < 55° or EMPYREAN SERIES 3 (Cu source, λ = 1.5406 Å) in the 2θ range of 10°–60°. Rietveld refinements were performed by Dr. Damian Goonetilleke (KIT), and Dr. Simon Schweidler (KIT).

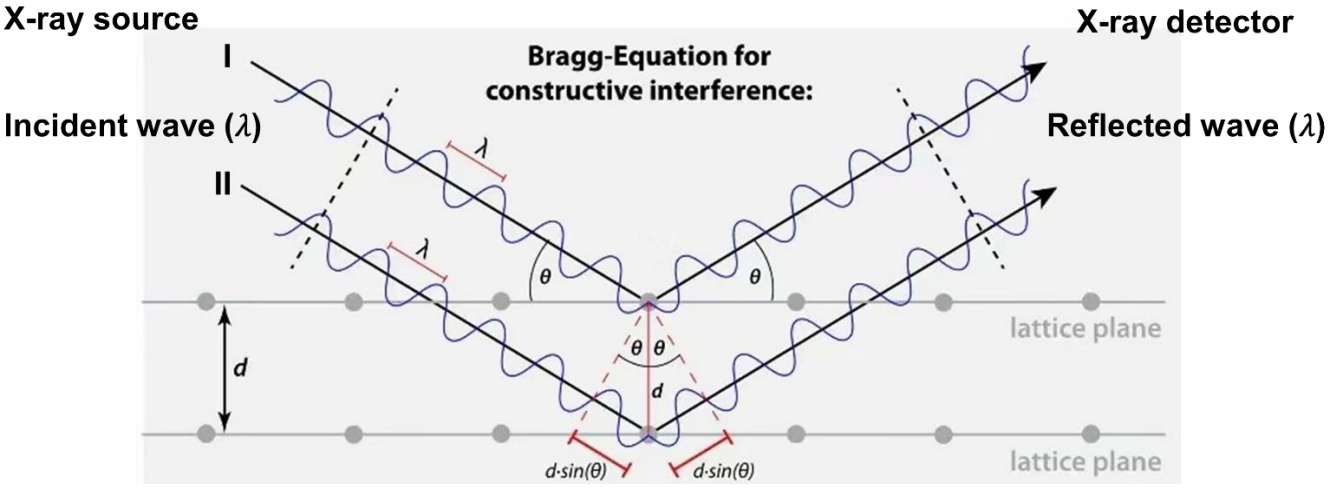

Figure 4.1 The schematic of working principle for an XRD device. The X-ray source and the detector are symmetrically rotated as the degree θ change. The black dots stand for atoms in a crystal plane, with two planes at a distance d apart, from ref[114].

4.1.2. Thermogravimetric Analysis (TGA)

TGA is used to assess the thermal stability of materials by measuring changes in the sample's mass as the temperature changes. The sample is heated in a given environment (air, N_2, CO_2, He, Ar, etc.) at controlled rate. In this thesis, TGA was performed at a heating rate of 5 °C min^{-1} under Ar atmosphere using a TA Instruments Q5000 device. This measurement provides some physical phenomena, such as absorption, desorption as well as chemical phenomena including chemisorption, thermal decomposition, and solid-gas reactions (e.g., oxidation or reduction).

4.1.3. Differential Scanning Calorimetry (DSC)

DSC is a thermal analysis technique that measures the heat flow associated with material transitions as a change of temperature. In this dissertation, DSC was performed from room temperature to 500 °C at a heating and cooling rate of 5 °C min^{-1} with Al-crucible under Ar using NETZSCH DSC 204F1

Phoenix. The content of crystal water (n) was estimated from the weight loss in the temperature range of 40–130 °C. For this purpose, the specific enthalpy of dehydration ($\Delta H, J/g$) was used, which can be estimated as follows:

$$\Delta H = \int_{t1}^{t2} \frac{q}{m} dt, \qquad \textbf{(Equation 4.2)}$$

where q, m, and t represent the heat flux (mW), mass (mg), and time (s), respectively.[116,117] The molar enthalpy of dehydration is estimated to be 15.81 kJ mol^{-1}.[117] The total molar content in the measured sample ($n_{\mathrm{H_2O,total}}$) is estimated according to:

$$n_{\mathrm{H_2O,total}} = \frac{\Delta H}{15.81 * 1000}. \qquad \textbf{(Equation 4.3)}$$

Then, the content of crystal water per mol (x) is derived from:

$$n_{\mathrm{H_2O,total}} = \frac{m_{\mathrm{sample}}}{M_{\mathrm{sample}}} * x, \qquad \textbf{(Equation 4.4)}$$

where m is measured sample mass (g) and M_{sample} represents the molar mass (g mol^{-1}). The M_{sample} is calculated via:

$$M_{\mathrm{sample}} = M_{\textit{without crystal water}} + xM_{\mathrm{H_2O}}. \qquad \textbf{(Equation 4.5)}$$

DSC measurement was assisted by Jing Lin (KIT).

4.1.4. Scanning Electron Microscopy (SEM)

As shown in **Figure 4.2a**, a primary electron beam emitted from an electron gun is used to scan the surface of materials. The primary electrons interact with sample electrons at the surface and produce different scattering signals, for instance, backscattered electrons, secondary electrons and X-rays, to deliver materials information of morphology and composition.[118] There are different detectors since such different interactions of the primary electrons with the sample. **Figure 4.2b** illustrates the different signals from the electron beam with the sample. Backscattered electrons originate from the elastic scattering of primary electrons across a wide region within the interaction volume. So they are elastically scattered by the electric field of the sample atoms, and interact with the materials directly. As displayed in **Figure 4.2b**, backscattered electrons have a penetration depth of several hundred nanometers, relying on the sample nature and beam energy.[118] The backscattered electrons detectors are positioned above the sample, arranged concentrically around the electron beam in a “doughnut” configuration. In contrast, the inelastic scattering of primary electrons results in the ejection of secondary electrons, which primarily originate from the surface or near-surface regions of the sample. In this case, electrons lose energy as they interact with the sample’s electrons, often causing excitations. This is typically involved in weakly bound valence electrons from the sample atoms, which results in

low kinetic energies of secondary electrons (only a few eV) and thereby leading to limitation of the depth that they can escape the sample to a few nanometers. The secondary electrons detector is positioned on the side of the electron chamber at an angle (see **Figure 4.2a**). They are very beneficial for the inspection of the topography of the sample's surface. The aforementioned two types of electrons are the most commonly used signals by SEM users for imaging.

Finally, the X-rays (produced by inelastic scattering) originate from the energy difference when an outer-shell electron transitions to an inner-shell vacancy created by the ejection of an inner-shell electron from an atom in the sample. The production of X-rays occurs in two stages: ionization followed by relaxation. In detail, an incident electron from the SEM beam collides with an inner-shell electron of an atom in the sample, causing the ejection of the inner electron and creating a vacancy. This ionizes the atom and puts it in an unstable state. To regain stability, an outer-shell electron relaxes to fill the vacancy, releasing energy in the form of X-rays. Since each element has specific ionization energies for each subshell, the difference between these energies is characteristic of the element that produces the X-ray photon. The X-rays detection is equipped with an energy-dispersive X-ray spectroscopy (EDS) detector to investigate the elemental distribution of the sample surface.[119] EDS operates by measuring the energy and intensity of X-rays emitted from a sample. High intensities or brighter colors indicate areas with higher element concentrations, while low intensities or darker colors correspond to regions with lower concentrations. In this thesis, the morphology of samples was characterized by Zeiss LEO 1530.

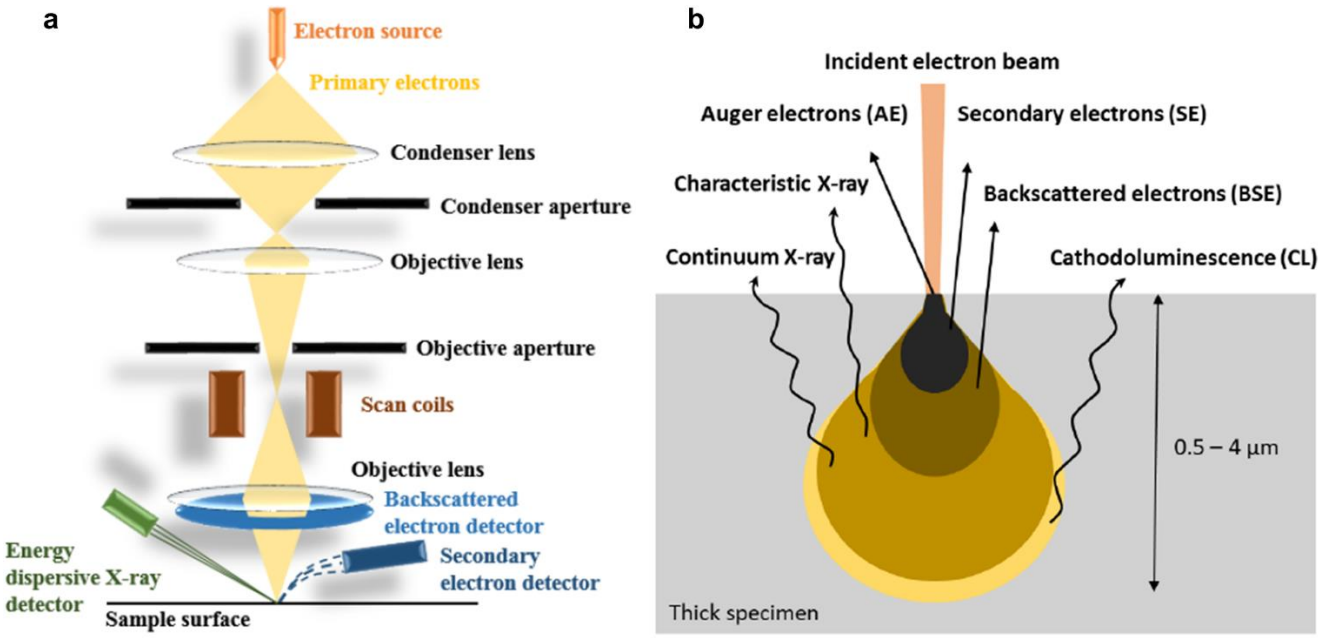

Figure 4.2. (a, b) The schematic of working principle for an SEM microscope and corresponding illustration of different signals from beam with a sample, from ref.[119].

4.1.5. Transmission Electron Microscopy (TEM)

TEM is an essential and powerful tool for characterizing structure of samples, providing insights into their morphology, compositions, crystal lattice and even atomic-level details.[120] As shown in **Figure 4.3**, it uses a high-energy electron beam generated by an electron gun, typically operating between 80 to 300 keV. These electrons possess very short wavelengths, allowing for high-resolution imaging. The sample depth has to be thin (typically less than 100 nm), to ensure sufficient electrons transmission through the material.[121] When the electron beam passes through the specimen, it interacts with the sample's atoms. This interaction results in different types of electron scattering, including both elastic and inelastic scattering. In principle, both elastically and inelastically scattered electrons provide information about the specimen. The transmitted (unscattered) and scattered electrons are collected to form an image. Different imaging modes, such as bright-field and dark-field, are achieved by selectively allowing or blocking specific electrons to create contrast in the image. The most commonly used mode is bright-field imaging, where only unscattered electrons pass through the objective aperture to create an image. For further structural insights, dark-field imaging is employed by blocking the central, unscattered electrons and allowing only scattered electrons to contribute to the image. This mode provides enhanced contrast for features such as specific crystal orientations or lattice defects, as these structural elements scatter electrons uniquely, making them stand out against the background. Finally, high-resolution TEM (HRTEM) combines both scattered and unscattered electrons to produce interference patterns that reveal atomic-level detail. This phase-contrast technique enables the direct visualization of lattice structures, inter-atomic distances, and individual atomic columns, allowing for high-resolution study of crystal defects and nanoscale structure.

In this dissertation, high-angle annular dark-field scanning TEM (HAADF STEM) measurements were performed on a Thermo Fisher Themis Z equipped with a probe-corrector (S-CORR) at 300 kV. The element distribution was determined by drift-corrected mapping via energy-dispersive X-ray spectroscopy (EDS) utilizing a Thermo Fisher Super-X detector. TEM measurement was performed by Dr. Yushu Tang (KIT) and Yuting Dai (KIT).

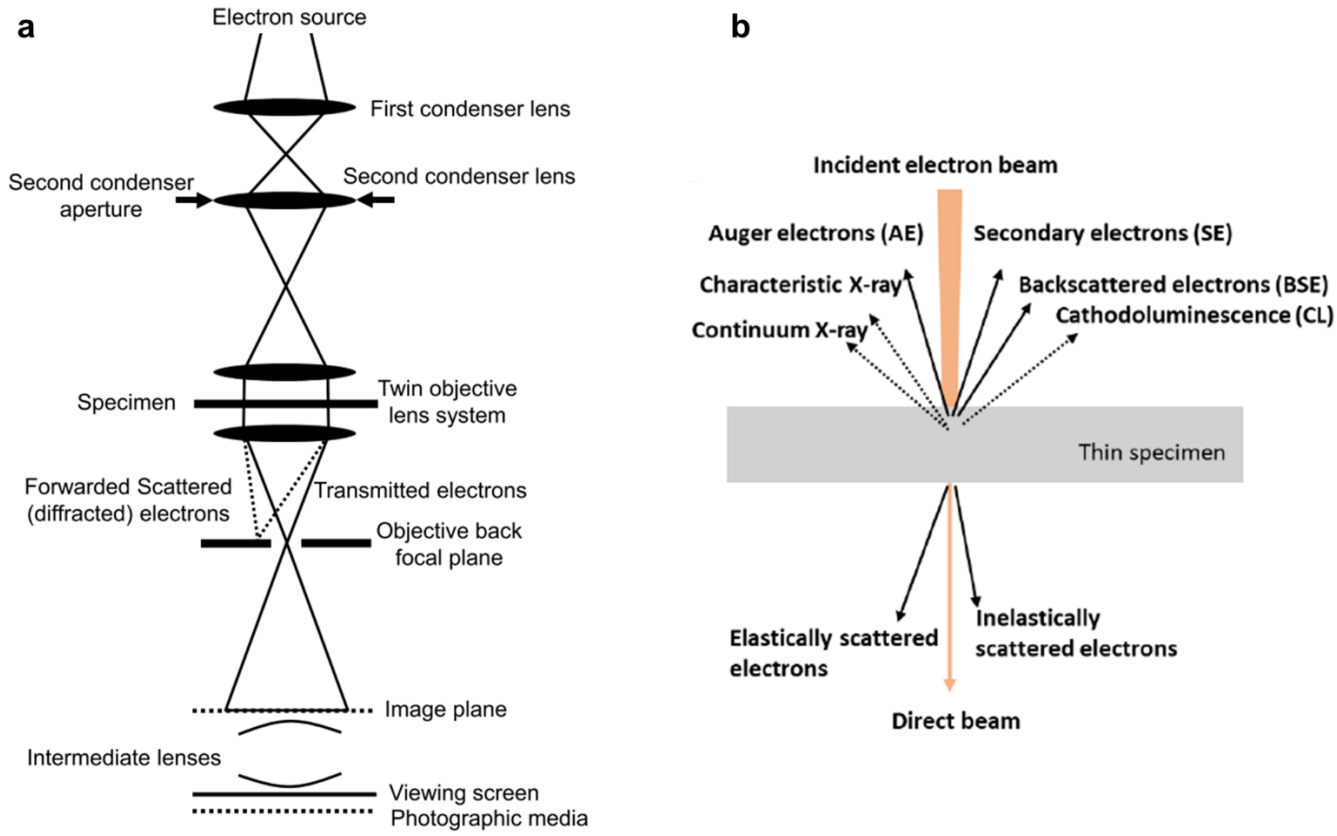

Figure 4.3. (a, b) The schematic of working principle for a TEM microscope, and corresponding illustration of different signals from beam with a thin specimen, from ref[122].

4.1.6. X–Ray Photoelectron Spectroscopy (XPS)

XPS is a technique based on the photoelectric effect that analyses the composition, chemical state, electronic structure, and density of electronic states of elements at the surface of a material.[123,124] The depth of analysis in XPS is limited to top few nanometers of a sample surface. This is because electrons generated deeper within the material undergo interactions with atoms above them before they can escape into the vacuum and be detected by the instrument.[121] X-rays (photons) are shot onto a sample (**Figure 4.4**, see below), and when electrons in the sample absorb enough energy, they are ejected from the sample with a certain kinetic energy. The energy of those ejected electrons is analyzed by a detector and a lot of these energies and relative numbers of electrons are produced. Electrons with different energies follow different paths through the detector, which allows the computer to differentiate the electrons and produce the spectra.

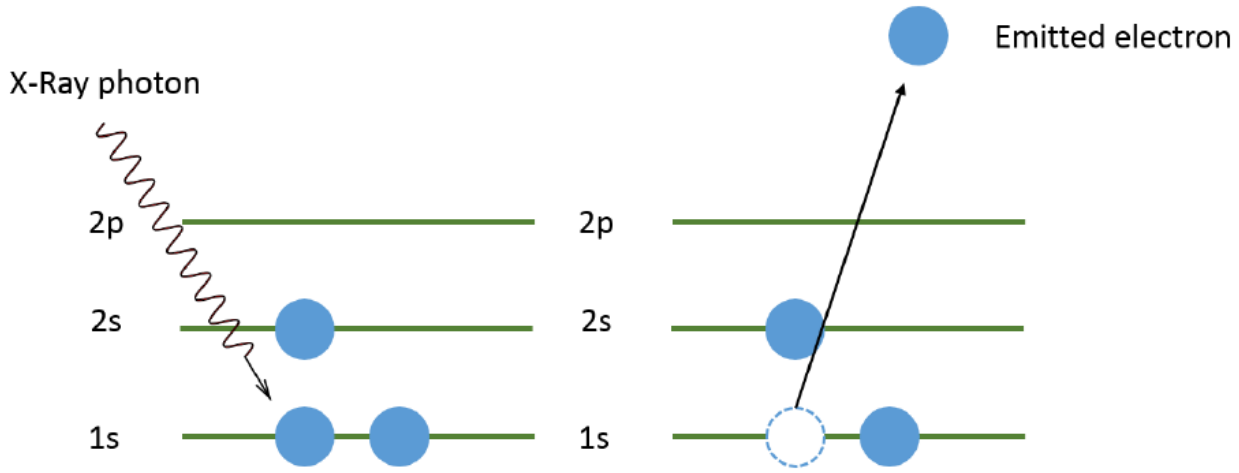

Figure 4.4. Scheme of electrons (blue circles) in the different energy levels of a lithium atom, and how the photoelectric effect works on it: when an electron absorb X-ray photon (left), it gets ejected from the atom (right).

The binding energy (refer to $E_{binding}$) is a measure of how much energy is required to remove an electron from the orbit of an atom. It can be determined as below:[121]

$$E_{binding} = E_{photon} - (E_{kinetic} + \emptyset) \quad \textbf{(Equation 4.6)}$$

Photon energy (E_{photon}) is the energy of X-ray photons being used by the spectrometer, the kinetic energy ($E_{kinetic}$) is the energy of the ejected electrons from the sample and measured by the detector, and $\emptyset$ is the work function of the spectrometer.

As electrons are in orbitals farther from the nucleus, less energy is required to eject them, so the binding energy is lower for higher orbitals. Electrons contained in different subshells (s, p, d, etc.) have different energies as well. By detecting the energy of electrons emitted from a material, XPS allows for the composition of a material to be determined. XPS depends not only on the electron's shell but also on its chemical environment. Specifically, it reflects the interactions and bonds that the atom forms within its molecular or crystalline structure. This sensitivity allows XPS to differentiate between different chemical states of the same element based on how electrons are bound in different molecular environments or chemical bonds. Thus, XPS provides detailed information about the chemical composition and bonding configurations of the surface layer of materials.

In this dissertation, XPS measurements were performed on a SPECS XPS system with PHOIBOS 150 energy analyzer using monochromatic Al-K_α radiation (1486.6 eV) with pass energies at the electron analyzer of 30 eV (for detail scans) and 90 eV (for survey scans). The take-off angle was set to 45°. The C1s peak of adventitious carbon at 284.8 eV was used for calibration of binding energies. XPS measurements were conducted by Dr. Thomas Diemant (HIU).

4.1.7. Transmission X–Ray Absorption Spectroscopy (XAS)

XAS as a well-established characterization technique is widely used to investigate the oxidation state, site symmetry, and coordination environment of materials.[125] XAS is based on the interaction between X-rays and matter, particularly the absorption of X-rays by core-level electrons in an atom. When the energy of the incident X-ray matches or exceeds the binding energy of a core electron, the electron is ejected (photoelectric effect). This causes an increase in absorption at a specific energy, known as the absorption edge. Absorption features provide information about electronic transitions and local atomic environments. Generally, XAS can be assigned into the soft (<2000 eV) and hard (>2000 eV) X-ray regime, based on the photon energy of the incident X-ray beam. Soft XAS is used to measure lighter elements, focusing on the *K*-edges of elements like C, N, and O and the *L*-edges of transition metals. It has a lower penetration depth, typically in the nanometer range, making it highly sensitive to surface properties and thin films. In contrast, hard XAS is better suited for heavier elements, targeting the *K*-edges of elements like Fe, Ni, and Cu and the *L*-edges of heavier elements, such as rare earths. It offers a much higher penetration depth, often reaching up to several millimeters, enabling the study of bulk materials and operando condition. The X-ray absorption near edge structure (XANES) covers the energy range up to 50 eV from pre-edge and the extended X-ray absorption fine structure (EXAFS) starts above the XANES region reaching up to several hundreds of eV above the main edge. In the XANES, the pre-edge feature arises from transitions of a core electron (e.g., from the 1s state) to specific unoccupied states, such as nd or hybridized orbitals, depending on the element and its local chemical environment. In contrast, EXAFS is a phenomenon that occurs beyond the absorption edge and is caused by the scattering of the ejected photoelectron by surrounding atoms. Therefore, XANES provides information about the electronic structure, oxidation state, and chemical environment near the absorbing atom, while EXAFS analyses oscillations beyond the absorption edge to determine bond lengths, coordination numbers, and disorder in the local structure. The *K*-edge corresponds to the excitation of a 1s-core level electron. The L_1-edge pertains to the excitation of a 2s-electron, while the L_2 and L_3-edges correspond to the spin-orbit split $2p_{1/2}$ and $2p_{3/2}$ levels and so on for M_1 and M_5.

X-ray emission spectroscopy (XES) is a technique used to study the electronic structure of a material by analysing the characteristic X-ray photons emitted after the material interacts with high-energy X-rays. As shown in **Figure 4.5**, when the incident X-ray energy (E) is absorbed by an atom in the sample, the photon energy at the edges is sufficient to excite an electron from a strongly bound core level (e.g., 1s) to a high-energy unoccupied state above the Fermi energy, resulting in the electron being ejected beyond the ionization limit into the continuum of states.[126] The atom is left in an excited state with an empty electronic level (a core hole). A short time later, a higher-lying electron decays and the core

state is eventually filled with electrons of lower binding energy, emitting a fluorescent X-ray or an Auger electron (see **Figure 4.5**). The Auger electrons can further undergo inelastic scattering with other electrons in the sample, leading to a cascade of low-energy secondary electrons. The energy of the emitted X-ray is characteristic of the element and its electronic environment. The emitted X-rays are collected and analysed to produce an emission spectrum. *K*α transition occurs when an electron from the *L*-shell (2p orbital) fills a vacancy in the *K*-shell (1s orbital). *K*β transition occurs when an electron from the *M*-shell (3p or 3d orbital) transitions to fill a vacancy in the *K*-shell (1s orbital).

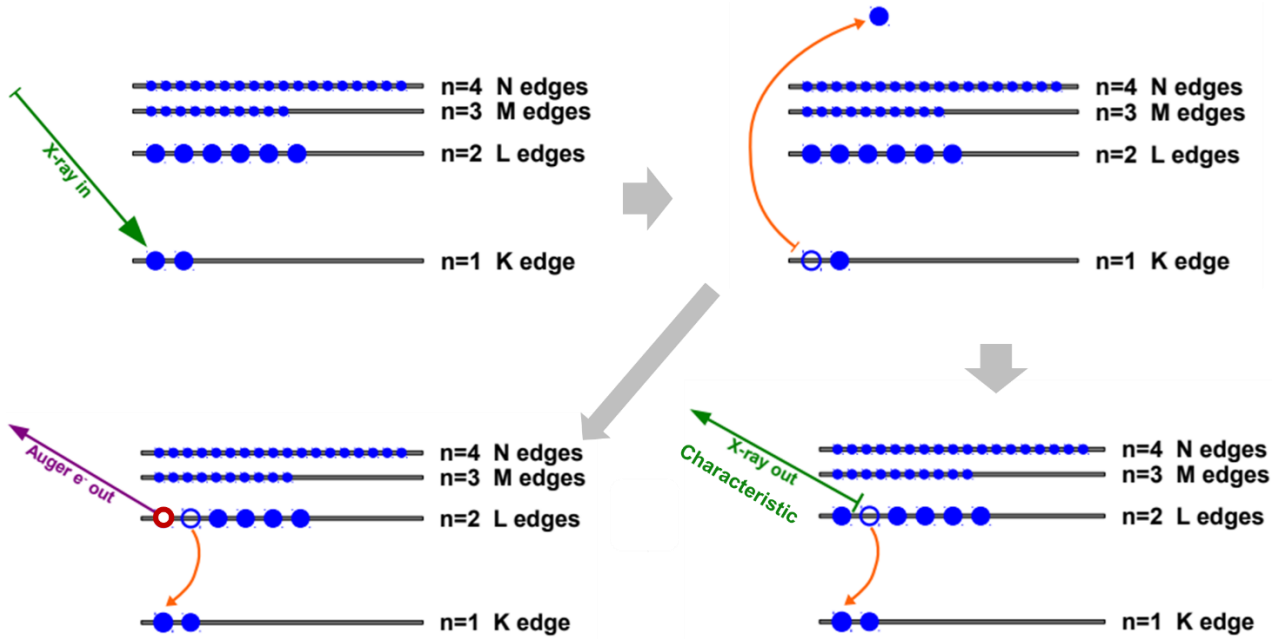

Figure 4.5. The schematic of working principle of XAS.[125] An incident X-ray of energy E is absorbed, destroying a core electron of binding energy E^0 and emitting a photo-electron with kinetic energy ($E - E^0$). The core state is eventually filled, ejecting a fluorescent X-ray or an Auger electron. When the incident X-ray energy is larger than the binding energy, there is a sharp increase in absorption.

XAS was performed using a laboratory Rowland-circle based instrument (easyXAFS300+, easy XAFS LLC, Renton, WA, USA).[127] The Mn, Fe, Co, Ni and Cu *K*-edges were measured on pelletized samples, with active materials diluted by cellulose, together with selected reference standards. For the Mn and Fe *K*-edges, the mass loading of HE-PW and Mn-PW was calculated such to obtain a 1 to 1.5 unit-edge step;[128] the Co, Ni and Cu *K*-edges of HE-PW were measured with a mass loading allowing for a compromise between total absorption and signal-to-noise ratio due to low concentrations. An energy step of 0.25 eV was used for the XANES region and a step of 0.03 $Å^{-1}$ for the post-edge region. Multiple scans were collected for each sample. Metal reference foils (Goodfellow or Exafs Materials, Danville, CA, USA) were used for energy calibration and monitoring the energy drift. The absorption

spectra were calculated according to the transmission relation $\mu(E) \approx \ln(I_0/I_t)$ through a python-based software (easy XAFS LLC, Renton, WA, USA), which was also used for dead time correction and energy calibration.

X-ray emission spectroscopy (XES) was performed on the Mn- and Fe-*K*β emission lines. An industrial Pd tube source (VAREX) was operated at 35 kV and 2 mA, and the sample fluorescence was analyzed and refocused at the detector position through the 0.5 mm slit. To obtain better quality extended X-ray absorption fine structure (EXAFS) data, synchrotron transmission XAFS was conducted on the Mn, Fe, Co, Ni and Cu *K*-edges for HE-PW at the ROCK beamline (SOLEIL synchrotron). More details on sample preparation and data acquisition are provided elsewhere.[101]

The XAFS data were further analyzed using the Larch software.[129] Absorption spectra were normalized by regressing polynomials to the data before and after the edge step, then subtracting the pre-edge polynomial from the spectra and dividing by the edge step. Normalized XANES spectra were compared with standards of well-known oxidation states. EXAFS spectra were extracted using the AUTOBK algorithm,[130] with the χ(k) data being isolated by subtracting a smooth background polynomial with R_{bkg} = 1. The magnitude ($|\chi(R)|$) of the Fourier transformed (FT), k^3-weighted χ(k) was obtained after applying a Hanning window function over an appropriated data range. XES *K*β emission spectra were normalized using the peak maximum intensity. Dr. Yang Hu (HIU) assisted in XAS, XES and XAFS measurements and analysis.

4.1.8. Inductively Coupled Plasma Optical Emission Spectroscopy (ICP–OES)

The composition of the sample is analysed by ICP-OES.[131] Usually samples dissolved in acid solution are nebulized and transported into a plasma environment. Plasma is the forth state of matter, next to the solid, liquid and gaseous state. The plasma is extremely hot, 6000-7000 K. In the induction zone it can even reach 10000 K. In the torch desolvation, atomization and ionization of the sample take place. In such case, the atoms of the elements experience excitation, wherein their electrons are promoted to higher energy levels. These excited electrons drop back to ground state give rise to the emission of light (photons). Each element has an own characteristic emission spectrum (characteristic wavelengths), and it could be detected by an optical spectrometer. The intensity of the emissions from various wavelengths of light are proportional to the concentrations of the elements within the sample.[132] Hence, the ICP-OES technique enables the identification and quantification of different elements in the sample. In the Chapter 5, 6 and 7, ICP-OES was carried out on a SPECTRO ARCOS SOP instrument.

4.2. Battery Fabrication and Testing Techniques

This section provides fabrication process of SIBs as well as the specific characterization techniques employed in Chapter 5 and 6.

4.2.1. Electrode Preparation

Electrode tapes were made from the active material (70 wt.%), Super C65 carbon black (TIMCAL Ltd., 20 wt.%) and polyvinylidene difluoride (PVdF 5130, Solvay, 10 wt.%), dispersed in N-methyl-2-pyrrolidone (NMP, Sigma-Aldrich) using a Thinky ARE-250 mixer (two times, each for 3 min). The resulting slurry was uniformly coated onto Al foil by a laboratory doctor blade (150 µm wet-film thickness) and then dried in a vacuum at 120 °C for 24 h. The electrodes were punched into circular disks of 13 mm diameter and further dried for 10 h at 120 °C. The active material loading was about 1.5 mg cm^{-2}. The specific energy of the cells is calculated by integration of voltage with the specific capacity.

4.2.2. Cell Assembly

Sodium metal was used as counter and reference electrode, glass microfiber filter (GF/D, Whatman) as separator and 1 M $NaClO_4$ in ethylene carbonate/dimethyl carbonate/propylene carbonate (EC:DMC:PC, 1:1:1 by volume) with 5% fluoroethylene carbonate (FEC) as electrolyte. All cells were assembled in an Ar glovebox (MBraun UNIlab, with [H_2O] and [O_2] < 0.1 ppm). Major electrochemical measurements were performed in climatic chambers with a set temperature of 25 (±1) °C, while the cycling performance for high temperature was tested at 50 °C.

Full cell fabrication process: the cathode was prepared as described above. The anode was fabricated by spreading a slurry of hard carbon, Super C65, and PVdF (weight ratio: 8:1:1) onto the Cu foil. To activate the anode, the hard carbon was initially discharged and charged for 2 cycles at 10 mA g^{-1} between 0.02 − 2.0 V (vs. Na^+/Na) in a hard carbon||Na metal cell and then charged to 0.5 V (vs. Na^+/Na) to obtain the pre-cycled hard carbon anode for assembling the HEPBA||pre-cycled hard carbon full cell. To construct the full cell, the mass ratio of HEPBA cathode to hard carbon was calculated to be 2 to 1. The calculation of the specific capacities and energy densities for full cells was based on the mass of cathode materials in the cells.

4.2.3. Electrochemical Characterization

Galvanostatic cycling

Galvanostatic cycling (also known as constant current or charge/discharge experiments) is the most fundamental technique to evaluate the performance of a battery. A constant current is applied to the counter electrode and the working electrode. When one of the cut-off potentials is reached or a defined time is passed, the current is reversed. Galvanostatic cycling was carried out using either MACCOR (Model 4300) or LAND (CT3001A) battery test systems in standard CR2032 coin cells in this dissertation.

Cyclic voltammetry

Cyclic voltammetry (CV) is a potentiodynamic analysis technique allowing the investigation of electrochemical processes. CV was measured in the same potential range using a VMP3 potentiostat (BioLogic).

Theoretical capacity

The theoretical capacity is calculated using the equation:

$$Capacity = \frac{nF}{3600 \times M} \quad \textbf{(Equation 4.7)}$$

where n is the number of electrons involved in the electrochemical process, F is Faraday constant (F=96500 C/mol) and M is the molecular weight of active material used in the electrode.

Capacity retention

Capacity retention, which is always used to evaluate cycling stability, is the ratio of discharge specific capacity to initial discharge specific capacity for the cycles. The cycling stability and lifetime of a cell are determined by the number of cycles for which the capacity retention is higher than 80%.

Capacity rate

Charge and discharge rates of a battery are determined by capacity rate (C-rates). In this dissertation, 1 C is assumed to equal 100 mAh g^{-1} for PBA materials. This means that the capacity of a battery is rated based on discharging at 100 mA for 1 h. For example, if a battery is discharged at 0.5 C, it would provide 50 mA for 2 h, and at 2 C, it would deliver 200 mA for 30 min.

Coulombic efficiency

The Coulombic efficiency is used to describe the electrochemical reversibility. It refers to the ratio of the discharge capacity after the full charge and the charging capacity of the same cycle. Side reactions, such as solid-electrolyte-interphase (SEI) formation, that consume charge carrier ions (e.g., lithium-ions) can significantly lower the first cycle Coulombic efficiency.

4.2.4. *Operando* Characterization Techniques

***Operando* XRD**

The structural evolution of the samples was probed using a STOE STADI P diffractometer with a Ga-jet X-ray source (Ga-K_β radiation, λ = 1.20793 Å). In this case, the electrodes had a higher areal loading of active material, ~4.5 mg cm^{-2}, and customized coin cells with Kapton windows of 4 mm diameter were used. Galvanostatic cycling was conducted on a SP-150 potentiostat/galvanostat (BioLogic). XRD patterns were collected every 23 min.

***In-situ* gas analysis**

Differential electrochemical mass spectrometry (DEMS) was carried out to investigate the gassing behavior of materials. The cells were assembled from a 30 mm diameter cathode (~4.5 mg cm^{-2} areal loading) with a 4 mm hole in the center, a 40 mm GF/D glass microfiber separator, a 32 mm diameter Na metal anode and 700 µL electrolyte in a custom cell housing. The cells were cycled at 25 °C between 1.5 V and 4.2 V vs. Na^+/Na, while a constant stream of He carrier gas (purity 6.0, 2.5 mL min^{-1}) was passed through. After condensing electrolyte traces in a cold trap [−8 °C, as not to condense $(CN)_2$], the resulting gas mixture was analyzed using a mass spectrometer (Omni Star GSD 320, Pfeiffer Vacuum GmbH). Further details can be found in the literature.[133–135] To amplify the signal of $(CN)_2$ at *m/z* = 52, the secondary electron multiplier voltage was increased to 1250 V from 1010 V (with the latter being the maximum voltage where no saturation of *m/z* = 28 was observed when monitoring the ratio between *m/z* = 28 and *m/z* = 32 in ambient air). As possible electron multiplier saturation would affect the gas quantification, the linearity of the strongest relevant signal (H_2, *m/z* = 2) was ensured over the calibration range (400 ppm H_2). The same figure shows that very similar calibration curve slopes, i.e. detector sensitivities, were obtained, allowing to directly compare also the *m/z* = 52 signal without adjusting for differences in secondary electron multiplier gain, as will be discussed in follow-up sections.

S. L. Dreyer (KIT) performed and analyzed the DEMS experiments.

Operando electrochemical impedance spectroscopy (EIS) Analysis

EIS measurements were conducted using a Bio-logic VSP-300 potentiostat device at various specific currents between 25 and 800 mA g^{-1} in the Chapter 6. Impedance spectra were recorded at all even voltages (1.6, 1.8, 2.0 V ···), in fully charged (4.5V) and in fully discharged state (1.5V) during cycling in the frequency range from 100 kHz to 1Hz.

Operando stress analysis

Operando curvature measurements were conducted using a custom-built substrate curvature cell. The electrodes were glued onto 15 mm x 4 mm borosilicate glass cantilevers with a thickness of 155 μm. The cantilevers consist of four layers (substrate | glue | current collector | composite electrode) and are clamped into the test cells. The clamp affixes the cantilever and ensures electrical contact by pressing it onto a contact region within the test cell. Curvature measurements are performed at a distance from the clamp to avoid stress irregularities due to the mechanical constraints caused by the clamping force. Mechanical stress within the composite electrode leads to a response of the four-layer cantilever in the form of curvature. To measure the radius of curvature, two laser beams are used. They enter and leave the cell through a window and are reflected at the backside of the cantilever. The angle between the laser beams is tracked by a CMOS camera[136,137] and measured as a distance between two spots on the camera. This distance linearly correlates with the radius of the cantilever. The curvature is the inverse of this radius and for thin layers on rigid thick substrates, the curvature is directly proportional to the mechanical stress within the thin layer (Stoney's relation[138]).

$$\Delta\kappa = \frac{1}{r_1} - \frac{1}{r_0} = \frac{\Delta d}{2*L*l} \qquad \textbf{(Equation 4.8)}$$

In this equation, $\Delta\kappa$ is the change in the curvature (the inverse of the radius of curvature) and can be determined by using simple geometry from the change in displacement of the distance d between the two laser spots on the camera. L is the distance between the camera sensor and the cantilever and l is the distance between the two laser spots on the cantilever. r_0 corresponds to the radius at the start of the measurement and $1/r_0$ is subtracted from the curvature to achieve zero curvature (stress/volume change) at the beginning. Here, a multilayer system with a thick active film made of a composite material is analysed.[136] Stoney's relation cannot be used and it is therefore not easily possible to directly relate curvature and stress. Nevertheless, curvature relates to mechanical stress and volume changes. The simple assumption that for geometrically similar films the as-measured substrate curvature and volume changes of the active particles correlate linearly is used.

The active material loadings of the electrodes were 5 mg/cm² for the cubic phase and 4.5 mg/cm² for the monoclinic phase of HEPBA. The electrode material area that was investigated is about 40 mm² in

the potential range between 1.5 and 4.5 V vs Na^+/Na with a specific current of 10 mA/g. 1 M $NaClO_4$ in EC/DMC/PC (1:1:1) with 5 vol% FEC was used as electrolyte. Two different cells per composition were investigated in a three-electrode configuration in the substrate curvature setup.
Tolga Akcay and Reiner Mönig (KIT) assisted in *in-situ* stress measurement and analysis.

4.2.4. DFT Calculations

First-principle density functional theory (DFT) calculations were performed using the Vienna Ab initio Simulation Package (VASP) in the Chapter 5.[139] The spin-polarized generalized gradient approximation (GGA) with the PBE exchange-correlation functional[140,141] was chosen for the electronic structure calculations. The projector-augmented wave (PAW)[142] pseudopotentials and a plane-wave cutoff energy of 500 eV were used with an electronic and force convergence criteria of 10^{-4} eV and 10^{-3} eV/Å, respectively. The *k*-point mesh for each system was carefully tested and validated to ensure reliable and accurate results, as the three systems were calculated with different supercell sizes. The simplified rotationally invariant approach to the DFT+*U*[143] was used to correct for the self-interaction error in strongly-correlated 3*d* electrons. The values of the Hubbard *U* parameters for Co, Cu, Fe, Mn and Ni were taken from reference[144] and were 3.4, 4.0, 4.0, 3.9 and 6.0 eV, respectively. The disordered structures were generated using the special quasirandom structure (SQS) method,[145] which is implemented in the open-source Alloy Theoretic Automated Toolkit (ATAT).[146,147] The composition was adjusted slightly to reduce the number of atoms needed to match the specific crystal structure while maintaining the configurational entropy similar to that of the synthesized material, as shown in **Table 4.1**. The reported formation enthalpies are derived from the energy difference between reactants and products according to: $x MnCl_2 + (1-x)/5(FeCl_2 + NiCl_2 + CuCl_2 + Cd(NO_3)_2 + CoCl_2) + Na_4Fe(CN)_6 \rightarrow NaMn_x(TMs)_{(1-x)/5}[Fe(CN)_6] + 2(x+4)/5NaCl + 2(1-x)/5NaNO_3 + Na$. The TMs are the mixed transition metals, namely Fe, Ni, Cu, Co and Cd. The calculated formation Gibbs free energies (ΔG_f) were estimated as a difference between the formation enthalpy (ΔH_f) and the entropy term ($T\Delta S_{conf}$), assuming the configurational entropy (see **Equation 3.4**) of the compound as being the sole contributor to the entropy of formation.

Table 4.1. The configurational entropy of HE-PW, ME-PW and LE-PW. The adjusted composition used in the DFT calculations gives a similar configurational entropy to that calculated using Equation 3.4. The TM species are the mixed transition metals, namely Fe, Ni, Cu, Co and Cd.

	HE-PW	**ME-PW**	**LE-PW**
Material	$Na_xMn_{0.4}(TMs)_{0.12}Fe(CN)_6$	$Na_xMn_{0.6}(TMs)_{0.08}Fe(CN)_6$	$Na_xMn_{0.8}(TMs)_{0.04}Fe(CN)_6$
Configurational entropy	1.640 *R*	1.320 *R*	0.820 *R*
Adjusted PW	$Na_xMn_{0.375}(TMs)_{0.125}Fe(CN)_6$	$Na_xMn_{0.583}(TMs)_{0.083}Fe(CN)_6$	$Na_xMn_{0.792}(TMs)_{0.042}Fe(CN)_6$
Computed unit in DFT	$Na_xMn_3(TMs)_1Fe_8(CN)_{48}$	$Na_xMn_7(TMs)_1Fe_{12}(CN)_{72}$	$Na_xMn_{19}(TMs)_1Fe_{24}(CN)_{144}$
Configurational entropy	1.667 *R*	1.350 *R*	0.847 *R*

Yin-Ying Ting and Dr. Piotr M. Kowalski (RWTH Aachen University) performed the DFT calculations.

4.3. Memristor Fabrication and Testing Techniques

This section provides fabrication process of memristors as well as the specific characterization methods for memristors that were employed in Chapter 7. The device is specifically fabricated using a combination of inkjet printing and microplotting technologies.

4.3.1. Printing Methods

Here, two digital printing methods, namely inkjet printing and microplotting, are discussed. Printing techniques are generally divided into two major classes: contact printing, where inks are deposited through direct contact between the printing plate and the substrate, and non-contact printing, which deposits ink on the substrate without any direct contact. The inkjet fabrication technique, illustrated in **Figure 4.6a**, is the most widely used technology in the non-contact category, enabling precise drop-on-demand printing.[148] It employs a piezoelectric actuator to jet ink from a cartridge, depositing droplets onto the substrate. **Figure 4.6a** shows a piezoelectric sheet attached to the nozzles, activated by a tunable sinusoidal potential. The nozzle moves longitudinally relative to the substrate at an adjustable height. The sinusoidal potential affects the size and volume of the emerging droplet, enabling controlled deposition of printed patterns. Inkjet printing techniques offer several advantages,

including affordability, simplicity, adaptability in fabrication processes, reduced material waste, and the ability to achieve high-resolution patterning.

Microplotting is another a drop-on-demand printing technique that utilizes piezoelectric principles for precise liquid dispensing. In this method, a capillary tube filled with ink is attached to a piezoelectric actuator, forming the core of the printing mechanism. When a voltage is applied to the piezoelectric material, it deforms, causing a controlled pressure that ejects small droplets of liquid from the capillary. It should be noted that the capillary is in contact with the substrate. The printing of patterns on a substrate by microplotting is akin to the functioning of a fountain pen, making contact with the substrate is necessity, as shown in **Figure 4.6b**. The diameter of the capillary tip can be easily adjusted to accommodate ink containing particles of various sizes. This process enables accurate deposition of liquids onto a substrate, making microplotting suitable for applications requiring high-resolution patterning and precise material placement.

The two methods allow for the precise, low-cost and on-demand fabrication for large-scale devices.[36,149] While other fabrication methods, such as atomic layer deposition,[150] spin coating,[151] sputtering,[35] pulsed laser deposition and photolithographic techniques[28,152] inevitably require complex process and high-cost. For these reasons, both of the aforementioned printing techniques are highly intriguing for the fabrication of memristors. Further in-depth study of the printed memristors is necessitated in this dissertation.

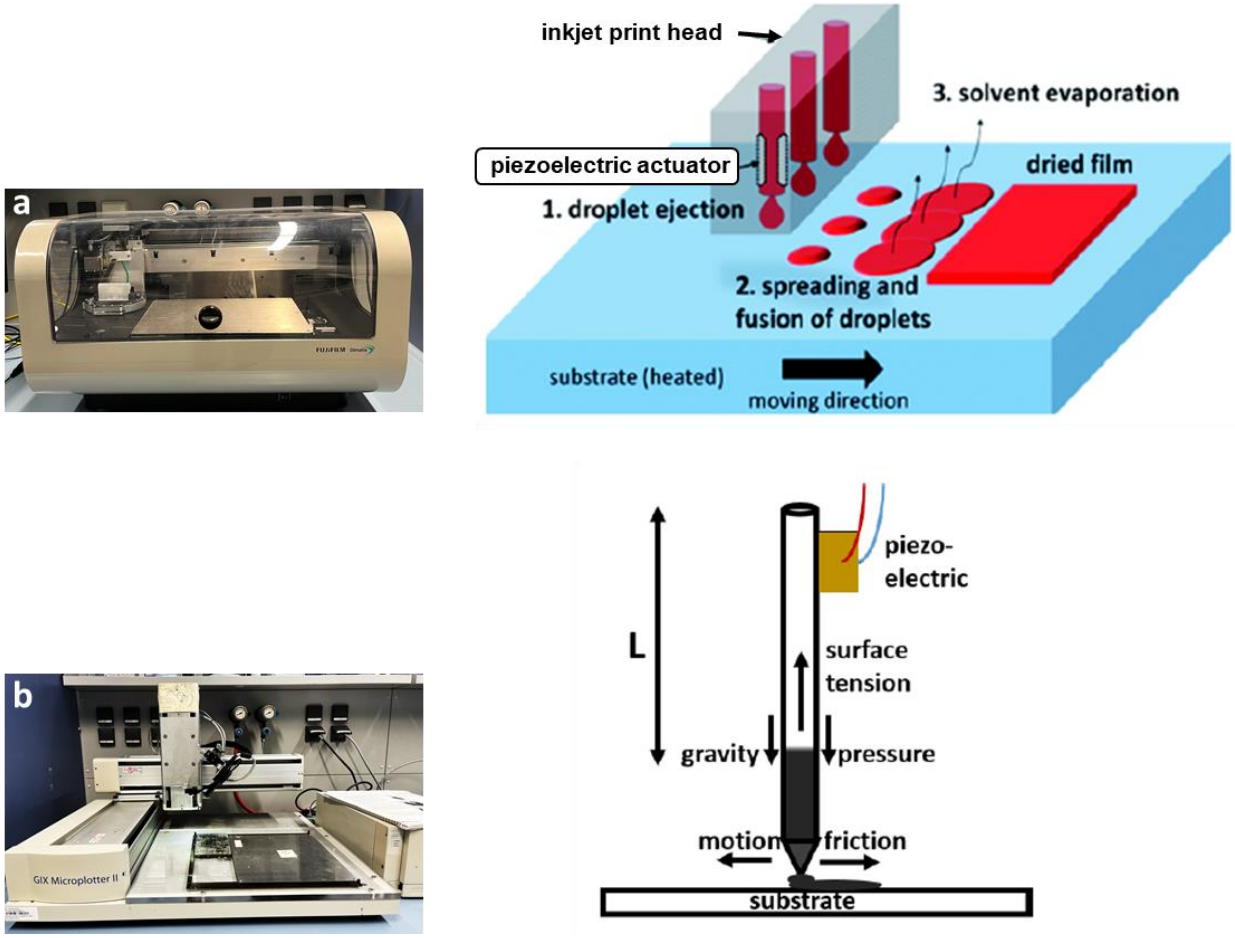

Figure 4.6. (a) Inkjet printer and corresponding principle of a drop-on-demand inkjet printing system, from ref[148]. (a) Microplotter and corresponding schematic of microplotter capillary.

4.3.2. Ink Preparation

The viscosity of the ink plays a critical role in drop formation during printing. If the viscosity is too high, drops may not form properly, resulting in printing aberrations. Conversely, if the viscosity is too low, the ink becomes too diluted, also causing issues in the printing process. Ink viscosity significantly affects the flow rate through the nozzles and directly influences the thickness of the film formed on the substrate. Finding the right viscosity is crucial for achieving optimal printing results. In addition to viscosity, optimizing the ink's surface tension in air and at the substrate interface is vital for achieving uniform printed layers. One typical challenge is addressing the "coffee ring effect", a phenomenon driven by Marangoni flow in the liquid.[153] In this dissertation, 13 mg HE-PBA powder was dispersed in 0.4 mL deionized water for ink preparation. The dispersion process involved ultrasonication for 30 min, followed by magnetic stirring at 1200 rpm for 4 h. After achieving full dispersion, 0.014 mL dimethyl sulfoxide (DMSO) was added to the ink to reduce the coffee ring effect. Final, the mixture was stirred for another 4 h to ensure formation of a well-dispersed ink.

4.3.3. Manufacturing Process

Preprocessing procedure: Commercially available indium tin oxide (ITO)-coated glass substrates (Präzisions Glas & Optik GmbH) with a SiO_2 passivation layer were used. The substrate dimensions were about 20 mm × 20 mm with a thickness of 1.1 mm. Laser ablation was conducted using a TRUMPF TruMicro 5000 ps laser at an average power of 1.5 W to pattern the ITO. After that, isopropanol and acetone were used for cleaning by ultrasonication for 1 h. A 2 min plasma treatment (Zepto, Diener electronic) was then applied to the ITO surface to establish a hydrophilic environment.
Printing HE-PBA: HE-PBA as the middle storage layer, covering the ITO bottom electrode, was fabricated by microplotting. A capillary tube (~60 μm diameter tip) filled with the as-prepared HE-PBA ink is attached to a piezoelectric actuator. When a voltage of ~ 4 V is applied to the piezoelectric material, it deforms, causing a controlled pressure that ejects small droplets of liquid from the capillary onto the substrate. Two droplets are printed to form two layers of the HE-PBA film. The wet storage layer was dried in a vacuum oven at 100 °C for 12 h.
Printing Ag ink: A commercial silver nanoparticle ink (Silverjet DGP, Sigma-Aldrich) was used to create the top electrode by coating the storage layer via inkjet-printing using a DMP2831 printer (Fujifilm), followed by drying in a vacuum oven at 120 °C for 1 h. The inkjet printer features a disposable ink cartridge and a print head with 12 nozzles, each capable of ejecting 2.4 pL ink droplets. However, only one nozzle is used for printing, and the printing platform is heated to 50 °C. The drop spacing is 10 μm, with a drop position array of 0.13 mm in the *x*-direction and 0.05 mm in the *y*-direction. All devices were fabricated on a glass substrate with dimensions of ~1 × 1 cm^2.

4.3.4. Electrical Characterization

The electrical performance measurements were carried out on a probe station (MPS150, Cascade) equipped with a semiconductor parameter analyzer (4200A SCS, Keithley) at room temperature. The bias voltage was applied to the Ag top electrode throughout current-voltage (*I–V*) characterization, while the ITO bottom electrode was grounded. Retention tests were conducted by switching the device to LRS, applying a read voltage of 0.01 V every 20 s for over 4×10^4 s, then resetting it to HRS and repeating the process. Gold-coated glass slides were purchased from Merck KGaA. They had an Au layer with a thickness of 100 nm and a purity of 99.999%. A titanium (Ti) adhesion layer was used to bind the gold to the aluminosilicate glass cover slip.

A focused ion beam (FIB) system (FEI Strata 400S) was used at 30 kV accelerating voltage with an ion beam current of 0.92 nA to obtain cross-sectional information on the devices. The surface

properties were probed using atomic force microscopy (AFM, Dimension Icon, Bruker). To this end, an Ag/HE-PBA/ITO device was positioned near the silver electrode without direct contact to avoid any effects from Ag during the measurements. The surface properties of substrates were characterized by measuring the contact angle using the OCA-20 system (DataPhysics Instruments GmbH) with the sessile drop technique. A dosing volume of 3.0 µL was applied for each measurement, and three measurements were performed on each sample to ensure accuracy. Micro X-ray fluorescence (µXRF) measurements were conducted using the XGT-9000 micro-XRF analyzer (HORIBA) with the following settings: 50 ms pixel time, P4 processing time, 15 µm capillary, 50 kV voltage, 1000 µA current, and measurement time of 8192 s. Fourier transform infrared (FT-IR) spectra were collected on a Bruker Tensor 27 in the range of 4000–400 cm^{-1} with standard KBr beamsplitter. Raman spectra were acquired with the help of a LabRAM HR Evolution microscope (HORIBA) with HeNe laser of wavelength 632.8 nm (E_{laser} = 1.9876 eV), further using a 600 g mm^{-1} grating and a 100× objective. At least three spectra were taken on each sample.

4.3.5. DFT Calculations

DFT calculations were performed with the Quantum-ESPRESSO plane-wave code, gpu-enabled version 7.2 for the Chapter 7.[154,155] The spin-polarized calculation were performed with the PBEsol exchange-correlation functional[156] specifically for the structural relaxation and electronic structure calculations. This approach has previously demonstrated improved accuracy in calculating structural parameters for cathode materials in lithium-ion batteries.[157,158] Ultrasoft pseudopotentials[159] and a plane-wave cutoff energy of 50 Ry were employed. The electronic and force convergence criteria of 10^{-4} eV and 10^{-3} eV/Å were applied, respectively. The Brillouin zone was sampled with a Monkhorst-Pack[160] 2×2×2 k-point grid. The Hubbard *U* correction scheme (DFT+*U*) was applied to improve the description of strongly-correlated 3*d* electrons.[143,161] The values of the Hubbard *U* parameters for Co, C-coordinated Fe (Fe_1), N-coordinated Fe (Fe_2), Mn, Ni and Cu, as applied in previous studies, are 3.4,[144] 7.0,[161] 3.0,[161] 3.9,[144] 4.0[162] and 3.0 eV,[163] respectively, for the listed elements. The 2×2×1 supercell model with a face-centered cubic structure (space group *Fm*−3*m*), containing 224 atoms per cell (excluding sodium atoms), was constructed to represent the structure of HE-PBA, with Co/Fe2/Mn/Ni/Cu randomly distributed at 4b site. To match the specific crystal structure while maintaining configurational entropy close to that of the synthesized material, the modelled atomic composition was slightly adjusted, as detailed in **Table 4.2**. The random distribution of transition metal atoms was constructed using the Special Quasirandom Structure (SQS) method,[145] applying the Alloy Theoretic Automated Toolkit (ATAT).[164,165] Following the distribution of transition metal atoms,

sodium atoms were distributed based on Coulombic energy minimization scheme. The first 20 structures with the lowest Coulombic energy for the structural relaxation were selected. The relaxed structure with the lowest DFT total energy was then chosen for the derivation of the Density of States (DOS).

Yin-Ying Ting and Dr. Piotr M. Kowalski (RWTH Aachen University) performed the DFT calculations.

Table 4.2. The composition and configurational entropy of synthesized and computed HE-PBA.

	Synthesized HE-PBA	**Computed HE-PBA**
Composition	$Na_xMn_{0.3}Fe_{0.3}(NiCuCo)_{0.133}[Fe(CN)_6]$	$Na_xMn_{0.3125}Fe_{0.3125}(NiCuCo)_{0.125}[Fe(CN)_6]$
Configurational entropy	1.53 *R*	1.51 *R*

Part III. Results and Discussion

Outline of Part III:

This section includes three Chapters that primarily illustrate the application of the high-entropy approach to PBAs, showcasing their potential as promising materials for SIBs and memristor applications.

The results presented here have been published as first author in *Angew. Chem. Int. Ed.* 2024, *136* (7), e202315371, *ACS Nano*. 2024, 18 (35), 24441-24457 and *Adv. Mater*. 2024, 2410060. Permission has been obtained to reuse the published content. For the submitted manuscripts, this process will be completed after acceptance.

Chapter 5[166] presents a series of monoclinic Mn-based PWs cathodes, part of the PBAs family, featuring six-metal entropy sites. The synthesis, electrochemical characterization, energy-storage mechanism and entropy-mediated effects are investigated on high-entropy PW, medium-entropy PW, low-entropy PW and conventional PW.

Chapter 6[167] examines two HEPBAs with similar composition but differing structures: one cubic and the other monoclinic. The electrochemical behaviors of HEPBAs in a wider electrochemical window and harsh operation conditions were investigated. The energy-storage mechanism of cubic and monoclinic HEPBAs was explored and compared. Practical applications as full-cell and high-temperature testing were performed and evaluated additionally.

Chapter 7[168] demonstrates a promising non-volatile, bipolar printed memristor based on HEPBA. Printing technologies were used to prepare the memristor, namely inkjet printing and microplotting. The electrical behavior and underlying resistive switching mechanism of HEPBA-based memristors were thoroughly studied.

5. Entropy-Mediated Stable Structural Evolution of Prussian White for sodium–ion Batteries

Low-cost manganese-based hexacyanoferrate cathodes ($Na_xMn[Fe(CN)_6]$), commonly referred to as Prussian white materials (PWs), are named for their distinctive white powder. They belong to the large family of PBAs and have been demonstrated as ideal, cost-effective host materials that facilitate easy insertion and extraction of Na^+ ions. Numerous studies have found that PWs with minimal defects, low water content, and high sodium levels are promising for optimal electrochemical performance for SIBs application. However, these materials often undergo multiple phase transitions, resulting in low-symmetry, non-cubic structures.[44,46,64,169] In addition to the rhombohedral and cubic structure of PWs,[170,171] monoclinic PWs can accommodate more sodium within their framework, making them an intriguing subject for further study.[74,172] However, monoclinic PWs remain prone to internal structural changes and pronounced Jahn-Teller distortions, stemming from significant lattice strain in the Mn-N_6 octahedra during the intercalation and deintercalation of Na^+ ions.[74,173,174] Conventional monoclinic PW materials have also been reported to suffer from rapid capacity fading and poor reversibility, attributed to the strong multiple phase transitions between monoclinic ($Na_2MnFe(CN)_6$), cubic ($NaMnFe(CN)_6$), and tetragonal ($MnFe(CN)_6$) phases during cycling.[74] Previous efforts to address the structural deformation of PWs primarily involved strategies such as partial atom replacement,[68–70] removal of interstitial water and vacancies,[57,71] incorporation of complexing agents[47,72,73] or constructing cation vacancies.[74] However, the high-entropy approach has not yet been applied to low-symmetry monoclinic PWs.

In this chapter, high-entropy approach is applied to monoclinic PW sodium-ion cathodes to address the challenge of unfavorable multilevel phase transitions during electrochemical cycling. A high-entropy site comprising six metals was established at the Mn position within the conventional $Na_xMn[Fe(CN)_6]$, resulting in the formation of a high-entropy Mn-based PW (denoted as HE-PW) with composition of $Na_{1.65}Mn_{0.4}Fe_{0.12}Ni_{0.12}Cu_{0.12}Co_{0.12}Cd_{0.12}[Fe(CN)_6]_{0.92}\square_{0.08}\cdot 1.09H_2O$. Through a comprehensive combination of analytical techniques, including *operando* XRD, *operando* DEMS, XPS, XAS, XES, as well as DFT simulations, two significant benefits conferred to the HE-PW cathode material by the enhancement of configurational entropy were elucidated. These benefits notably include suppressed phase transitions and reduced gas evolution during battery operation, which result from mitigated structural degradation throughout the operational cycle. Compared with medium-entropy PW (ME-PW), low-entropy PW (LE-PW) and conventional single-metal PW (Mn-PW), HE-PW exhibits improved tolerance for lattice expansion and shrinkage during cycling, thereby enhancing

cyclability, rate capability, and leading to a longer cycle life for SIBs. Predictably, considerable structure optimization via the application of high-entropy approach to PWs will be achieved to extend the materials system and optimize the electrochemical performance of multicomponent materials.

5.1. Materials Synthesis

Monoclinic structured HE-, ME-, LE- and Mn-PW materials were synthesized by co-precipitation at 70 ℃. In detail, 8 mmol $Na_4Fe(CN)_6 \cdot 10H_2O$ and corresponding proportions of $FeCl_2 \cdot 4H_2O$, $MnCl_2 \cdot 4H_2O$, $NiCl_2 \cdot 6H_2O$, $CuCl_2 \cdot 2.5H_2O$, $Cd(NO_3)_2 \cdot 4H_2O$ and $CoCl_2 \cdot 6H_2O$ (in total 6 mmol metal precursors) were dissolved in 100 ml deionized water, respectively, to form solution A and B. After the complete dissolution (ultrasonication for 0.5 h and then stirring for 0.5 h), 18 mmol sodium citrate were added to solution A and B, respectively, continuing to stir for 1 h. Then, the solution B was slowly dropped into solution A while continually stirring at 70 ℃. After reaction for 6 h, the obtained mixed solution was further aged at room temperature for 24 h. The resultant precipitates were collected by centrifugation, washed several times with deionized water and dried at 60 °C overnight. The products were carefully ground into a fine powder and further dried at 100 °C in a vacuum oven for 24 h.

5.2. Structural and Compositional Analysis

The crystal structure of the as-synthesized samples was characterized by XRD. The patterns obtained for all samples, as depicted in **Figure 5.1a**, exhibited Bragg reflections associated with a monoclinic structure. These reflections included characteristic peak splitting observed at $2\theta \approx 10.8°$-$11.1°$ (−211/211), $17.1°$-$17.5°$ (031/013) and $21.7°$-$22.3°$ (42−2/422), consistent with those typically observed in monoclinic PW materials.[72,74] The structural identification of the samples was enhanced through Rietveld refinements, a method commonly employed in crystallography. An illustration of the profile for the HE-PW sample is presented in **Figure 5.2a**, accompanied by the corresponding structural parameters provided in **Table 5.1**.

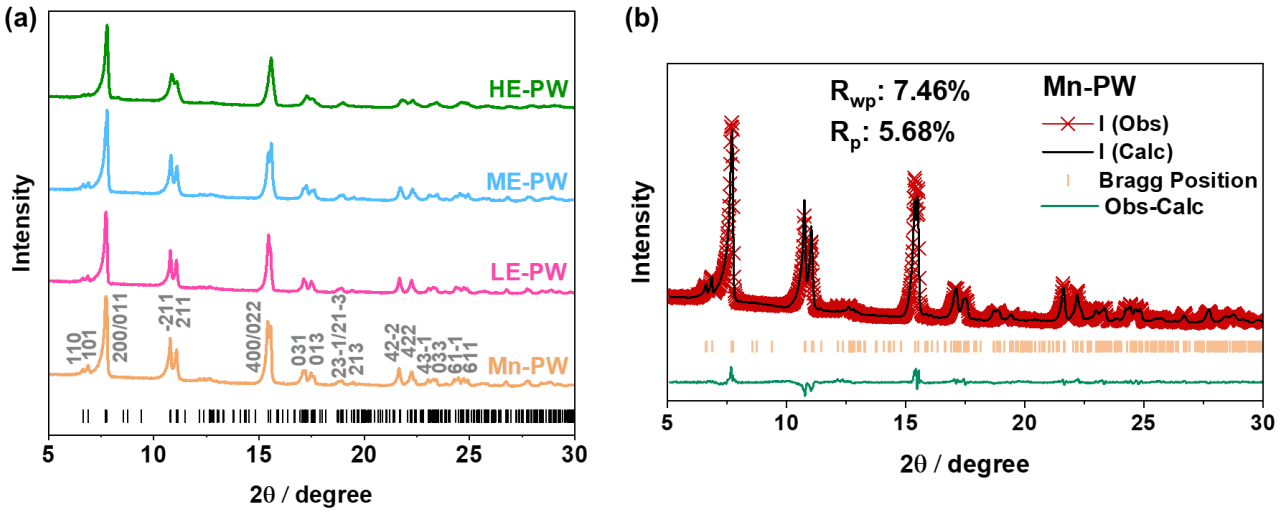

Figure 5.1. (a) XRD patterns of the HE-, ME-, LE- and Mn-PW materials. (b) XRD pattern and Rietveld refinement plot for Mn-PW.

The results reveal that HE-PW possesses a monoclinic unit cell with lattice parameters a = 10.476(7) Å, b = 7.465(6) Å, and c = 7.368(6) Å, refined against a structural model with space group $P2_1/n$ (ICSD collection code 266392).[175] The local structure of HE-PW sample suggests 6-metal atoms occupy the same N-coordinated (Mn) position in the 2*a* sites with Mn predominating. While the C-coordinated Fe1 atoms take 2*d* sites in PW lattice ($Na_xMn[Fe_1(CN)_6]$), forming linear chains of Fe_1−C≡N−Mn/Cd/Cu/Ni/Co/Fe_2−N≡C−Fe_1 along the monoclinic edges, as illustrated in **Figure 5.2b**. In comparison to conventional Mn-PW, HE-PW exhibits a remarkably similar crystal structure and lattice parameters, affirming the successful creation of multi-element high-entropy sites while preserving the crystal structure integrity of traditional PW materials (see **Figure 5.1b** and **Table 5.2**). The chemical compositions of the as-synthesized products were analyzed by ICP-OES. TGA measurement was used to determine the content of crystal water (see **Table 5.3**). The chemical formulation of HE-PW was determined to be $Na_{1.65}Mn_{0.4}Fe_{0.12}Ni_{0.12}Cu_{0.12}Co_{0.12}Cd_{0.12}[Fe(CN)_6]_{0.92}\square_{0.08}\cdot 1.09H_2O$. Similar water content observed across all materials rules out its influence on the crystal structure, phase transitions, and electrochemical performance of the HE-, ME-, and LE-PWs.[71,176–178] The chemical composition as determined by ICP was used to inform the site occupancies of the refined structural models discussed above. According to **Equation 3.4** (see Introduction Part), which stems from statistical thermodynamics[179] for HEMs, HE-PW has a calculated ΔS_{conf} of 1.64 *R*. Meanwhile, ME-PW and LE-PW show lower ΔS_{conf} values of 1.32 *R* and 0.82 *R*, respectively. Hence, by tailoring the composition at the Mn positions within the conventional PW structure, PWs with varying configurational entropy, namely HE-, ME-, and LE-PWs were produced.

Table 5.1 Structural parameters and quality of fit determined by refinement of structural models against the XRD pattern of HE-PW.

Atom	**Wyckoff pos.**	**Atomic pos.**			**Occ**
		x	*y*	*z*	
N1	4e	0.4994	0.3042	0.7220	0.918
N2	4e	0.2907	0.4968	0.4971	0.918
N3	4e	0.4993	0.2905	0.2950	0.918
C1	4e	0.5057	0.1911	0.8242	0.918
C2	4e	0.1835	0.5017	0.5025	0.918
C3	4e	0.5024	0.1798	0.1888	0.918
Na	4e	0.2488	0.4401	0.0418	1.000
Fe1	2d	0.5	0	1	0.918
Ni	2a	0.5	0.5	0.5	0.120
Cu	2a	0.5	0.5	0.5	0.120
Co	2a	0.5	0.5	0.5	0.120
Cd	2a	0.5	0.5	0.5	0.120
Mn	2a	0.5	0.5	0.5	0.400
Fe2	2a	0.5	0.5	0.5	0.120
a = 10.476(7) Å, b = 7.465(6) Å, c = 7.368(6) Å, β = 92.106°, V = 575.76(77) Å^3, R_{wp} = 5.94%, R_p = 4.52%, $P2_1/n$ space group.					

Table 5.2. Structural parameters and quality of fit determined by refinement of structural models against the XRD pattern of Mn-PW.

Atom	Wyckoff pos.	Atomic pos.			Occ
		x	*y*	*z*	
C1	4e	0.5057	0.1911	0.8242	0.918
C2	4e	0.1835	0.5017	0.5025	0.918
C3	4e	0.5024	0.1798	0.1888	0.918
N1	4e	0.4994	0.3042	0.7220	0.918
N2	4e	0.2907	0.4968	0.4971	0.918
N3	4e	0.4993	0.2905	0.2950	0.918
Na	4e	0.2488	0.4401	0.0418	1.000
Fe1	2d	0.5	0	1	0.918
Mn	2a	0.5	0.5	0.5	1.000
a = 10.598(3) Å, b = 7.544(2) Å, c = 7.318(2) Å, β = 92.117°, V = 584.64(29) Å^3, R_{wp} = 7.46%, R_p = 5.68%, $P2_1/n$ space group.					

Table 5.3. ICP-OES results for the HE-, ME-, LE- and Mn-PW materials and corresponding configurational entropies.

Material	Composition	ΔS_{conf}
HE-PW	$Na_{1.65}Mn_{0.4}Fe_{0.12}Ni_{0.12}Cu_{0.12}Co_{0.12}Cd_{0.12}[Fe(CN)_6]_{0.92}\square_{0.08}\cdot 1.09H_2O$	1.64 *R*
ME-PW	$Na_{1.63}Mn_{0.6}Fe_{0.08}Ni_{0.08}Cu_{0.08}Co_{0.08}Cd_{0.08}[Fe(CN)_6]_{0.93}\square_{0.07}\cdot 1.07H_2O$	1.32 *R*
LE-PW	$Na_{1.62}Mn_{0.8}Fe_{0.04}Ni_{0.04}Cu_{0.04}Co_{0.04}Cd_{0.04}[Fe(CN)_6]_{0.93}\square_{0.07}\cdot 1.08H_2O$	0.82 *R*
Mn-PW	$Na_{1.65}Mn[Fe(CN)_6]_{0.92}\square_{0.08}\cdot 1.09H_2O$	0 *R*

TGA was used to determine the content of crystal water. The weight loss between 120 and 200 °C was determined to be ~7 wt.%, which can be attributed to the elimination of adsorbed (surface) water.[75,101,170] The interstitial water in PWs has a profound effect on the cycling stability. In this study, all samples were dried in a vacuum to reduce the crystal water content, according to the method proposed by Song, Goodenough and co-workers.[71] It is in a close range of 1.07-1.09 mol for all PW materials employed in this section.

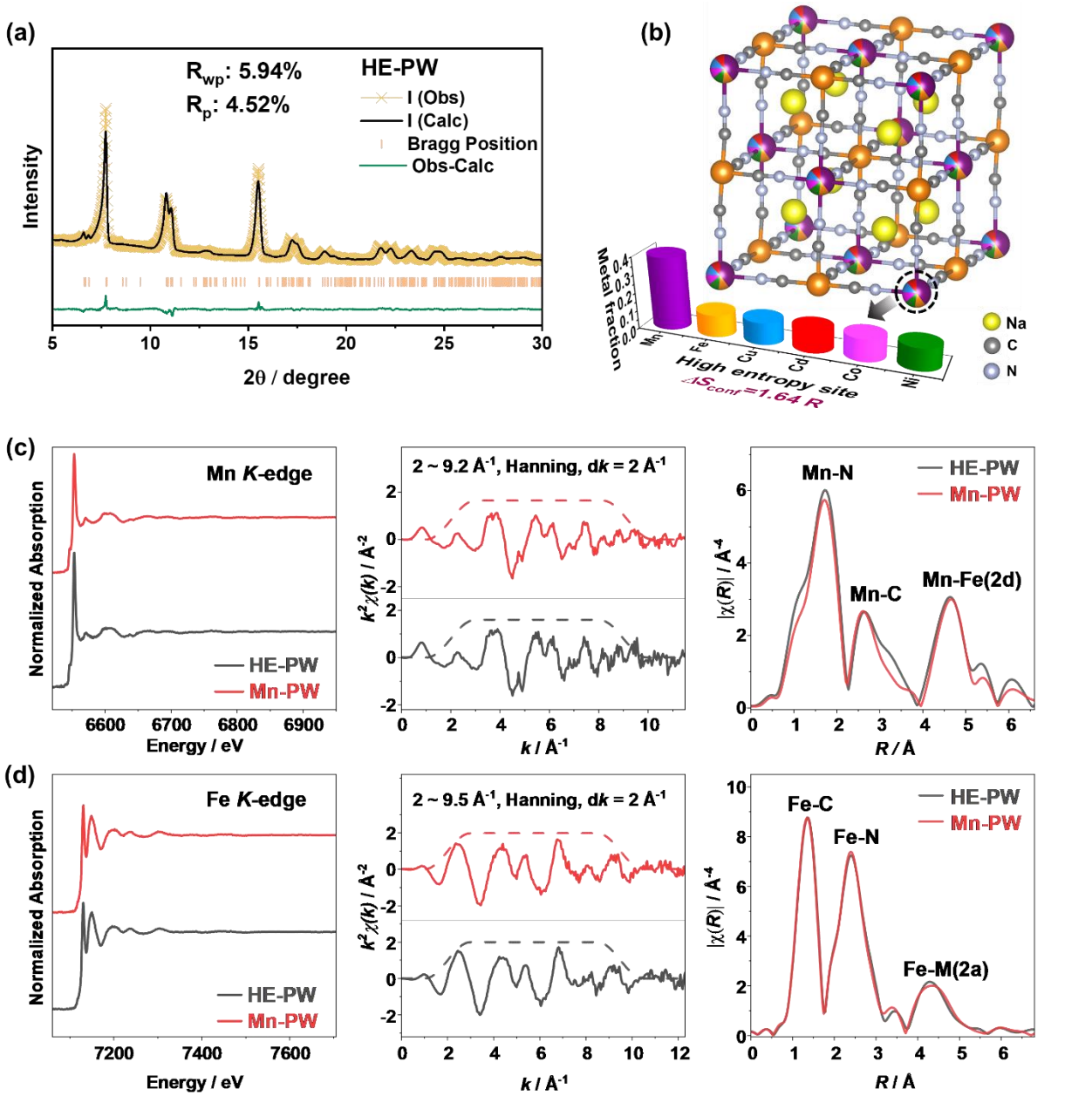

Figure 5.2. Structural analysis of the HE-PW and Mn-PW samples. (a) Powder XRD pattern of HE-PW and corresponding Rietveld refinement profile. (b) Schematic illustration of the crystal structure of HE-PW. (c) Mn and (d) Fe *K*-edge EXAFS of HE-PW and Mn-PW. Left to right: normalized absorption spectra; k^2-weigthed χ(k) spectra and corresponding *k* range and window function (Hanging, dashed lines) for the Fourier transform; and magnitude (|χ(R)|) of the Fourier-transformed, k^3-weigthed χ(k).

The local coordination environments of the diverse metal ions were investigated through transmission XAS. **Figure 5.2c** presents a comparison of the Mn *K*-edge extended X-ray absorption fine structure (EXAFS) spectra between HE-PW and Mn-PW. The utilization of synchrotron-based EXAFS enables precise characterization of the atomic-scale structure, offering valuable insights into the compositional uniformity and structural integrity of the material. In detail, similar radial distribution of interatomic

distances were observed on the magnitude (|χ(R)|) of Fourier transformed, k^3-weigthed χ(k), which demonstrated three distinct features corresponding to the Mn(2*a*)−N, Mn(2*a*)−C and Mn(2*a*)−Fe(2*d*) (−CN−) coordination shells.[180,181] This finding indicates that the coordination environment of manganese at the high-entropy site in HE-PW closely resembles that of manganese in Mn-PW, i.e., −Fe(2*d*)−C≡N−M(2*a*)−N≡C−Fe(2*d*)−. The slight variation in |χ(R)| between HE-PW and Mn-PW can be attributed to structural and electronic modulations induced by the presence of other metals in HE-PW. Particularly, comparable |χ(R)| magnitudes were observed at Fe *K*-edge, as the C-coordinated Fe (2*d*) is dominating for both HE- and Mn-PW, supported by the almost identical Fe(2*d*)−C and Fe(2*d*)−N features (see **Figure 5.2d**). Furthermore, synchrotron-based EXAFS analysis **(Figure 5.3)** also corroborated the similar local structure for Mn, Co, Ni, and Cu in HE-PW. Similar Fourier transformed k^3-weighted χ(k) were observed, and the three main features in the |χ(R)| magnitude corresponded to the nearest M(2*a*)−N, the second nearest M(2*a*)−C and the third M(2*a*)−Fe(2*d*) coordination shells. This finding underscores the consistency in the coordination environment of these metal ions across the high-entropy sites.

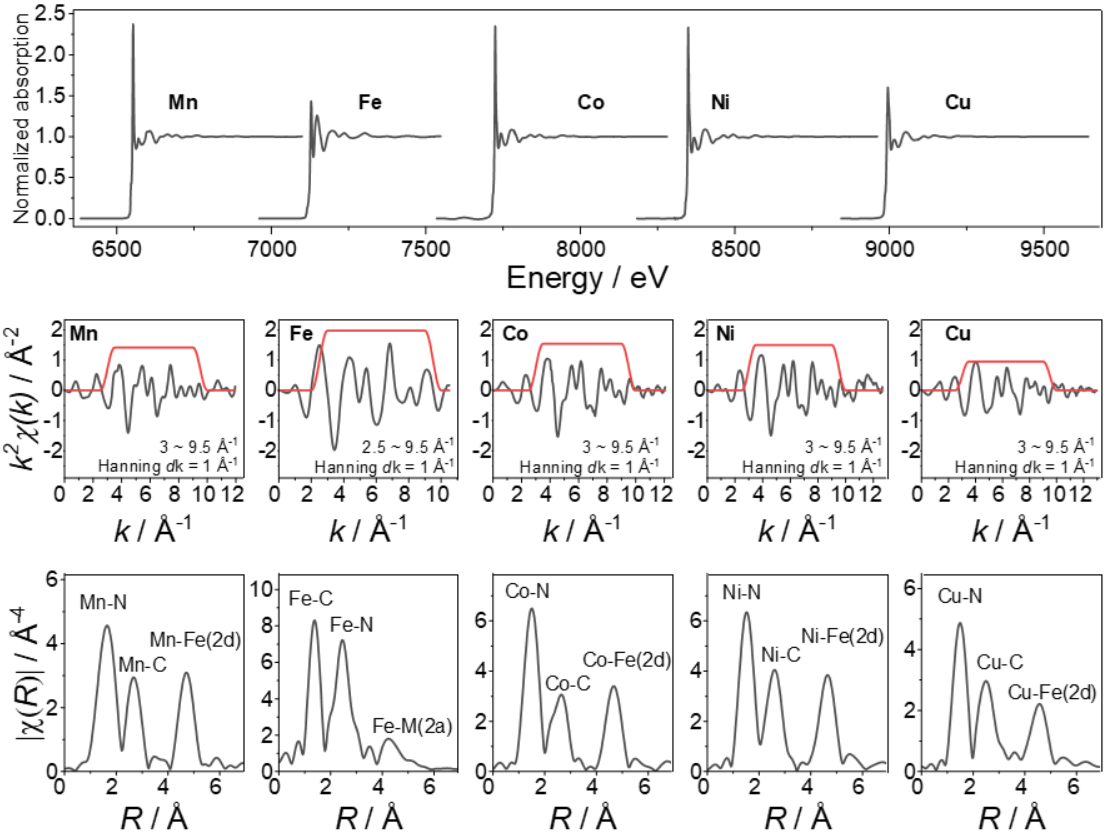

Figure 5.3. Synchrotron transmission XAFS of HE-PW (ROCK beamline, SOLEIL synchrotron). (top) Normalized absorption spectra of the respective metal *K*-edges; (middle) k^2-weighted χ(k) spectra and corresponding *k* range and window function (red) for the Fourier transform; (bottom) |χ(R)| of the Fourier transformed, k^3-weighted χ(k) (the main features represent the three neighboring coordination shells as denoted).

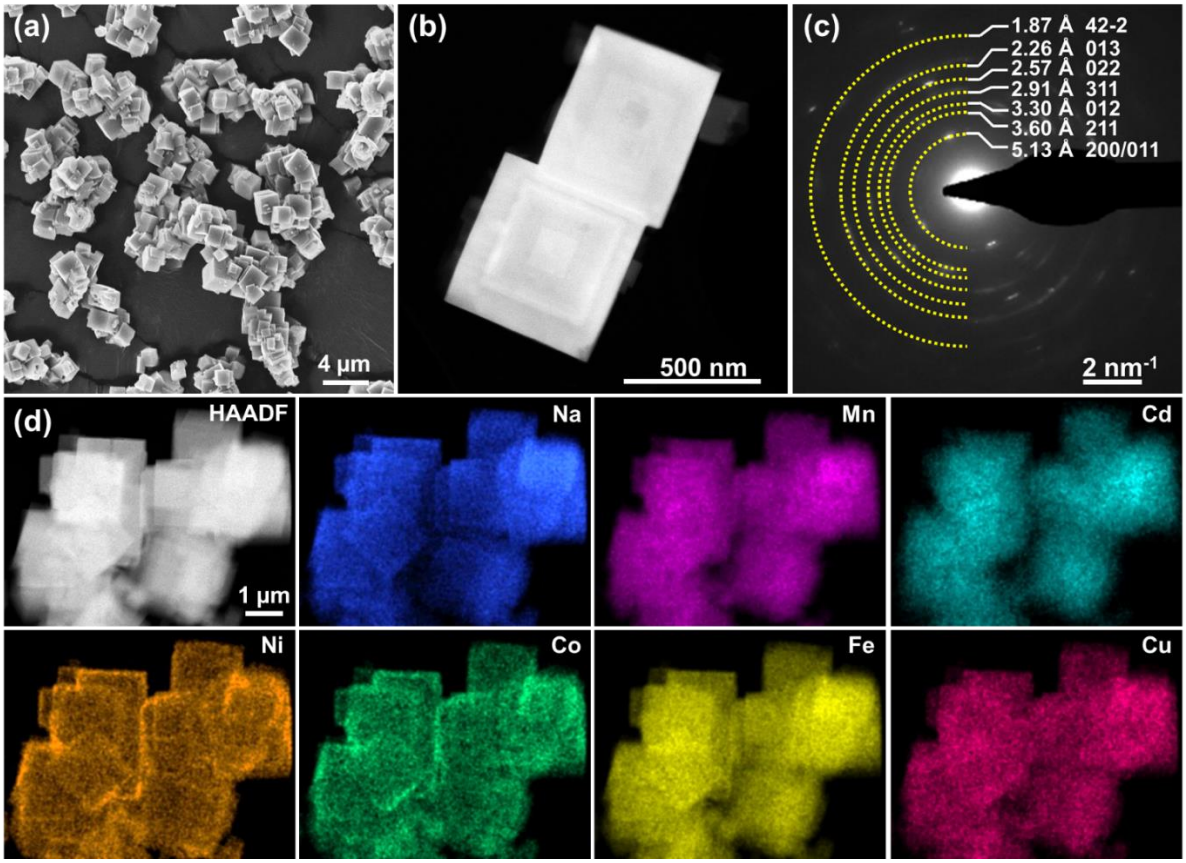

Figure 5.4. Electron microscopy of the HE-PW sample. (a) SEM image, (b) TEM image, (c) SAED pattern, (d) HAADF STEM image and EDS elemental maps.

The morphology of the materials was analyzed using SEM and TEM. The micrographs obtained from the HE-PW sample, as depicted in **Figure 5.4a** and **b**, reveal cubic particles with an average size ranging from 2 to 3 μm. The lattice planes indexed as (200), (211), (012), (311), (022), (013), and (42–2) observed in the selected-area electron diffraction (SAED) pattern (**Figure 5.4c**) are consistent with the monoclinic phase, providing additional confirmation of the $P2_1/n$ space group for HE-PW. Furthermore, the high-angle annular dark-field STEM (HAADF STEM) image, accompanied by the corresponding EDS elemental maps, clearly illustrates the each metal components present in the HE-PW cathode material (Na, Mn, Cd, Cu, Ni, Co, and Fe), as depicted in **Figure 5.4d**. Additionally, both ME- and LE-PW exhibited similar morphology, featuring uniform distribution of multi-metals across the micron scale, as shown in **Figure 5.5**.

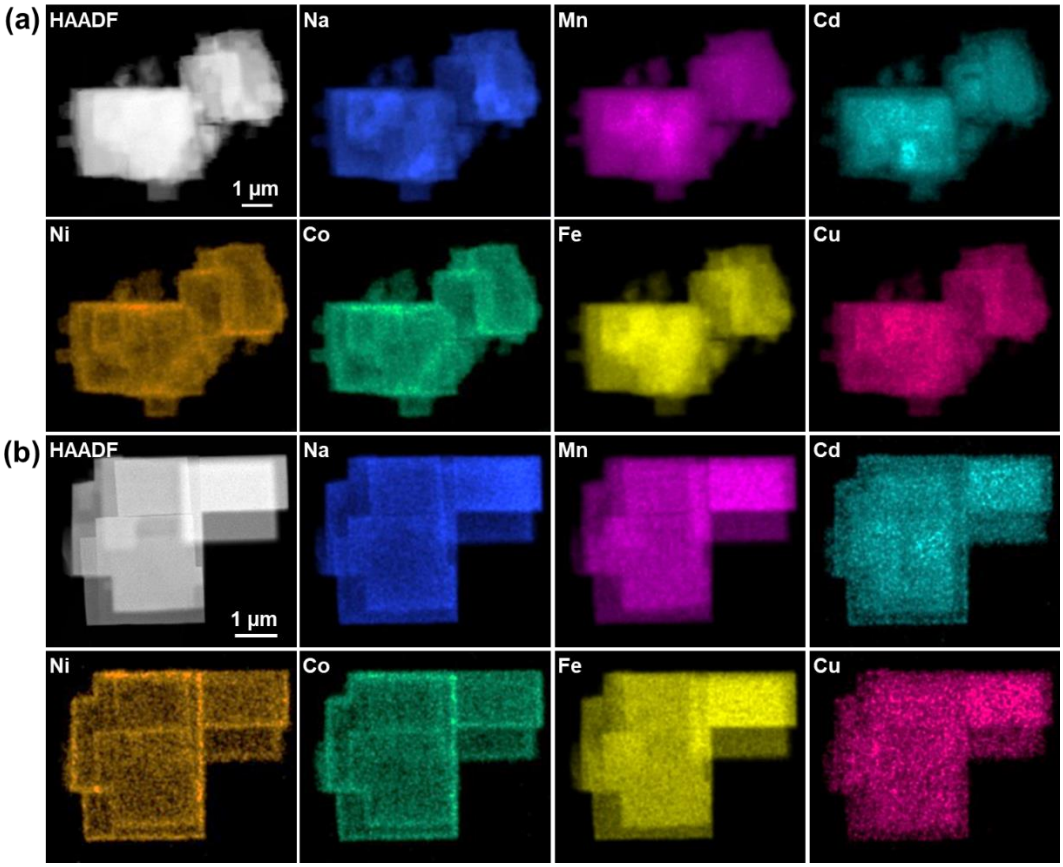

Figure 5.5 HAADF STEM images and corresponding EDS elemental maps for (a) ME-PW and (b) LE-PW.

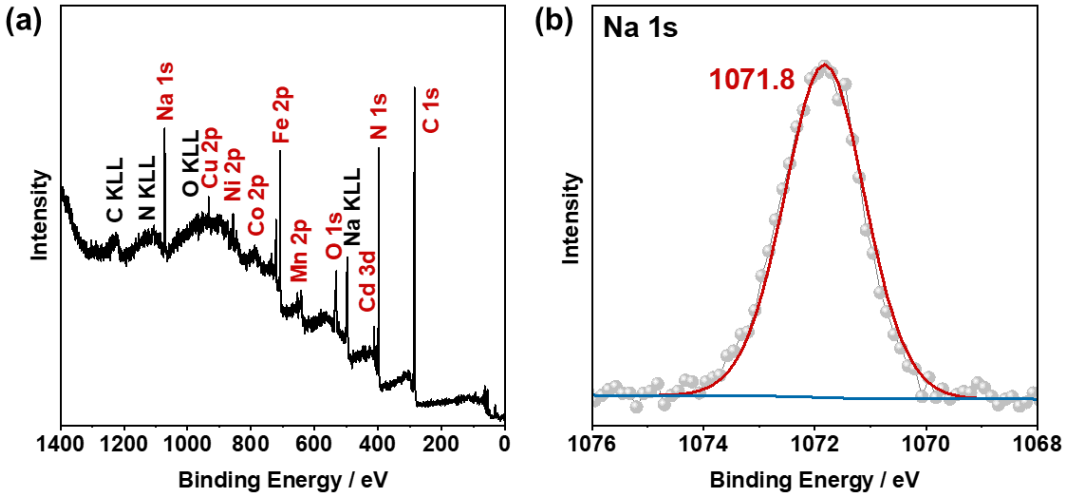

Figure 5.6. (a) XPS survey spectrum collected from HE-PW and (b) corresponding detail spectrum of the Na 1s region.

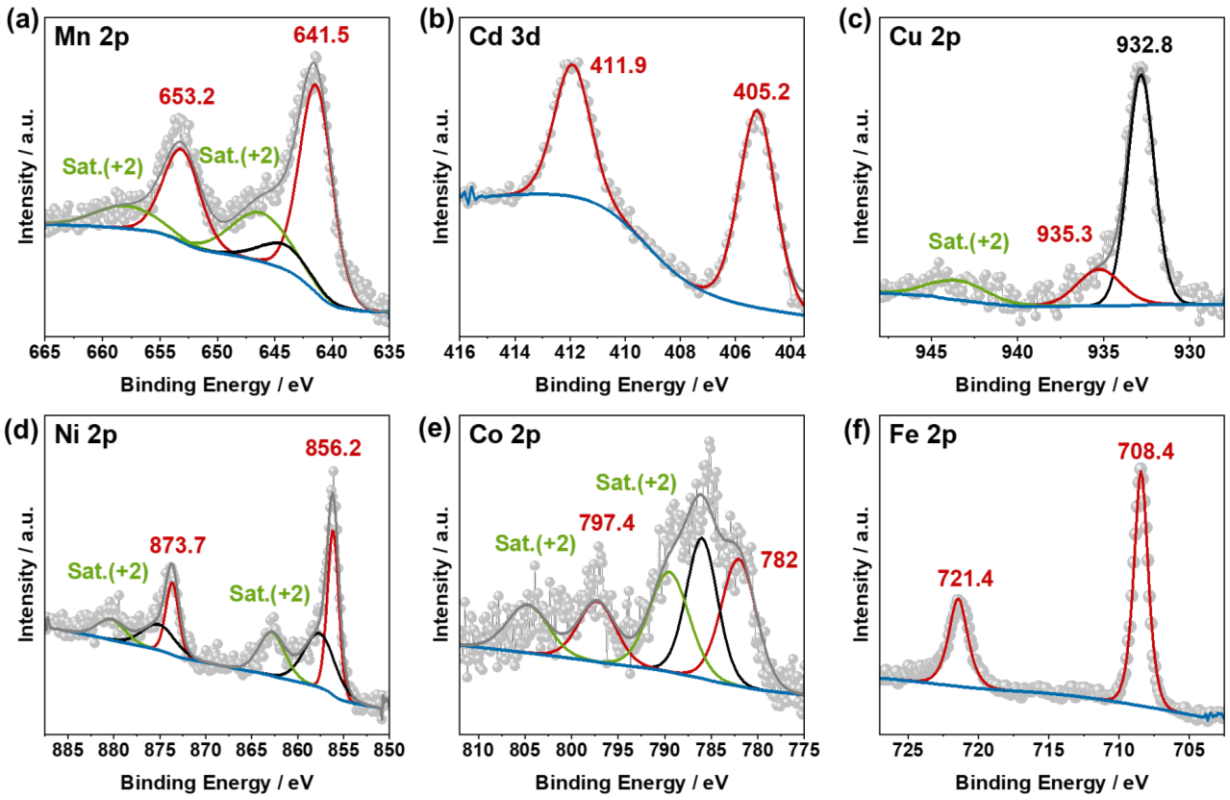

Figure 5.7. XP spectra of the (a) Mn 2p, (b) Cd 3d, (c) Cu 2p, (d) Ni 2p, (e) Co 2p and (f) Fe 2p regions.

XPS analyses were carried out to determine the elemental composition, oxidation states, and surface chemistry of the HE-PW sample, offering insights into the initial charge compensation mechanisms. The survey spectrum (**Figure 5.6a**) confirmed the presence of the expected metal species (Na, Mn, Cd, Cu, Ni, Co and Fe) in pristine HE-PW. In the detailed measurements, a single peak in the Na 1s spectrum (**Figure 5.6b**) located at a binding energy of 1071.8 eV can be assigned to Na^+.[75] The Mn 2p spectrum (**Figure 5.7a**) displayed major peaks at 641.4 (Mn $2p_{3/2}$) and 653.1 eV (Mn $2p_{1/2}$), accompanied by distinct satellite peaks at 646.2 and 657.9 eV as well as a broad Ni Auger feature appeared at ~644 eV. The dominant oxidation state of Mn in the HE-PW sample is inferred to be +II, based on the position of the main peak doublet and the presence of satellite structures typically observed for Mn^{2+} only.[75,182] A single Cd 3d peak doublet (**Figure 5.7b**) was observed at 405.2 (Cd $3d_{5/2}$) and 411.9 eV (Cd $3d_{3/2}$), consistent with the typical values for Cd in its preferred oxidation state of +II. It is noteworthy that the XPS chemical shift from metallic to oxidized Cd is relatively small.[183,184] The detail spectrum in the Cu $2p_{3/2}$ region (**Figure 5.7c**) is detected with the peak of Cu^+ species at 932.8 eV[75] and the peak of Cu^{2+} at 935.3 eV together with its corresponding shake-up satellite at 943.5 eV can also be detected.[87,185] The appearance of Cu^+ suggests that an internal redox reaction (surface reduction) from Cu^{2+} to Cu^+ occurred during the synthesis.

The Ni 2p spectrum (**Figure 5.7d**) showed the major peak doublet at 856.2 (Ni $2p_{3/2}$) and 873.7 eV (Ni $2p_{1/2}$), another doublet at slightly higher binding energy of 857.6 and 875.1 eV and satellite features at ~863 and 880 eV.[124] Determining the oxidation state of Ni based on these findings is challenging because the Ni 2p binding energies are generally unreliable for distinguishing between various Ni oxidation states in oxidized Ni compounds. Additionally, peaks from oxidized Ni species often exhibit multiple splitting, further complicating the analysis. Therefore, the splitting observed in this measurement could be attributed to this effect rather than indicating the presence of different Ni oxidation states.[101] The Co 2p spectrum (**Figure 5.7e**) featured rather distinct satellite peaks at 789.5 and 804.7 eV, together with the main peak doublet at 782.0 (Co $2p_{3/2}$) and 797.2 eV (Co $2p_{1/2}$) and a Fe Auger peak at ~786 eV. In the case of Co, such prominent satellite features are commonly observed only in the presence of Co^{2+}, indicating that the oxidation state of Co is likely to be +II.[75,101] Finally, the spectrum of the Fe 2p region (**Figure 5.7f**) was constituted by a single peak doublet at binding energy of 708.4 (Fe $2p_{3/2}$) and 721.4 eV (Fe $2p_{1/2}$). This result aligns with previously reported values for $[Fe^{+II}(CN)_6]^{4-}$, while the doublet of $[Fe^{+III}(CN)_6]^{3-}$would be expected at higher binding energy (~710/723 eV).[101] The absence of additional features suggests that the free Fe ions, coordinated to nitrogen, were also part of the doublet and likely in a +II oxidation state.[47,186,187]

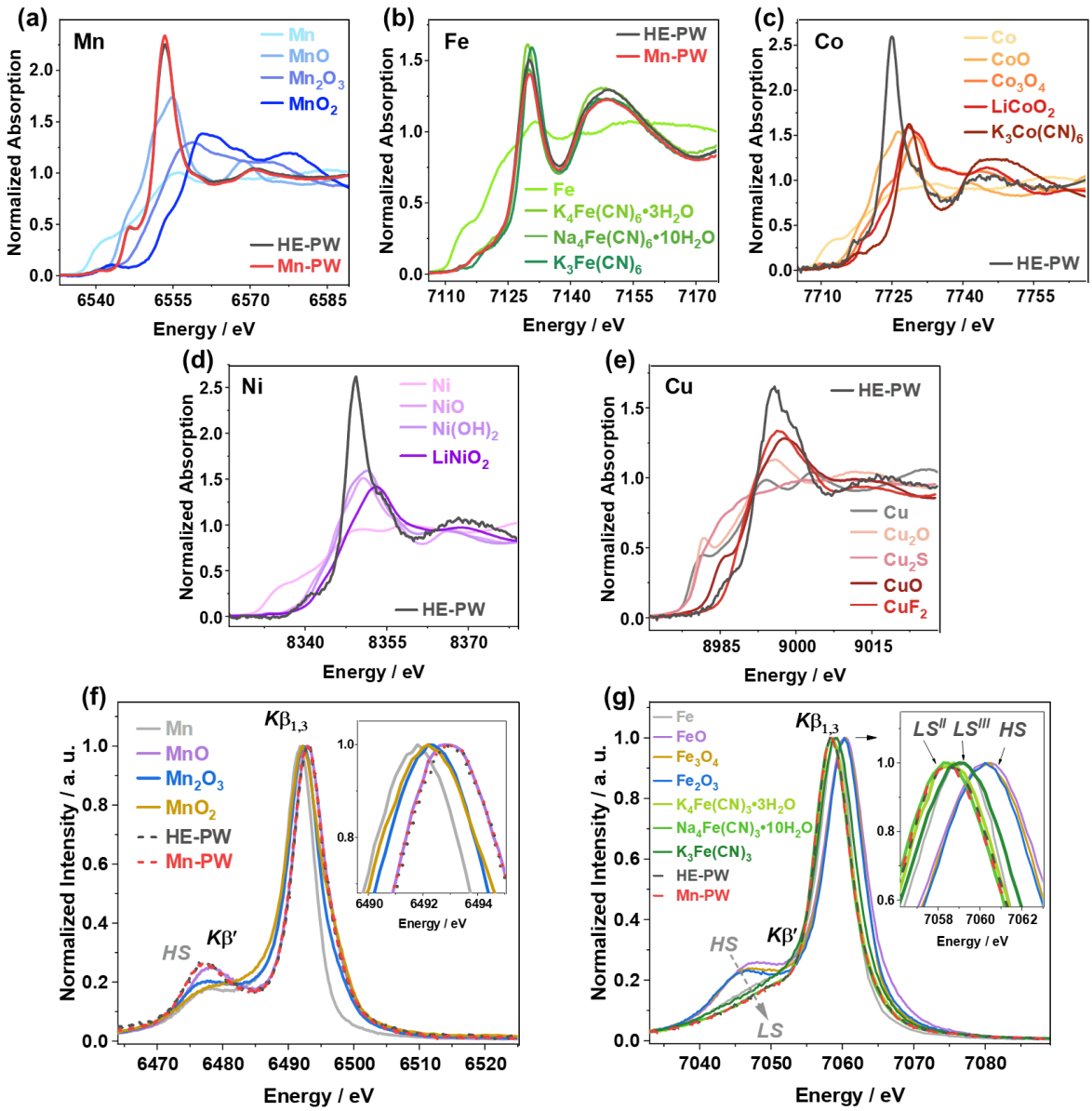

Figure 5.8. XANES and XES analysis of the HE-PW and Mn-PW samples. Normalized (a) Mn, (b) Fe, (c) Co, (d) Ni and (e) Cu *K*-edge XANES data. (f) Mn and (g) Fe *K*β XES of HE-PW, Mn-PW and various reference materials. Insets show the $K\beta_{1,3}$ lines. The emission spectra were normalized by maximum peak intensity. *LS* and *HS* denote low- and high-spin configurations.

Also, XAS was employed to further examine the oxidation states of transition metals. **Figure 5.8** shows the normalized X-ray absorption near edge structure (XANES) spectra for the respective metal *K*-edge. HE-PW and Mn-PW demonstrated near-edge structures that were comparable to reported conventional PW materials.[188–192] They exhibited almost identical Mn *K*-edge features, with edge energy position close to $Mn^{II}O$, thus indicating a formal oxidation state of 2+ (see **Figure 5.8a**, **Table 4.4**). In our previous investigation,[101] a combination of low-spin (*LS*) Fe^{2+} in the –Fe(4*a*)–CN–coordination and high-spin (*HS*) Fe^{3+} in the –Fe(4*b*)–NC–coordination was detected in the hexacyanoferrates materials,

with the Fe spin-state influencing the absorption *K*-edge. Considering the low nominal concentration (0.12) of N-coordinated Fe (2*a*) in HE-PW (zero concentration in Mn-PW), only standards with *LS* Fe were used here (**Figure 5.8b**). HE-PW and Mn-PW displayed edge energy positions akin to those observed for $K_4Fe^{II}(CN)_6 \cdot 3H_2O$ and $Na_4Fe^{II}(CN)_6 \cdot 10H_2O$, which were slightly lower than that of $K_3Fe^{III}(CN)_6$, indicating an average oxidation state of (*LS*) Fe +2. On the other hand, HE-PW showed a Co *K*-edge with the energy position between that of $Co^{II}O$ and $Co^{II,III}{}_3O_4$, but considerably lower than $K_3Co^{III}(CN)_6$, hinting a Co^{2+} in HE-PW (**Figure 5.8c**). Similarly, the Ni (**Figure 5.8d)** and Cu (**Figure 5.8e**) *K*-edge absorption spectra of HE-PW exhibited an edge energy close to $Ni^{II}O$, $Ni^{II}(OH)_2$ and to $Cu^{II}O$, $Cu^{II}F_2$, respectively. This points toward a formal oxidation state of +2 for Ni and Cu. It should be noted that no appearance of Cu^+ is found from XANES, suggesting that the minor amounts of Cu^+ only appeared on the material surface (from XPS results).

*K*β XES (X-ray emission spectroscopy) was performed to probe the formal oxidation states of Mn and Fe as well as their spin states, as shown in **Figure 5.8e** and **f**. The *K*β emission lines of 3*d* transition metals arise from a dipole-allowed $3p \rightarrow 1s$ decay process, which fills a core hole ($1s^1 3p^6 3d^n$) and leaves a $1s^2 3p^5 3d^n$ final state. The 3*p*-3*d* exchange coupling results in a $K\beta_{1,3} - K\beta'$ energy splitting, where the intensity of the *K*β′ feature varies with the number of unpaired 3*d* electrons, reflecting the spin states of the transition metal ions.[193,194] As shown in **Figure 5.8f**, $Mn^{II}O$ with five unpaired 3*d* electrons ($1s^2 3p^5 t_{2g}{}^3 e_g{}^2$, $S = 2.5$) demonstrated the strongest *K*β′ satellite. With increasing oxidation states and fewer 3*d* electrons in $Mn_2{}^{III}O_3$ ($1s^2 3p^5 t_{2g}{}^3 e_g{}^1$, $S = 2$) and $Mn^{IV}O_2$ ($1s^2 3p^5 t_{2g}{}^3 e_g{}^0$, $S = 1.5$), the weaker exchange interaction diminishes the *K*β′ intensity and shifts the $K\beta_{1,3}$ mainlines towards lower energy as the nominal spin values decrease.[126,195,196] HE-PW and Mn-PW showed almost identical Mn *K*β XES spectra, with a strong *K*β′ satellite feature and the same $K\beta_{1,3}$ energies as that of MnO, suggesting a high-spin (*HS*) Mn^{2+} in the –Mn(*2a*)–NC– configuration. On the other hand, the Fe *K*β emission lines of all hexacyanoferrates showed very weak *K*β′ features, indicative of the *LS* Fe in the –Fe(*2d*)–CN– configuration (**Figure 5.8g**). In contrast, Fe oxide standards displayed pronounced satellite features, characteristic of *HS* Fe coordinated with oxygen ligands.

Only minor distinctions were evident between HE-PW and Mn-PW, as the *K*β emission lines from HE-PW were dominated by C-coordinated *LS* 2*d* Fe, considering the very small concentration of *HS* 2*a* Fe in the N-coordinated sites.[101] Both HE-PW and Mn-PW showed *K*β′ features almost superimposed with $K_4Fe^{II}(CN)_6 \cdot 3H_2O$ and $Na_4Fe^{II}(CN)_6 \cdot 10H_2O$, characteristic of the same *LS* Fe^{2+} ($1s^2 3p^5 t_{2g}{}^6 e_g{}^0$, $S = 0$), which was slightly weaker than that of $K_3Fe^{III}(CN)_6 \cdot 3H_2O$ ($1s^2 3p^5 t_{2g}{}^5 e_g{}^0$, $S = 0.5$). They exhibited $K\beta_{1,3}$ mainlines at energies comparable to those of $K_4Fe^{II}(CN)_6 \cdot 3H_2O$ and $Na_4Fe^{II}(CN)_6 \cdot 10H_2O$ and slightly lower than that of $K_3Fe^{III}(CN)_6 \cdot 3H_2O$. In short, Mn and Fe *K*β

emission lines obtained from HE-PW and Mn-PW showed an agreement with XANES results on the average oxidation states. The *K*β′ features also revealed the *HS* configuration of N-coordinated Mn in addition to the *HS* Fe on the same site, as well as the *LS* configuration of C-coordinated Fe. Taken together, combining several complementary test results of XPS, XAS, and XES discussed above, the average oxidation state of both the C-coordinated Fe_1 and the N-coordinated high-entropy site (Mn, Cd, Cu, Ni, Co and Fe_2) is determined to be close to +II in the monoclinic HE-PW structure with the liner chains of $-Fe^{2+}-C\equiv N-M^{2+}-N\equiv C-Fe^{2+}-$.

Table 5.4. Chemical formula, formal oxidation state, XES final state, spin state and nominal spin value for ME-PW and Mn-PW and standard reference materials probed using XAFS.

Material				
HE-PW	$Na_x(Mn_{0.4}Fe_{0.12}Co_{0.12}Ni_{0.12}Cu_{0.12}Co_{0.12}Cd_{0.12})[Fe(CN)_6]$			
Mn-PW	$Na_xMn[Fe(CN)_6]$			
Reference samples				
Compound	**Formal oxidation state**	**Spin state**	**Final state**	**Nominal spin value *S***
MnO	+2	HS	$1s^2 3p^5 t_{2g}^3 e_g^2$	2.5
Mn_2O_3	+3	HS	$1s^2 3p^5 t_{2g}^3 e_g^1$	2
MnO_2	+4	HS	$1s^2 3p^5 t_{2g}^3 e_g^0$	1.5
FeO	+2	HS	$1s^2 3p^5 t_{2g}^4 e_g^2$	2
Fe_3O_4	+2/+3	HS		2.33
Fe_2O_3	+3	HS	$1s^2 3p^5 t_{2g}^3 e_g^2$	2.5
$K_4[Fe(CN)_6]\cdot 3H_2O$	+2	LS	$1s^2 3p^5 t_{2g}^6 e_g^0$	0
$Na_4Fe^{II}(CN)_6\cdot 10H_2O$	+2	LS	$1s^2 3p^5 t_{2g}^6 e_g^0$	0
$K_3[Fe(CN)_6]$	+3	LS	$1s^2 3p^5 t_{2g}^5 e_g^0$	0.5

5.3. Electrochemical Performance

After establishing the structural and chemical characteristics of the PW samples and verifying the successful formation of high-entropy sites, the electrochemical performance of HE-, ME-, LE-, and Mn-PW as cathodes in SIB cells was examined and compared. **Figure 5.9a** illustrates that all PW electrodes demonstrated a promising first-cycle specific discharge capacity at 10 mA g^{-1}. Specifically, HE-PW, ME-PW, and LE-PW exhibited capacities of 129 mAh g^{-1}, 118 mAh g^{-1} and 112 mAh g^{-1},

while Mn-PW achieved 126 mAh g^{-1}, approaching the theoretical specific capacity of around 130 mAh g^{-1}. The observed differences in initial capacities may be attributed to the slight variation in sodium content. As for HE-PW, the reduced polarization (see **Figure 5.10** and discussion below) indicates a lower overpotential, which allows a further (de)sodiation at a given voltage range and current, leading to its higher initial capacity than ME- and LE-PW.

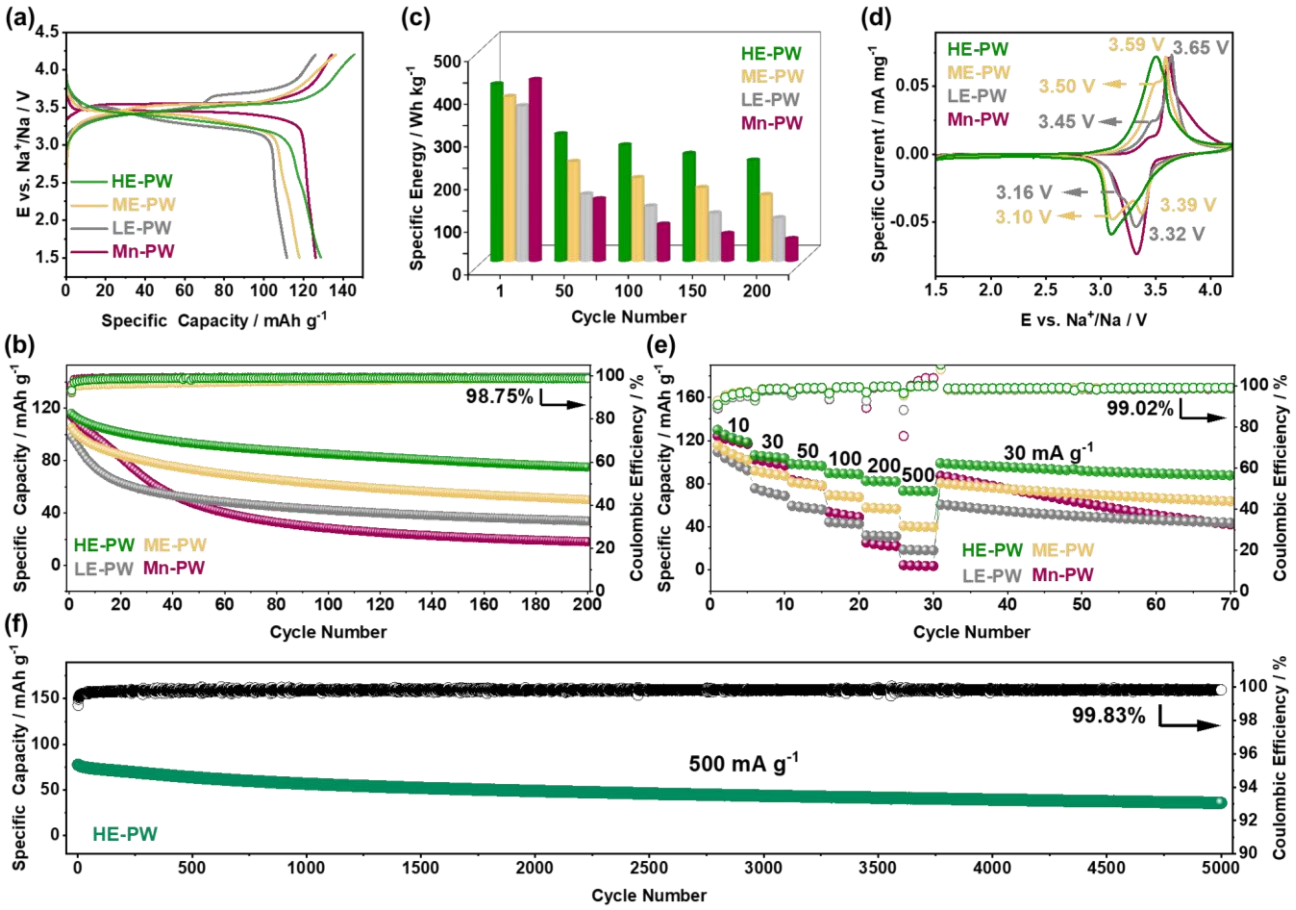

Figure 5.9. Electrochemical performance of the HE-, ME-, LE- and Mn-PW cathodes in SIB cells. (a) First-cycle charge/discharge curves at 10 mA g^{-1}, (b) specific discharge capacity versus cycle number at 30 mA g^{-1}, (c) comparison of specific energies for selected cycles, (d) initial cyclic voltammograms at 0.05 mV s^{-1}, (e) rate capability for specific currents ranging from 10 to 500 mA g^{-1} and (f) long-term cycling performance of HE-PW at 500 mA g^{-1}.

A more substantial difference is observed in long-term cycling results, where the degree of the compositional disorder appears to have a profound effect on cycling stability, following the trend of Mn-PW < LE-PW < ME-PW < HE-PW, see **Figure 5.9b**. For instance, Mn-PW exhibits a capacity retention of only 24.8% at the 100th cycle, whereas the capacity retention is enhanced by 1.7, 2.4, and 3.0 times for LE-PW, ME-PW, and HE-PW, respectively. This advantage is also reflected in the

gravimetric specific energy when considering sodium metal as the anode in a theoretical full cell (see **Figure 5.9c**). The specific energy and corresponding average voltage of Mn-PW decline rapidly after a few cycles. An initial specific energy of 425 Wh kg^{-1} was achieved for Mn-PW, which then dramatically declined to 145 and 86 Wh kg^{-1} at the 50^{th} and 100^{th} cycle, respectively. Eventually, only 12.3% remained after 200 cycles. **Figure 5.9c** underscores the benefits of employing high-entropy methods. At the 100^{th} and 150^{th} cycle, for instance, HE-PW still maintains a specific energy of 272 and 252 Wh kg^{-1}, respectively. This is 1.4/1.5, 2.1/2.2 and 3.2/3.9 times that of ME-PW, LE-PW and Mn-PW, respectively.

Figure 5.9d illustrates a comparison of the initial cyclic voltammograms (CV) of all PWs. ME-PW and LE-PW exhibit very similar behavior compared to conventional PWs. Two distinct pairs of redox peaks are evident for both samples: 3.45/3.16 V (LE-PW) and 3.50/3.10 V (ME-PW), corresponding to the redox reactions of C-coordinated Fe^{III}/Fe^{II} (low-spin), while 3.65/3.32 V (LE-PW) and 3.59/3.39 V (ME-PW), relating to the N-coordinated Mn^{III}/Mn^{II} (high-spin) redox couples, respectively.[101,170] For HE-PW, the features mainly merged into a single broad and asymmetric peak with a further increase in ΔS_{conf} of the system. **Figure 5.10** illustrates the CV profiles obtained at various sweep rates, ranging from 0.05 to 2.0 mV s^{-1}, with six cycles of charge-discharge conducted at each sweep rate. Notably, the redox polarization of HE-PW was much lower than that of other PWs, especially compared to LE- and Mn-PW, suggesting an improved Na^+ insertion/extraction in PW structure, benefiting from cocktail effects generated from an increased ΔS_{conf} of the system.[75]

Furthermore, the superior rate capability of HE-PW is apparent. **Figure 5.9e** compares the rate performance of HE-, ME-, LE-, and Mn-PW electrodes across various specific currents ranging from 10 to 500 mA g^{-1}. In any case, HE-PW consistently yields the highest specific discharge capacities across all elevated specific currents. At the highest rate of 500 mA g^{-1}, for instance, HE-PW can still deliver a capacity of 73 mAh g^{-1}, compared to 41 mAh g^{-1} for ME-PW, 19 mAh g^{-1} for LE-PW and only 5 mAh g^{-1} for Mn-PW, respectively. Furthermore, upon reducing the specific current back to the initial lower rate, the capacity of HE-PW was promptly restored and remained stable at around 100 mAh g^{-1}. In contrast, the LE-PW and Mn-PW cathodes experienced rapid capacity fading, demonstrating that the increased ΔS_{conf} enhances the reversibility of Na^+ storage. Remarkably, when applying a high rate of 500 mA g^{-1}, HE-PW can deliver very stable ultra-long cycling of around 60 (±15) mAh g^{-1}, with a Coulombic efficiency of nearly 100% for more than 5000 cycles (**Figure 5.9f**). **Table 5.5** compares the electrochemical performance of HE-PW with conventional single- or dual-metal hexacyanoferrates used as cathode materials in SIBs, underscoring the superior performance of HE-PW. This suggests that the increased ΔS_{conf} of the system enables the optimization of the

electrochemical performance for multicomponent PW materials. Besides, the clear structural outperformance of HE-PW was also evident at high temperature. Significant thermal tolerance at high temperature was observed for HE-PW due to its robust structure, as shown in **Figure 5.10**. The effect of configurational entropy on thermal stability for HEMs is further studied in the next section (see Chapter 6).[197]

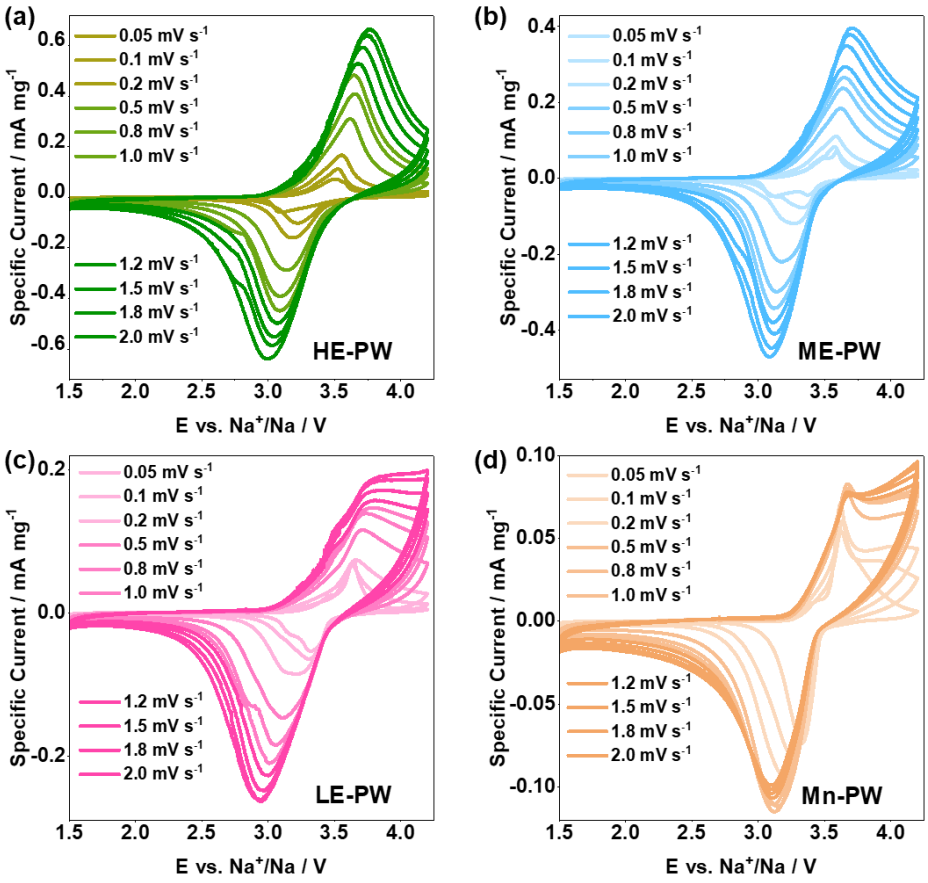

Figure 5.10. (a-d) Cyclic voltammograms at different sweep rates ranging from 0.05 to 2.0 mV s^{-1} for the HE-, ME-, LE- and Mn-PW cathodes (with six cycles for each sweep rate).

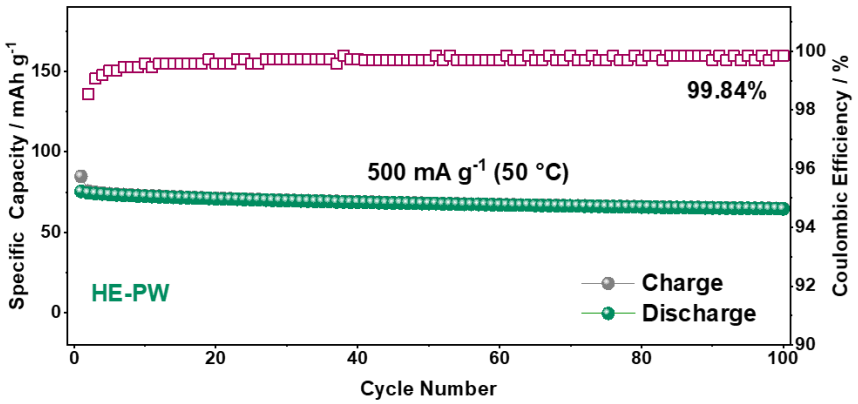

Figure 5.11. Cycling performance of HE-PW at elevated temperature (50 °C).

Table 5.5 Comparison of the cycling performance of HE-PW and conventional (single- and dual-metal) hexacyanoferrates as cathode materials in sodium-ion cells.

Material	Initial specific discharge capacity (mAh g^{-1})	Specific current (mA g^{-1})	Cycle no.	Specific discharge capacity (mAh g^{-1})	Ref.
HE-PW	78	500	5000	60	This work
$Na_xMn[Fe(CN)_6]_y$	129	C/5	100	13	[173]
$Na_{1.89}Mn[Fe(CN)_6]_{0.97}$	120	200	500	45	[47]
$Na_{1.58}Mn[Fe(CN)_6]_{0.8}$	126	30	50	75	[198]
$Na_xMn[Fe(CN)_6]_y$	130	1/20 C	30	121	[199]
$Na_xMn[Fe(CN)_6]_y$	97	100	800	61	[200]
$Na_{1.76}Mn_{0.88}Ni_{0.12}[Fe(CN)_6]_{0.98}$	96	100	800	80	[200]
$Na_xMn[Fe(CN)_6]_y$	130	50	300	35	[170]
$Na_{1.6}Mn_{0.833}Fe_{0.167}[Fe(CN)_6]$	120	100	1000	60	[170]
$Na_{1.67}Ni_{0.39}Co_{0.61}[Fe(CN)_6]$	92	50	100	82	[201]
$Na_xFeCu[Fe(CN)_6]$ (Cu doping)	89	50	1000	72	[202]
$Na_xFeNi[Fe(CN)_6]$ (Ni doping)	90	200	90	80	[203]
$Na_{0.39}Fe_{0.77}Ni_{0.23}[Fe(CN)_6]_{0.79}$	106	10	100	101	[204]

5.4. Energy-Storage Mechanism and Entropy-Mediated Effects

Operando XRD measurements were performed on HE-, ME-, LE-, and Mn-PW to assess the influence of the incorporated multiple elements in high-entropy materials on crystal structure variations during cycling and to elucidate the reasons for the differences in electrochemical behaviors among the PWs. As illustrated in **Figure 5.12a**, Mn-PW underwent distinct multi-step phase changes throughout the entire cycling process. In the early stages of charging, the diffraction peaks at approximately 13.2° and 14.2°, corresponding to the (200) and (110) crystal planes of the initial monoclinic phase, gradually shifted to lower angles, indicating unit cell expansion. The doublets merged into a single peak at 13.1°, representing the (200) planes of cubic structure when the cell was charged to 3.55 V. Simultaneously, other new peaks emerged corresponding to the (220), (400), (420), and (440) crystal planes, indicating the phase transition from the monoclinic to the symmetric cubic structure. During further charging, these characteristic peaks of the cubic phase in Mn-PW electrodes shifted markedly to higher angles, corresponding to unit cell contraction due to the further sodium ion extraction. New diffraction peaks corresponding to the (110), (020), (004), (114), and (224) planes appeared in Mn-PW electrodes, indicative of a transition from cubic to tetragonal phase. This shift, resulting from unit cell deformation, points to the second phase transition from the face-centered cubic structure.[74,205] During subsequent re-sodiation, the structure transitioned back from tetragonal to cubic as the cell discharges to 3.4 V, indicating a reverse phase transformation. The monoclinic phase reappeared at the fully sodiated state, as shown in **Figure 5.12b$_1$** and **b$_2$**. However, these transformations may decrease the crystallinity of the material during cycling, leading to broader and less intense XRD reflections. As also discussed in previous reports,[47,74] transitions between monoclinic, cubic and tetragonal phases during Na^+ insertion/extraction easily trigger severe (anisotropic) volume changes, i.e., the Mn-PW unit cell strongly suffers from lattice expansion/contraction, as illustrated in **Figure 5.12c**.

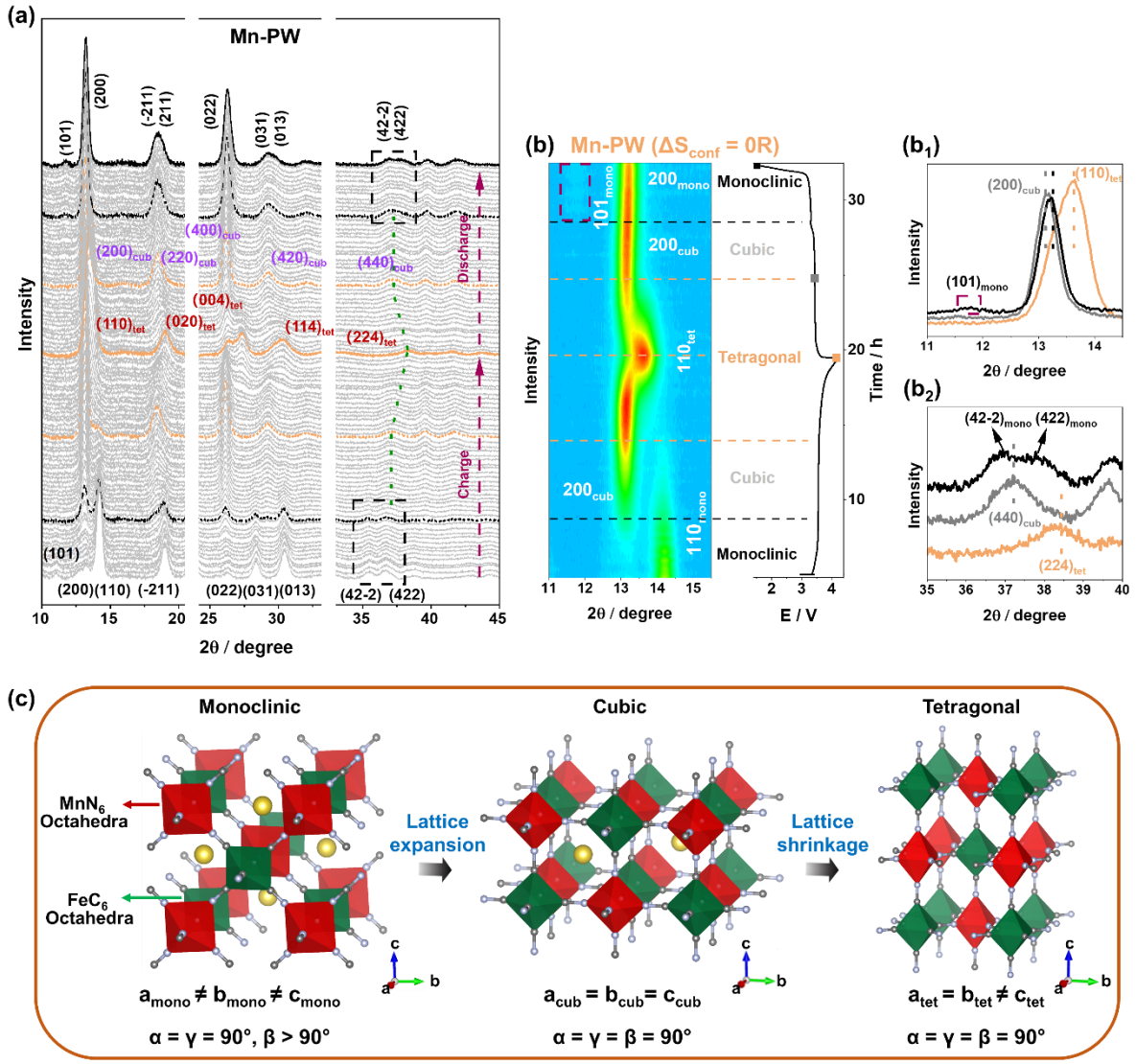

Figure 5.12. *Operando* XRD characterization of the Mn-PW cathode. (a) Waterfall plot (scans between 10° to 45° 2-theta). (b) Contour plot and corresponding voltage profile. (b_1, b_2) XRD patterns collected at the end of charge and during subsequent discharge [see orange, gray and black squares marked in the dis-/charge profile in panel (b)]. (c) Schematic illustration of the structural evolution of Mn-PW during battery operation.

Conversely, HE-PW demonstrates a significantly more robust structural evolution, and is fully capable of preserving high structural symmetry during cycling. In detail, during the initial de-sodiation process, HE-PW underwent a phase transition from monoclinic to cubic phase, as depicted in **Figure 5.13a**, upon charging to 3.55 V. Subsequently, HE-PW exhibited a solid-solution type behavior with minimal reflection changes, maintaining a highly symmetrical cubic phase even when Na^+ is fully extracted from the lattice cell (fully charged to 4.2 V, see **Figure 5.13b**). Remarkably, the structure remained stabilized in the cubic phase even during the subsequent sodiation process, suggesting a preference for highly symmetric structures in high-entropy materials and their capacity for enduring stability. When the ΔS_{conf} is decreased to 1.32 and 0.82*R*, a similar unit cell expansion and shrinkage behavior

happened in ME- and LE-PW electrodes as obtained in conventional Mn-PW (see **Figures 5.13c**, **d** and **Figures 5.14** and **5.15**). In contrast to Mn-PW, these materials exhibit significantly reduced degrees of lattice expansion and contraction, as evidenced by contour plots of *operando* XRD in **Figures 5.13c**, **d** and **5.12b**. These findings suggest that increasing ΔS_{conf} can effectively suppress structural deformation to some extent. Of particular note with ME-PW is the smaller shift observed at higher angles where the tetragonal structure takes place, indicating a less pronounced expansion of the unit cell compared to LE- and traditional Mn-PW, particularly evident during the second cycle. Multiple structural transitions during cycling seem to be mainly responsible for the poor cycling stability of LE- and Mn-PW cathodes described in **Figure 5.9**. For a detailed analysis, an *ex-situ* measurements of HE-PW and LE-PW electrodes at the fully sodiated state (charged to 4.2 V) were conducted as well. As shown in **Figure 5.16**, LE-PW shows a clear reappearance of the monoclinic phase, while the HE-PW stabilizes at the cubic form after a full battery cycle.

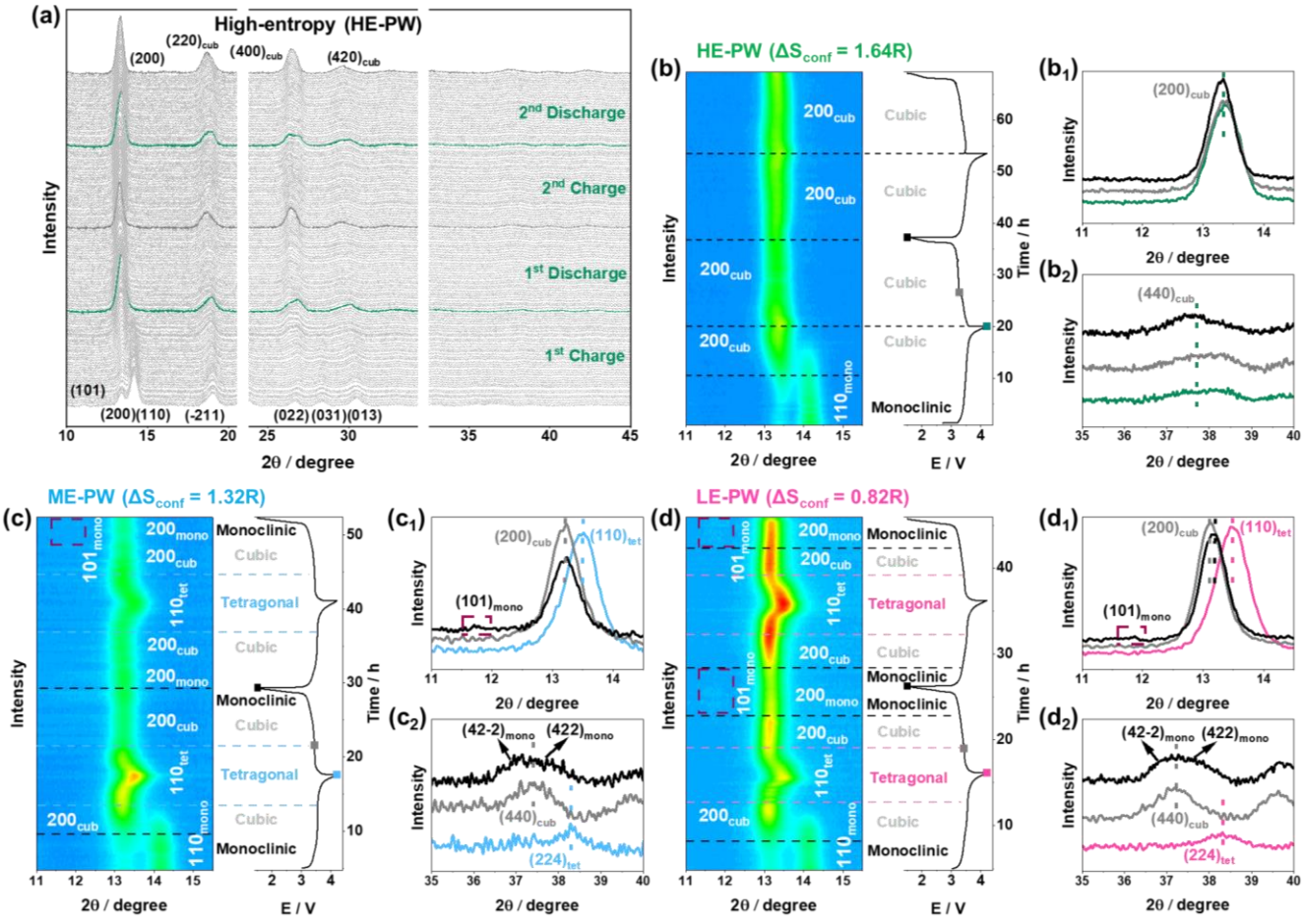

Figure 5.13. *Operando* XRD characterization of the HE-, ME- and LE-PW cathodes over the first two cycles. (a) Waterfall plot (scans between 10° to 45° 2-theta) for HE-PW. (b-d) Contour plots and corresponding voltage profiles for HE-, ME- and LE-PW. (b_1-d_1, b_2-d_2) XRD patterns collected at the end of first charge and during subsequent discharge [denoted by squares in the respective dis-/charge profiles in panels (b, c and d)].

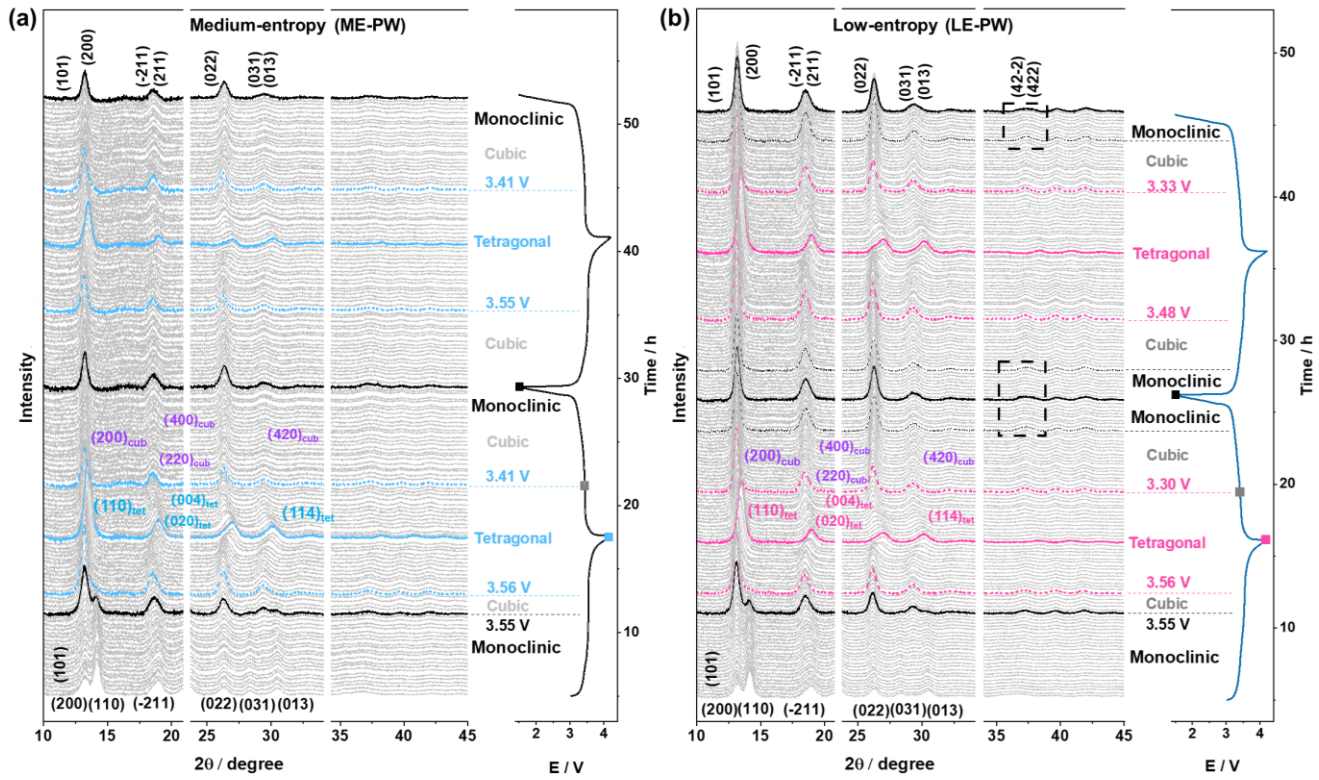

Figure 5.14. *Operando* XRD characterization with waterfall plots of the first two cycles and corresponding voltages profiles for (a) ME-PW and (b) LE-PW.

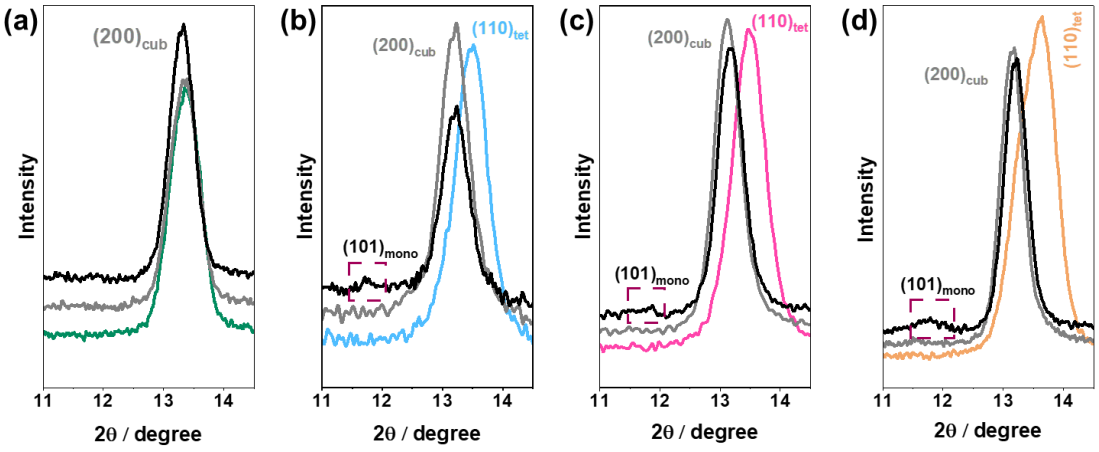

Figure 5.15. (a-d) Comparison of zoomed-in XRD patterns [(101) reflection region] for HE-, ME-, LE- and Mn-PW.

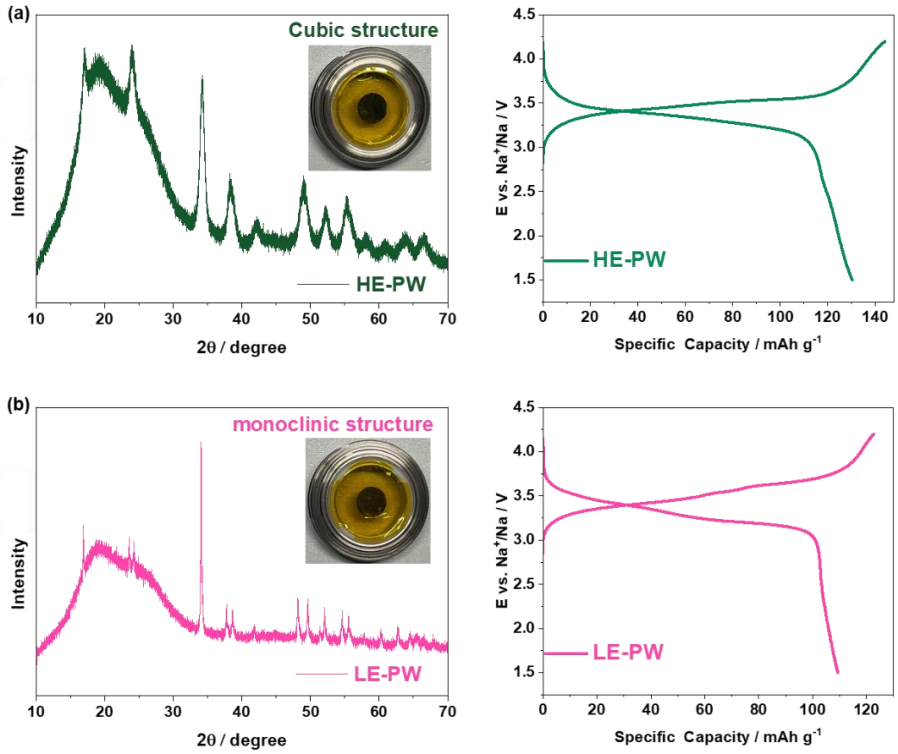

Figure 5.16. (a, b) *Ex situ* XRD patterns of HE- and LE-PW after the first cycle and corresponding voltage profiles. The cathodes were covered with Kapton tape (producing the background signal below 30° 2θ) to avoid oxidation/reduction.

In summary, the *operando* XRD findings vividly illustrate the advantages of employing the high-entropy strategy to enhance the structural resilience of PW frameworks. Higher configurational entropy within the PW system correlates with greater suppression of phase changes towards monoclinic and tetragonal structures, thereby preserving structural symmetry and stability. The trend observed in the structural degradation of Mn-PW < LE-PW < ME-PW < HE-PW also accounts for the superior cycling performance of the latter materials with higher ΔS_{conf} described above. Additionally, it is proved that the preferable high-symmetrical structure of HE-PW, i.e., stabilized at the cubic crystal structure during the battery cycle within this Chapter.

To further explore the structural degradation of the PW materials, their gas emission behavior using DEMS by comparing the qualitative and quantitative aspects of gas evolution between LE-PW and HE-PW was examined.[206,207] **Figure 5.17** illustrates the gas evolution profiles of both materials during the initial three cycles, focusing on the most notable gases, while **Table 5.6** presents all quantifiable gas amounts. Hydrogen (H_2, m/z = 2) is produced through the reduction of water and degradation of protic electrolyte species at the anode. The early detection of H_2 during the initial charging phase is probably due to the release of crystal water or coordinated water. This coincides with the transition from monoclinic to cubic structure. It is reasonable to suggest that the phase transition

prompts the release of water as a result of structural rearrangement. This observation becomes particularly pronounced when considering that the early release of H_2 during charging recurs in subsequent cycles, with LE-PW exhibiting a notably stronger effect. Simultaneously, a significantly reduced H_2 evolution was noted for HE-PW, despite both materials being subjected to identical drying conditions and found to possess a similar water content, as indicated in **Table 5.3**. Of note is that no concurrent carbon dioxide (CO_2, m/z = 44) evolution was observed during the early charge, which can be formed as a byproduct of ethylene carbonate hydrolysis.[208] At elevated potentials and state of charge (SOC), the evolution of H_2 increases as the coordinated water is released in the form of $Na(OH_2)^+$, attributed to reduced binding energy.[209,210]

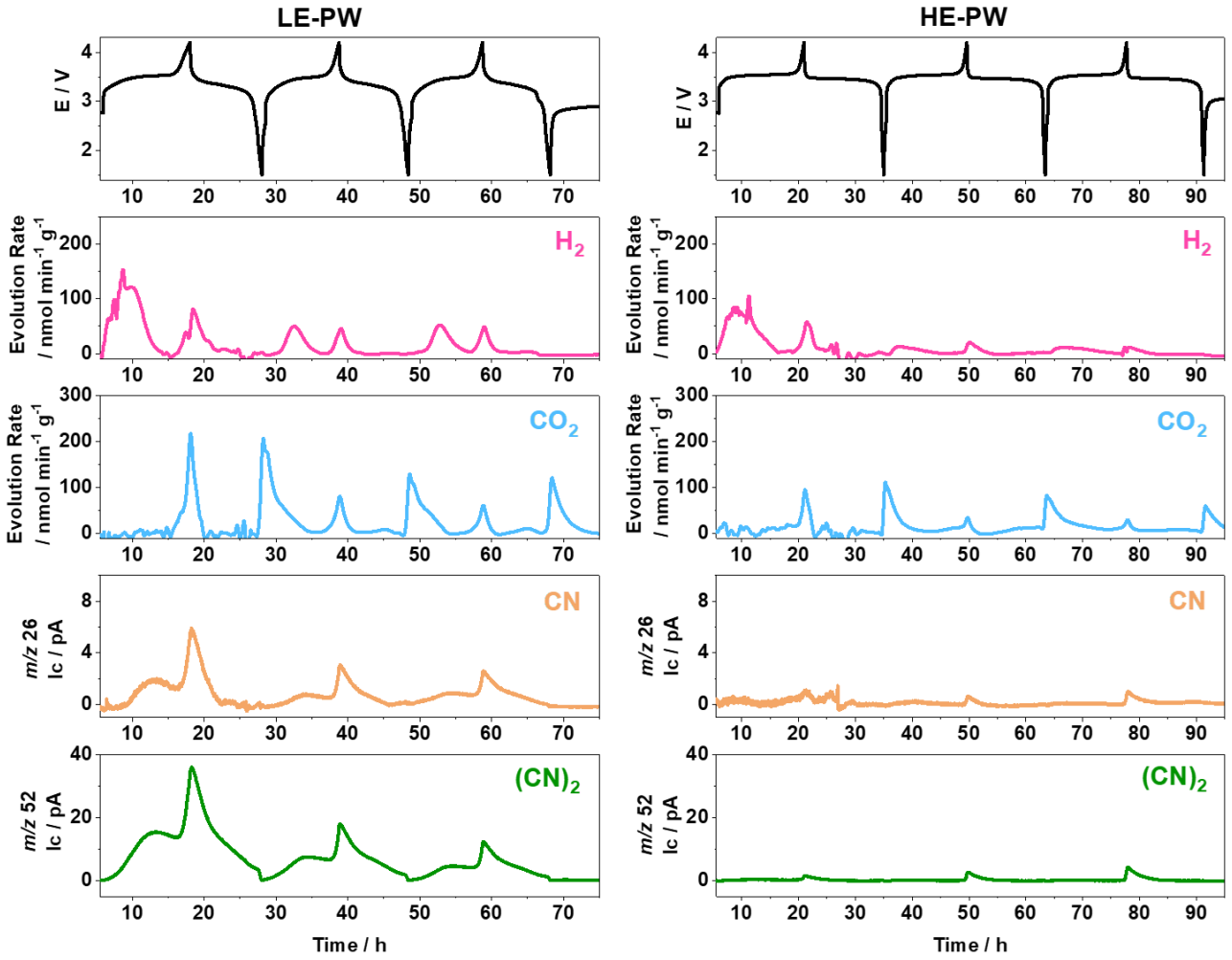

Figure 5.17. *In-situ* gas analysis. Gas evolution profiles for the LE-PW and HE-PW cathodes as obtained via DEMS.

Table 5.6. Gas amounts determined by DEMS.

Material	Property	Cycle			
		1	2	3	Total
HE-PW	H_2 evolution / µmol g^{-1}	38.1	6.5	6.6	51.2
	CO_2 evolution / µmol g^{-1}	44.2	27.2	17.3	88.7
LE-PW	H_2 evolution / µmol g^{-1}	48.3	14.0	13.0	75.3
	CO_2 evolution / µmol g^{-1}	76.7	29.3	21.8	127.8

CO_2 is evolved from the electrochemical electrolyte oxidation and/or degradation of surface impurities, such as carbonates, which have been recently identified in PWs as well.[211–213] The increased quantity of CO_2 observed in the initial cycle is likely attributed to surface impurities, as their decomposition predominantly occurs during this phase,[212] while the relatively consistent gas levels between the second and third cycles suggest a recurring reaction. Once more, gas evolution was more pronounced in LE-PW, despite HE-PW exhibiting higher specific capacity and SOC. Considering the slight differences in the shapes of the voltage profiles, it could be suggested that the increased gas evolution is predominantly influenced by the prolonged exposure to elevated potentials. Therefore, the gas evolution rate, depicted in **Figure 5.18a** as a function of potential, illustrates that at any given potential, the rate of CO_2 evolution is higher for LE-PW compared to HE-PW. Additional CO_2 release, without H_2 production, was observed towards the end of discharge at potentials below 1.8 V. This behavior, consistent with previous findings for P2-type layered oxide SIB materials, is likely attributed to the reduction of fluoroethylene carbonate at the cathode. This reduction process is known to release CO_2 exclusively, without generating H_2, especially at lower potentials.[214,215]

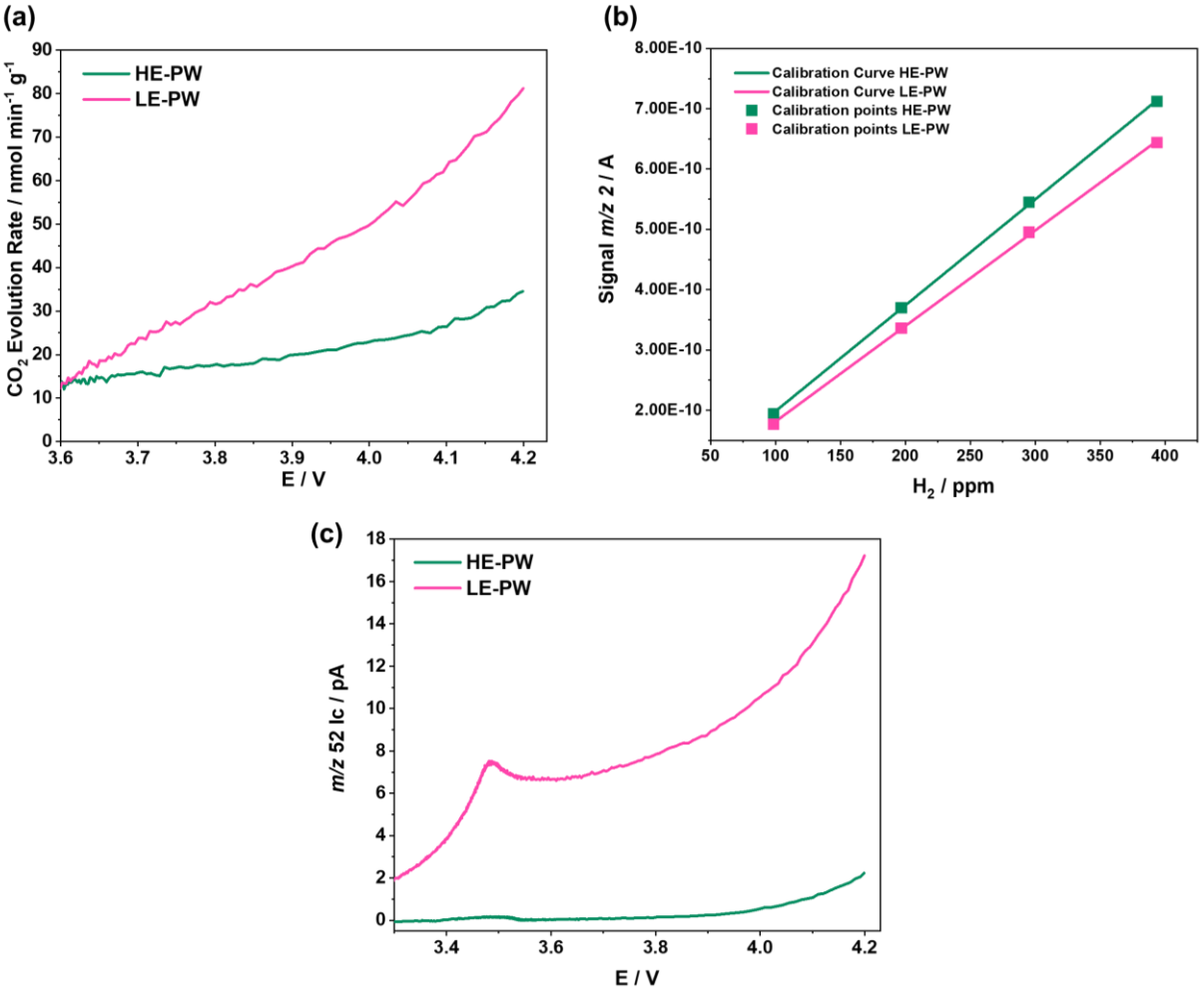

Figure 5.18. (a) Carbon dioxide evolution rates as a function of potential in the second cycle. (b). Linearity of the *m/z* = 2 signal in the calibration range is ensured even after increase of the secondary electron multiplier voltage. Similar absolute signal strength allows direct comparison of *m/z* = 52 signals. (c) $(CN)_2$ evolution (*m/z* = 52) as a function of potential in the second cycle.

Finally, cyanogen gas [$(CN)_2$] was detected at both at *m/z* = 52 and 26, while no hydrogen cyanide (HCN, *m/z* = 27), consistent with previous findings.[75] The release of $(CN)_2$ usually results from the thermal decomposition of PW/PBA cathodes,[216,217] while in this case, it originates from electrochemical decomposition. Absolute detector currents are reported due to the absence of a calibration gas mixture, which are higher in this section due to the discussed modifications outlined in the Experimental Methods (Chapter 4). However, as shown for the *m/z* = 2 signal (see **Figure 5.18b**), the absolute signal intensity was similar between both materials, as they were measured in direct succession without changes in parameters and baseline values and with electrodes of same active material content. Hence, the *m/z* = 52 and 26 signals can be considered proportional to the $(CN)_2$ evolution rate. A drastic difference was observed between curve shape and evolution signal for LE-PW and HE-PW. In LE-PW, the $(CN)_2$ evolution rate exhibited a prominent recurring shoulder, albeit

diminishing in intensity, during the early stages of each charge cycle. This phenomenon coincided with the previously discussed H_2 evolution, attributed to the transition from monoclinic to cubic phase. Overall, phase transitions seem to underlie another degradation mechanism: the release of $(CN)_2$ from the active material. Additionally, both materials exhibited $(CN)_2$ evolution at high potentials towards the end of charge. However, the interpolated evolution rate at any specific potential was significantly higher for LE-PW compared to HE-PW, as illustrated in **Figure 5.18c**. Interestingly, in **Figure 5.18c**, a small shoulder of $(CN)_2$ evolution around 3.5 V is also pronounced in the HE-PW. Earlier studies have linked the release of $(CN)_2$ at high potentials and SOC to the evolution of O_2 from layered oxides.[211,218] with both adhering to the abstract concept of oxidative dimerization of host structure anions.[75] The evolution of $(CN)_2$ at low SOC necessitates a reconsideration of this analogy, as it is not observed for lattice oxygen. However, in the case of layered oxides, another significant source of gas evolution is the decomposition of surface carbonates.[207,212] These may decompose to CO_2 either chemically, via acid protons or electrochemically by oxidation, generating both CO_2 and O_2. It should be noted, however, that the relative contributions of these mechanisms remain a subject of debate.[207,219–221] Drawing an analogy to this electrochemical oxidation, the oxidation of surface cyanide species, such as NaCN or $Na_4[Fe(CN)_6]$,[222] may contribute to the $(CN)_2$ evolution. Recurred phase transitions, causing particle fracture and exposure of fresh surfaces, may then explain the gas evolution in the following cycles.

In summary, the simultaneous evolution of H_2 and $(CN)_2$ at the onset of charging provides strong evidence of the detrimental impact of phase transitions, as the structural rearrangement induces gas-evolving degradation reactions. The structural evolutions derived from *operando* XRD and DEMS measurements are summarized in **Figure 5.19**. As demonstrated, the high-entropy approach fosters the preparation of a PW material with significantly mitigated gas evolution and phase transitions, making it an effective optimization strategy.

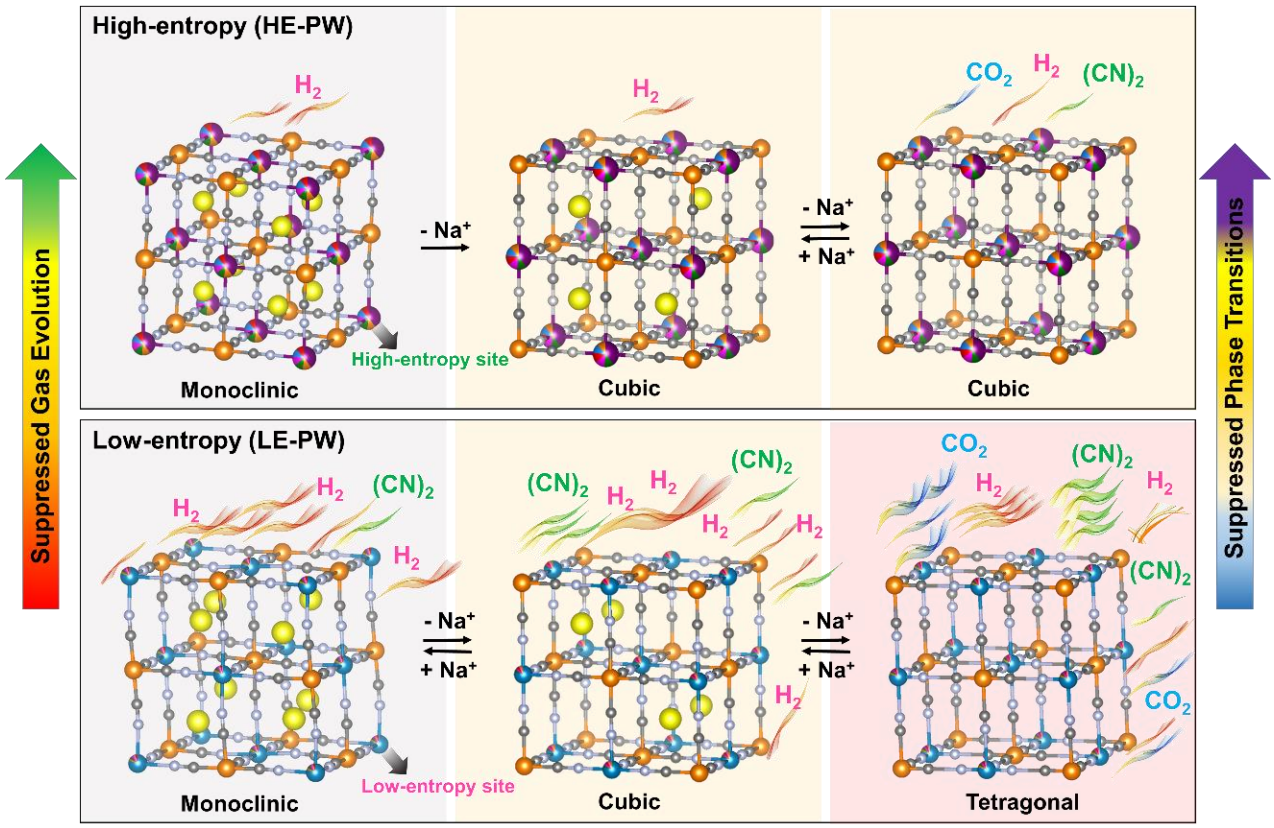

Figure 5.19. Schematic illustration of the structural evolutions and corresponding gassing behavior of HE-PW and LE-PW.

Finally, first-principles DFT calculations were conducted to determine the Gibbs free energy of the relevant phases and explore the influence of configurational entropy on stability. **Table 5.7** presented the computed results for the HE-, ME- and LE-PW materials based on different degrees of de-/sodiation. For the fully de-sodiated state (x = 0), the cubic ($Fm\bar{3}m$ space group) and tetragonal ($I\bar{4}m2$ space group) structures were examined and compared. Our results suggest that upon complete removal of Na^+ ions from the lattice ($Na_xTM[Fe(CN)_6]$ with $x = 0$), HE-PW exhibits a high-symmetry cubic phase, while both ME- and LE-PW adopt a tetragonal structure since the thermodynamic is more stable at these states (see **Figure 5.20a**). This discovery corroborates the XRD findings and confirms the experimentally observed phase transitions during charging.

Table 5.7. The computed thermodynamic parameters for the HE-, ME- and LE-PW materials (for different degrees of sodiation, i.e., x in $Na_xTM[Fe(CN)_6]$). For $x = 0$, the enthalpy difference between the cubic and tetragonal phases is presented. For $x = 1$, the formation enthalpy, the configurational entropy contribution to the Gibbs free energy at 298 K and the Gibbs free energy of formation are reported (given in units of kJ mol^{-1}). For $x = 1.5$, the enthalpy difference between the cubic and monoclinic phase in HE-PW is given.

	Energy	HE-PW	ME-PW	LE-PW
$x = 0$	$\Delta H = H_{cubic} - H_{tet}$	−171.165	9.070	33.191
$x = 1$	ΔH_f	−403.018	−403.790	−404.369
	$-T\Delta S_{conf}$ at 25 °C	−4.130	−3.345	−2.099
	$\Delta G_f = \Delta H_f - T\Delta S_{conf}$	−407.148	−407.135	−406.467
$x = 1.5$	$\Delta H = H_{cubic} - H_{mono}$	−13.351	-	-

In the sodiated state ($x = 1$), the cubic phase emerges as most stable structure for all three materials. To evaluate their relative stability, Gibbs free energies of formation (ΔG_f) were computed and compared. Despite the formation enthalpy (ΔH_f) of LE-PW is lower by 1.4 and 0.6 kJ mol^{-1} (more negative) than that of HE-PW and ME-PW, respectively, the difference can be readily offset by the entropy term ($-T\Delta S_{conf}$) at room temperature (see **Figure 5.20b**). This suggests a certain stabilization attributed to configurational entropy for HE-PW. Therefore, the overall Gibbs free energies of formation at room temperature for HE-, ME-, and LE-PW in the sodiated state closely align (within 1 kJ mol^{-1}), establishing a structural stability sequence of LE-PW < ME-PW < HE-PW.

In the highly sodiated state ($x = 1.5$), mirroring the composition as synthesized, the structural stability of the cubic and monoclinic phases in HE-PW was explored. The latter material demonstrated a consistent pattern of structural stabilization in response to electrochemical cycling. According to the DFT results, for x = 1.5, the cubic structure exhibits greater stability compared to its monoclinic counterpart, characterized by a lower energy state (about −13.35 kJ mol^{-1}). One possible explanation for the synthesis of monoclinic HE-PW could be attributed to kinetics. In accordance with thermodynamic principles, a system typically progresses towards its most stable state, characterized by the lowest energy. However, kinetic factors may hinder the system from reaching this state. If the energy barrier between the monoclinic and cubic phases is significant, the system may become confined to the monoclinic phase, despite the cubic phase being energetically preferable. This phenomenon is often termed kinetic stabilization or kinetic trapping. In simpler terms, even though the cubic phase is energetically more stable, as confirmed by DFT calculations, transitioning to it might be energetically challenging. The system might lack sufficient thermal energy to surpass the energy barrier, thus becoming confined to a metastable monoclinic phase. Yet, throughout cycling, the

infusion of external energy facilitates the phase transition, enabling the system to achieve and sustain the more stable cubic phase. Indeed, the structural parameters calculated via DFT for the HE-, ME-, and LE-PW materials are detailed in **Table 5.8**. The mean voltages calculated for the most stable structures, as shown in **Table 5.9**, were observed to closely correspond with the electrochemical measurements. These computational findings suggest that compositional disorder enhances the robustness of the structure, facilitating accommodation of electrochemical reactions. Furthermore, the preference for the high-symmetry structure of HE-PW is corroborated. This aligns closely with the experimental data discussed earlier and underscores the significance of configurational entropy in enhancing material stability.

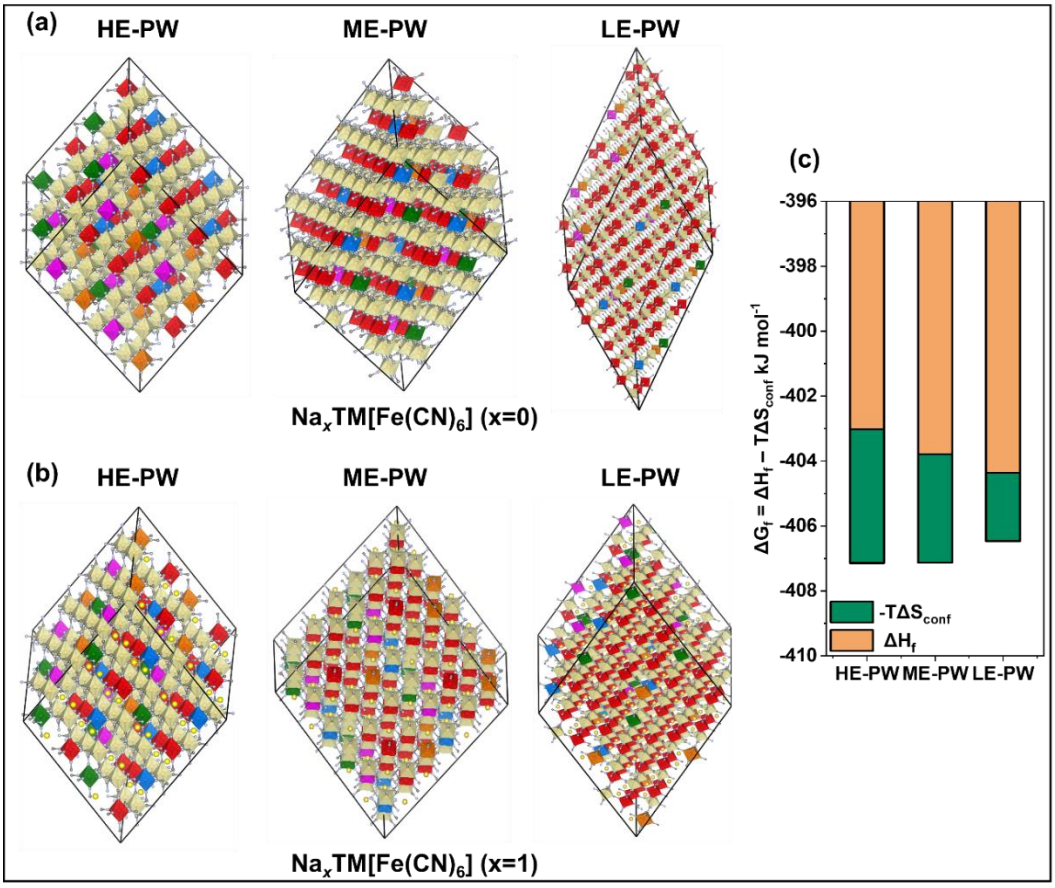

Figure 5.20. Crystal structures of (a) HE-PW (cubic), ME-PW (tetragonal) and LE-PW (tetragonal) in the fully charged state (x = 0 in Na$_x$TM[Fe(CN)$_6$]). (b) Corresponding structures for x = 1 (cubic). (c) The Gibbs free energy of formation of the three systems at 298 K.

Table 5.8. DFT-calculated structural parameters for HE-PW, ME-PW and LE-PW. Cubic structure is defined by $a = b = c$ and $\alpha = \beta = \gamma = 90°$, while tetragonal structure is characterized by $a = b \neq c$ with $\alpha = \beta = \gamma = 90°$. Volume of tetragonal structure (in parentheses) is scaled to the stoichiometry of the cubic phase for direct comparison.

	Sodium content	**Structure**	***a* (Å)**	***c* (Å)**	***V* (Å^3)**
HE-PW	$x = 1.5$	Cubic	10.039	-	1011.705
	$x = 1.0$	Cubic	10.007	-	1002.158
	$x = 0$	Cubic	10.014	-	1004.239
ME-PW	$x = 1.0$	Cubic	10.170	-	1051.763
	$x = 0$	Tetragonal	7.026	9.983	492.848 (985.696)
LE-PW	$x = 1.0$	Cubic	10.366	-	1113.779
	$x = 0$	Tetragonal	7.193	10.289	532.335 (1064.670)

Table 5.9. The most stable structures of HE-, ME- and LE-PW at $x = 1$ and $x = 0$ in $Na_xTM[Fe(CN)_6]$ and corresponding (calculated) mean voltage.

	HE-PW	**ME-PW**	**LE-PW**
$x = 1$	Cubic	Cubic	Cubic
$x = 0$	Cubic	Tetragonal	Tetragonal
Mean voltage / V	3.249	3.332	3.123

6. Leveraging Entropy and Crystal Structure Engineering in Prussian Blue Analogue Cathodes for Sodium-Ion Batteries

HEPBAs as cathodes for SIBs application exhibit fast charge/discharge kinetics and prolonged lifetimes compared to conventional PBA cathodes,[101,166,223] as demonstrated in the Chapter 5.[166] Despite this, the fundamental mechanisms related to the impact of high-entropy configurations on structure-property relationships remain unclear, particularly regarding how configurational entropy influences cationic redox processes in multicomponent hexacyanoferrate cathodes at high potentials. Most of the prevailing research has concentrated on multicomponent PBAs below a cut-off potential of 4.2 V vs. Na^+/Na. However, no study has yet conducted a comparative evaluation of the effect of configurational entropy on PBAs with different structures during high-voltage operation (> 4.2 V vs. Na^+/Na). It should be noted that the high-voltage operation tends to trigger structural distortion and cationic recombination, which is closely related with irreversible phase transition. In the realm of PBAs, these phenomena appear as a phase transition from cubic to tetragonal when charged to 4.2 V,[47,74] leading to sluggish sodium-ion kinetics and significant capacity decay.[166] Yet, stable host structure of HEPBAs alleviates lattice deformation and collapse, crucial for high-voltage operation, thus boosting the specific capacity and energy density of battery materials. Therefore, the key to mitigating structural degradation is to build a robust host structure capable of enduring high potentials. To date, despite numerous strategies to mitigate the structural degradation of PBAs to improve the structural stability, the high-entropy approach has never been applied to stabilize hexacyanoferrate cathodes at high voltage (> 4.2V vs. Na^+/Na).

In this chapter, integration of composition disorder with crystal structure engineering was employed to modulate PBAs with distinct crystallographic configurations, achieved through meticulous control of reaction temperatures. Five metal ions (Mn, Co, Fe, Ni, and Cu) were incorporated to produce a cubic structured HEPBA material having the chemical formula of $Na_{1.46}Mn_{0.3}Co_{0.3}Fe_{0.133}Ni_{0.133}Cu_{0.133}[Fe(CN)_6]_{0.86}\square_{0.14}\cdot 1.74H_2O$ (referred to as Cub-HEPBA), and a monoclinic structured HEPBA possessing a similar composition of $Na_{1.48}Mn_{0.3}Co_{0.3}Fe_{0.133}Ni_{0.133}Cu_{0.133}[Fe(CN)_6]_{0.87}\square_{0.13}\cdot 1.12H_2O$ (termed as Mono-HEPBA). To explore the impact of the high-entropy concept on various PBA structures, several characterization

methods were employed, such as *operando* XRD, *operando* DEMS, *operando* EIS, and *operando* stress analysis, in conjunction with high-temperature performance studies and full cell testing. By employing this multifaceted strategy, it is demonstrated that the crucial role of high-entropy methods in enhancing the overall stability of structures (both cubic and monoclinic PBAs), with a profound impact on crystal structure selectivity. Specifically, the robust structure of Cub-HEPBA displays remarkable electrochemical performance, preserving a specific capacity of approximately 60 mAh g^{-1} even after 10000 cycles at 800 mA g^{-1}, characterized by high reversibility even when subjected to high-voltage conditions (4.5 V vs. Na^+/Na). In contrast, Mono-HEPBA delivers high capacities at low specific currents of ≤ 10 mA g^{-1}, but shows limitations at higher currents. The prevalent monoclinic structure exacerbates lattice distortions, resulting in compromised transport kinetics and notable degradation during cycling. This finding underscores the advantageous role of the highly symmetrical cubic PBA structure in enhancing stability and improving cycle durability.

6.1. Materials Synthesis

Cubic and monoclinic, high-entropy $Na_xMn_{0.3}Co_{0.3}Fe_{0.133}Ni_{0.133}Cu_{0.133}[Fe(CN)_6]_{1-y}\cdot nH_2O$ materials were prepared by a simple co-precipitation method at different temperatures. Typically, 8 mmol $Na_4Fe(CN)_6\cdot 10H_2O$ and stoichiometric amounts of $FeCl_2\cdot 4H_2O$, $MnCl_2\cdot 4H_2O$, $NiCl_2\cdot 6H_2O$, $CuCl_2\cdot 2.5H_2O$, and $CoCl_2\cdot 6H_2O$ (in total 6 mmol metal precursors) were dissolved in 100 mL deionized water to form solutions A and B. After complete dissolution (ultrasonication for 0.5 h and then stirring for 0.5 h), sodium citrate (5.35 g) was added to both solutions under stirring to obtain homogeneous solutions. Then, the two solutions A and B were slowly and simultaneously added dropwise to 200 mL deionized water under stirring to form solution C. The mixture was kept stirring for 4 h at 25 °C for Cub-HEPBA and at 70 °C for Mono-HEPBA, and aged for 12 h without stirring before centrifugation. The synthesis process is illustrated in **Figure 6.1**. The precipitate was washed several times with deionized water, and the wet powder was finally dried in a vacuum oven at 100 °C for 12 h. To prevent the samples from absorbing water, they were quickly transferred into an Ar-filled glovebox.

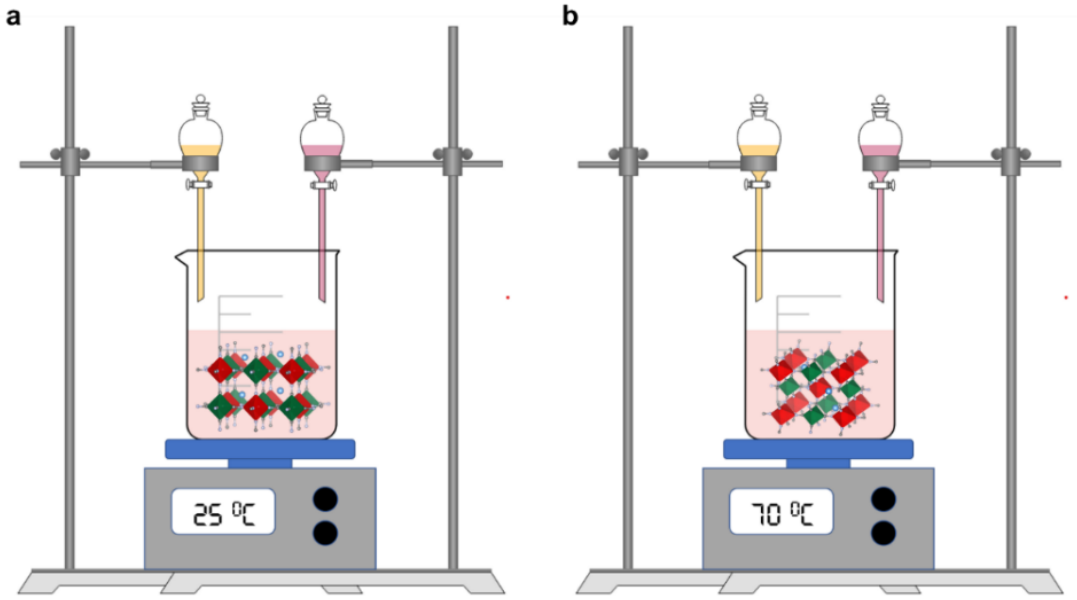

Figure 6.1. (a, b) Schematic illustration of the synthesis of Cub- and Mono-HEPBA. To diminish heat loss, the beaker was fully wrapped in aluminum foil. A temperature detector was used to monitor the change in temperature in real time.

6.2. Structural and Compositional Analysis

This chapter examines and compares two HEPBAs with similar compositions but different structures: one cubic and the other monoclinic. Initially, XRD measurements followed by refinement analyses were performed to investigate the crystal structure of Cub- and Mono-HEPBA. The results confirmed the expected differences in crystal structures. **Figure 6.2a** shows that the structure of Cub-HEPBA, synthesized at 25°C, belongs to the face-centered cubic crystal lattice (*Fm*-3*m*, ICSD coll. code 193354),[224] with $a = b = c$ =10.411(2) Å, $\alpha = \beta = \gamma = 90°$, and V = 1128.5(8) Å^3. While Mono-HEPBA (**Figure 6.2b**), obtained at 70 °C, is well indexed to a monoclinic structure with the $P2_1/n$ space group[225] (ICSD coll. code 266392). The calculated lattice parameters of Mono-HEPBA are a = 10.461(1) Å, b = 7.484(1) Å, c = 7.228(1) Å, $\alpha = \gamma = 90°$, β = 91.36(1)°, V = 565.7(1) Å^3. The primary distinction in the XRD patterns between the cubic and monoclinic structures is the noticeable peak splittings found in Mono-HEPBA at 18.69°, 19.10° (-211 / 211), 29.81°, 30.38° (031 / 013), and 37.78°, 38.65° (42-2 / 422), respectively. On the contrary, no splitted peaks in the (200), (220), (400) and (420) crystal planes can be found in the XRD pattern of Cub-HEPBA.[72,199] The corresponding results of the refinement of the structures are summarized in **Table 6.1 and Table 6.2**.

The local structure model of the samples identifies 5-metal atoms (Mn, Co, Fe, Ni, and Cu) share the same N-coordinated positions, with Mn and Co predominating. Particularly, within Cub-HEPBA, the high entropy positions are at 4*b* sites, whereas in Mono-HEPBA, they are situated on the 2*a* sites. At the same time, C-coordinated Fe ions (Fe_1) are located at the 4a sites in Cub-HEPBA and at the 2d sites in Mono-HEPBA. This result reveals the structure of PBAs is composed of linear chains of Fe_1−C≡N−M(Mn/Co/Ni/Cu/Fe_2)−N≡C−Fe_1 along the edges of the unit cell,[72,101] as illustrated in **Figure 6.2c**. Moreover, the monoclinic structure exhibits a tilt of the bond angles, i.e., (−C≡N−M−) is shifted from the typical 180° in a cubic phase to 159°; at the same time the distance of Fe1···M elongates from 5.205 Å in cubic phase to 5.230 Å.

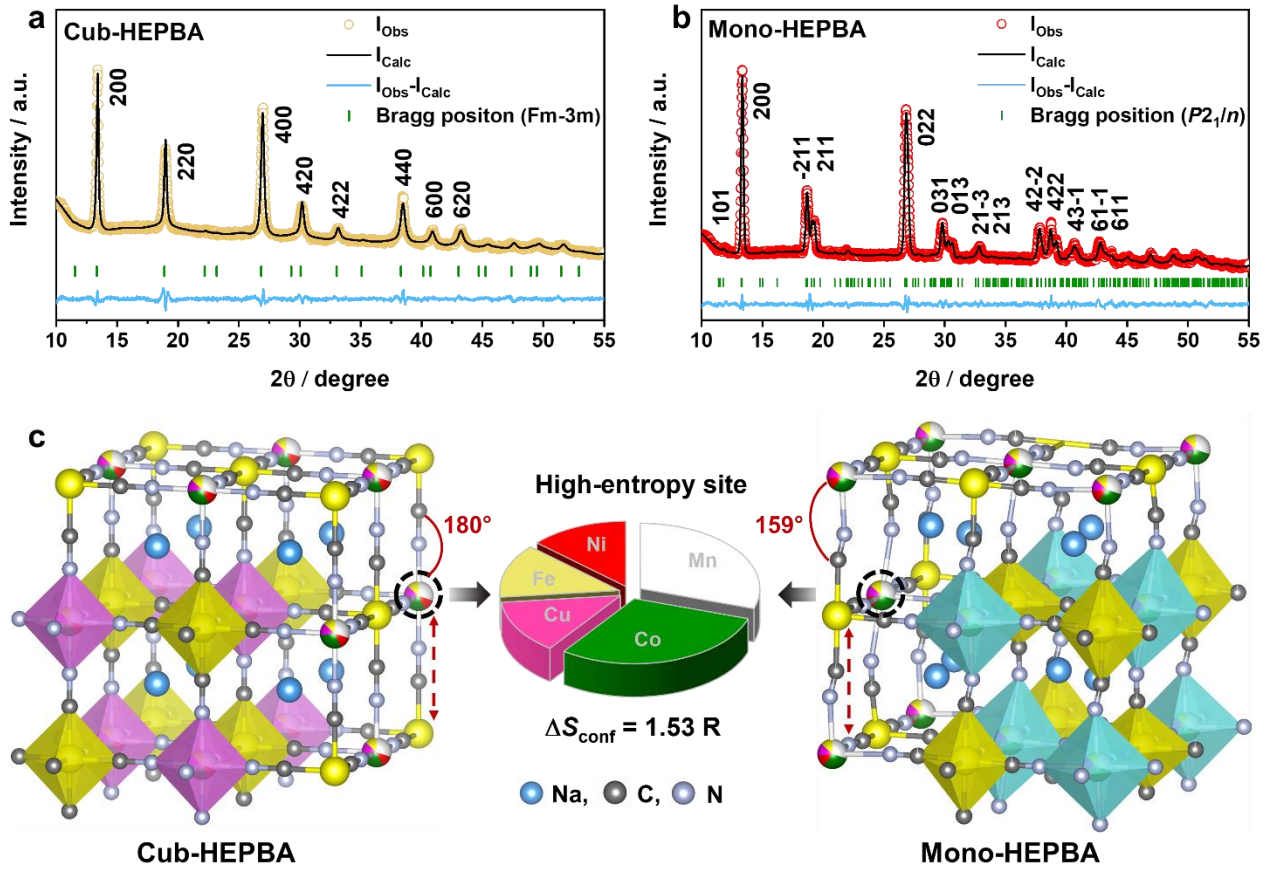

Figure 6.2. (a, b) Rietveld refinement patterns of XRD data collected from Cub- and Mono-HEPBAs and (c) corresponding schematic illustrations of the crystal structure.

ICP-OES (**Table 6.3**) and DSC (**Figure 6.3**) were conducted to analyze the chemical composition and water content of the as-synthesized materials. The chemical formulas were determined to be

$Na_{1.46}Mn_{0.3}Co_{0.3}Fe_{0.133}Ni_{0.133}Cu_{0.133}[Fe(CN)_6]_{0.86}\square_{0.14}\cdot 1.74H_2O$ for Cub-HEPBA, and $Na_{1.48}Mn_{0.3}Co_{0.3}Fe_{0.133}Ni_{0.133}Cu_{0.133}[Fe(CN)_6]_{0.87}\square_{0.13}\cdot 1.12H_2O$ for Mono-HEPBA, respectively. According to the derived definition of statistical thermodynamics of configurational entropy[179] (ΔS_{conf}, see **Equation 3.4** in Introduction Part), both samples show the same ΔS_{conf} of 1.53 *R* based on similar chemical compositions and therefore can be classified as HEPBAs.

Table 6.1. Structural parameters and quality-of-fit parameters from refinement of structural models against the XRD pattern of Cub-HEPBA.

Atom	Wyckoff pos.	Atomic pos.			Occ
		x	*y*	*z*	
Fe1	4a	0	0	0	0.860
Na	8c	0.25	0.25	0.25	1.000
Mn	4b	0.5	0.5	0.5	0.300
Fe2	4b	0.5	0.5	0.5	0.1333
Ni	4b	0.5	0.5	0.5	0.1333
Cu	4b	0.5	0.5	0.5	0.1333
Co	4b	0.5	0.5	0.5	0.300
C	24*e*	0.225 (11)	0	0	0.860
N	24*e*	0.272(7)	0	0	0.860
$a = b = c = 10.411(2)$ Å, $\alpha = \beta = \gamma = 90°$, $V = 1128.5(8)$ Å^3, $R_{wp} = 2.6\%$, *Fm*−3*m* space group.					

Table 6.2. Structural parameters and quality-of-fit parameters from refinement of structural models against the XRD pattern of Mono-HEPBA.

Atom	Wyckoff pos.	Atomic pos.			Occ
		x	*y*	*z*	
N1	4e	0.539(6)	0.329(5)	0.769(9)	0.870
N2	4e	0.270(3)	0.512(3)	0.486(9)	0.870
N3	4e	0.471(3)	0.256(5)	0.324(6)	0.870
C1	4e	0.473(4)	0.162(6)	0.779(9)	0.870
C2	4e	0.177(3)	0.462(6)	0.534(6)	0.870

C3	4e	0.557(5)	0.218(5)	0.162(8)	0.870
Na	4e	0.257(5)	0.487(5)	0.006(13)	1.000
Fe1	2d	0.5	0	1	0.870
Ni	2a	0.5	0.5	0.5	0.1333
Cu	2a	0.5	0.5	0.5	0.1333
Co	2a	0.5	0.5	0.5	0.300
Mn	2a	0.5	0.5	0.5	0.300
Fe2	2a	0.5	0.5	0.5	0.1333

a = 10.461(1) Å, b = 7.484(1) Å, c = 7.228(1) Å, β = 91.36(1)°, V = 565.7(1) Å^3, R_{wp} = 1.7%, $P2_1/n$ space group.

Table 6.3. ICP-OES results for Cub- and Mono-HEPBA and corresponding configurational entropies.

Material	Measured composition	ΔS_{conf}
Cub-HEPBA	$Na_{1.46}Mn_{0.3}Co_{0.3}Fe_{0.133}Ni_{0.133}Cu_{0.133}[Fe(CN)_6]_{0.86}\square_{0.14}\cdot 1.74H_2O$	1.53R
Mono-HEPBA	$Na_{1.48}Mn_{0.3}Co_{0.3}Fe_{0.133}Ni_{0.133}Cu_{0.133}[Fe(CN)_6]_{0.87}\square_{0.13}\cdot 1.12H_2O$	1.53R

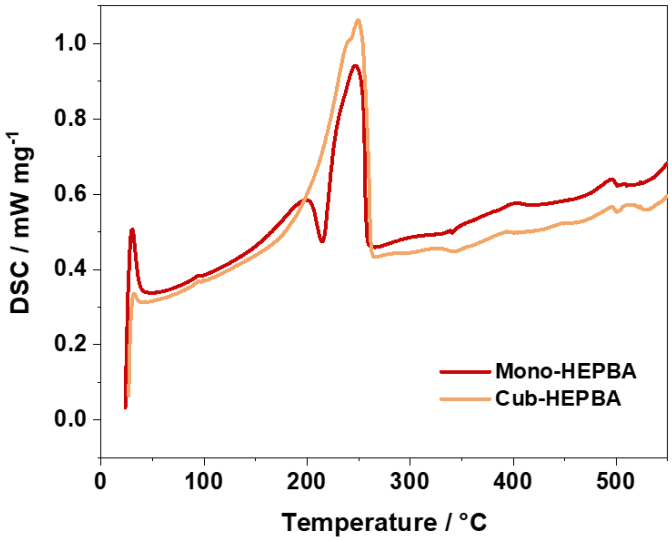

Figure 6.3. DSC analysis of Cub- and Mono-HEPBA. The content of crystal water was estimated from the weight loss in the temperature range of 40–130 °C (dehydration).[75,170] Mono-HEPBA presents an extra endothermal peak between 210 and 220 °C, which could be due to mesophase transition or melting.[226] At 230–330°C, an exothermal peak is detected for both Cub- and Mono-HEPBA, indicating release of $(CN)_2$ and further decomposition.

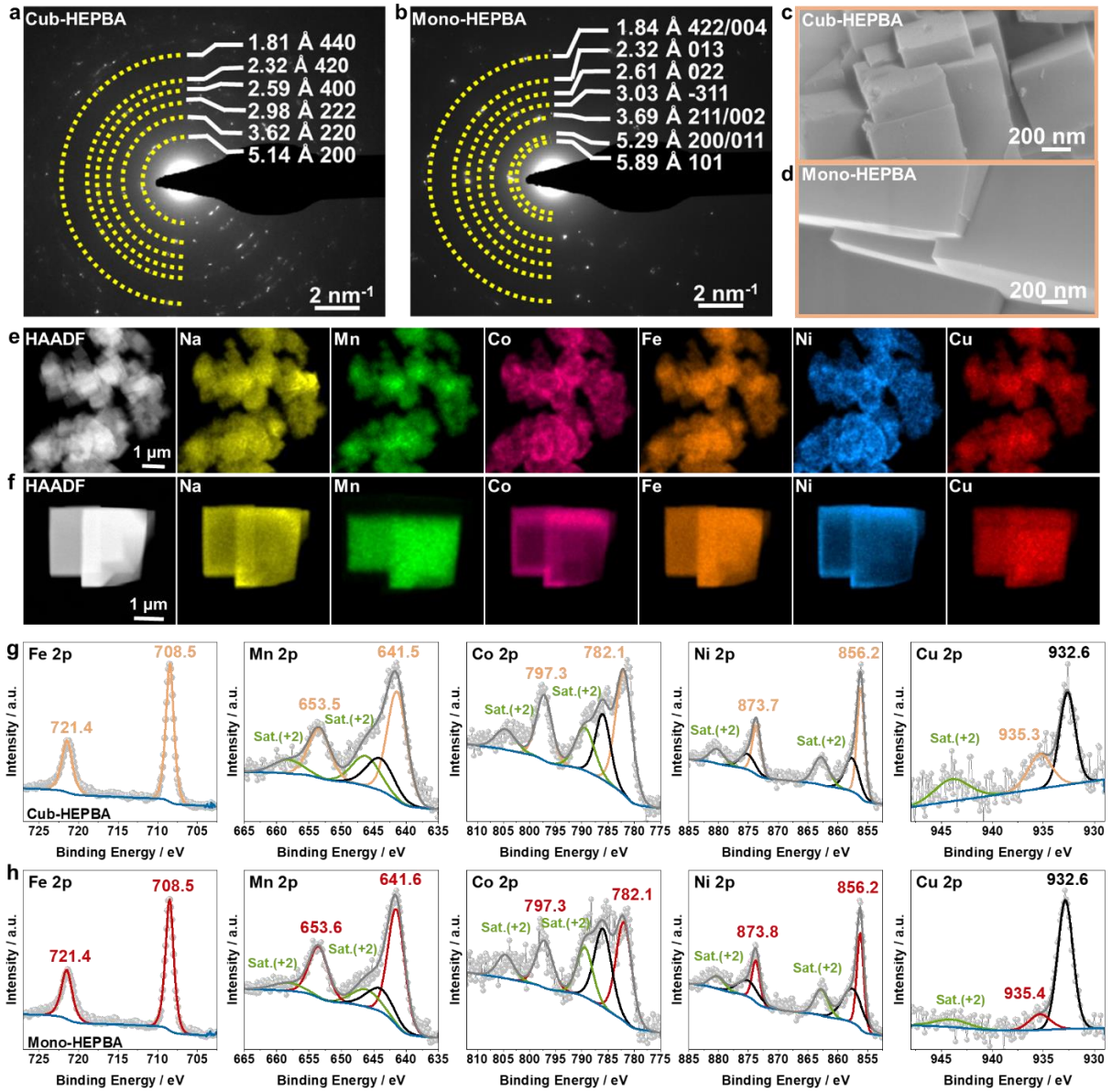

Figure 6.4. Structural and morphological characterization of Cub- and Mono-HEPBAs. (a, b) SAED patterns, (c, d) SEM images, and (e, f) STEM-EDS elemental maps. (g, h) XPS analysis with detail spectra of the Fe, Mn, Co, Ni, and Cu 2p core level regions.

Selected-area electron diffraction (SAED) (**Figure 6.4a** and **b**) was performed to further confirm the structure and phase purity of the samples. The (200), (220), (400) and (420) planes of the cubic structure can be observed for Cub-HEPBA, while the (101), (211), (022) and (013) planes of the monoclinic phase could be seen for Mono-HEPBA. As evidenced by SEM, a mass of aggregated small cube particles is piled up to form micron-sized Cub-HEPBA, with an average size of 2 μm (see **Figure 6.4c**). Meanwhile, Mono-HEPBA exhibits a cubic morphology as well, but with less pronounced

aggregation (**Figure 6.4d**). Further characterization through HAADF STEM (high-angle annular dark-field STEM) and corresponding EDS mapping confirms the uniform distribution of Na, Mn, Co, Fe, Ni, and Cu in both samples (**Figure 6.4e, f**).

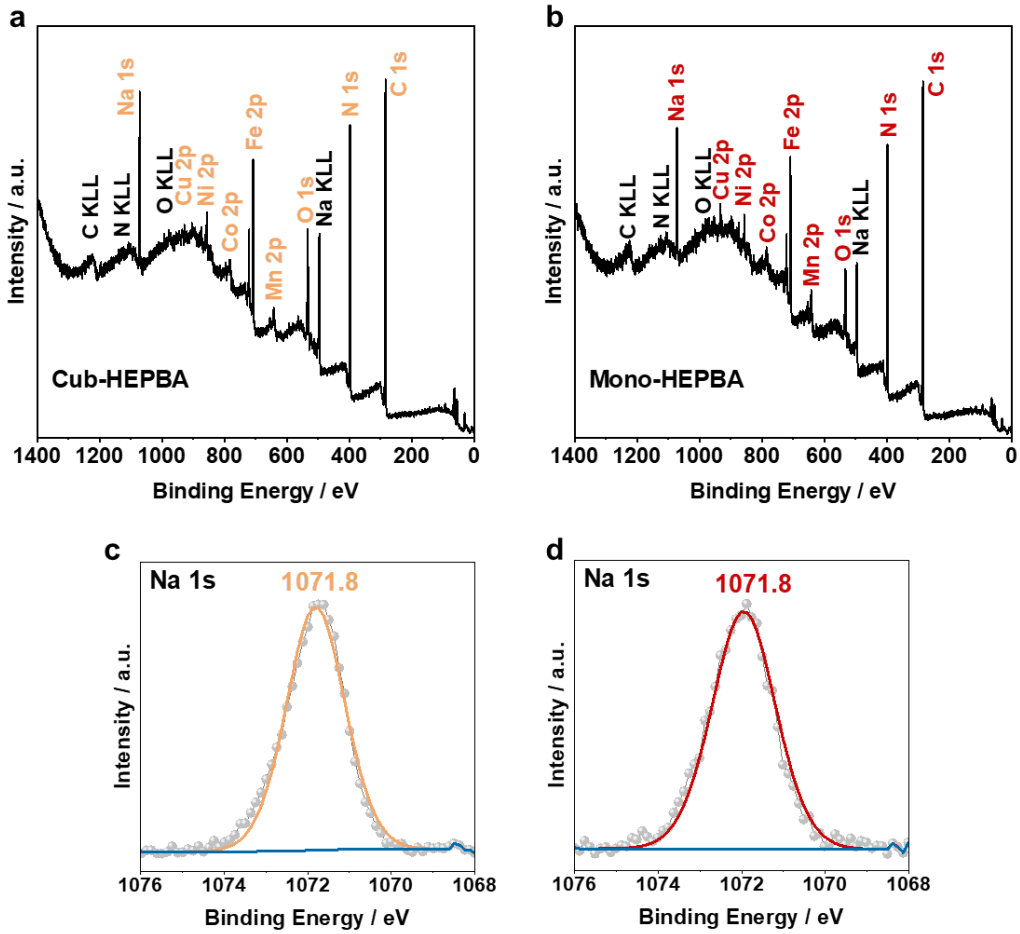

Figure 6.5. Survey and detailed Na 1s spectra for (a, c) Cub- and (b, d) Mono-HEPBA.

An in-depth analysis of the surface chemical composition was conducted using XPS, with the relevant results shown in **Figure 6.4g, h** and **6.5**. The survey spectra of Cub- and Mono-HEPBA (**Figure 6.5a** and **b**) verify the presence of the previously mentioned elements (Na, Mn, Co, Fe, Ni, and Cu). Remarkably, the Na 1s detailed spectrum of Cub-HEPBA prominently shows a single peak at a binding energy of 1071.8 eV (**Figure 6.5c**), which aligns with the result for the Mono-HEPBA sample (**Figure 6.5d**). A comparison of the detailed spectra for the other metals (**Figure 6.4g and h**) demonstrates that the results of Cub-HEPBA are very similar to those of Mono-HEPBA, with only minor shifts in

binding energy. Starting with the detail spectra in the Fe 2p region, a peak doublet at 708.5 and 721.4 eV is detected for both materials. It is indicative of Fe^{2+} within the $[Fe^{+II}(CN)_6]^{4-}$ unit.[47,101,186,187] In contrast, the peak doublet of $[Fe^{+III}(CN)_6]^{3-}$ would be expected to occur at higher binding energy (~710/723 eV).[6] Moreover, the lack of additional characteristics additionally indicates that the N-coordinated Fe ions are also in the +2 oxidation state. The Mn 2p detail spectra exhibit in both cases binding energies of the main Mn $2p_{3/2}$ and Mn $2p_{1/2}$ peaks of approximately 641.5 and 653.5 eV, as well as pronounced satellite peaks at 646.4 and 658.3 eV, respectively. Additionally, there is a noticeable broad Ni Auger feature observed at approximately 644 eV. Given that significant satellite structures are typically exclusive to Mn^{2+} compounds, the findings suggest that manganese primarily exists in an oxidation state of +II in both HEPBAs.[75,182] Similarly, the Co 2p spectra exhibits distinctive satellite peaks at 789.6 and 804.8 eV in addition to the primary peak doublet at 782.1 (Co $2p_{3/2}$) and 797.3 eV (Co $2p_{1/2}$), accompanied by a Fe Auger peak at ~786 eV.[75,101] In a manner akin to manganese, the existence of prominent satellite features similarly indicates a +II oxidation state for cobalt. For the Ni 2p spectra, the main peak doublet at 856.2 (Ni $2p_{3/2}$) and 873.7 eV (Ni $2p_{1/2}$) is coupled with an additional doublet at slightly higher binding energy of 857.6 and 875.3 eV, together with satellite features at ~863 and 880 eV.[101] The multiplet splitting observed in the spectra of oxidized nickel species makes it difficult to accurately determine the specific oxidation state of nickel. It is worth noting that the Ni $2p_{3/2}$ peak of NiO typically occurs around 854 eV, while the Ni $2p_{3/2}$ peak of $Ni(OH)_2$ is detected at approximately 856 eV, a binding energy akin to that of Ni_2O_3.[124] Hence, discerning the oxidation state of nickel for Cub- and Mono-HEPBA is intricate. Nevertheless, prior research findings from normalized *K*-edge XANES (X-ray absorption near edge spectroscopy, Chapter 5) analysis points to an oxidation state of +II for Ni.[101,166] Finally, the main peak in the Cu $2p_{3/2}$ region at 932.6 eV can be assigned to Cu^+.[75] Additionally, the identification of a smaller peak observed at higher binding energy (935.3 eV), along with its corresponding shake-up satellite at 943.8 eV indicates the existence of some Cu in oxidation state +II,[87,185] aligning with observations in Mono-HEPBA material.

6.3. Electrochemical Properties

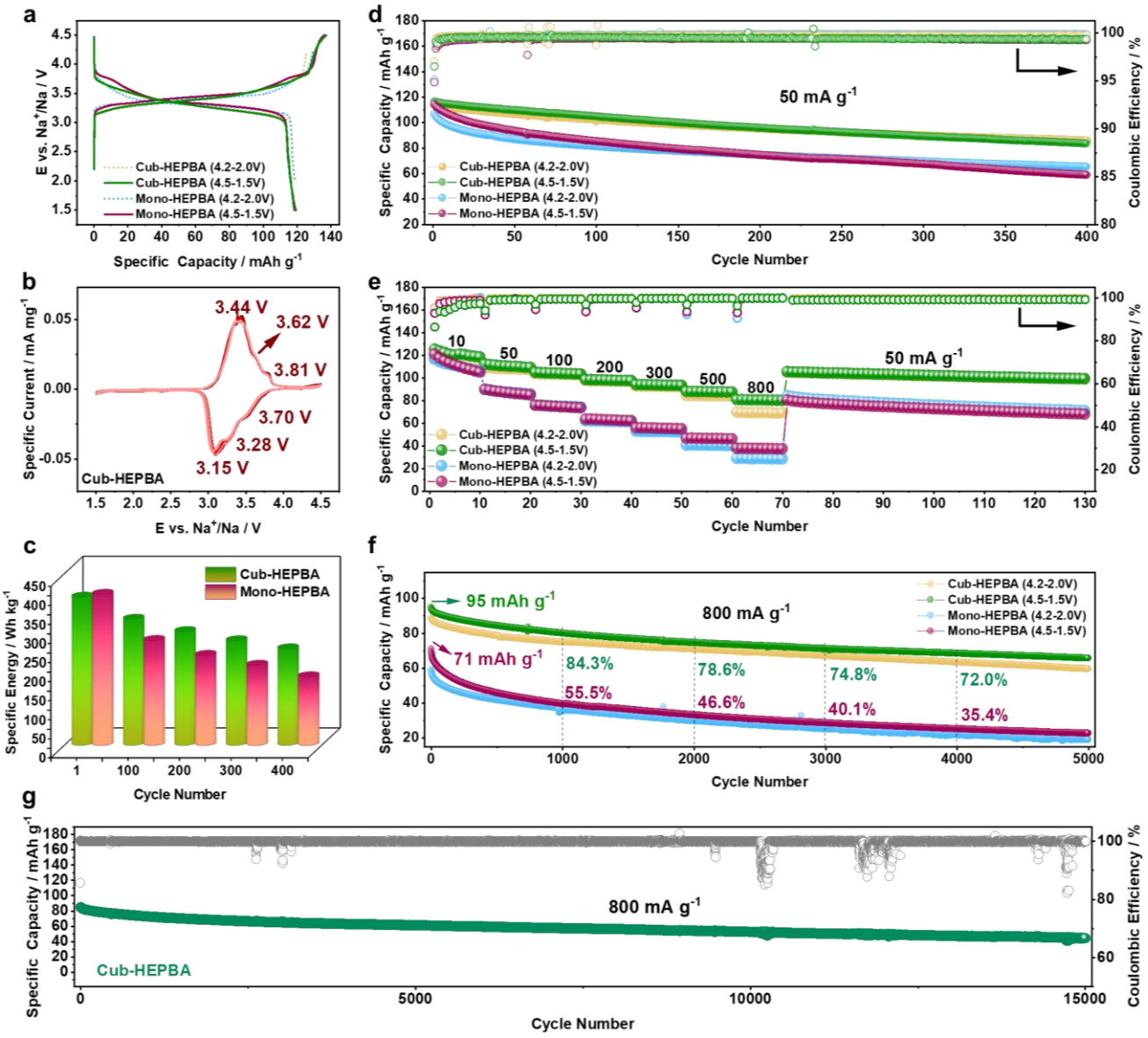

Figure 6.6. Electrochemical properties of Cub- and Mono-HEPBA cells with cut-off voltages of 1.5 – 4.5 V or 2.0 – 4.2 V (vs. Na^+/Na). (a) Initial charge–discharge curves at 10 mA g^{-1}, (b) first 4 cyclic voltammograms of Cub-HEPBA cell at 0.05 mV s^{-1}, (c,d) selected specific discharge energies (in the 1st, 100th, 200th, 300th and 400th cycle) and corresponding long-term cycling performance at a specific discharge capacity of 50 mA g^{-1}, (e) rate capability at various specific currents between 10 and 800 mA g^{-1}, (f) comparison of high-rate cycling performance of Cub- and Mono-HEPBA at 800 mA g^{-1} for 5000 cycles, and (g) 15000 cycles of Cub-HEPBA at 800 mA g^{-1}.

Galvanostatic charge–discharge (GCD) tests conducted on Cub- and Mono-HEPBA electrodes at a current of 10 mA g^{-1} exhibited a comparable first-cycle specific discharge capacity of ~ 120 mAh g^{-1}, and promising specific discharge energies (396.3 Wh kg^{-1} for Mono-HEPBA, 389.0 Wh kg^{-1} for Cub-HEPBA), as displayed in **Figure 6.6a**. Upon further scrutiny of the voltage profile, the results unveiled a relatively high initial average discharge voltage, achieving 3.32 V for Mono-HEPBA and 3.30 V for Cub-HEPBA, along with a small voltage hysteresis of 0.20 V. The cyclic voltammograms (**Figure 6.6b** and **6.7**) showed the distinct redox pairs at 3.44/3.15 V and 3.62/3.28 V, which correspond to the oxidation/reduction of C-coordinated Fe^{III}/Fe^{II} (low-spin, LS) and N-coordinated Mn^{III}/Mn^{II} (high-spin, HS),[44] respectively. Furthermore, peaks at 3.81/3.70 V were associated with the Co^{III}/Co^{II} (HS) redox couple bonded to the N atoms of $C{\equiv}N^-$ ligands.[227] Significantly, after four cycles, these primary redox pairs converged into a single broad peak, consistent with the properties of HEPBAs observed in other studies.[75,101] The redox potentials in HEPBAs result from the complex interactions among the different metal ions and their specific coordination environments. These factors collectively dictate the electrochemical behavior observed in these materials.

The structural configuration of PBAs significantly impacts cycling stability, with Cub-HEPBA outperforming Mono-HEPBA. This advantage persists even under the more challenging operational conditions with a wider cut-off voltage range (1.5 V – 4.5 V), as shown in **Figure 6.6c, d**. For instance, in the 100^{th}, 200^{th}, 300^{th}, and 400^{th} cycle at 50 mA g^{-1}, Cub-HEPBA continued to deliver specific capacities of 104.7, 95.7, 89.1, and 83.5 mAh g^{-1}, respectively. Conversely, Mono-HEPBA exhibited a decline in capacity retention to 51.4% in the 400^{th} cycle, with a reversible capacity of 58.8 mAh g^{-1} only. Also, the corresponding gravimetric specific energy (**Figure 6.6c**) with sodium metal as the anode in a theoretical full cell, demonstrated the positive impact of the cubic structured HEPBA on cyclability. Specifically, at the 300^{th} and 400^{th} cycle, Cub-HEPBA enabled deliver a specific energy of 274.7 Wh kg^{-1} and 253.5 Wh kg^{-1}, respectively, while Mono-HEPBA provided 210.4 Wh kg^{-1} and 180.3 Wh kg^{-1} only. A comparative analysis of low-entropy PBAs (LEPBAs) with cubic and monoclinic structures (comprising solely equimolar quantities of Mn and Co, with ΔS_{conf} = 0.69R) highlights the significantly improved cycling stability of Cub-HEPBA at both low and high discharge rates of 50 mA g^{-1} and 800 mA g^{-1}, respectively (see **Figure 6.8**). This observation highlights the

positive effect of the increased ΔS_{conf} on the electrochemical performance for multicomponent PBA materials.

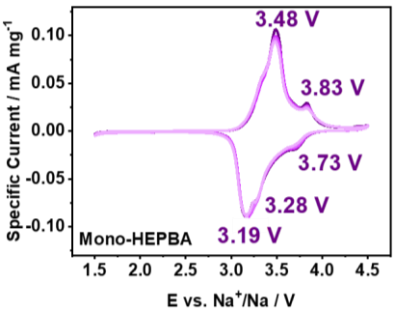

Figure 6.7. Cyclic voltammograms of the first four cycles for Mono-HEPBA at 0.05 mV s^{-1}.

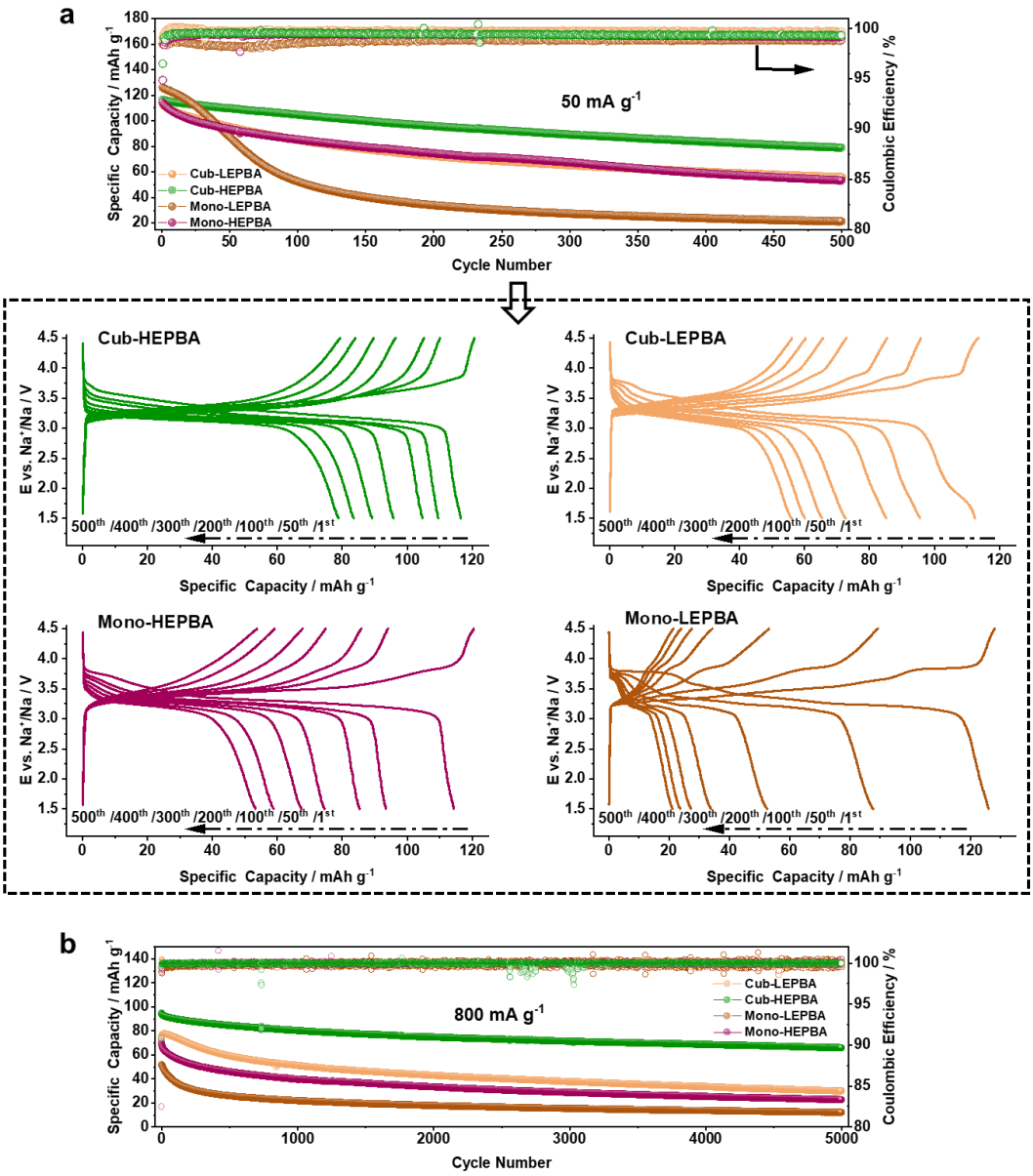

Figure 6.8. Comparison of the long-term cycling performance of HEPBAs and LEPBAs with cubic and

monoclinic structures. (a) At 50 mA g^{-1} and (b) at 800 mA g^{-1}.

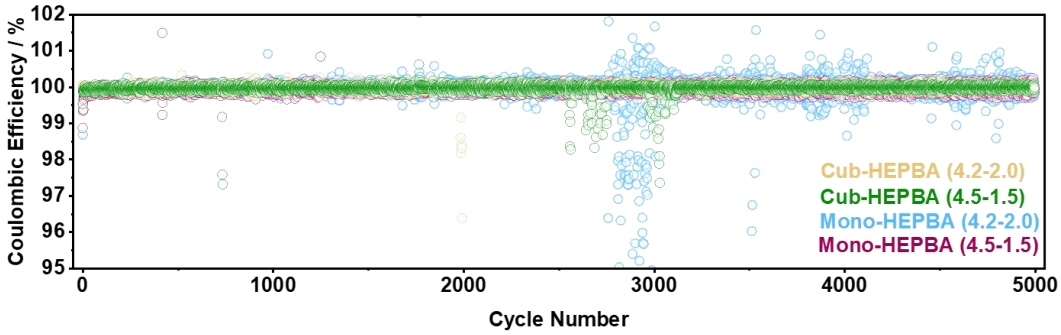

Figure 6.9. Comparison of the Coulomb efficiency of Cub- and Mono-HEPBA at 800 mA g^{-1} over 5000 cycles.

As expected, the superior performance of Cub-HEPBA was also evident when assessing its rate capability at specific currents ranging from 10 to 800 mA g^{-1}, as depicted in **Figure 6.6e**. Cub-HEPBA continuously demonstrated outstanding electrochemical performance, attaining an impressive specific capacity of up to 80.6 mAh g^{-1} even at the demandingly high rate of 800 mA g^{-1}. Furthermore, when the specific current was lowered to 50 mA g^{-1}, Cub-HEPBA maintained a significant specific capacity of 105.2 mAh g^{-1}. In contrast, Mono-HEPBA experienced a notable reduction in rate capability, with its specific capacity decreasing to 37.6 mAh g^{-1} at 800 mA g^{-1}. Interestingly, the specific capacity of Mono-HEPBA at 50 mA g^{-1} was comparable to that of Cub-HEPBA at 800 mA g^{-1}. The disparity in performance between cubic and monoclinic structures primarily becomes apparent at high rates, necessitating the utilization of a high current of 800 mA g^{-1} for prolonged cycling assessments.

As shown in **Figure 6.6f**, after 1000, 2000, 3000, and 4000 cycles, Mono-HEPBA exhibited a consistent decline in capacity retention, decreasing progressively from 55.5% to 46.6%, 40.1%, and finally to 35.4%. Conversely, Cub-HEPBA exhibited outstanding stability, maintaining an exceptionally long cycling performance with a capacity of around 70 mAh g^{-1} and a Coulombic efficiency of 99.97% (see **Figure 6.9**), even after more than 5000 cycles, while Mono-HEPBA only achieved a capacity of 22.6 mAh g^{-1} under the same conditions (see **Figure 6.6f**). **Figure 6.6g** showcases the extended cycling performance of Cub-HEPBA over 15000 cycles at 800 mA g^{-1}, underscoring once more the advantages of cubic structured HEPBA in de-/sodiation reactions. In

general, structural degradation and cationic recombination are likely to take place during high-voltage operation (>4.0 V), leading to slow Na-ion kinetics and notable capacity degradation,[75,228] consistent with the swift performance decline witnessed for Mono-HEPBA during cycling. However, Cub-HEPBA, characterized by its robust structural integrity (as further detailed in the following section), consistently retained a high capacity of approximately 60 mAh g^{-1} even after 10000 cycles, showing minimal capacity degradation, despite enduring harsh fast-charge conditions (1.5 − 4.5 V, 800 mA g^{-1}). Considering the morphological differences among the samples employed in this section, the aggregated primary particles of Cub-HEPBA result in a smaller surface-to-volume ratio, unlike the monocrystalline morphology of Mono-HEPBA. This apparently facilitates effective connectivity with the conductive carbon black and the current collector during prolonged cycling,[197] thereby enabling Cub-HEPBA to demonstrate stable and rapid sodium storage performance.

6.4. Electrochemical Mechanisms

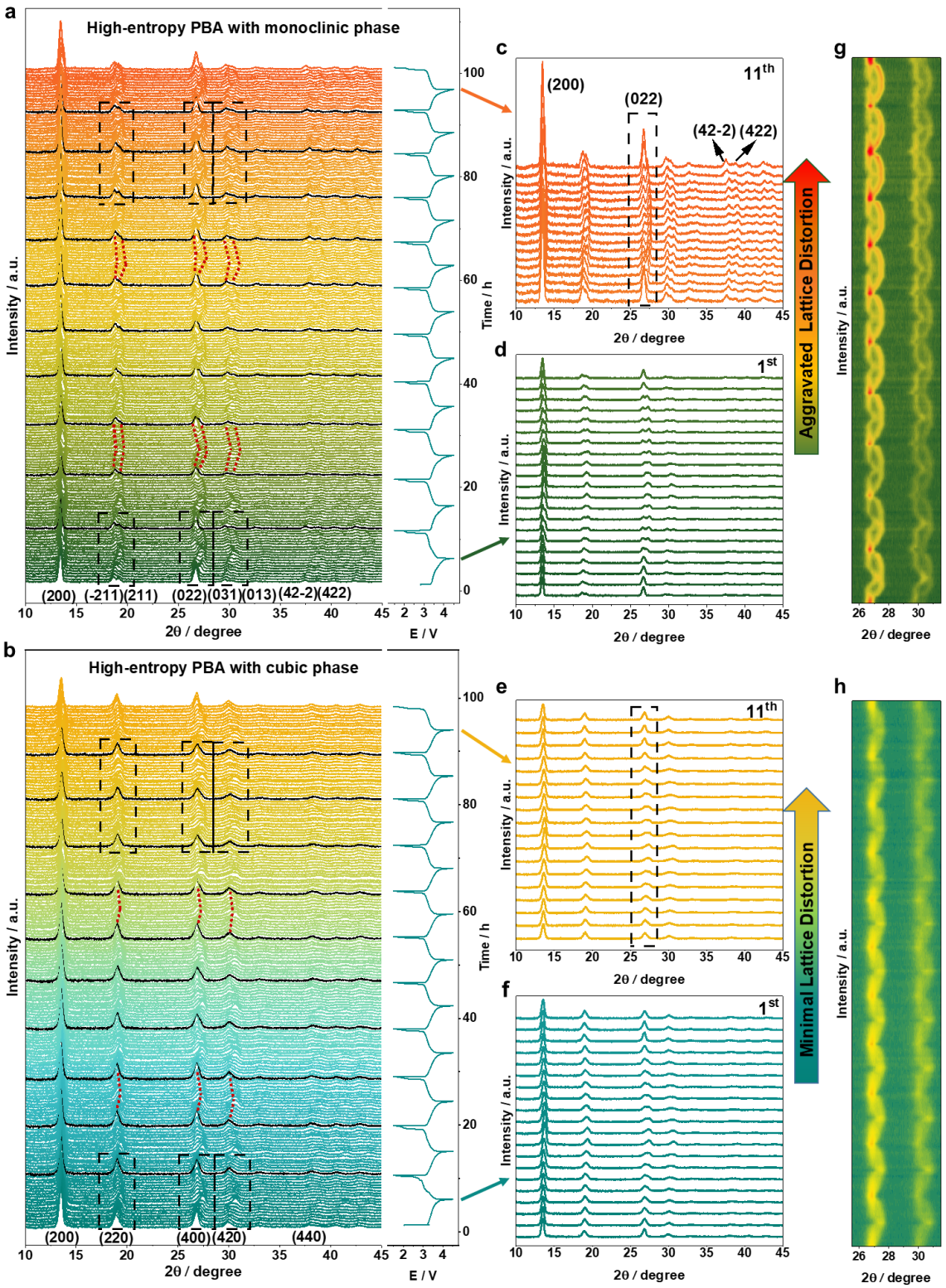

Figure 6.10. (a, b) *Operando* XRD characterization and corresponding voltage profiles of Mono-and Cub-HEPBAs over 11 cycles at 25 mA g^{-1}. Select XRD patterns (1st and 11th cycle) for (c, d) Mono-HEPBA and (e, f) Cub-HEPBA. (g, h) Closer view on the region between 25 and 32° in waterfall plots during cycling.

To comprehend the underlying reasons for the electrochemical variances between cubic and monoclinic structured HEPBAs, comprehensive *operando* XRD investigations were conducted. These measurements were carried out to track the structural transformations during battery operation. The initial pattern of the as-prepared materials in the coin cells (depicted as the first pattern above the x-axis, see **Figure 6.10a, b**), confirmed either the monoclinic or cubic structure, respectively. The distinct peak splits in **Figure 6.10a**, corresponding to (−211/211), (031/013) and (42−2/422), are characteristic of monoclinic PBA materials. While the non-splitted corresponding peaks for Cub-HEPBA in **Figure 6.10b**, (200), (220), (400), (420) and (440), verify the cubic structure. For Mono-HEPBA, the applied current significantly affects the structural changes during cycling. *Operando* XRD measurements conducted at a small current of 7 mA g^{-1} (**Figure 6.11**) uncovered a substantial structural transformation within Mono-HEPBA. The distinctive peak splitting associated with the monoclinic structure, as described earlier, disappeared during cycling, and the characteristic feature evolved into a single peak representing the (440) plane. Simultaneously, novel peaks corresponding to the (200), (220), (400) and (420) crystallographic planes appeared, when the cell was charged to 3.44 V vs. Na^+/Na.[47,74,101] This suggests the formation of a cubic structure. Such symmetrical cubic structure remained intact until the discharge reached 2.9 V, at which point it reverted back to the monoclinic structure (evidenced by the reappearance of split diffraction peaks, such as (031/013) and (42−2/422)).

It's worth mentioning that, at low currents, Mono-HEPBA attained comparable capacities to Cub-HEPBA, even after transitioning to a cubic state. Nonetheless, when the current was raised to 25 mA g^{-1}, Mono-HEPBA demonstrated a significantly distinct structural evolution during Na-ion insertion/extraction, which had a profound effect on the electrochemical performance. Although **Figure 6.10d** indicates the absence of new diffraction peaks beyond the monoclinic structure under the initial discharge/charge process at 25mA g^{-1}, noticeable changes were nonetheless observed in the Mono-HEPBA material during consequent cycling. First of all, a splitting of the (022) peak was observed as the sodium ions underwent extraction/insertion. As the cycles progressed, this peak splitting became more pronounced, particularly evident from the 5^{th} cycle onwards. A thorough analysis uncovered a more pronounced splitting and heightened intensity of the (022) reflection, as

illustrated in **Figure 6.10c**. Likewise, the intensity of the (200) reflection for Mono-HEPBA increased tenfold compared to its initial state. Additionally, the (42−2) and (422) reflections, which were less prominent in the first cycle, became significantly more pronounced by the 11th cycle. Concurrently, the pre-existing reflections corresponding to (−211/ 211) and (031/013) displayed a more evident splitting. These changes in the reflections of the monoclinic structure indicate a substantial and irreversible structural variation. This suggests a pronounced deformation of the unit cell in monoclinic structured PBA, leading to exacerbated degradation during successive cycling. This phenomenon provides a clear rationale for the suboptimal electrochemical performance of Mono-HEPBA, as illustrated in **Figure 6.6**.

On the contrary, the Cub-HEPBA displayed a resilient structural stability throughout the charging and discharging process, as indicated by the *in-situ* XRD patterns (**Figure 6.10b**). In particular, upon comparing the 1st and 11th cycles (**Figure 6.10e, f**), a solid-solution-type behavior[75] was evident. This behavior is characterized by slight reflection alterations along with modest peak broadening, attributed to the unit cell contraction during Na^+ extraction and insertion. This emphasizes remarkable reversibility and minimal structural distortion during cycling, which could be ascribed to material's "quasi-zero-strain" characteristic.[65] The corresponding parameters derived from the refinement of structural models against the XRD patterns of Cub- and Mono-HEPBA are presented in **Figure 6.12**. The data corroborate the superior reversibility of redox processes in the case of Cub-HEPBA. Moreover, the corresponding waterfall plots of *operando* XRD offered additional evidence supporting the structural superiority of Cub-HEPBA during desodiation/sodiation reactions. As illustrated in **Figure 6.10h**, Cub-HEPBA maintained its intact cubic structure throughout the 11th cycle, demonstrating its exceptional ability to withstand structural changes and recover effectively after Na^+ extraction/insertion. In contrast, Mono-HEPBA exhibited evident structural degradation starting from the 5th discharging/charging cycle onwards (**Figure 6.10g**), indicating its susceptibility to rapid Na^+ extraction and insertion owing to its monoclinic structure. This observation aligns with the swift capacity degradation observed for Mono-HEPBA under the high specific currents of 800 mA g^{-1} during prolonged cycling. In summary, although monoclinic structured HEPBA showed promising capacities at low current (7 mA g^{-1}), along with transitioning to the cubic phase during cycling, the

exacerbated lattice distortion was much more pronounced when the cell was subjected to higher currents (25 mA g^{-1}). This emphasizes the importance of a higher symmetrical cubic configuration in PBA, which enhances structural stability and performance. Benefiting from its robust structure optimized through the high-entropy approach, Cub-HEPBA demonstrates high reversibility, unparalleled endurance, and negligible structural distortion throughout cycling, thereby delivering superior cycling performance and outstanding rate capability.

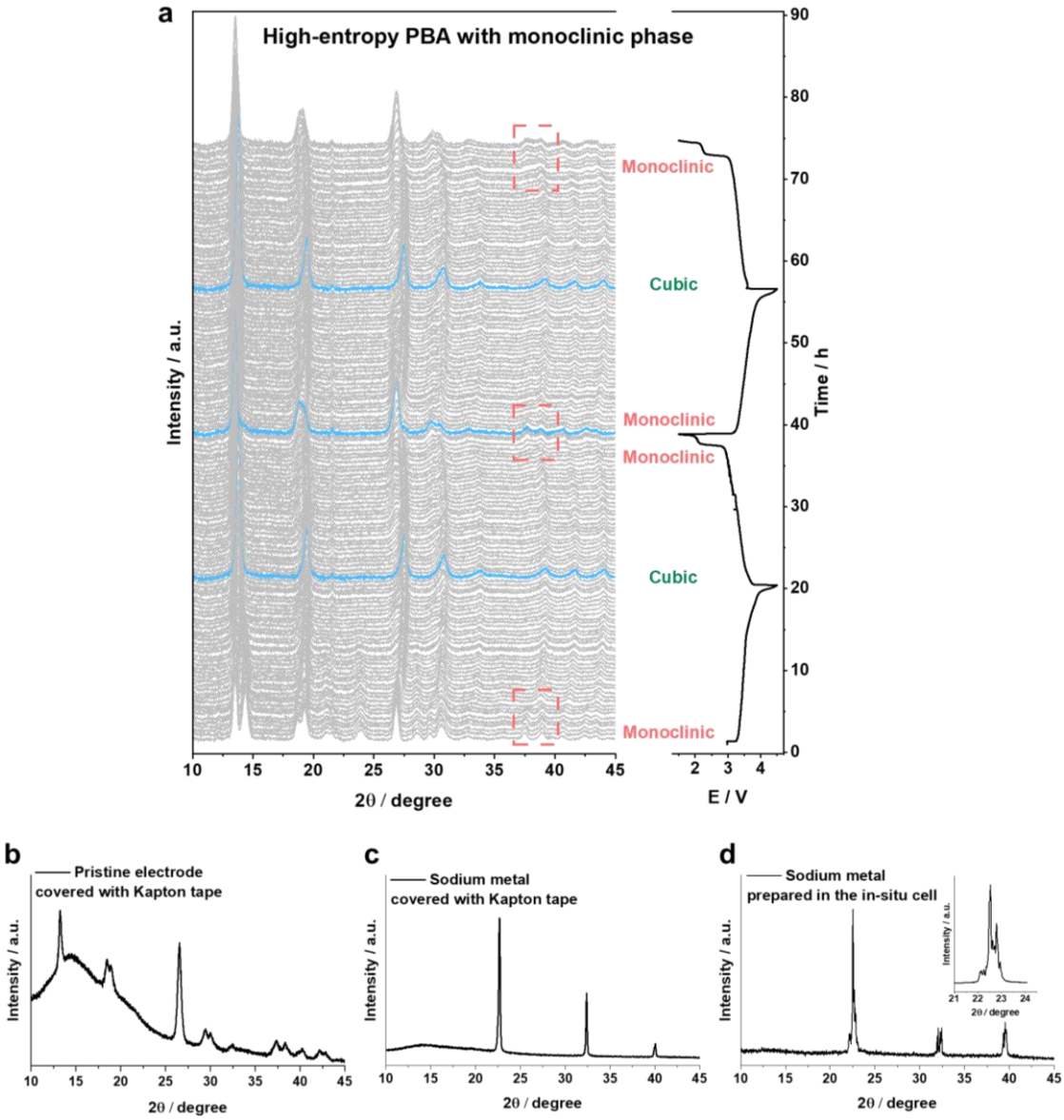

Figure 6.11. (a) *Operando* XRD characterization and corresponding dis-/charge profiles of Mono-HEPBA at 7 mA g^{-1}. Compared to the pristine cathode that was only covered with Kapton tape (b), severe peak splitting was apparent in the range of 12–15°, caused by improper cell preparation. When the X-rays pass through the *in-situ* cell in transmission mode, reflection takes place leading to peak splitting (due to space between Kapton tape

and sample). This is further confirmed by panels (c) and (d), where Na metal was used in the *in-situ* cell or only covered by Kapton tape. During charge, the phase transition from monoclinic to cubic structure leads to volume expansion, so the peak splitting vanishes.

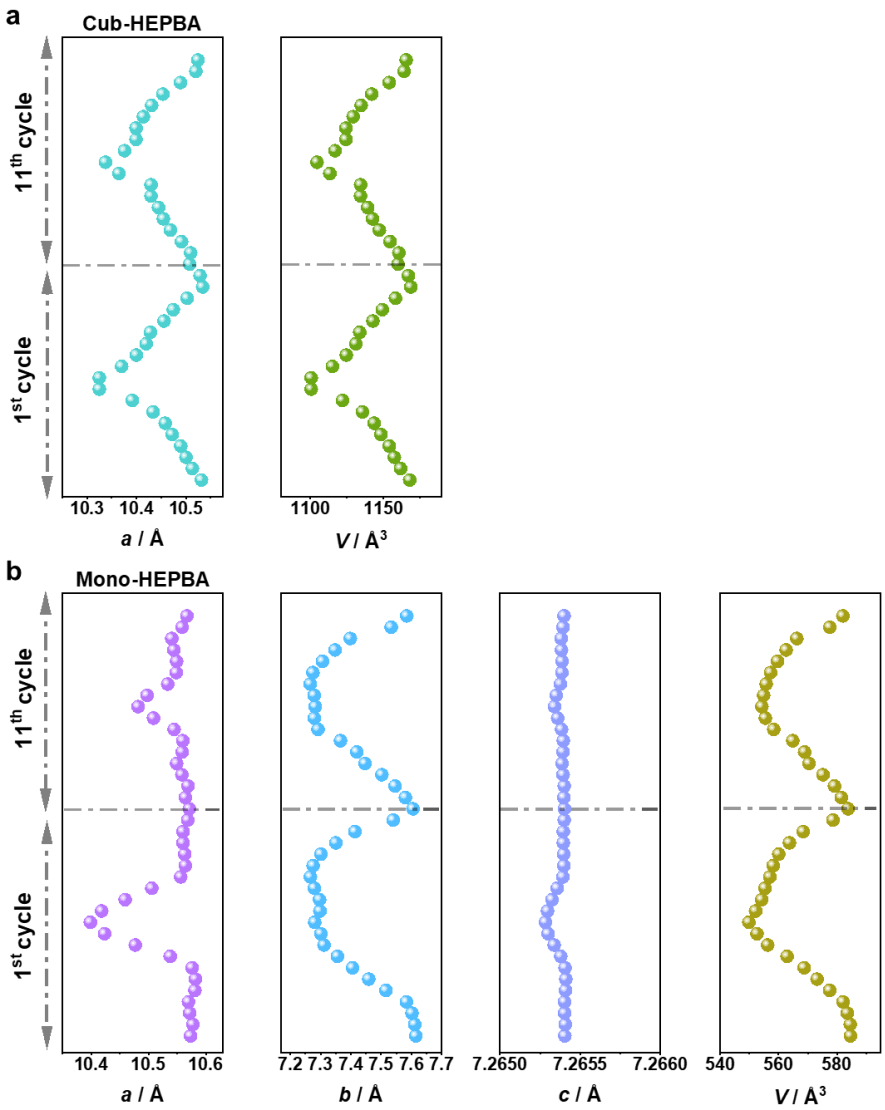

Figure 6.12. Structural parameters from refinement of structural models against the *operando* XRD patterns of Cub- and Mono-HEPBA.

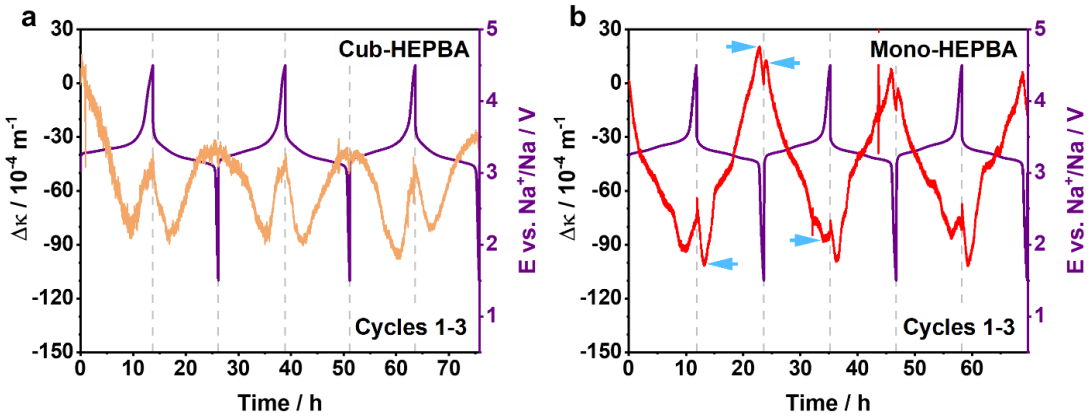

Figure 6.13. *Operando* curvature data and corresponding charge/discharge curves for (a) Cub-HEPBA and (b) Mono-HEPBA in the potential range between 1.5 and 4.5 V vs. Na^+/Na at 10 mA g^{-1}.

Significant volume changes and mechanical stresses can occur in an electrode due to the extraction and insertion of Na-ions. To analyse the mechanical stress evolution during galvanostatic cycling, *operando* stress analysis using the substrate curvature method was employed.[137] The curvature results revealed both similarities but also distinctive features, as illustrated in **Figure 6.13**. In **Figure 6.13a**, the Cub-HEPBA curvature decreased at first, then changed direction, shifting from compressive to tensile stresses. This change took place around 3.42 V versus Na^+/Na and aligned with the potential of the redox pair of C-coordinated low-spin Fe^{III}/Fe^{II} at 3.44 V (**Figure 6.6b**). As the sodiation progresses, a comparable alteration in the curvature/stress direction occurred around 3.31 V, matching the potential of the redox pair involving N-coordinated high-spin Mn^{III}/Mn^{II} at 3.28 V (**Figure 6.6b**). During galvanostatic cycling, the curvature of the cantilever oscillates. However, at the cut-off voltages of 4.5 V and 1.5 V, the curvature (or mechanical stress) reached similar levels. These observations suggested that Cub-HEPBA applied similar forces on the current collector and passive components of the electrode, irrespective of its sodiated or desodiated state. It also aligns with the close-to-zero structural distortions observed in *operando* XRD (**Figure 6.10b**) and implies that Cub-HEPBA may qualify as a zero-strain material. The distinctive shape of the curvature, as shown in **Figure 6.13a**, remained unchanged throughout the ten cycles conducted. Within individual cycles, the curvature exhibited a smooth and continuous shape, with no apparent signs of sudden volume changes or phase transitions. These observations might stem from the resilient structure of Cub-HEPBA, potentially elucidating its exceptional cycling performance (see **Figure 6.6g**).

Although Mono-HEPBA shared similarities with Cub-HEPBA in its trends, it also presented variances. For instance, **Figure 6.13b** illustrated that the initial downward slope possessed more pronounced features, potentially resulting from more complex phase transitions. Around 3.5 V versus Na^+/Na, the curvature reached its lowest point, coinciding with the structural transition of Mono-HEPBA from monoclinic to cubic phase (see **Figure 6.11a**). Similar to Cub-HEPBA, Mono-HEPBA also experienced a change in curvature direction, leading to a shift in stress of electrode from compression to tension. When comparing **Figure 6.13a** and **b**, it can be seen that the curvature amplitude of this change was quite weak for Mono-HEPBA. Specifically, the curvature or stress levels of Mono-HEPBA exhibited dissimilarities before and after sodiation. In the sodiated state, the electrode displayed greater tensile stress compared to the desodiated state. The curvature oscillation amplitude during the cycling of Mono-HEPBA was roughly double that of Cub-HEPBA. These observations could be explained by substantial changes in the lattice parameters of Mono-HEPBA during the extraction and insertion of Na-ions, as depicted in **Figure 6.10a**, leading to more pronounced features in the curvature data. Mirror symmetry in curvature around the fully sodiated and desodiated states represented by dashed lines in **Figure 6.13** reflects symmetrical reaction pathways. In the case of Mono-HEPBA, the mechanisms of sodiation and desodiation seem to exhibit less symmetry, attributable to the distinct differences between both states (highlighted by arrows in **Figure 6.13b**). Furthermore, the features present in the curvature data for Mono-HEPBA exhibited minor alterations with each successive cycle. These observations may suggest early signs of structural degradation in the electrode, potentially resulting from phenomena such as particle rearrangements and/or binder/carbon black motion.

To investigate the influence of the diverse structures of HEPBAs on the kinetics of Na^+ diffusion in cationic redox processes, *operando* EIS analysis was conducted on Mono- and Cub-HEPBA cathodes for a range of currents (25,100, 200, 400 and 800 mA g^{-1}). **Figure 6.14** and **Figure 6.15** illustrate the EIS plots, which showcase characteristic traits, featuring a semicircle at high frequency and a straight line at low frequency.[229] The charge transfer resistance (R_{ct}) is characterized by the diameter of the semicircle, while the diffusion impedance is reflected in the slope of the line.[230–232] Selected EIS spectra were further fitted using an equivalent circuit, which is shown in **Figure 6.15**. Comparative

analysis of the first and second cycles at 25 mA g^{-1} shows a significant enlargement of the semicircle in the case of Mono-HEPBA (see **Figure 6.14a**), indicating an increased R_{ct} (from 277.2 to 367.8 **Ω** at the fully discharged state, see **Table 6.4**). Conversely, Cub-HEPBA exhibits minimal change in resistance following two cycles at 25 mA g^{-1} (see **Figure 6.14b**), with a consistent value of around 280 **Ω** observed at deep discharge (see **Table 6.5**), indicating exceptional reversibility.

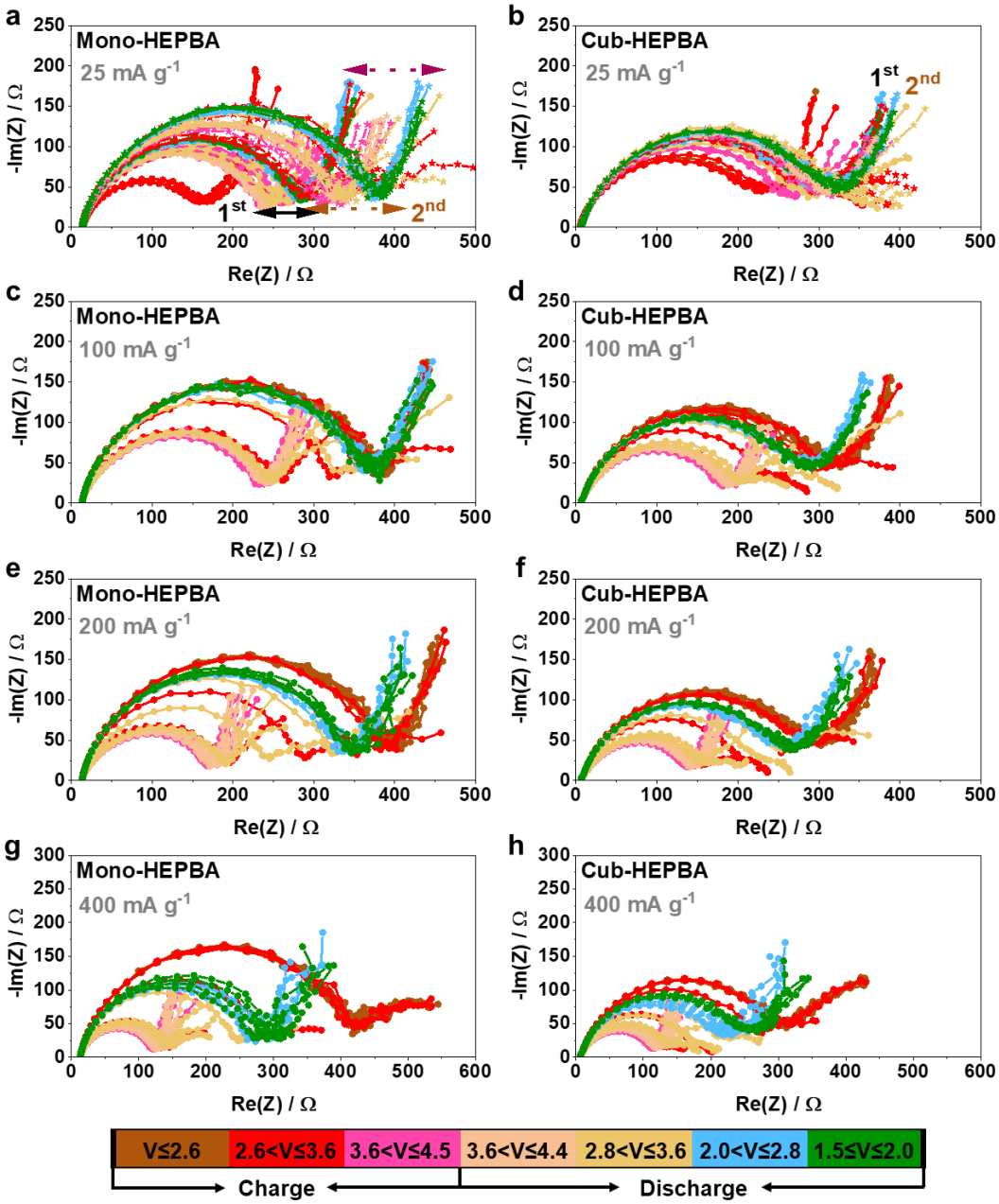

Figure 6.14. *Operando* EIS analysis of the electrochemical extraction/insertion of Na^+ from/into the HEPBAs at specific currents ranging from 25 and 400 mA g^{-1}. Nyquist plots (a, c, e, g) for Mono-HEPBA and (b, d, f, h) for Cub-HEPBA. Different charging and discharging states are indicated by colored symbols and lines (see

color code at the bottom). Note that data for the first two cycles are shown for 25 mA g^{-1}.

The resistance change does not exhibit a consistent trend of continuous increase, as seen in **Figure 6.14a**, where the resistance keeps rising during charging at 25 mA g^{-1}. When the cells were subjected to higher specific currents, both materials demonstrated higher R_{ct} when operated at ≤ 3.6 V compared to the range between 3.6 – 4.5 V during deintercalation of Na^+ at 100, 200 and 400 mA g^{-1}, respectively (see **Figure 6.14c-h**). The observed phenomenon can be attributed to oxidation processes primarily involving C-coordinated Fe^{III}/Fe^{II} and N-coordinated Mn^{III}/Mn^{II} within this potential window.[230] Obviously, R_{ct} is always much bigger for Mono-HEPBA than for Cub-HEPBA before charging to 3.6 V. For instance, R_{ct} values of 337.9, 334.7 and 375.5 **Ω** are found for Mono-HEPBA at 3.2 V for the specific currents of 100, 200 and 400 mA g^{-1}, while the corresponding values are 264.0, 219.3 and 228.0 **Ω** for Cub-HEPBA under the same conditions, as summarized in **Figure 6.15c**. The findings indicate a significant suppression in the increase of interfacial impedance between the cathode and electrolytes in Cub-HEPBA, likely attributed to the robust cubic structure of Cub-HEPBA. In addition, the smaller primary particle size appears to facilitate charge transfer across the interface.[197] During Na^+ intercalation, both electrodes exhibited higher resistance states in the late discharge period (2.8 – 1.5 V) compared to other discharge states, indicating that achieving full insertion of Na^+ necessitates overcoming more resistance. Nevertheless, the consistently smaller R_{ct} observed in Cub-HEPBA, even within the range of 2.8 – 1.5 V, suggests that the symmetrical cubic structure facilitates more accessible intercalation of Na^+. Remarkably, Cub-HEPBA shows no discernible change in resistance within this voltage range, even with an increase in specific current from 25 to 400 mA g^{-1}. This highlights the exceptional stability of cubic structure in HEPBA, indicating its resilience against unfavorable side reactions between the electrolyte and highly oxidized transition metals, which are typically triggered by elevated currents and voltages.[231] In contrast, the increase in applied current unavoidably induces an increased lattice distortion of the monoclinic structure for Mono-HEPBA, as verified by *operando* XRD analysis (see **Figure 6.10a**). Consequently, Mono-HEPBA experienced relatively severe interfacial side reactions, compromising transport kinetics and exacerbating degradation throughout cycling.

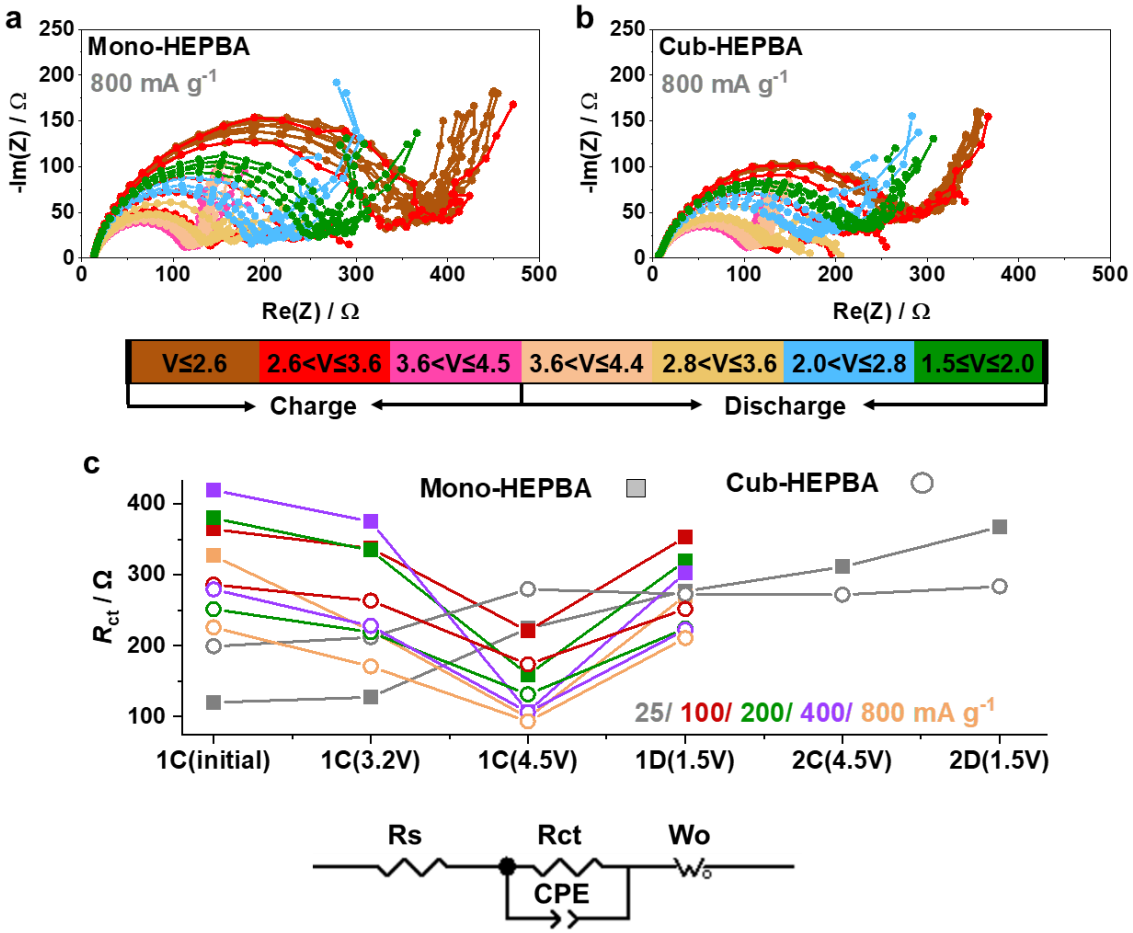

Figure 6.15. *Operando* EIS analysis of the electrochemical extraction/insertion of Na^+ ions from/into HEPBA at 800 mA g^{-1} for (a) Mono- and (b) Cub-HEPBA. (c) Comparison of R_{ct} between Cub- and Mono-HEPBA. Note that equivalent circuit is used to fit the Nyquist data.

Table 6.4. Fitted values of R_{ct} for Mono-HEPBA.

	R_{ct} (Ω)					
	1st C (Initial)	**1st C (3.2 V)**	**1st C (4.5 V)**	**1st D (1.5 V)**	**2nd C (4.5 V)**	**2nd D (1.5 V)**
25 mA g^{-1}	119.9	127.4	224.7	277.2	311.3	367.8
100 mA g^{-1}	364.5	337.9	220.8	353.7	-	-
200 mA g^{-1}	380.2	334.7	159.1	319.8	-	-
400 mA g^{-1}	420.1	375.5	107.1	303.2	-	-
800 mA g^{-1}	326.9	221.3	98.7	270.5	-	-

Table 6.5. Fitted values of R_{ct} for Cub-HEPBA.

	R_{ct} (Ω)					
	1st C (Initial)	**1st C (3.2 V)**	**1st C (4.5 V)**	**1st D (1.5 V)**	**2nd C (4.5 V)**	**2nd D (1.5 V)**
25 mA g^{-1}	199.2	212.1	279.9	273.0	272.1	283.8
100 mA g^{-1}	286.2	264.0	173.7	251.9	-	-
200 mA g^{-1}	251.8	219.3	131.5	224.5	-	-
400 mA g^{-1}	279.6	228.0	106.2	222.5	-	-
800 mA g^{-1}	225.9	170.7	93.3	210.8	-	-

Moreover, notable distinctions in interfacial impedance between Mono-HEPBA and Cub-HEPBA were accentuated, particularly under an applied current density of 800 mA g^{-1}, as illustrated in Figures **6.15a** and **b**. Particularly, the R_{ct} value for Cub-HEPBA is much lower than that for Mono-HEPBA over the whole cycle. For instance, Mono-HEPBA exhibited a pronounced variation in resistance, decreasing sharply from 326.9 Ω in the initial state to 98.7 Ω at the deep charge state, and subsequently rising to 270.5 Ω upon discharge to 1.5 V. Meanwhile, the R_{ct} shifted from 225.9 down to 93.3 Ω during charging, before returning to 210.8 Ω following the complete discharge of Cub-HEPBA cell. The smaller R_{ct} variation in Cub-HEPBA suggests improved Na^+ diffusion associated with the cubic lattice modification. This can be attributed to the more robust cubic structure of Cub-HEPBA, which enables facile charge transport even under harsh operation conditions (a wider electrochemical window).

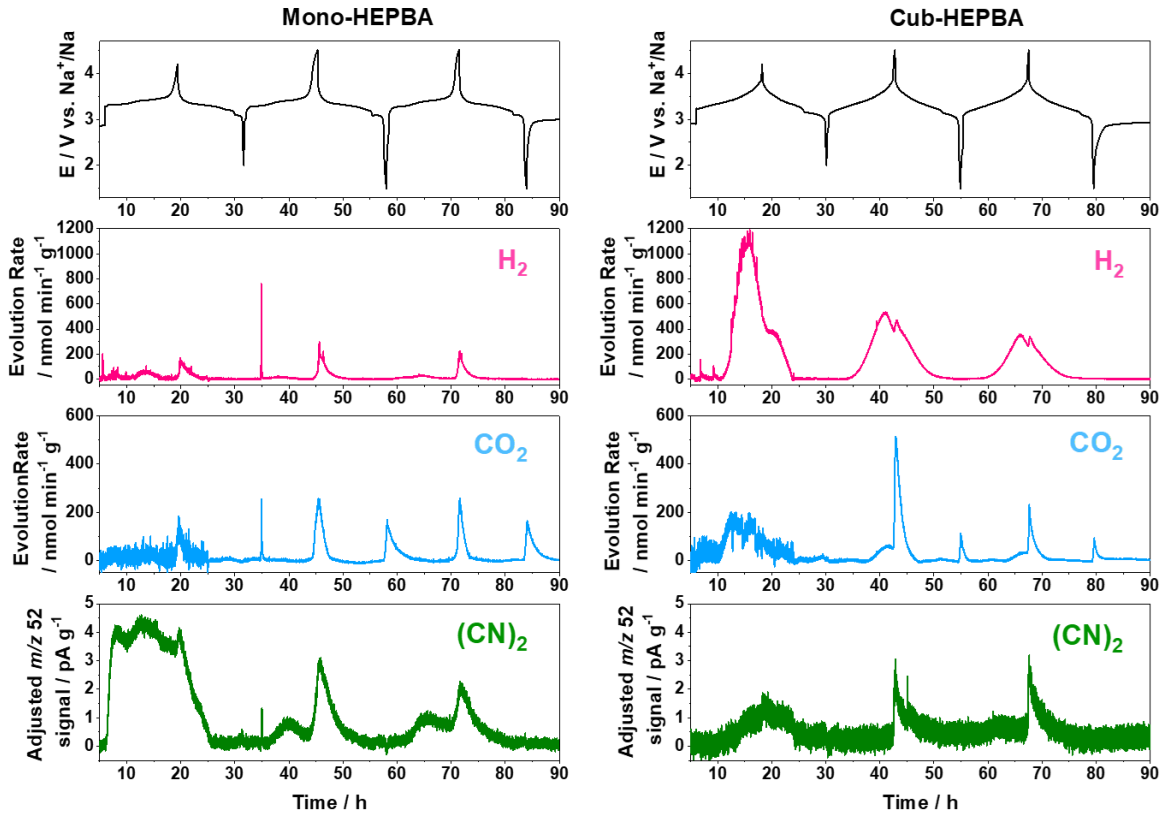

Figure 6.16. Gas evolution during cycling of the Mono- and Cub-HEPBA cathodes, as determined via DEMS. The spike at 35 h in Mono-HEPBA is an artefact.

The evolution of gasses from both cathode materials during cycling was studied via DEMS, utilizing a customized open headspace cell setup.[58,233,234] Moisture and coordinated water typically contribute to the formation of H_2 (m/z = 2), while surface carbonates and electrolyte decomposition lead to CO_2 (m/z = 44) evolution.[206,207] In oxide cathode materials used in sodium- and lithium-ion batteries, gas evolution is influenced by the release of O_2 through the oxidation of lattice oxide anions at high states of charge. This oxygen release also contributes to CO_2 formation through subsequent electrolyte oxidation.[211,235] In hexacyanoferrate cathodes, as demonstrated in our earlier studies, cyanide anions can be oxidized to form gaseous cyanogen [$(CN)_2$, m/z = 52] upon charging. This reaction degrades the active material, particularly in the presence of $NaClO_4$.[58,75,166] The gas evolution of both Cub- and Mono-HEPBA is displayed in **Figure 6.16**. In the first cycle, the potential window was limited to 2.0–4.2 V vs. Na^+/Na, whereas the potential range was expanded to 1.5–4.5 V vs. Na^+/Na for the second and third cycles. **Table 6.6** reports the evolved gas amounts, i.e. curve integrals, and specific capacities for each cycle and material.

Table 6.6. DEMS measurement results. Total gas amounts determined by integration of gas evolution rate peak around the end of charge. Of note: 1st cycle measured between 2.0 V and 4.2 V vs. Na^+/Na.

Property	Cub-HEPBA	Mono-HEPBA
1st cycle charge capacity / mAh g^{-1}	122	134
1st cycle discharge capacity / mAh g^{-1}	118	121
2nd cycle charge capacity / mAh g^{-1}	122	132
2nd cycle discharge capacity / mAh g^{-1}	120	126
3rd cycle charge capacity / mAh g^{-1}	121	129
3rd cycle discharge capacity / mAh g^{-1}	119	124
1st cycle H_2 evolution / µmol g^{-1}	391	30
1st cycle CO_2 evolution / µmol g^{-1}	60	11
2nd cycle H_2 evolution / µmol g^{-1}	239	28
2nd cycle CO_2 evolution / µmol g^{-1}	52	23
3rd cycle H_2 evolution / µmol g^{-1}	150	26
3rd cycle CO_2 evolution / µmol g^{-1}	20	18
total H_2 evolution / µmol g^{-1}	780	94
total CO_2 evolution / µmol g^{-1}	132	52
1st cycle integral of adjusted m/z = 52 signal / pAh g^{-1}	14	61
2nd cycle integral of adjusted m/z = 52 signal / pAh g^{-1}	11	16
3rd cycle integral of adjusted m/z = 52 signal / pAh g^{-1}	10	16
total integral of adjusted m/z = 52 signal / pAh g^{-1}	35	93

Table 6.7. Adjustment factors applied to the m/z = 52 signal to account for differences in absolute signal strength due to SEM gain variation between measurements.

Material	H_2 calibration slope / pA ppm^{-1}	Factor to reach higher slope for H_2	CO_2 calibration slope / pA ppm^{-1}	Factor to reach higher slope for CO_2	Average factor, applied to m/z = 52 signal
Cub-HEPBA	0.159	1.910	0.104	1.981	1.946
Mono-HEPBA	0.304	1	0.205	1	1

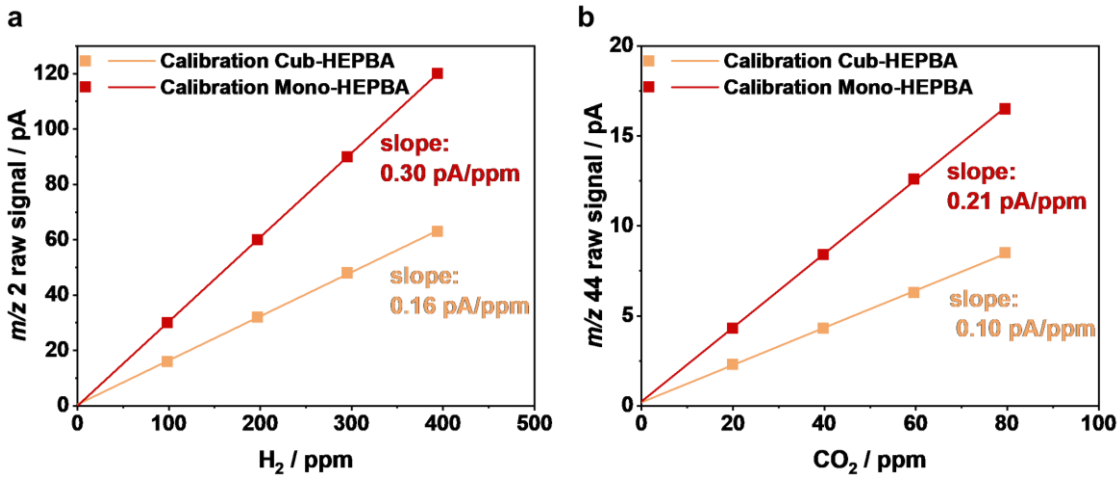

Figure 6.17. (a, b) DEMS calibration curves for H_2 and CO_2 signals.

In light of their inherent moisture content, substantial H_2 evolution is anticipated for hexacyanoferrates.[75,166] As coordinated water is predominantly released towards the end of the charging process, primarily in the form of $Na(OH_2)^+$, the rate of H_2 evolution increases with higher potentials.[58,209,210] In the case of Cub-HEPBA, both an earlier start of H_2 evolution and a higher total volume of H_2, compared to Mono-HEPBA, are observed. In addition, the highest evolution rate in the first cycle is not observed at the end of charge, but around 3.5 V, indicating that release of lattice water is contributing to the H_2 evolution. The latter appears to be present only to a much lesser extent in Mono-HEPBA, where the H_2 evolution is restricted to smaller amounts around the end of charge. The findings align well with the difference in water content of both materials (see **Table 6.3**). Nevertheless, the potential influence of the smaller particle size and greater specific surface area of Cub-HEPBA (**Figure 6.4c–f**) on the water release characteristics of the materials cannot be ignored. A dent-like decrease of H_2 evolution rate in Cub-HEPBA when charged to 4.5 V is likely due to H_2 being partially displaced by the strong CO_2 evolution setting in at this point.[58] This strong CO_2 evolution occurs arising from electrochemical electrolyte oxidation at potentials above ~4.3 V, equal to ~4.6 V vs. Li^+/Li, which represents the stability limit for organic carbonates, such as ethylene carbonate (EC).[211] Before this onset, Cub-HEPBA exhibits a weaker evolution of CO_2, which occurs simultaneously with H_2 evolution, i.e. water release, stems from hydrolysis of EC under release of CO_2.[58,236–238] While the electrochemical electrolyte oxidation appears to be independent of the cathode material, as evidenced by similar CO_2 evolution from both materials in the third cycle, the higher CO_2 evolution observed in

Cub-HEPBA during the first two cycles can once again be attributed to its higher water content, as demonstrated previously.[58] Finally, additional CO_2 evolution, independent of the cathode material, was observed towards the end of discharge when the voltage dropped below 2.0 V. This phenomenon was previously attributed to the reduction of fluoroethylene carbonate in the electrolyte at low potentials.[214,215]

The evolution of $(CN)_2$ has previously been studied both during thermal runaway of Prussian white cells and during cell charge.[58,75,166,216] A direct quantification of $(CN)_2$ evolution via DEMS was not feasible due to the absence of appropriate calibration gas mixtures required to convert ion currents recorded in the mass spectrometer into concentrations in the gas mixture. In the case of $(CN)_2$, no such calibration curve can be obtained, thus the measured detector currents (m/z = 52) are commonly reported, still allowing for a semi-quantitative analysis.[233,234] To ensure accurate comparison of gas evolution across various measurements, it's essential to account for and, if required, compensate for any fluctuations in the secondary electron multiplier (SEM) gain between these measurements. The SEM gain decreases over time due to aging and degradation, with the effect most pronounced in newly installed SEMs, although it can be roughly compensated for by applying a higher voltage.[239,240] As H_2 and CO_2 are part of the calibration gas mixture, a relative comparison of SEM gain can be made from the calibration curve slopes of these gasses, as outlined in **Figure 6.17** and **Table 6.7**. For a fair comparison of evolution rates, the $(CN)_2$ raw signal is then both adjusted by the factor between these calibration slopes and normalized by electrode weight. This adjusted signal is depicted in **Figures 6.16**. A more detailed report of experimental considerations in the DEMS study of hexacyanoferrates can be found in the literature.[58] In addition, it has been shown that while the water content of the cathode material influences H_2 evolution, the conductive salt plays a crucial role in CO_2 and $(CN)_2$ evolution. $NaClO_4$, as used herein, results in the necessary electrolyte basicity for hydrolysis of EC under CO_2 evolution to occur, and increases the $(CN)_2$ evolution rate, associated with the formation of a cathode electrolyte interphase due to its oxidative properties. The rate of $(CN)_2$ evolution for a specific phase or material is thus inversely correlated with its susceptibility to oxidation by reactive ClO_x species.

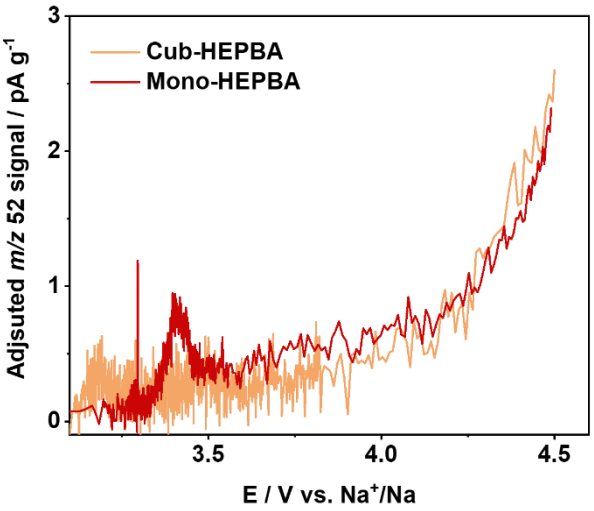

Figure 6.18. Interpolation of adjusted $(CN)_2$ evolution rate over potential during the second charge.

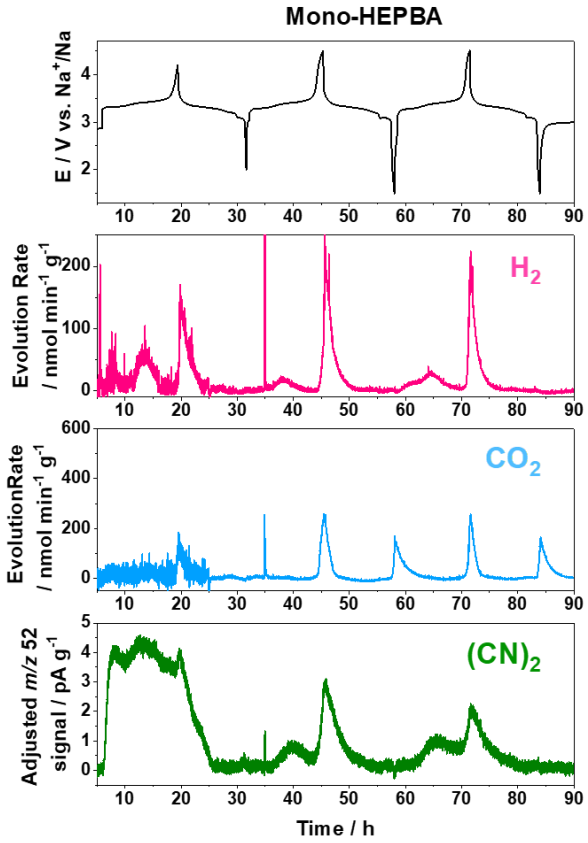

Figure 6.19. Closer inspection of H_2 evolution in Mono-HEPBA reveals shoulder peak, thus supporting the phase transition hypothesis.

In this chapter, across all cycles, the primary distinction in the $(CN)_2$ evolution profiles between the samples is the presence of a shoulder peak in Mono-HEPBA, particularly prominent in the first cycle, which is not observed in Cub-HEPBA. Moreover, during the second and third cycles, the $(CN)_2$ evolution profiles are narrower for Cub-HEPBA than for Mono-HEPBA. As illustrated by the extrapolated evolution rates in **Figure 6.18**, this distinction arises solely from the slight variations in the voltage profiles towards the end of charge. Above the observed peak shoulder, the $(CN)_2$ evolution rates are nearly identical for both materials. This is also reflected in similar peak integrals, as shown in **Table 6.6**. Previous studies of low- and high-entropy Prussian whites reported the presence of a peak shoulder during charging only in the low-entropy material, with this phenomenon being linked to a phase transition (see Chapter 5).[166] The phase transition-induced gas evolution was attributed to simultaneous degradation mechanisms, including surface destabilization, crack formation leading to increased surface exposure, and possibly the presence of cyanide-laden surface impurities in contact with the electrolyte. In the previous study, simultaneous to the phase transition and $(CN)_2$ evolution, also H_2 evolution was observed. Owing to the generally stronger H_2 evolution in this investigation, attributed to both the elevated cut-off potential and the material properties, especially of Cub-HEPBA, this phenomenon is not clearly discernible in **Figure 6.16**. Nevertheless, **Figure 6.19** reveals concurrent H_2 evolution for Mono-HEPBA. Given these findings, the presence of a peak shoulder near 3.4 V in Mono-HEPBA is likely due to the transition to the cubic phase. Apart from the variation in the applied potential window, the primary distinction between the previous study and our research lies in the composition of the materials. Unlike previous comparisons involving low-entropy and high-entropy Prussian whites, which were characterized by differences in configurational entropy arising from distinct compositions, the present study examines materials with comparable compositions but varying preparation methodologies and resultant crystal structure. Following the pattern observed in the previous study, the rate of $(CN)_2$ evolution initially reaches a peak during the phase transition of Mono-HEPBA. Subsequently, this rate becomes comparable between the Cub- and Mono-HEPBA samples once the phase transition has taken place, as anticipated for materials sharing the same phase and composition at that stage. In contrast, materials with varied compositions exhibited distinct $(CN)_2$ evolution rates, indicating differing material stability against oxidation.[58,166]

In short, Mono-HEPBA exhibited a more pronounced $(CN)_2$ evolution relative to Cub-HEPBA, a trend attributed to the additional release of this gas during the phase transition approximately at ~3.44 V vs. Na^+/Na. This result suggests structural degradation as a consequence of the transition, underscoring once more the importance of incorporating disorder (entropy) into crystal structure optimization in the field of electrode engineering.

6.5. High-Temperature Stability and Full Cell Properties

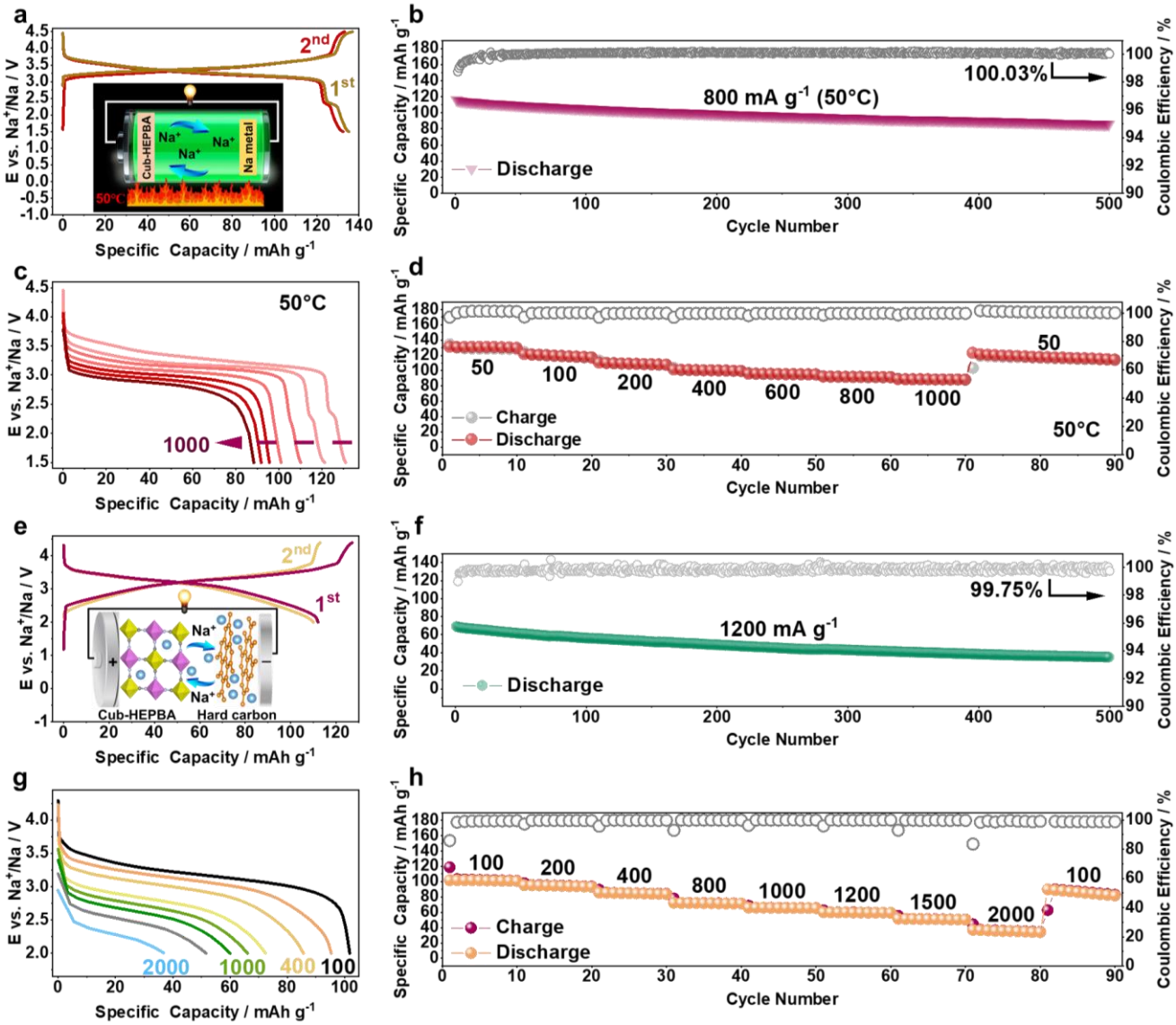

Figure 6.20. (a–d) Electrochemical properties of Cub-HEPBA at 50 °C. (a) GCD curves at 50 mA g^{-1} for the first two cycles, (b) long-term cycling performance at 800 mA g^{-1}, and (c, d) initial GCD curves at specific currents ranging from 50 to 1000 mA g^{-1} and corresponding rate capability. (e–h) Na-ion full cell performance of Cub-HEPBA in the 2.0–4.4 V range. (e) GCD curves of coin cells at 20 mA g^{-1} for the first two cycles, (f)

long-term cycling performance at 1200 mA g^{-1}, and (g, h) initial GCD curves at specific currents ranging from 100 and 2000 mA g^{-1} and corresponding rate capability.

Given the critical role of thermal stability in meeting the safety standards of SIBs, this study also extensively investigated the electrochemical performance of Cub-HEPBA at elevated temperatures. **Figure 6.20a** shows the first two GCD voltage profiles of Cub-HEPBA at 50 °C. The Cub-HEPBA cathode demonstrated a high initial specific discharge capacity (135.2 mAh g^{-1}) and specific discharge energy (435.7 Wh kg^{-1}). The electrochemical reactivity of the LS-Fe and HS-Fe redox couples was notably higher at 50 °C compared to 25 °C, as illustrated in **Figure 6.21**. Remarkably, leveraging its robust structure, Cub-HEPBA exhibits remarkable Na^+ ion storage capabilities, demonstrating exceptional cycling stability and rate capability even at elevated temperatures. Specifically, it delivered a reversible capacity of approximately 90 mAh g^{-1} after 500 cycles at a specific current of 800 mA g^{-1}, as depicted in **Figure 6.20b**. Furthermore, Cub-HEPBA also exhibits a very stable rate capability at specific currents between 50 and 1000 mA g^{-1}. As shown in **Figure 6.20c** and **d**, even at the highest applied current of 1000 mA g^{-1}, Cub-HEPBA still delivered a noteworthy specific discharge capacity of 89.6 mAh g^{-1}. In comparison to the majority of conventional hexacyanoferrate materials reported,[197,241] such high and stable performance of Cub-HEPBA at elevated temperatures indicates that the incorporation of compositional disorder (configurational entropy) has a significant and beneficial impact on the thermal stability of HEMs.

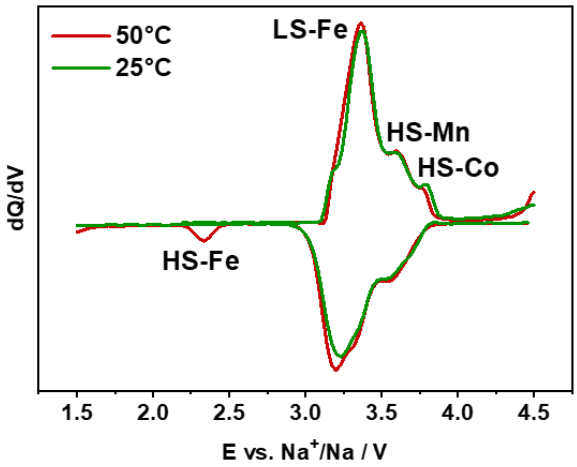

Figure 6.21. Comparison of the initial d*Q*/d*V* curves at 25 and 50 °C for Cub-HEPBA.

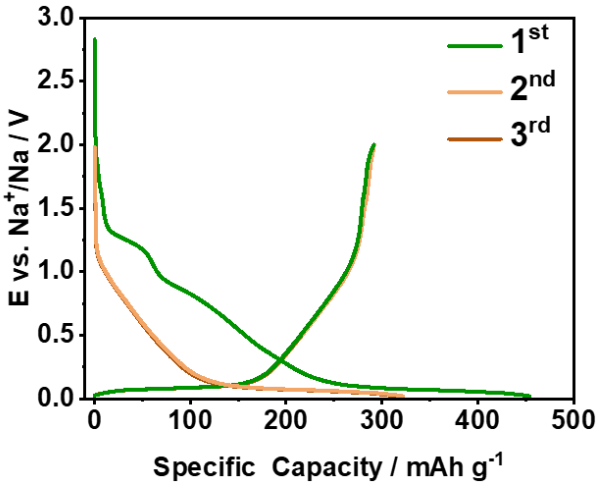

Figure 6.22. The first three charge/discharge curves of hard carbon at 10 mA g^{-1}. For full cell studies, the hard carbon was initially cycled for two cycles at 10 mA g^{-1} between 0.02 and 2.0 V vs. Na^+/Na in a hard carbon || Na-metal cell and then charged to 0.5 V.

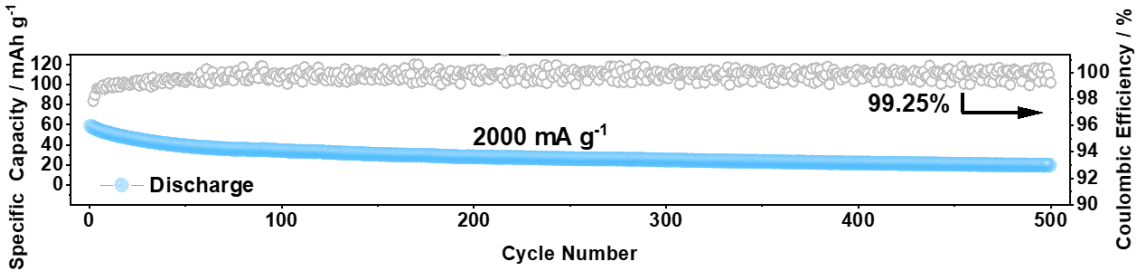

Figure 6.23. Long-term performance of a Na-ion full cell using Cub-HEPBA (2.0–4.4 V, 2000 mA g^{-1}).

To assess the practical application of Cub-HEPBA, full cells were assembled using Cub-HEPBA as the cathode active material and hard carbon as the anode active material. The specific capacities and energy densities of the full cells were calculated based on the mass of Cub-HEPBA in the cathodes. To activate the hard carbon anode, the hard carbon was initially discharged-charged for 2 cycles at 10 mA g^{-1} between 0.02 – 2.0 V (vs. Na^+/Na) in a hard carbon||Na metal cell and then charged to 0.5 V (vs. Na^+/Na) to obtain the pre-cycled hard carbon anode (see **Figure 6.22)**. According to **Figure 6.20e**, the hard carbon||Cub-HEPBA battery showcased an initial specific discharge capacity of 112.0 mAh g^{-1} at 20 mA g^{-1}. This converts to an energy density of 344.5 Wh kg^{-1}, coupled with an average discharge voltage of 3.1 V. **Figure 6.20f** and **6.23** demonstrate the outstanding electrochemical performance of Cub-HEPBA, particularly evident when subjecting the full cell to high specific

currents of 1200 and 2000 mA g^{-1}. The discharge capacity of Cub-HEPBA was under these conditions still stabilized at about 50 mAh g^{-1} and 35 mAh g^{-1}, respectively, after 500 cycles, resulting from fast insertion and extraction at these high specific currents. This result reveals again ultra-high stability of the cubic structure in Cub-HEPBA. The clear outperformance of Cub-HEPBA was also evident in rate capability (**Figure 6.20g, h**). For instance, at 100, 400, 1000 and 2000 mA g^{-1}, it was still capable to deliver 102, 86, 66 and 37 mAh g^{-1}, respectively. In summary, the findings of this chapter underscore the potential of HEPBA with a cubic structure as a promising candidate for secondary batteries, particularly in the realm of fast-charge cells, owing to its robust structure and excellent cyclability.

7. Printed High-Entropy Prussian Blue Analogues for Advanced Non-Volatile Memristive Devices

The previous sections[166,167] (Chapter 5 and 6) have demonstrated that HEPBAs serve as robust cathode materials for SIBs applications and exhibit promising potential in the field of reversible energy storage. Specifically, cubic structural HEPBAs as insertion materials have been characterized as zero-strain materials. Given its other considerable advantages, such as high Na^+ diffusion coefficient (~10^{-9} cm^2 s^{-1}),[49,50] and favorable ionic conductivity,[242] HEPBAs can be also considered as an ideal candidate for memristors applications. PBAs integrated with high-entropy approach are endowed high flexibility for designing memristive devices with promising performance. However, the application of HEPBAs as insertion materials in memristors is still underexplored, and their conduction mechanisms are not well understood.

In this chapter, a promising Na^+-modulated non-volatile bipolar memristor with low power consumption, self-compliance and forming-free nature was proposed.[168] Five metal ions (Mn, Fe, Co, Ni, and Cu) were introduced to PBAs with composition of $Na_{1.38}Mn_{0.3}Fe_{0.3}Co_{0.133}Ni_{0.133}Cu_{0.133}[Fe(CN)_6]_{0.84}\square_{0.16}\cdot 0.92H_2O$ (denoted as HE-PBA) as an active storage layer in the resistive switching (RS) device. The device, composed of Ag top electrodes (TE), HE-PBA active layer and laser-ablated indium tin oxide (ITO) bottom electrodes (BE) is fabricated by inkjet printing and microplotting. The resistive switching mechanism underlying the HE-PBA-based memristor was comprehensively investigated for the first time using a combination of complementary characterizations and DFT calculations. The results indicate that the transition between the high-resistance state (HRS) and low-resistance state (LRS) is driven by an insulating-to-metallic phase transition, initiated by the extraction and insertion of highly mobile Na^+ ions under an applied electric field. DFT calculations revealed that a Na-deficient switching layer in HE-PBA leads to the metallic conduction behavior observed in the Ag/HE-PBA/ITO device. The printed memristor utilizes a low-energy process involving Na^+ shuttling, similar to the working principle of SIBs. Consequently, Ag/HE-PBA/ITO device shows enormous advantage for memristor applications, such as low operation voltage, favorable retention stability and a high R_{OFF}/R_{ON} ratio, which could be a promising candidate as non-volatile memory.

7.1. Materials Synthesis

A simple precipitation method was used to synthesize the high-entropy Prussian blue (PBA) materials. Typically, 8 mmol $Na_4Fe(CN)_6 \cdot 10H_2O$ and the corresponding stoichiometric amounts of $FeCl_2 \cdot 4H_2O$, $MnCl_2 \cdot 4H_2O$, $NiCl_2 \cdot 6H_2O$, $CuCl_2 \cdot 2.5H_2O$, and $CoCl_2 \cdot 6H_2O$ (in total 6 mmol metal precursors) were dissolved in 100 mL deionized water to form solutions A and B. After complete dissolution (ultrasonication for 0.5 h and then stirring for 0.5 h), 5.35 g sodium citrate was added to solutions A and B, followed by stirring for another 1 h. Then, solution B was slowly added (dropwise) to solution A to obtain a homogeneous solution. The mixture was kept stirring at room temperature for 2.5 h and aged for 12 h before centrifugation. The precipitate was washed several times with deionized water, and finally the wet powder was dried in a vacuum oven at 100 °C for 12 h.

7.2. Structural Analysis

Figure 7.1a displays the specific fabrication process of Ag/HE-PBA/ITO device. A commercial ITO electrode was patterned using laser ablation on ITO-coated glass substrates, serving as BE. Following this, a plasma treatment was conducted to enhance the hydrophilicity of the surface, resulting in a significantly reduced water contact angle, as demonstrated in **Figure 7.2a**. This treatment ensured optimal conditions for the application of ink. The latter ink was formed by dispersing pre-synthesized HE-PBA powder in a mixture of deionized water (97% vol.) and dimethyl sulfoxide (DMSO, 3% vol.), which helps to minimize “coffee ring effect” during the printing process, as shown in **Figure 7.2b**. In comparison to aqueous inks, DMSO exhibits a higher boiling point, lower evaporation rate, and greater viscosity. These properties help mitigate the coffee ring effect by slowing the drying process and reducing particle migration to the edges during evaporation. Additionally, DMSO balances surface tension forces, promoting a more uniform particle distribution and preventing the formation of ring-like deposits typically associated with water. The fabrication procedure of the device involves a two-step process that primarily microplotting and inkjet printing methods, as illustrated in **Figure 7.1a**. Notably, capillary microplotting overcomes the limitation of inkjet printing techniques, which are unable to print slightly larger particles (greater than 200 nm). In detail, the HE-PBA layer was

deposited on the ITO BE, using microplotting. To get dense HE-PBA film, the device need to be dried in a vacuum oven at 100 °C overnight. After that, a commercially available Ag ink was inkjet-printed as TE on the top of HE-PBA before the device is dried again in the vacuum oven at 120 °C for 1 h. Detailed fabrication steps can be found in the 4.3 Experimental Section. **Figure 7.1b** depicts a 3D topography of the printed device, highlighting the structure of the three stacked layers. The Ag-based TE forms a raised circular section in the center (marked in red) of the underlying, round area (shown in blue/green), which corresponds to the HE-PBA material. The patterned ITO layer beneath these printed sections is exposed at the edges, as indicated.

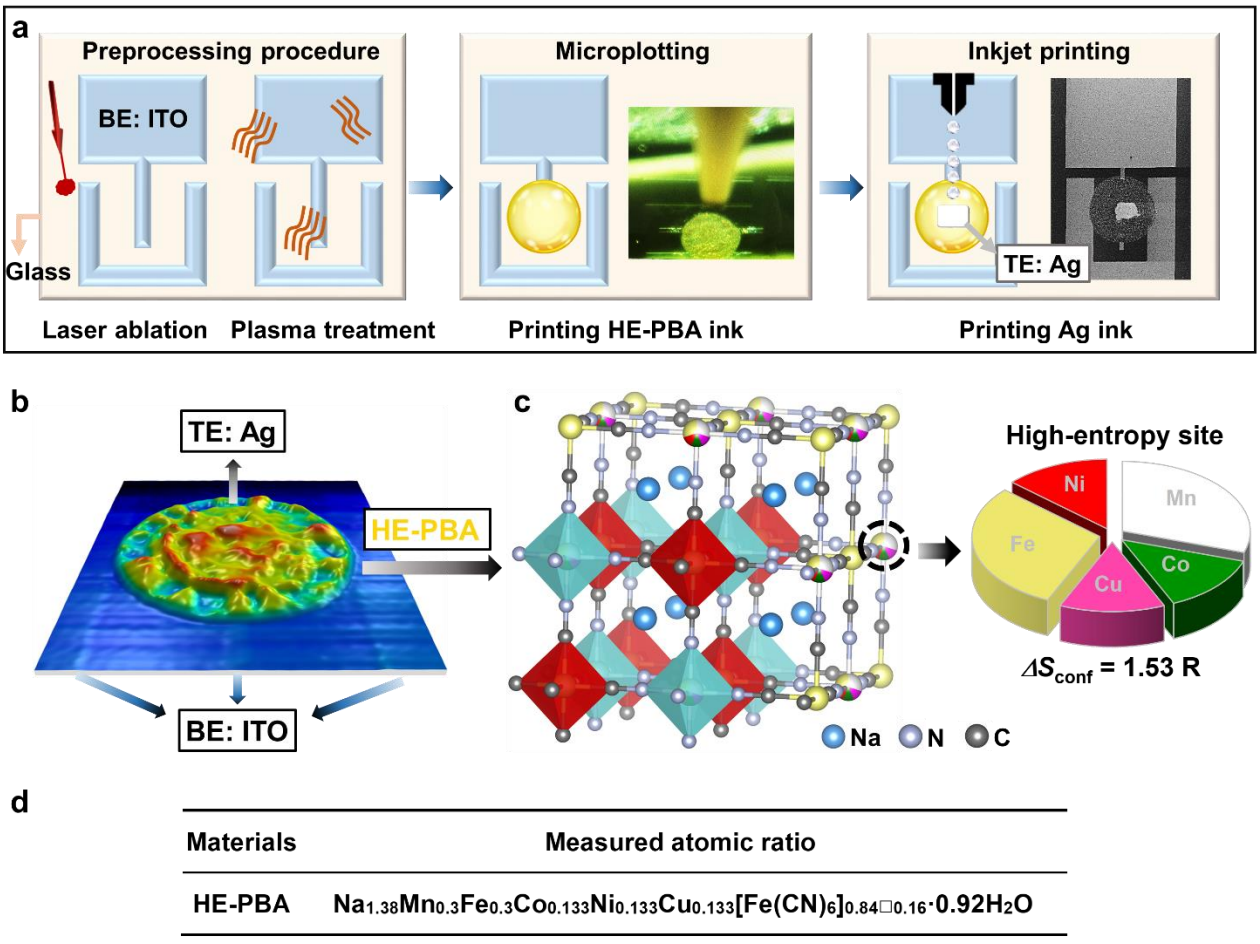

d

Materials	Measured atomic ratio
HE-PBA	$Na_{1.38}Mn_{0.3}Fe_{0.3}Co_{0.133}Ni_{0.133}Cu_{0.133}[Fe(CN)_6]_{0.84}\square_{0.16}\cdot 0.92H_2O$

Figure 7.1. (a) Schematics of the device fabrication process. Since the ITO is invisible (glass is visible) under microplotting microscope, it is hard to print to a specific area without a reference line. Thereby, the U-shaped ITO are designed for easy printing. (b) 3D top view of the Ag/HE-PBA/ITO memristor. (c) Crystal structure of the HE-PBA from Rietveld refinement analysis and (d) composition of the tailored multi-elemental site in HE-PBA, measured using ICP-OES and DSC.

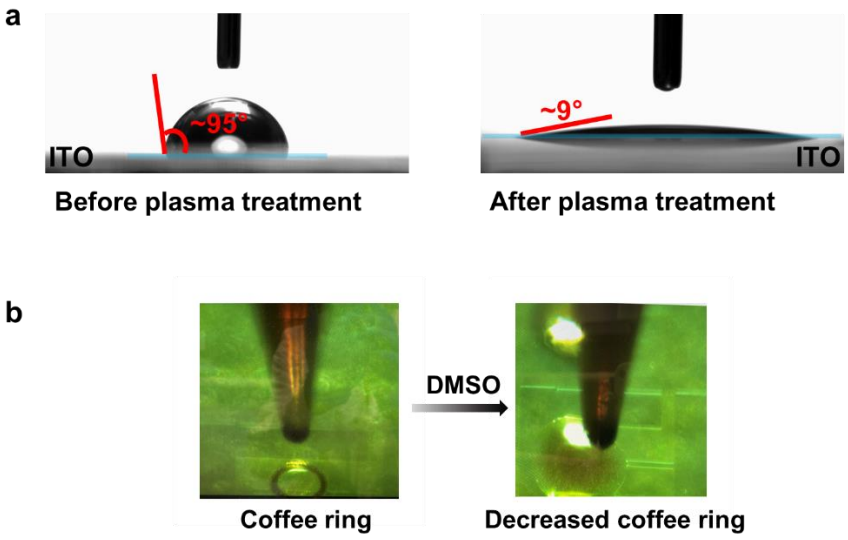

Figure 7.2. (a) Water contact angle of the ITO surfaces was measured before and after plasma treatment. Before treatment, the contact angle was approximately 95°, indicating a hydrophobic surface. After plasma treatment, the contact angle significantly decreased to around 9°, reflecting improved surface hydrophilicity. (b) Effect of DMSO addition to the HE-PBA ink during microplotting.

Considering that the HE-PBA was applied for the first time as a middle storage layer of the memristor, the structure and chemical components in the initial state need to be confirmed before investigating electrical properties of the Ag/HE-PBA/ITO device. The local structure model of HE-PBA shows the Fe_1 atoms at the C-coordinated 4*a* sites of the lattice ($Na_xM[Fe_1(CN)_6]$), while other metal atoms M (M = Mn, Fe_2, Co, Ni, and Cu) occupy the N-coordinated 4*b* positions in a random manner, leading to the formation of linear chains of Fe_1−C≡N−Mn/Fe_2/Co/Cu/Ni−N≡C−Fe_1 along the lattice edges,[75,101] as illustrated in **Figure 7.1c**. ICP-OES was used to analyze the chemical composition of the HE-PBA, and DSC (see **Figure 7.3**) was conducted to estimate the content of crystal water in the sample.[170] As listed in **Figure 1d**, the chemical formula was determined to be $Na_{1.38}Mn_{0.3}Fe_{0.3}Co_{0.133}Ni_{0.133}Cu_{0.133}[Fe(CN)_6]_{0.84}\square_{0.16}\cdot 0.92H_2O$. Murty *et al.*[179] suggested an empirical classification for such materials based on the ΔS_{conf}, which can be calculated for materials with purely random distribution by statistical thermodynamics (see **Equation 3.4** in Introduction Part). In this case, HE-PBA, with a ΔS_{conf} of 1.53 *R*, can be classified as a HEM.

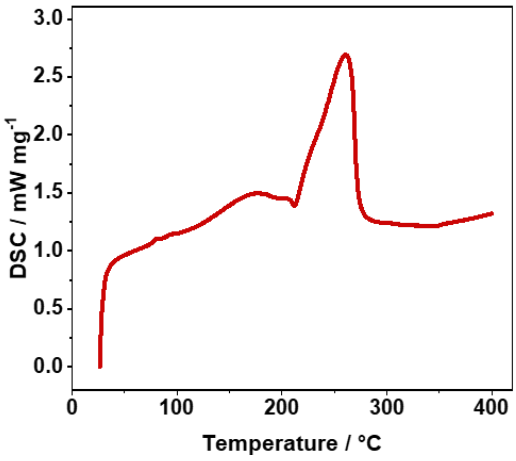

Figure 7.3. DSC analysis of HE-PBA. The content of crystallite water was estimated by DSC from the weight loss in the temperature range of ~40–120 °C, which can be assigned to dehydration.[75,170] At ~230–330 °C, an exothermic peak is detected, demonstrating release of $(CN)_2$ and further decomposition.

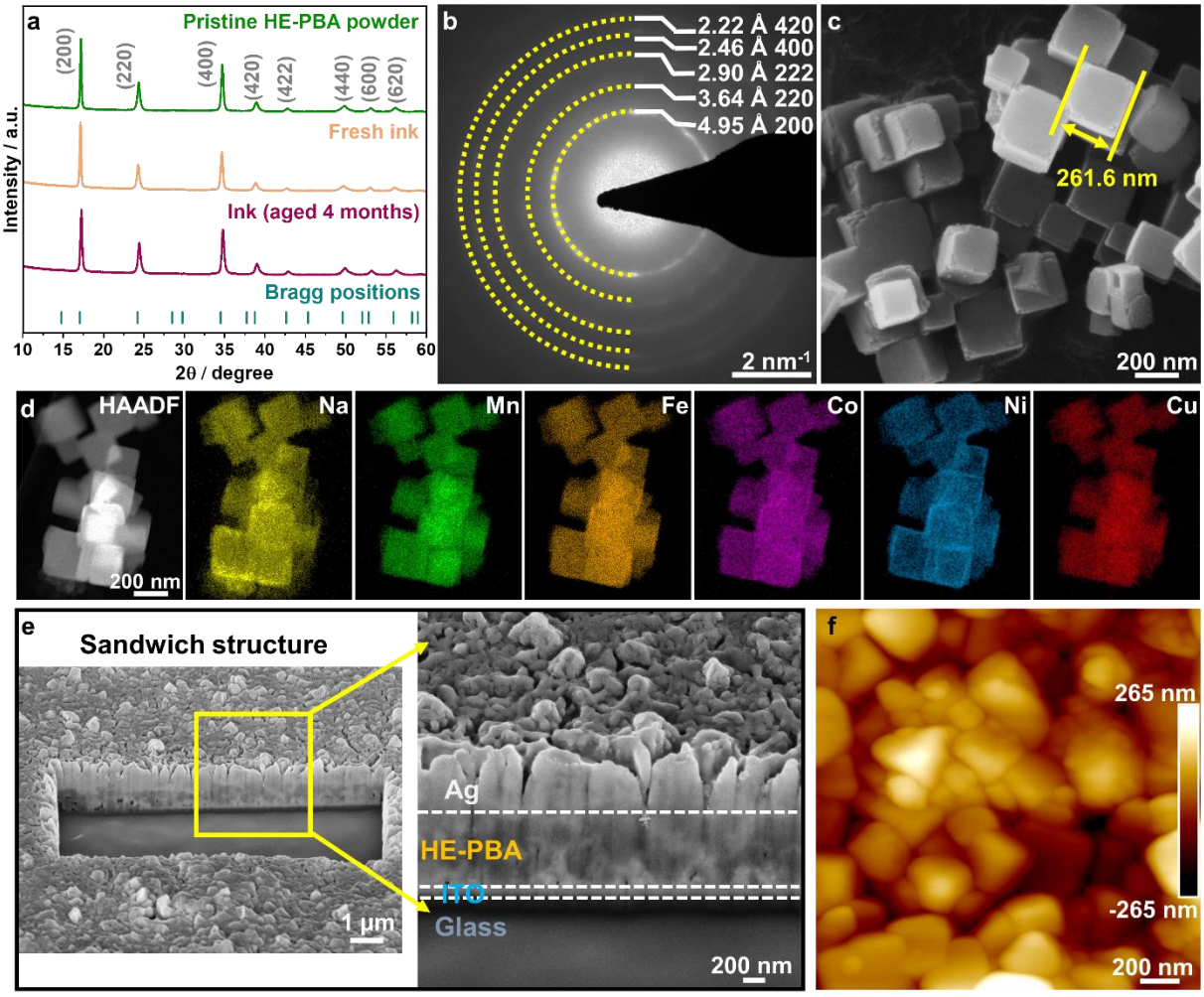

Figure 7.4. Structural and morphological characteristics of HE-PBA: (a) XRD pattern, (b) SAED pattern, (c)

SEM micrograph, and (d) STEM-EDS elemental mapping of HE-PBA. (e) Cross-sectional SEM image of the device structure, showing three layers of materials, namely Ag, HE-PBA, and ITO. (f) Surface analysis of the HE-PBA film via AFM.

The crystal structure of the as-synthesized samples was investigated by powder XRD. **Figure 7.4a** exhibits the diffraction peaks of HE-PBA with (200), (220), (400), (420) and (422) crystal planes, which well matches with the face-centered cubic structure with *Fm*-3*m* space group (ICSD coll. code 193354).[72,199] There is no difference in the XRD patterns between pristine HE-PBA powder and ink-based HE-PBA. Notably, the crystal structure of the sample remained unchanged even after the ink had been deposited for nearly four months, indicating high ink stability (see **Figure 7.4a**). In addition, a SAED (selected-area electron diffraction) analysis (**Figure 7.4b**) was carried out to further characterize the crystal structure of HE-PBA. The lattice fringes with d-spacings of 4.95, 3.64, 2.90, 2.46 and 2.22 Å can be associated to the (200), (220), (222), (400) and (420) planes of the cubic structure in HE-PBA, which further elaborate the *Fm*-3*m* space group in the sample. SEM (**Figure 7.4c**) shows that the HE-PBA nanoparticle are cubic in shape with an average size of 200-300 nm. Next, the presence of Na, Mn, Fe, Co, Cu and Ni at the given resolution (**Figure 7.4d**) were confirmed by high-angle annular dark-field STEM (HAADF STEM) imaging in conjunction with EDS mapping. Minor Ni enrichment at the grain boundaries was detected, likely resulting from diffusion and/or surface energy effects during the material's formation. The proportions of each element in HE-PBA obtained by STEM-EDS mapping analysis align with the ICP result (see **Table 7.1**).

Furthermore, the printed memristor was characterized to verify its structural integrity and fabrication success. A focused ion beam (FIB, see **Figure 7.4e**) cut of the printed memristor was prepared. The effective area of the Ag/HE-PBA/ITO devices, defined as the overlap between BE and TE, measures approximately 30 × 120 μm^2. The cross-section SEM image depicted in **Figure 7.4e** shows the device was fabricated in a vertical sandwich structure with ~800 nm thickness for the active layer of HE-PBA. The surface properties of the HE-PBA film were investigated using AFM, as shown in **Figure 7.4f**. Since the HE-PBA film is made up of an array of nano-cube particles in a disorderly manner, the surface has a relatively large root mean square roughness value (R_q) of ~70 nm. μXRF measurements

displayed in **Figure 7.5** measurements confirmed the presence of the aforementioned elements in the active layer and revealed that no changes in elemental composition occur during device fabrication.

Table 7.1. Proportion of each element in HE-PBA from STEM-EDS mapping analysis.

Element	Atomic fraction (%)	Atomic error (%)	Mass fraction (%)	Mass error (%)	Fit error (%)
Na	7.96	1.74	10.07	2.07	1.7
Mn	2.52	0.41	7.63	1.09	0.14
Fe	4.73	0.77	14.54	2.07	0.08
Co	1.09	0.18	3.53	0.50	0.06
Ni	1.10	0.18	3.55	0.51	0.07
Cu	1.11	0.18	3.89	0.56	0.08
C	54.97	5.08	36.34	1.88	0.4
N	26.53	5.9	20.46	4.27	3.03

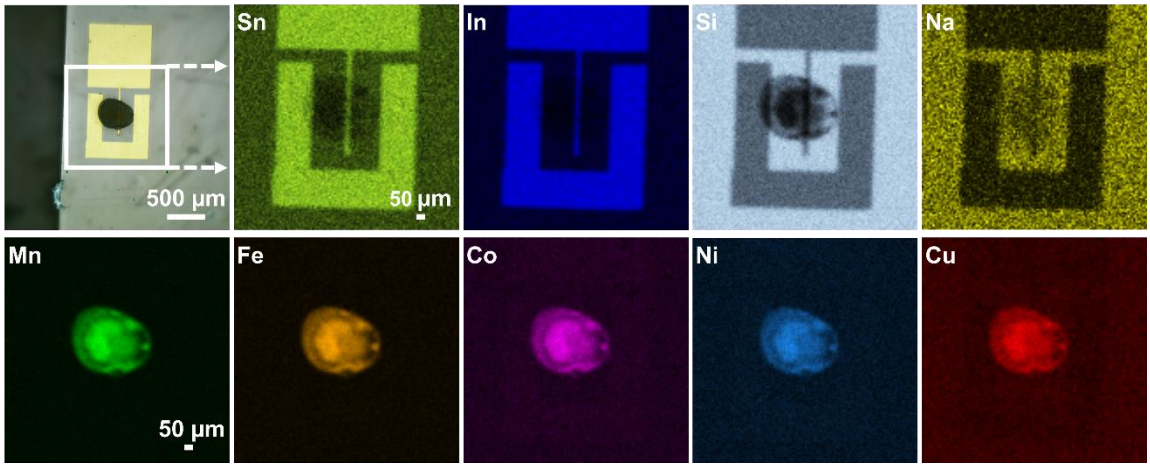

Figure 7.5. Elemental distribution of the active layer measured by µXRF.

The Fourier transform infrared (FT-IR) spectrum of HE-PBA in **Figure 7.6a** shows sharp absorption bands at 1619 and 3552 cm^{-1}, indicative of the O-H stretching and H-O-H bending, respectively,

confirming the presence of crystal water in the material.[47,201] The pronounced broad peak at ~ 2080 cm^{-1} can be attributed to the stretching vibration from C≡N, and the sharp peak in the low wavenumber region at 595 cm^{-1} corresponds to the Fe-CN vibration. In addition, Raman spectroscopy was utilized to explore the interaction between the cyanides and transition-metal ions. This is due to the sensitivity of the frequency of the *ν*(CN) cyanide stretching vibration mode to the oxidation state of the iron cation and its surrounding coordination environment.[57,243–245] In **Figure 7.6b**, two prominent bands were observed at approximately 2098 and 2137 cm^{-1}, corresponding to Fe^{II}-CN-M interactions, akin to the *ν*(CN) bands identified in $K_4[Fe^{+II}(CN)_6]$ as reported by Samain *et al*.[244] In contrast, peaks at higher wavenumber are expected for the stretching vibration of $[Fe^{+III}(CN)_6]^{3-}$.[243,244] XPS measurements were conducted to analyze the surface chemical state of HE-PBA. The survey spectrum displayed in **Figure 7.6c** confirms the presence of expected elements (C, N, Na, Mn, Fe, Co, Cu and Ni). In the detailed measurements, a single peak at 1072.1 eV detected in the Na 1s spectrum (**Figure 7.6d**) is indicative of Na^+ ions in the PBA lattice. Mn 2p spectrum (**Figure 7.6e**) shows main peak doublet at 641.0 eV ($2p_{3/2}$) and 652.7 eV ($2p_{1/2}$), together with a distinct satellite peak doublet at 646.2/657.9 eV, as well as a broad Ni Auger line at ~644 eV. The presence of the main peak doublet binding energy, along with the shake-up satellite, strongly indicates an oxidation state of +II for Mn.[75,182] The Fe 2p spectrum (**Figure 7.6f**) displays a single Fe 2p peak doublet at 708.5 and 721.4 eV, which is assigned to Fe^{2+} in the $[Fe^{+II}(CN)_6]^{4-}$ unit.[47,101,186,187] Since no additional features were observed in the Fe 2p spectrum apart from this doublet, it suggests that the Fe ions coordinated with nitrogen are also in the +II oxidation state. **Figure 7.6g** shows the Co 2p spectrum, featuring a main Co 2p peak doublet (782.0/797.4 eV) and prominent shake-up satellite peaks (789.5/804.7 eV), along with a broad Fe Auger feature at ~786 eV. Since such satellite peaks are observed for Co^{2+} only, the spectrum suggests that Co is present in oxidation state +II.[75,101] The major peak in the Cu 2p spectrum (**Figure 7.6h**) located at 932.9 eV (Cu $2p_{3/2}$) can be assigned to Cu^+.[75] Besides, another peak detected at a higher binding energy (935.1 eV) together with its corresponding shake-up satellite at ~943 eV can be ascribed to the presence of Cu^{2+}.[87,185] The presence of Cu^+ in the spectrum suggests that an internal redox reaction (surface reduction), specifically the conversion of Cu^{2+} to Cu^+, took place internally during the synthesis. This phenomenon has been observed and confirmed in the previous

research (see Chapter 5).[166,167]

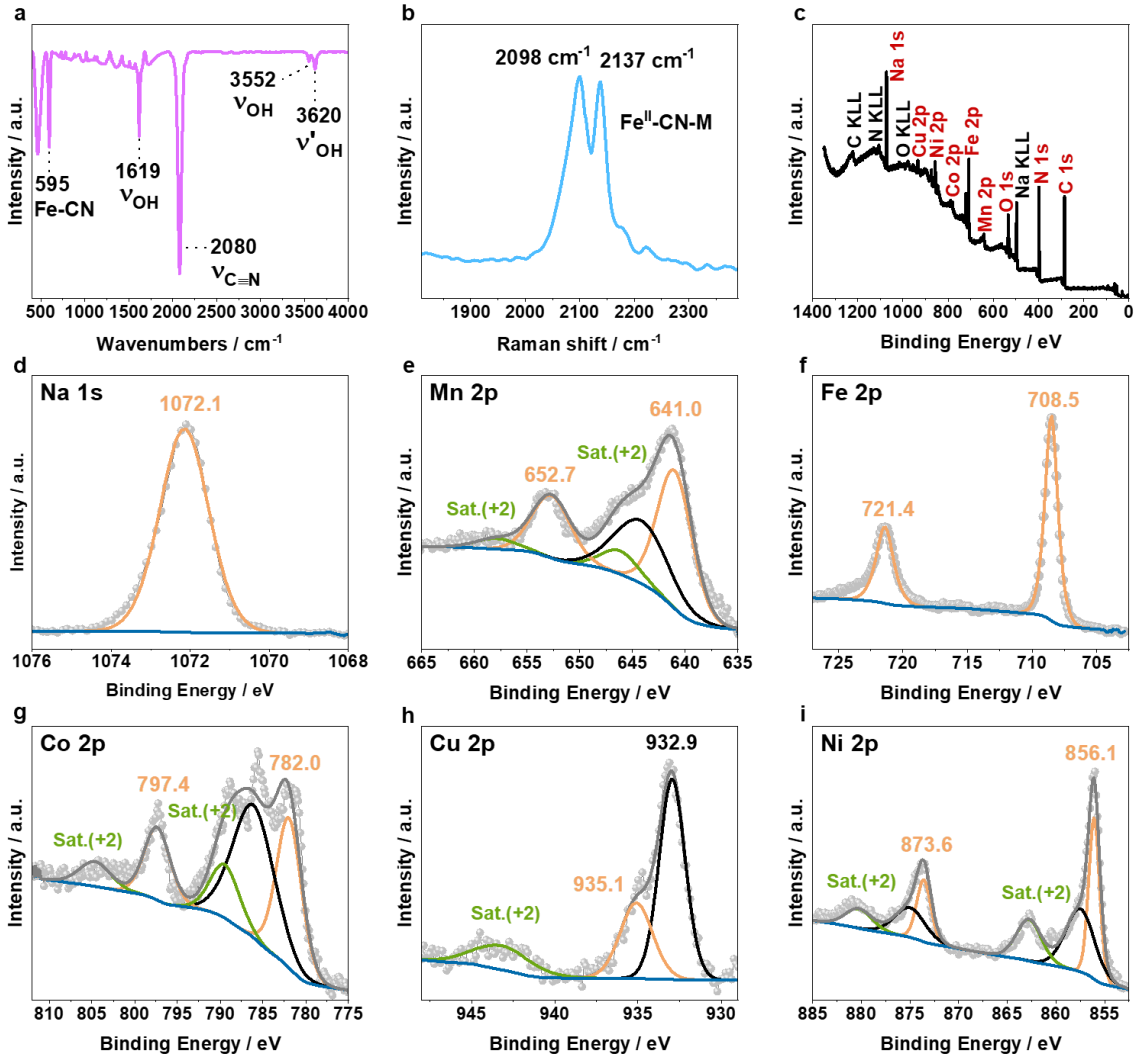

Figure 7.6. Structural characterization and surface chemical state of as-prepared HE-PBA sample: (a) FT-IR spectrum, (b) Raman spectrum. XPS analysis: survey spectra (c), detail spectra in the (d) Na 1s, (e) Mn 2p, (f) Fe 2p, (g) Co 2p, (h) Cu 2p and (i) Ni 2p regions.

Finally, the Ni 2p spectrum (**Figure 7.6i**) shows major peaks at 856.1 eV ($2p_{3/2}$) and 873.6 eV ($2p_{1/2}$), accompanied by another doublet at slightly higher binding energy of 857.6 and 875.1 eV, as well as satellite peaks at 862.8 and 880.3 eV.[101] The multiple peak splitting complicates the precise determination of the Ni oxidation state. Since the Ni $2p_{3/2}$ peak of NiO appears around ~854 eV, while the Ni $2p_{3/2}$ peak of $Ni(OH)_2$ is found near ~856 eV, close to the binding energy of Ni_2O_3.[124] However, prior results from normalized *K*-edge XANES (X-ray absorption near edge spectroscopy) confirms

oxidation state of +II in HE-PBA.[101,166] Hence, the initial average oxidation state of both Fe_1 binding to the carbon atoms and M (Mn, Fe_2, Co, Cu and Ni) cations binding to the nitrogen atoms of $C{\equiv}N^-$ ligands are determined to be +II, as expected for the PBA structure with linear chains of $Fe_1{-}C{\equiv}N{-}Mn/Fe_2/Co/Cu/Ni{-}N{\equiv}C{-}Fe_1$.

7.3. Electrical Properties

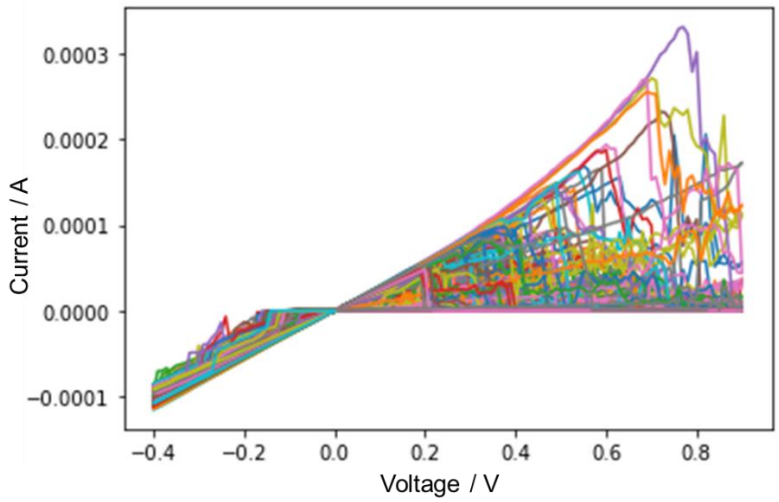

Figure 7.7. *I–V* curves for the whole measurement with 800 sweeping cycles.

The RS behavior of the Ag/HE-PBA/ITO device was examined by the *I–V* measurements. **Figure 7.7** shows the *I–V* curves for the whole measurement of 800 sweeping cycles, while **Figure 7.8a** focuses on selected representative *I–V* profiles plotted on a semilogarithmic scale (1^{st}, 2^{nd} ··· and 800^{th}). All sweeping voltage were conducted at a fixed rate of 0.01V/step. The bias voltages were applied to the Ag TE with ITO electrode grounded. As displayed in **Figure 7.8a**, the Ag/HE-PBA/ITO device exhibits a typical bipolar RS behavior.[246–248] The device at the pristine state was highly resistive state of 2.6×10^7 Ω. When a negative bias was applied from 0 to –0.4 V, the device transitioned from a HRS (OFF state) to a LRS (ON state, 5.3×10^3 Ω for the first cycle), indicating the "SET" process. This transition from HRS to LRS mirrors a "writing" process in data storage devices.[249] Conversely, increasing the sweeping voltage from 0 to 0.9 V caused a marked drop in current at ~0.5 V (green line in **Figure 7.8a**), indicating a reset of the device to a HRS of (2.5×10^6 Ω), commonly referred to as

the "RESET" process. This shift from LRS to HRS corresponds to an erasing process in digital memory devices.[249] The voltages at which RS occurs during the SET and RESET process, is referred to as V_{SET} and V_{RESET}, respectively. During the SET process, it's noteworthy that the LRS current shows a slight increase upon surpassing V_{SET}, indicating a low self-compliance behavior at ~44 μA (I_{SCOMP}). This feature highlights a significant advantage of the device, as it eliminates the need for current limitations to prevent permanent dielectric breakdown.[250–252] Usually, a compliance current (CC) is required to prevent devices from experiencing current overshoot. In this study, the device underwent more than 800 switching cycles and consistently displayed self-compliance bipolar RS loops, as depicted in **Figure 7.7**. Moreover, the Ag/HE-PBA/ITO devices also demonstrated comparable reversibility in comparison to many reported insertion devices without self-compliance behavior (see **Table 7.2)**.

The corresponding V_{SET} and V_{RESET} values of the 800 subsequent cycles were extracted and plotted in a histogram in **Figure 7.8 b**. The V_{SET} values showed a tight distribution between –0.33 and –0.22 V, while V_{RESET} ranged from 0.02 to 0.4 V, with minor outliers up to 0.9 V. The inserted box plots revealed mean values of V_{SET} and V_{RESET} as –0.26 V and 0.36 V, respectively, which are significantly lower than that of reported insertion materials.[42,250] The standard deviation (σ) with distribution width of 0.02 V for V_{SET} suggests a small cycle-to-cycle variability. Typically, during the initial electroforming process, a higher voltage is required compared to subsequent SET processes. This higher voltage is necessary to initiate the formation of a conductive path, such as a conductive filament.[9,247] However, it appears that the Ag/HE-PBA/ITO device exhibits excellent consistency in switching voltage right from the start, suggesting a forming-free mechanism. **Figure 7.9** depicts SET and RESET power data defined by the product of switching current and voltage.[252,253] The device exhibits low power consumption during the SET process (P_{SET}), ranging from 20.6 to 36.9 μW, with an average of 26.1 μW. For the RESET process (P_{RESET}), power consumption averages 8.0 μW, reaching up to 104.7 μW. This is significantly lower than other reported devices with self-compliance behavior,[150,254,255] as summarized in **Table 7.3**.

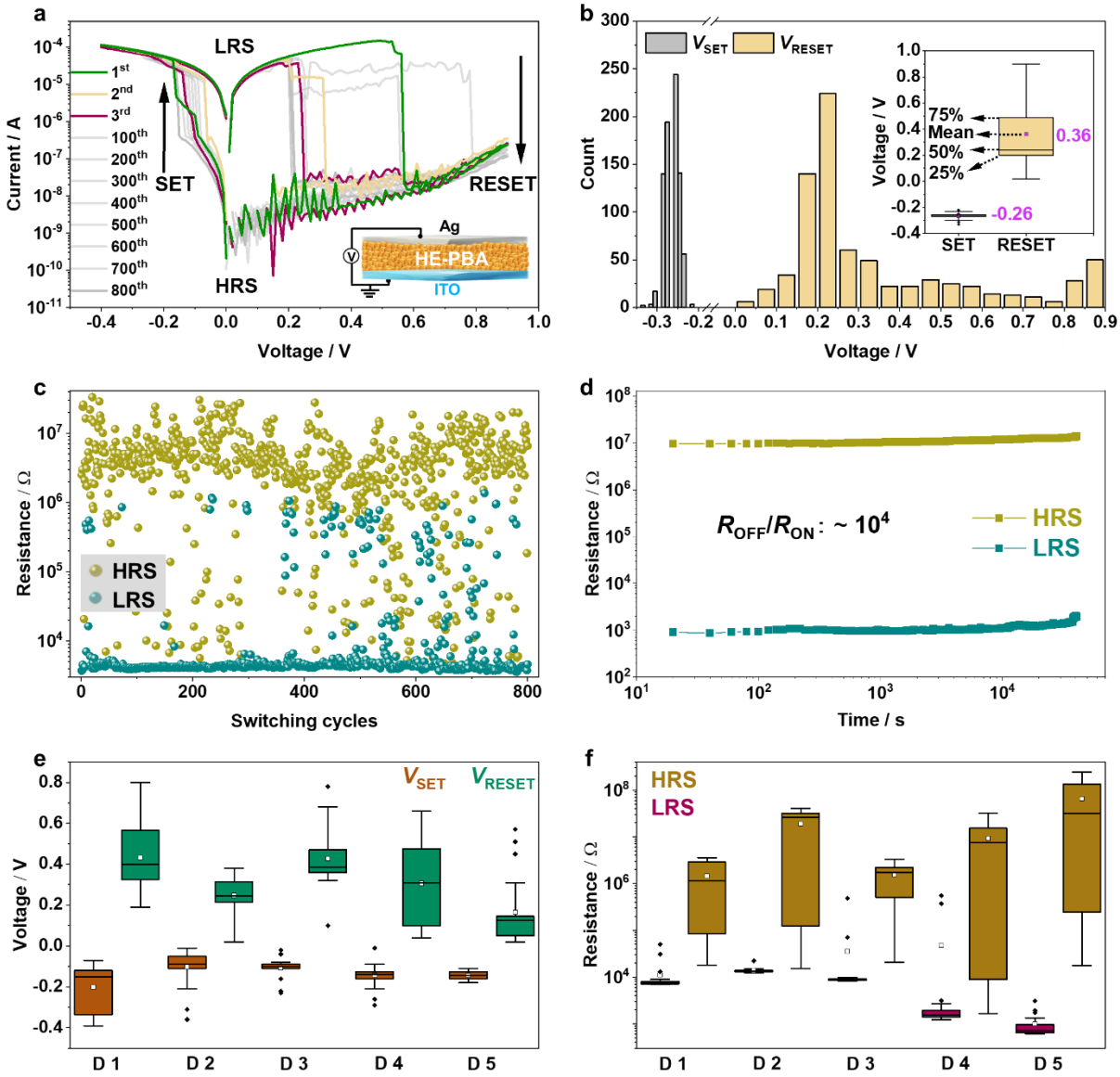

Figure 7.8. Electric characterization of the Ag/HE-PBA/ITO memristor. (a) Selected *I–V* curves plotted on a semi-logarithmic scale (1st, 2nd, 3rd, 100th, 200th, 300th, 400th, 500th, 600th, 700th, and 800th). (b) V_{SET} and V_{RESET} distribution extracted from 800 subsequent *I–V* sweeps. Inset: statistical analysis of V_{SET} and V_{RESET} by box plots. (c) Endurance over 800 sweeping cycles. (d) Device retention at HRS and LRS over 4×10^4 s. (e) Statistical analysis of V_{SET} and V_{RESET} from five different devices displayed in box plots. (f) Box plots depicting the distribution of HRS and LRS across the five devices.

The endurance of the Ag/HE-PBA/ITO device, characterized by the ratio of HRS and LRS values over cycling, is presented in **Figure 7.8c**. The R_{OFF}/R_{ON} ratio remains close to 10^4, with additional clarification provided by corresponding cumulative probability data in **Figure 7.10**. Notably, there is no significant degradation of the device after 800 switching cycles. The variation in conductivity

shown in **Figure 7.8c** will be discussed in more detail in the following section on the conduction mechanism. **Figure 7.8d** displays excellent retention characteristics of the device with a stable R_{ON}/R_{OFF} ratio of 10^4 after more than 4×10^4 s (around 10^7 Ω for HRS and 10^3 Ω for LRS). The results suggest the device could be a promising candidate for non-volatile memory applications.[256,257] Comparing the performance of HE-PBA with previously reported conventional PBAs (single-metal, $\Delta S_{conf} = 0R$) as storage layer in memristors (see **Table 7.4**),[66,67,258] emphasizes the substantial improvements in endurance and retention capabilities achieved with the Ag/HE-PBA/ITO devices. This result highlights the positive effect of the increased ΔS_{conf} on optimizing the electrical performance of memristors.

Table 7.2. Performance comparison of RS devices based on insertion materials.

Ref.	TE/storage layer/BE	V_{SET} (V)	V_{RESET} (V)	R_{OFF}/R_{ON}	Endurance (cycles)	Retention (s)	Self-compliance	Forming-free
This work	Ag/HE-PBA/ITO	−0.26	0.36	10^4	800	4×10^4	Yes	Yes
[259]	Pt/$LiFe_5O_8$/$SrRuO_3$	1.6	−1.9	15	4	-	No	No
[260]	Ti/Pt/ $LiNbO_3$/Ti/Pt	2.4	−2.8	100	100	-	No	No
[261]	Au/Li_xCoO_2/SiO_2/Si	−3.8	4	71	100	-	No	Yes
[39]	Pt/$Li_4Ti_5O_{12}$/Pt	3.8	−3.1	10^4	50	6×10^4	No	Yes
[42]	Pt/$LiCoO_2$/SiO_2/Si	3.2 to 6.9	−3.2 to −6.4	10^4	125	10^4 to 10^5	No	No

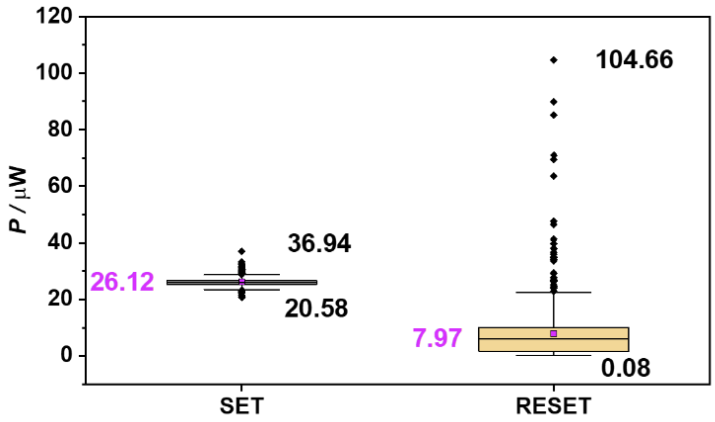

Figure 7.9. SET and RESET power data defined by the product of switching current and voltage.

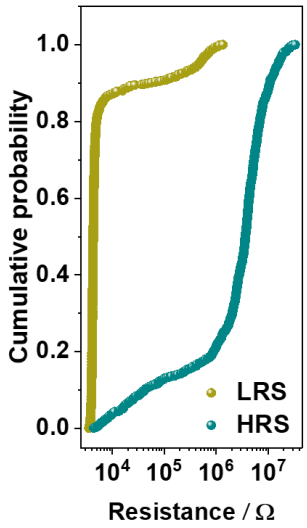

Figure 7.10. Cumulative probability of the endurance plotted in Figure 7.8c.

Table 7.3. Performance comparison of RS devices with self-compliance behavior.

Ref.	Storage layer	TE/BE	V_{SET} (V)	V_{RESET} (V)	R_{OFF}/R_{ON}	Retention (s)	P_{SET} (μW)
This work	HE-PBA	Ag/ITO	−0.26	0.36	10^4	4×10^4	26
[262]	PS/PCBM/TTF	Al/Al	2.6	−6.5	10^3	4.32×10^4	234
[252]	HfO_2	ITO/TiN	−0.2	1.6	40	10^4	160

[150]	HfO_x	TiN/ITO	0.6	−0.7	20	10^4	570
[263]	$AlO_\delta/Ta_2O_{5-x}/TaO_y$	Pt/Pt	−0.9	1.2	70	10^4	90
[254]	CuO_x (pH 9)/CuO_x (pH 11.5)	Pt/Pt	2.5	−3	10^3	10^4	1250
[264]	HfO_2/Al_2O_3	TiN/Pt	1.2	−1.4	72	10^4	1260
[265]	$Ta/TaO_x/TiO_2/Ti$	SiO_2/Si	5	−6	10	10^4	50
[258]	$K_xFe[Fe(CN)_6]$	Au/Ag	−0.6	0.6	10^3	-	13800

Table 7.4. Performance comparison of HE-PBA and conventional (single-metal) PBAs as storage layer in RS devices.

Ref.	**TE/storage layer/BE**	V_{SET} **(V)**	V_{RESET} **(V)**	R_{OFF}/R_{ON}	**Endurance (cycles)**	**Retention (s)**	**Self-compliance**	**Forming-free**	**Configurational entropy (R)**
This work	Ag/HE-PBA/ITO	−0.26	0.36	10^4	800	4×10^4	Yes	Yes	1.53
[67]	$Pt/K_xFe[Fe(CN)_6]$ /Au/Cr/Si	−0.5	0.45	10^2	500	10^3	Yes	Yes	0
[258]	$Au/K_xFe[Fe(CN)_6]$/ Ag	−0.6	0.6	10^3	200	-	Yes	Yes	0
[66]	$Pt/K_xFe[Fe(CN)_6]$ /Au/Cr/Si	−0.9	0.7	10^3	100	-	No	Yes	0

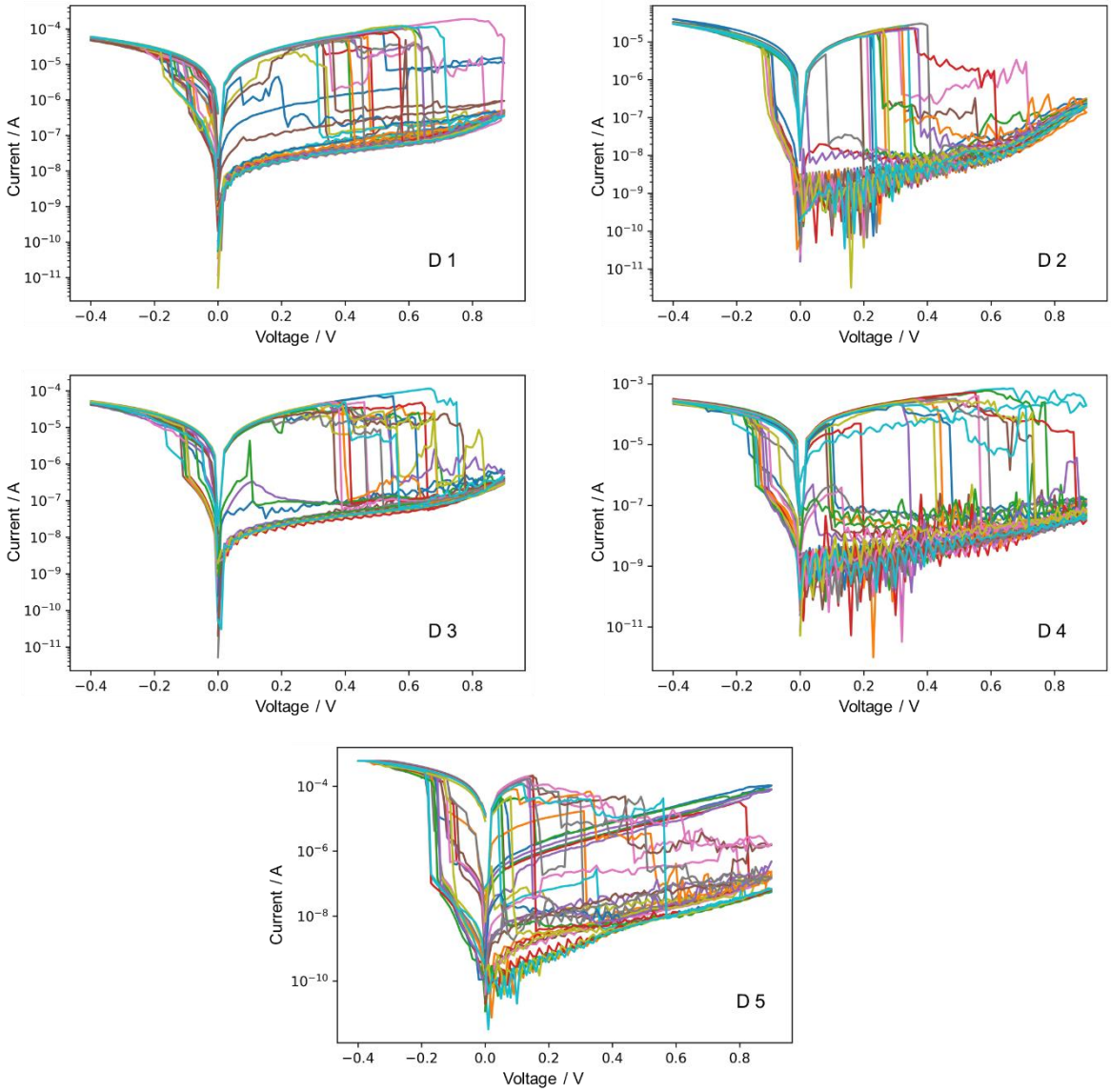

Figure 7.11. *I–V* curves for different devices.

In addition, *I–V* data were conducted on five different devices to assess the uniformity across devices. The devices exhibit clear bipolar RS behavior with self-compliance characteristics, as depicted in **Figure 7.11**. In detail, box plots of the extracted V_{SET} and V_{RESET} for each device are displayed in **Figure 7.8e**, and **Figure 7.12** shows the average values of V_{SET} and V_{RESET} yielded by box plots analysis. D2，D3, D4 and D5 show a similar mean value for V_{SET} (below –0.14 V), while ~ –0.20 V are found for D1. The mean V_{RESET} values are 0.43, 0.25, 0.43, 0.31 and 0.17 V, respectively, for D1 to D5. The fluctuation observed in the RESET process is below 0.9 V, indicating room for improvement through optimized measurement procedures or the implementation of advanced feedback algorithms in the

future studies.[266] The minimal variation in V_{SET} and V_{RESET} among different devices demonstrates that HE-PBA-based memristors can reliably operate at low SET and RESET voltages, making them suitable for low-power memory applications. D2, D4 and D5 also exhibit an R_{OFF}/R_{ON} ratio of more than 10^3, as shown in **Figure 7.8f**. To further examine the dynamic RS behavior of the device, pulsed operations for SET and RESET over 500 cycles were performed,[267] as shown in **Figure 7.13**. SET was achieved with a –0.4 V pulse, and RESET with a 0.5 V pulse, both without CC. The pulse width for both operations was 0.2 s. Resistance was measured with a 0.01 V read pulse lasting 0.2 s. The results show favorable characteristics of the printed memristor, which can switch between HRS and LRS with low applied voltage and without CC over extended cycles. Several studies have indicated that utilizing insertion materials remains challenging, primarily due to their frequently unfavorable operational characteristics, such as high voltages and elevated energy consumption,[39,42] as displayed in **Table 7.2**. Hence, in comparison to these insertion-type devices, the advantages of the Ag/HE-PBA/ITO device in terms of switching endurance, power consumption, and retention are even more pronounced, which underscores the significant advantage of using HEMs for such applications.

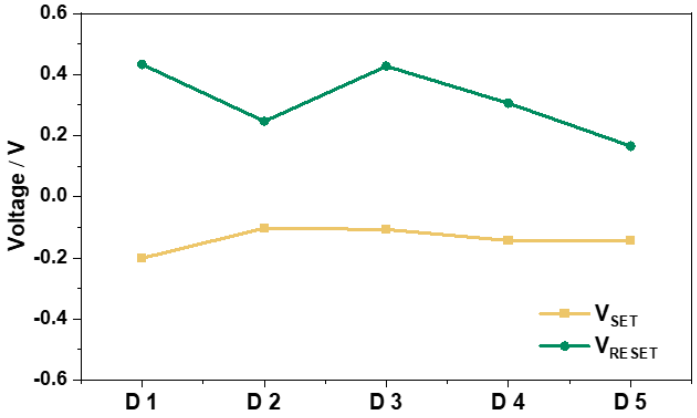

Figure 7.12. Average value for V_{SET} and V_{RESET} for different devices based on box plots analysis.

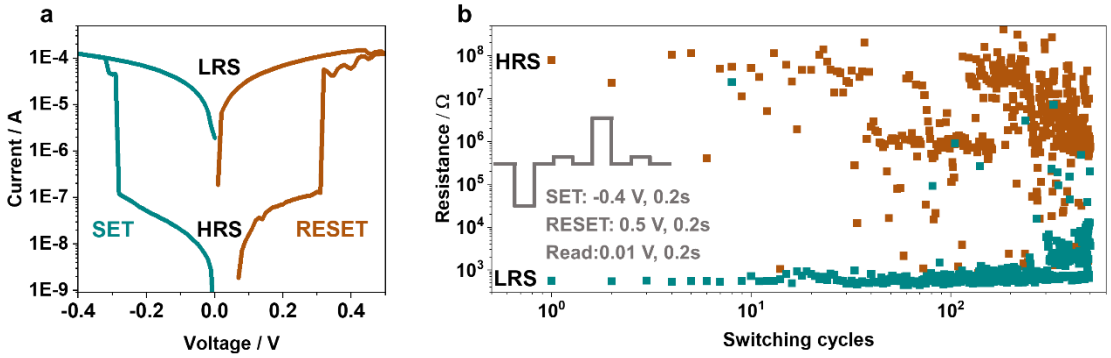

Figure 7.13. (a) *I–V* measurements were employed before pulsed operation, (b) endurance of the device subjected to pulsed voltage stimulation (500 cycles) along with the corresponding voltage waveform.

7.4. Resistive Switching Mechanism

Next, the aim was to elucidate the conduction mechanism of the Ag/HE-PBA/ITO device by performing a linear fitting on selected double-logarithmic *I–V* curves from the SET and RESET processes. After reaching the LRS of the device, the linear fitting with a slope close to 1 indicates an ohmic conduction mechanism (see **Figure 7.14a** and **b**), consistent with findings in Chiu's study.[268] After the current sharply drops in the OFF state during the RESET process, the presence of significant noise (see **Figure 7.14c** and **d**) makes it difficult to determine the conduction mechanism. Therefore, to investigate the conduction mechanism further, *I–V* measurements were conducted on a random device in its initial state, LRS, and HRS, ensuring that the maximum applied voltage remains well below the V_{SET} and V_{RESET} to prevent resistive switching. The curved profiles observed in the initial state and HRS (**Figure 7.14e and i**) were comparable, as neither crossed the origin of the diagram. However, following the SET process, the device demonstrated a distinct behavior, clearly crossing the origin in **Figure 7.14g**. The distinct *I–V* characteristics in the LRS points to a high conduction character of the device. Furthermore, **Figure 7.15** shows the temperature dependence of the resistivity in the LRS, i.e., an increase of resistance with increased temperature, which indicates a more "metallic" type of conduction. In short, it is evident that an ohmic conduction is dominant in the LRS based on the above results. Lee *et.al.*[255] reported that such internal ohmic resistance plays a critical role in the self-compliance property, since the ohmic load resistance limits current flow in the LRS.[252] This finding offers a reasonable explanation for the self-compliance characteristic observed in the Ag/HE-PBA/ITO

devices.

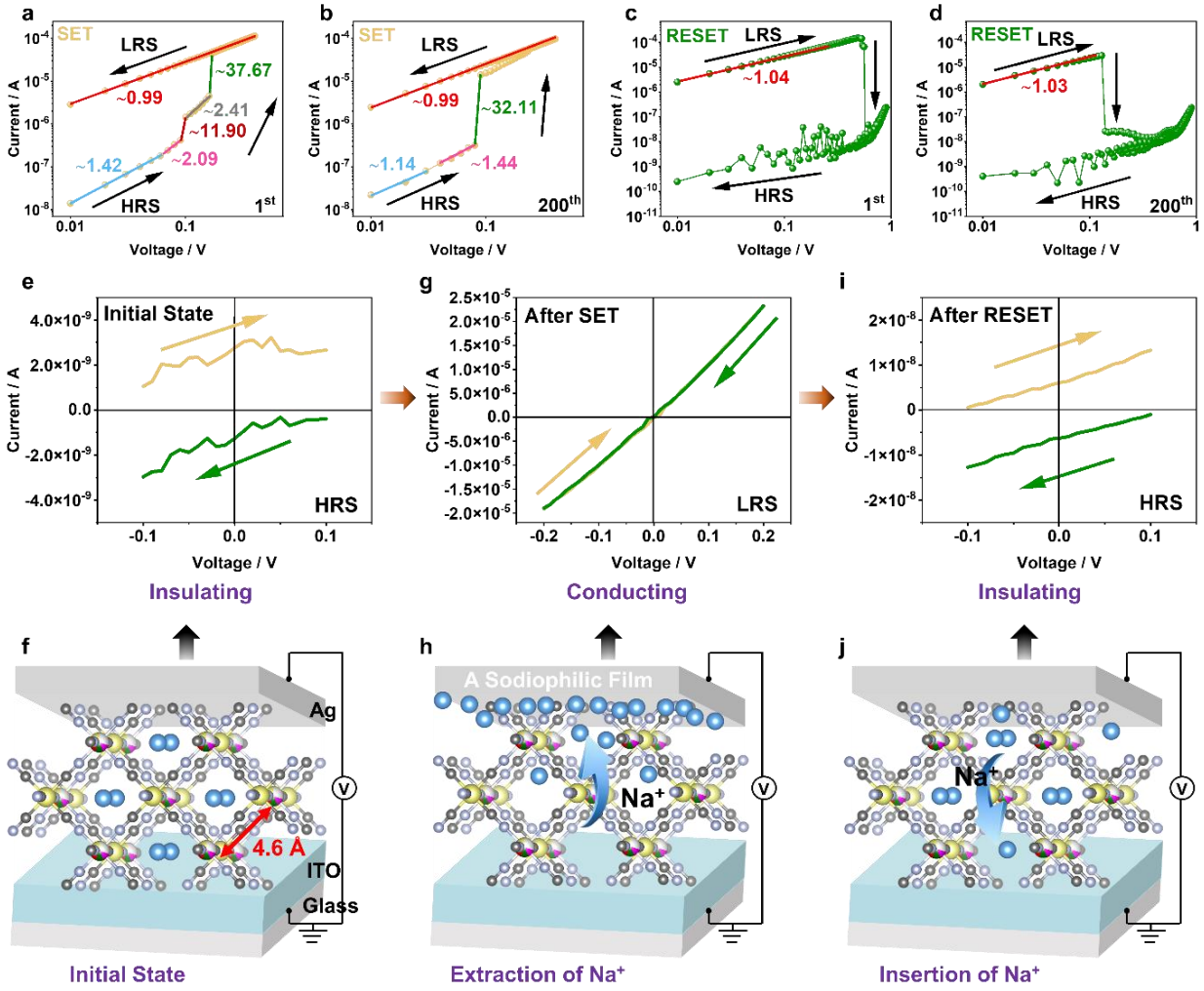

Figure 7.14. Analysis of the conduction mechanism. Double-logarithmic *I–V* curve for (a, b) SET process and (c, d) RESET process. (e, g, i) *I–V* measurements on a random device in the initial state, LRS and HRS, respectively, with a maximum applied voltage well below V_{SET} and V_{RESET}. (f, h, j) Corresponding schematic diagrams of the resistive switching mechanism.

To ascertain whether the self-compliance originates from the ITO or the HE-PBA, commercial Au was tested as BE in place of ITO (see **Figure 7.16a**). Laser ablation was used to pattern the Au electrode, following the same procedure as for ITO. The results confirm that the self-compliance behavior is indeed due to the internal ohmic resistance of the HE-PBA, as self-compliance is maintained even in the absence of ITO (**Figure 7.16b**). Additionally, *I–V* measurements were performed in the LRS, with the applied voltage kept well below V_{SET} to avoid triggering resistive switching. The resulting curve

(**Figure 7.16c**) crosses the origin and displays a steeper slope, indicating lower resistivity and more metallic-like conduction, consistent with the earlier discussions. However, it was also noted that the self-compliance current in the Ag/HE-PBA/Au configuration is relatively large, necessitating external CC in some cases to reduce power consumption and protect the device, especially during consecutive cycles. This observation suggests that the role of ITO in the self-compliance mechanism cannot be entirely discounted, likely due to the higher conductivity of Au, which increases the demand for external CC. Nevertheless, the internal ohmic resistance of the HE-PBAs plays a significant role in the self-compliance behavior, particularly in the Ag/HE-PBA/ITO configuration.

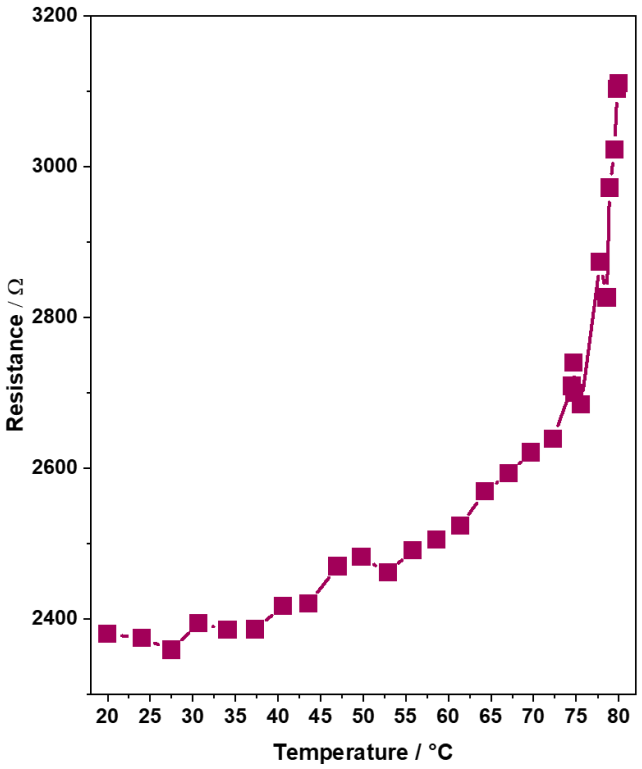

Figure 7.15. Temperature dependence of electrical resistance in the LRS of device.

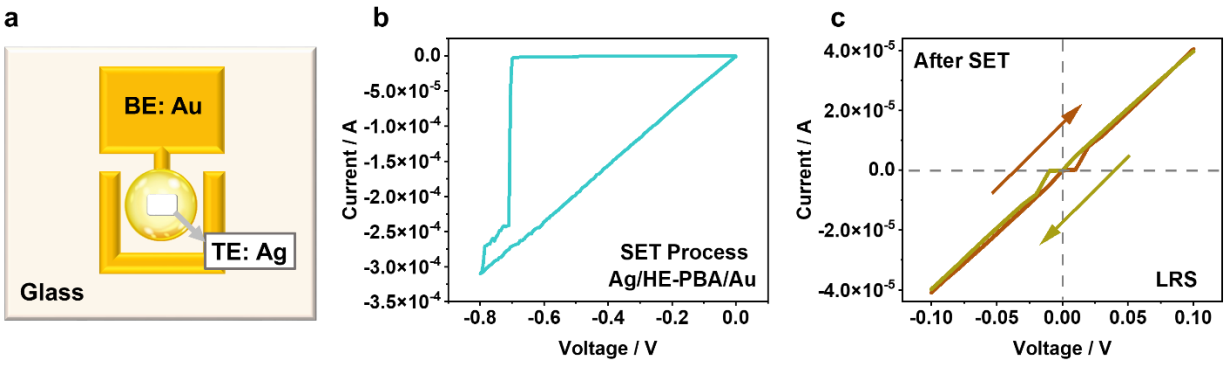

Figure 7.16. (a) Schematic of the Ag/HE-PBA/Au device. (b) SET process displayed by *I–V* curves. (c) *I–V* measurements in the LRS, with a maximum applied voltage well below V_{SET}.

Typically, internal ohmic conduction arises from the movement of mobile electrons in the conduction band and holes in the valence band.[268] The RS devices using insertion materials usually relies on ion-modulated electronic conductivity,[32,250] as the insertion or extraction of highly mobile ions often generates nearly free electrons or holes in the conduction or valence bands.[269,270] Na^+ ions certainly exhibit significant mobility within PBAs. As illustrated in **Figure 7.14f**, the open 3D framework structure of HE-PBAs provides large interstitial sites (~4.6 Å in diameter) where can accommodate large ions (Na^+: 1.02 Å in radii), as well spacious channels,[44,46] which enables rapid solid-state diffusion of various carrier ions. This property has been well-established through extensive research, particularly in the context of advanced SIBs, where the efficient transport of Na^+ ions is crucial for performance.[75,166] To thoroughly understand the working mechanism of the Ag/HE-PBA/ITO memristor, it is essential to investigate the Na^+ ion transport processes within the device.

More specifically, applying a negative voltage to the Ag electrode is expected to drive the positively charged Na^+ ions towards the TE under the influence of the electric field (see **Figure 7.14h**). This movement results in the oxidation of low-valence metal ions (Fe^{2+}, Mn^{2+}, Co^{2+}, etc.) to maintain the charge neutrality of the HE-PBA. Ag-based electrodes have been extensively studied for rechargeable lithium and sodium batteries, owing to their high conductivity, excellent mechanical flexibility, and inherent affinity for lithium and sodium (lithophilicity/sodiophilicity).[271–273] Therefore, it is proposed that the sodiophilic nature of the Ag electrode is crucial in facilitating the accommodation and diffusion of Na^+ ions under the influence of an electric field. Once a Na-Ag network forms at the interface due

to the intrinsic sodiophilicity of silver nanoparticles, Na^+ ions become effectively trapped and cannot easily return without the application of an external electric field. This could explain the excellent retention stability of over 4 $\times 10^4$ s as non-volatile memory for the device (see **Figure 7.8d**). Furthermore, when the polarity is switched to a positive potential, Na^+ ions reinsert back into the HE-PBA, which is reflected in a similar *I-V* curve to the initial state as well (see **Figure 7.14e** and **i)**. It is reasonable to assume that the diffusion of Na^+ ions, resulting in a Na deficiency in HE-PBA, combined with an applied potential generating an electric field across the device, can induce a change in conductivity. This suggests a bulk reaction throughout the HE-PBA layer, rather than the formation of a conducting filament as commonly observed in many filamentary memristive devices.[246]

Table 7.5. Calculated reaction enthalpies from DFT. ΔH_1 and ΔH_2 is the reaction enthalpies calculated from **Equation 7.1** and **7.2**, respectively. The mean voltage is calculated from $\bar{V} = \frac{\Delta H}{(x_1 - x_2)F}$, where *F* is the Faraday constant.

x_1	x_2	ΔH_1 (kJ/mol)	Mean voltage ($\bar{V}_1$)	ΔH_2 (kJ/mol)	Mean voltage ($\bar{V}_2$)
1.3750	1.3125	13.17	2.18	3.29	0.54
1.3125	1.2500	14.12	2.34	4.24	0.70
1.2500	1.0000	57.47	2.38	17.95	0.74

As mentioned above, it is hypothesized that upon applying a bias voltage of –0.4 V, Na^+ ions migrate towards the Ag electrode, thereby inducing conductivity in the system. To gain deeper insights into this mechanism, DFT calculations on HE-PBA with varying Na concentrations were conducted. Initially, it was essential to determine the critical Na concentration in HE-PBA where a transition from an insulating to a conducting state occurs. Using DFT calculations, it is determined that the reaction enthalpy (ΔH) associated with the changes in HE-PBA during the SET and RESET processes. It was

found that the Na concentration under experimental conditions at the given potentials ranged between 1.375 and 1 Na. This calculation was performed using the following chemical reaction:

$$Na_{x_1}Mn_{0.3}Fe_{0.3}Co_{0.133}Ni_{0.133}Cu_{0.133}[Fe(CN)_6] \rightarrow$$

$$Na_{x_2}Mn_{0.3}Fe_{0.3}Co_{0.133}Ni_{0.133}Cu_{0.133}[Fe(CN)_6] + (x_1 - x_2)Na \quad \textbf{Equation 7.1}$$

In this equation, x_1 represents the initial number of sodium ions intercalated into the crystal lattice, while x_2 denotes the number of sodium ions remaining in the lattice after the reaction. The difference ($x_1 - x_2$) corresponds to the number of sodium ions released from the lattice, which then forms sodium metal. The findings in **Table 7.5** highlight notable reaction enthalpies (ΔH_1) observed during the Na removal process across all examined concentrations, yielding an average voltage $\bar{V}_1$ (2.3 V) that exceeds the experimental average resistive switching voltage of V_{SET} (–0.26 V) and V_{RESET} (0.36 V). However, the depicted reaction illustrates an extreme scenario where Na is completely extracted from HE-PBA to form Na metal. The lower V_{SET} observed compared to the mean voltage derived from DFT calculations suggests that not all Na atoms are fully extracted from HE-PBA during the experiment. Instead, our hypothesis suggests that Na atoms initiate diffusion towards the Ag electrode under the applied electric field, where they adsorb at the Ag|HE-PBA interface. The reaction enthalpy (ΔH_2) for such a process is calculated considering the following reaction:

$$Na_{x_1}Mn_{0.3}Fe_{0.3}Co_{0.133}Ni_{0.133}Cu_{0.133}[Fe(CN)_6] + Ag \rightarrow$$

$$Na_{x_2}Mn_{0.3}Fe_{0.3}Co_{0.133}Ni_{0.133}Cu_{0.133}[Fe(CN)_6] + (x_1 - x_2)Na|Ag \quad \textbf{Equation 7.2}$$

In this equation, an Ag metal surface was employed where Na and Ag could interact, represented as Na|Ag. A suitable methodology was employed to calculate the adsorption of Na on the (100), (110), and (111) crystal planes of silver metal,[273] considering the average binding energies. After considering the binding effects detailed in **Table 7.5**, the reaction enthalpy notably decreases, resulting in an average voltage $\bar{V}_2$ of 0.66 V that closely matches the experimental V_{SET} and V_{RESET} values. The minor deviation between our theoretical predictions and experimental results could be attributed to the constraints of our current simplified model. While the model aims to simulate Na adsorption on the Ag electrode, it inherently oversimplifies the structure and interactions. Specifically, the model does not fully encompass the intricate and potentially infinite characteristics of the Ag crystal planes, nor does it comprehensively account for the complex interactions between Na and Ag. These

simplifications could be key factors contributing to the observed differences.[273] However, according to DFT results, Na atoms are not entirely extracted from HE-PBA to form Na metal. Instead, they are likely to bind at the interface with the Ag electrode, leading to a bulk transformation in HE-PBA. This characteristic contributes to the device's low power consumption and non-volatile nature. Moreover, previous molecular dynamic simulations have demonstrated the formation of a complex Na-Ag network at this interface.[273] In contrast to the findings of Nguyen *et al.*,[249] who demonstrated the migration of lithium from Li_xCoO_2 films into the silicon electrode in RS devices, our study proposes an alternative mechanism. Here, sodium atoms do not fully extract but instead diffuse towards and adsorb onto the Ag electrode.

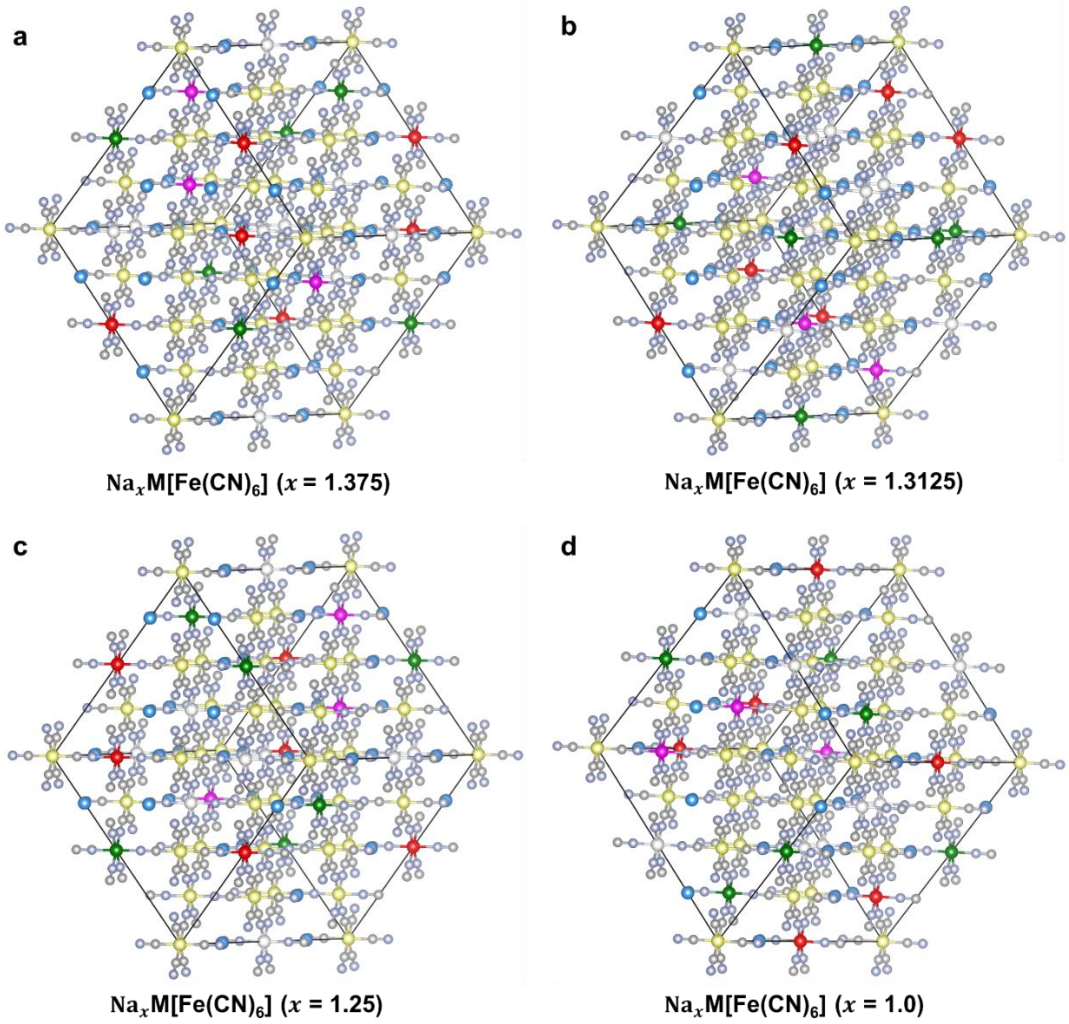

Figure 7.17. (a-d) Crystal structures of $Na_xM[Fe(CN)_6]$ with x = 1.375, 1.3125, 1.25 and 1.0.

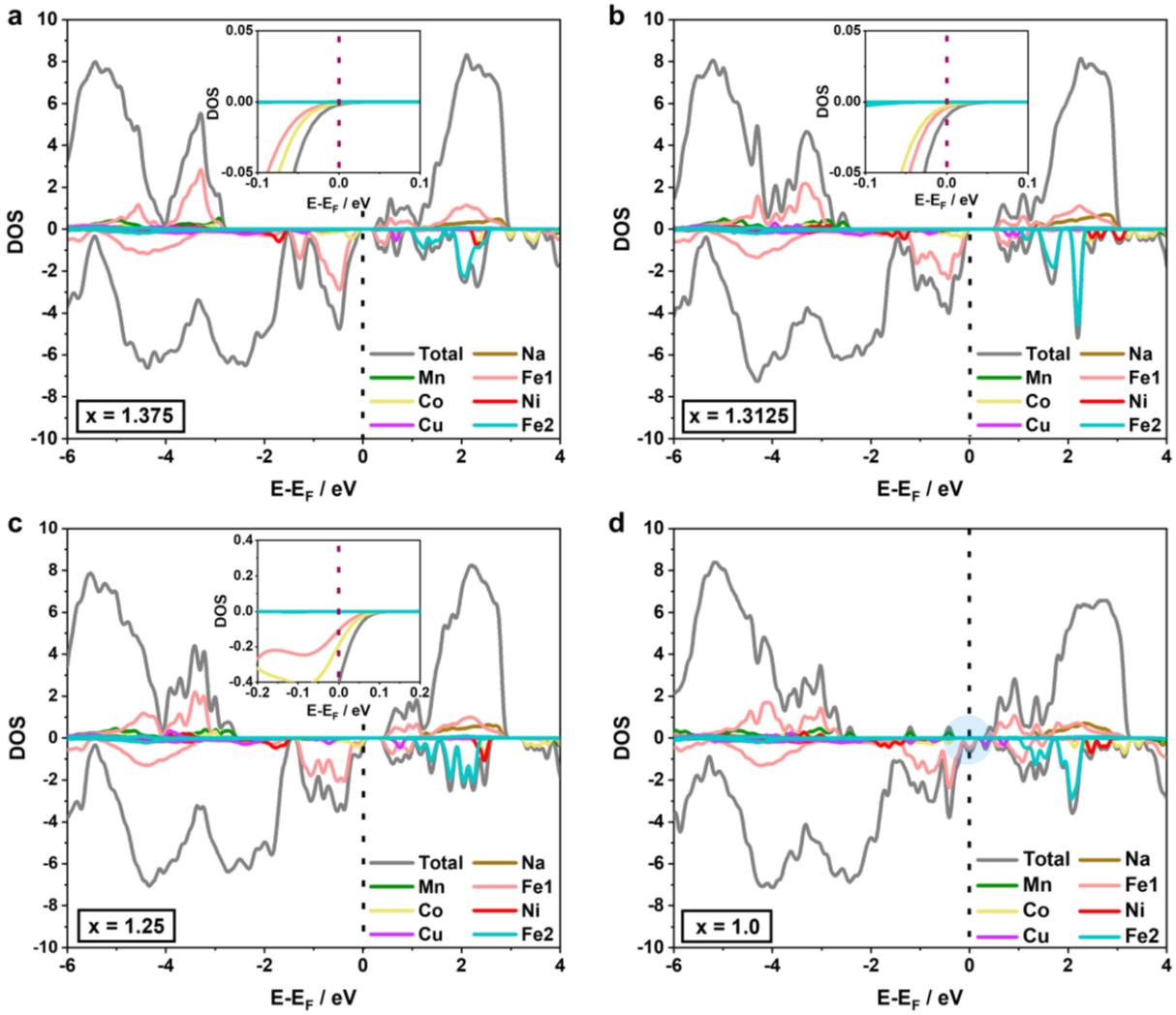

Figure 7.18. Total and projected DOS of $Na_xM[Fe(CN)_6]$ with (a) x = 1.375, (b) x = 1.3125, (c) x = 1.25 and (d) x = 1.0, with the Fermi energy is shift to 0. Panels (a), (b) and (c) include detailed zoom-in of the DOS near the Fermi energy. Fe_1 and Fe_2 denote the C-coordinated and N-coordinated Fe, respectively.

Using additional DFT calculations, the transition between the insulating and conducting states was explored within crucial concentration ranges of HE-PBA, specifically between 1.375 and 1.0. This range was selected based on previous findings that Li_xCoO_2 transitions from a ceramic to a metallic state with a minor adjustment in composition from x = 1 to x = 0.94.[84] Similarly, it is speculated that HE-PBA would demonstrate comparable behavior. Thus, the investigation concentrated on concentrations surrounding the synthesized compound's concentration, ranging from Na = 1.375 down to 1.0. **Figure 7.17** depicts the corresponding crystal structures with x = 1.375, 1.3125, 1.25 and 1.0 in $Na_xM[Fe(CN)_6]$. Considering that changes in Na content directly affect the electronic conductivity of

the Ag/HE-PBA/ITO device, the electronic structure of HE-PBA was investigated by analyzing the total and projected density of states (pDOS) for $Na_xM[Fe(CN)_6]$ with varying Na concentrations, as shown in **Figure 7.18**.

The results show there is a noticeable overlap of minor states related to Co and C-coordinated Fe (Fe_1) with the Fermi energy level at a Na concentration of 1.3125, as illustrated in the zoomed-in view in **Figure 7.18b**. This overlap leads to an increased density of states at the Fermi level, thereby enhancing the availability of charge carriers. At room temperature, electrons can easily transition to these states, functioning as free carriers capable of unrestricted movement within the material, thereby enhancing its electrical conductivity. The collective electronic system and density of states depicted in **Figure 7.18b** arise from interactions among the various elements within the high-entropy material. These so called cocktail effect seem significantly impact the electronic band structure, facilitating the overlapping of Fe_1 and Co states to impart electrical conductivity to the material. This effect becomes more prominent at x = 1.25 (see **Figure 7.18c**), where a significant increase in the density of states near the Fermi level indicates a transition to a metallic-like state. This transition suggests an expected enhancement in electrical conductivity. With a further reduction in Na content, such as x = 1.0 (see **Figure 7.18d**), the density of states at the Fermi energy level increases markedly, signifying a stronger metallic character. This slight decrease in sodium concentration seems sufficient to significantly alter the electrical properties of the films.[249] This phenomenon has been observed, for example, in Li_xCoO_2, where studies indicate a transition from nonmetallic to metallic behavior as lithium-ion concentration decreases.[274–276] In summary, the DFT results suggest that the Ag/HE-PBA/ITO device utilizes a low-energy Na-ion insertion/extraction process coordinated with the Ag electrode. Specifically, this process sustains non-volatile resistance switching through an insulating-to-metallic transition as the sodium-ion concentration decreases. This mechanism aligns well with the experimental findings presented.

To eliminate any potential influence of Ag metal filaments on the RS behavior of HE-PBA-based memristors, Pt and Au were also tested as inert TEs in place of Ag. However, when utilizing the reported DI water-based Pt ink,[277] a hole formed in the center of the HE-PBA film, likely due to the solvent dispersing the HE-PBA, which relies on the same solvent used in its preparation, as shown in

Figure 7.19. Moreover, the curing temperature for Au ink typically exceeds 200 °C, a temperature at which phase transitions and structural degradation of HE-PBA take place.[177] To address this, ~100 nm of Au was sputtered onto the surface of the HE-PBA layer (**Figure 7.20a**). Due to challenges in precisely controlling the sputtering area, a large HE-PBA film was prepared, and tape was used to isolate the Au deposition. Despite these difficulties, the device demonstrates self-compliance behavior, regardless of whether positive or negative voltages are applied to the Au electrode (**Figure 7.20b**). Because of the relatively high self-compliance of around 4 mA observed with the sputtered TE, an external CC of 0.3 mA was utilized to lower power consumption and protect the device. The Au/HE-PBA/ITO device demonstrated a switching voltage of approximately 1.5 V, exhibiting consistent switching behavior over 30 cycles and achieving an R_{OFF}/R_{ON} ratio greater than 10^2 (**Figure 7.20c**, **d**). These results indicate that Ag metal filaments are not mainly responsible for the device's RS behavior, as it functions effectively without Ag as TE, despite some small fluctuations observed between HRS and LRS (**Figure 7.20e**).

The application of a negative voltage to the Ag/HE-PBA/ITO device does not result in the formation of Ag metal filaments, as the electric field is oriented from the ITO to the Ag electrode. However, while the potential for Ag filament accumulation cannot be completely dismissed when a positive voltage is applied to initiate the RESET process—potentially affecting device performance—this risk persists even at low applied voltages (0.5 V) during pulsed operation. However, the formation of Ag conducting filaments extending from the ITO to the Ag electrode is unlikely at such a low positive voltage, as this process typically requires a significantly higher electroforming voltage, often exceeding 1 V or several volts.[278] This is further substantiated by **Table 7.6**, which compares the electroforming voltages of various memristors. The movement of vacancies in MOFs is either not feasible or can be regarded as equivalent to the proposed mechanism, since both ions and vacancies/holes are involved. This mechanism is also corroborated by literature studies,[249,279] which report the use of insertion materials to fabricate memristors with mechanisms similar to the one presented here. The high-entropy MOF utilized in this chapter can serve as an insertion-type electrode, facilitating Na^+ transport, which suggests that the mechanism is likely analogous to those previously reported.

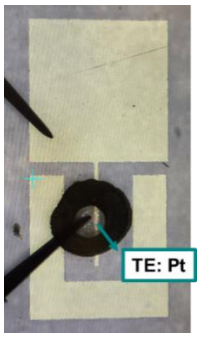

Figure 7.19. Using DI water-based Pt ink resulted in a hole in the HE-PBA film due to solvent incompatibility.

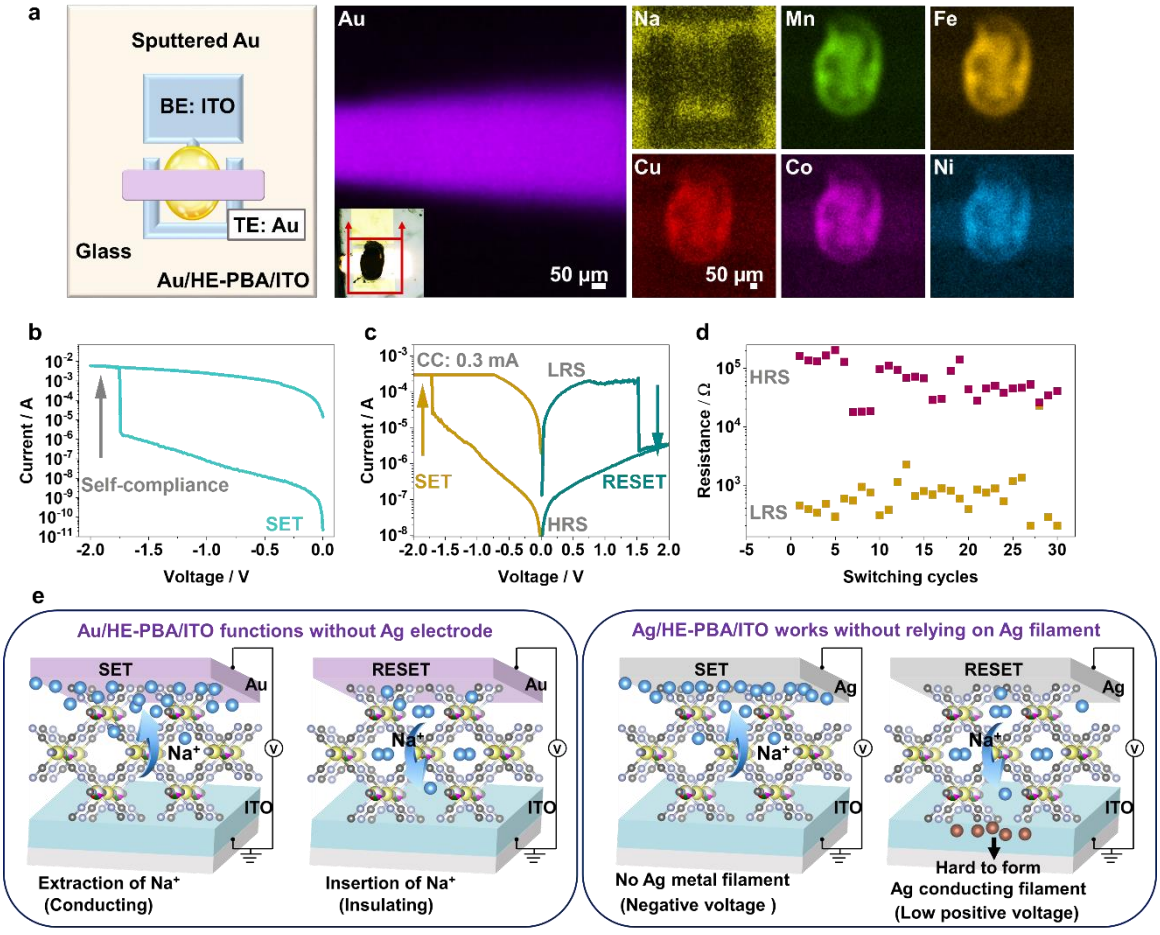

Figure 7.20. (a) Schematic and elemental distribution of the Au/HE-PBA/ITO device, showcasing sputtered Au as TE. Electric characterization of the device: (b) self-compliance behavior, (c) initial *I–V* curve and (d) endurance over 30 sweeping cycles. (e) Corresponding schematic representations of the resistive switching mechanism.

Table 7.6. Comparison of electroforming voltages for various memristors.

Ref.	TE/storage layer/BE	Storage layer thickness (nm)	Electroforming sweeping voltage (V)
[278]	$Ag/WO_{3-x}/Au$	600	$0 \rightarrow 5 \rightarrow 0$
[280]	Ag/MAPI/FTO	500	$0 \rightarrow 5 \rightarrow 0$
[281]	$Ag/HfO_2/Pt$	15	$0 \rightarrow 1 \rightarrow 0$
[282]	$Ag/AIST/MAPbI_3/FTO$	40/500	$0 \rightarrow 10 \rightarrow 0$
[283]	$Ta/Ta_2O_{5-x}/$ Pd	3.5	$0 \rightarrow 1.5 \rightarrow 0$
[284]	$Ag/Al_2O_3/PVA/ITO$	17/6	$0 \rightarrow 2 \rightarrow 0$
[285]	$Pt/Nb/Nb_2O_5/Pt$	30/12	$0 \rightarrow 5 \rightarrow 0$
[286]	$Pt/Cu_{0.1}Te_{0.9}/HfO_2/Pt$	40/10	$0 \rightarrow 4.5 \rightarrow 0$

Finally, the device exhibits promising non-volatile resistive switching performance; however, further enhancements are required, as discussed herein. The endurance data (**Figures 7.8c** and **7.13**) indicate that the LRS is more stable with reduced fluctuations, suggesting that Na^+ extraction is relatively facile, while the insertion process poses greater challenges. Several factors may influence this behavior, including the structural properties of the active layer (such as thickness, morphology, and intrinsic defects), ion mobility (kinetics), and the potential accumulation of Ag metal filaments. The thickness and quality of the active layer are critical factors in ensuring stable HRS and LRS, as indicated in other studies.[267] In the current study, the particle size of the HE-PBA, which ranges from 100 to 300 nm, presents challenges in forming dense films and achieving precise control over layer thickness. Increased film thickness may impede ion transport, resulting in fluctuations in the HRS and LRS. Enhancing the performance of the HE-PBA-based memristors by minimizing fluctuations between HRS and LRS, while maintaining low power consumption through optimized applied voltages and active layer thickness, is feasible, as illustrated in **Figure 7.21**. Nevertheless, further enhancements in cycling stability are essential for practical applications. A thorough investigation of alternative

electrodes may yield valuable opportunities to improve the device's long-term stability. In summary, this chapter proposes that Na^+ triggers the resistive switching—rather than relying on the formation/rupture of Ag conducting filaments—making the device promising as a non-volatile memristor with low power consumption.

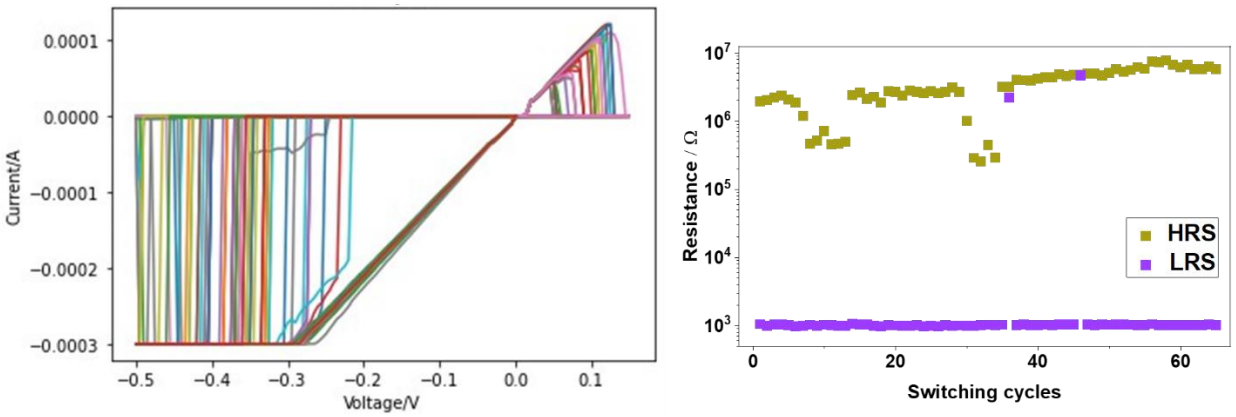

Figure 7.21. Improved *I–V* curve and corresponding endurance over 70 sweeping cycles.

Part IV. Summary and Outlook

8. Summary

HEMs are increasingly used in various applications, offering unexpected and diverse functionalities due to their customizable and adaptable compositions. In this dissertation, the high-entropy approach was applied to PBAs to develop a series of advanced insertion materials. These materials were evaluated for their potential use in SIBs and memristors, addressing various challenges in the development of long-life secondary batteries and advanced resistive switching devices. The ability to tailor properties through high-entropy design has expanded the potential applications of PBAs. This dissertation demonstrates that HEPBAs are suitable not only for energy storage devices like SIBs but also hold promise for emerging technologies such as memristors. The highlights of the dissertation are summarized as follows:

In the first section, the application of high entropy to PWs, a member of the PBA family, was evaluated by studying a series of Mn-based monoclinic PW cathode materials incorporating up to six different transition metals. The high-entropy PW, with ΔS_{conf} of 1.64 R, demonstrated superior long-life sodium storage properties, retaining a stable capacity significantly enhanced compared to medium-entropy (ΔS_{conf} = 1.32 R), low-entropy (ΔS_{conf} = 0.82 R), and conventional Mn-PW (ΔS_{conf} = 0 R) materials. Through a series of complementary experiments and simulation studies, this dissertation elucidated the mechanisms underlying the enhanced performance of HEMs. It was found that incorporating a high-entropy approach can suppress unfavorable phase transitions and mitigate side reactions that contribute to gas evolution during cycling. These effects are intrinsic to the improved structural integrity and cycling stability. Furthermore, the findings demonstrate the positive impact of increased entropy on structural evolution and electrochemical behavior, confirming for the first time the preference of HEMs for high-symmetry structures during battery cycling.

In the second section, a combination of high-entropy and crystal structure engineering was first introduced into PBAs to systematically investigate the effect of configurational entropy on PBAs with distinct structural differences. The resulting cubic and monoclinic HEPBAs, with similar configurational entropy, stoichiometry and elemental composition, were systematically investigated to analyze the performance of Na-ion electrodes only differing in the crystal structure (monoclinic and cubic). The cubic structural HEPBA has structural stability advantages, which lead to high reversibility,

excellent thermal stability, unprecedented endurance for high-voltage (4.5 V) and a nearly zero-structural distortion after 15000 cycles. These findings show a broad application prospect in secondary batteries, especially for fast charging batteries. Conversely, a significantly impaired performance of Mono-HEPBAs was observed, highlighting that the original structure is crucial for cycling, even with similar stoichiometries and configurational entropies. This investigation reveals a significant observation, underscoring the preference for highly symmetric HEMs during cycling and elucidating the complex relationship between structural characteristics and performance.

In the third section, a Na^+-modulated non-volatile printed memristor based on a high-entropy PBA material with the structure Ag/$Na_{1.38}Mn_{0.3}Fe_{0.3}Co_{0.133}Ni_{0.133}Cu_{0.133}[Fe(CN)_6]_{0.84}\square_{0.16}$ (HE-PBA)/ITO was present. The device presents considerable benefits, such as low power consumption, self-compliance, and a forming-free behavior in memristor applications. In the printed Ag/HE-PBA/ITO device, metallic behavior is observed in the low resistive state, while insulating behavior is noted in the high resistive state. A series of complementary experiments and simulation studies demonstrate that the insulating-to-metallic transition is driven by the extraction and insertion of Na ions, rather than the formation and rupture of Ag conductive filaments. Leveraging the low-energy processes associated with Na-ion insertion and extraction at the Ag electrode, the Ag/HE-PBA/ITO device exhibits robust retention stability, low operation voltage and a high R_{OFF}/R_{ON} ratio, promising characteristic of non-volatile memristors. This dissertation highlights the promise of high-entropy insertion materials in the development of printed memristors featuring a unique operational mechanism.

9. Outlook

The high-entropy approach endows PBAs with unique advantages. For instance, the robust structure of HEPBAs makes them suitable as cathode materials for SIBs applications. Additionally, their use as an active layer in memristors demonstrates non-volatile storage and low-energy consumption features. However, there are still room to further explore HEPBAs' potential as advanced materials.

There is ongoing development in the field of solid-state SIBs. These batteries are gaining attention because they offer a pathway to safer rechargeable battery technology by replacing flammable liquid electrolytes with solid alternatives. HEPBAs hold potential as effective cathode materials in solid-state battery applications. Their robust structure and unique properties make them particularly suitable for enhancing the safety, efficiency, and performance of next-generation energy storage devices.

Secondly, the field of pouch cells is another area slated for exploration and contribution. Pouch bag cells are a specific type of battery design that is widely used in commercial applications due to their practicality and scalability. They are characterized by a flexible, pouch-like packaging that accommodates the battery components and electrolytes. This design is particularly advantageous for maximizing space utilization and energy density while maintaining a compact form factor. In the realm of SIBs, pouch bag cells represent an area that has received relatively less attention compared to other battery formats. Most research in SIBs has focused on fundamental materials and cell designs, often using traditional configurations. However, as the demand for safer and more efficient energy storage solutions grows, there is increasing interest in exploring novel electrode materials like HEPBAs. Therefore, the exploration of HEPBAs in pouch bag cells represents a critical step towards advancing SIBs technology from laboratory-scale demonstrations to larger-scale commercialization. It involves assessing their compatibility with existing battery manufacturing processes, optimizing their electrochemical performance, and ultimately, validating their suitability for widespread adoption in various energy storage applications

Finally, integrating HEPBAs into memristors represents an initial step, marking the beginning of exploration into their potential applications. Memristors, as electronic devices, hold significant promise due to their ability to store information based on resistance changes and their potential for use in advanced computing technologies. The underlying mechanisms of HEPBAs in memristors warrant

further investigation. These materials exhibit unique properties such as robustness, non-volatility, and low energy consumption, which are advantageous for memristor applications. Understanding how HEPBAs interact at the atomic and electronic levels within the memristor structure can provide insights into enhancing device performance and reliability. Optimizing the performance of HEPBA-based memristors holds great promise. By fine-tuning the composition, structure, and fabrication techniques, researchers aim to maximize their storage capabilities and operational efficiency. This optimization is crucial in meeting the increasing demands of the current era of Big Data, where the AI and IoT require efficient processing and storage of massive datasets. The potential for developing next-generation memristors with superior storage abilities using HEPBAs is particularly exciting. These devices could revolutionize data processing technologies by offering enhanced speed, energy efficiency, and scalability compared to conventional memory technologies. Therefore, continued research and development efforts in this area are essential to unlock the full potential of HEPBAs in advancing memristor technology for future applications in AI, IoT, and beyond.

Part V. Index and Reference

10. List of Tables

11. List of Figures

12. References

[1] Y. Liang, C. Zhao, H. Yuan, Y. Chen, W. Zhang, J. Huang, D. Yu, Y. Liu, M. Titirici, Y. Chueh, H. Yu, Q. Zhang, *InfoMat* **2019**, *1*, 6–32.

[2] D. Larcher, J.-M. Tarascon, *Nat. Chem.* **2015**, *7*, 19–29.

[3] P. K. Nayak, L. Yang, W. Brehm, P. Adelhelm, *Angew. Chem. Int. Ed.* **2018**, *57*, 102–120.

[4] P. Hu, K. E. Aifantis, in *Recharg. Ion Batter.*, Wiley, **2023**, pp. 269–298.

[5] M. Chen, Q. Liu, S. Wang, E. Wang, X. Guo, *Adv. Energy Mater.* **2019**, *9*, 1803609.

[6] J. Xiao, X. Li, K. Tang, D. Wang, M. Long, H. Gao, W. Chen, C. Liu, H. Liu, G. Wang, *Mater. Chem. Front.* **2021**, *5*, 3735–3764.

[7] K. Mizushima, P. C. Jones, P. J. Wiseman, J. B. Goodenough, *Mater. Res. Bull.* **1980**, *15*, 783–789.

[8] L. Chua, *IEEE Trans. Circuit Theory* **1971**, *18*, 507–519.

[9] E. Carlos, R. Branquinho, R. Martins, A. Kiazadeh, E. Fortunato, *Adv. Mater.* **2021**, *33*, 2004328.

[10] D. Ielmini, R. Waser, *Resistive Switching: From Fundamentals of Nanoionic Redox Processes to Memristive Device Applications*, John Wiley & Sons, **2015**.

[11] M. Lanza, H.-S. P. Wong, E. Pop, D. Ielmini, D. Strukov, B. C. Regan, L. Larcher, M. A. Villena, J. J. Yang, L. Goux, A. Belmonte, Y. Yang, F. M. Puglisi, J. Kang, B. Magyari-Köpe, E. Yalon, A. Kenyon, M. Buckwell, A. Mehonic, A. Shluger, H. Li, T. Hou, B. Hudec, D. Akinwande, R. Ge, S. Ambrogio, J. B. Roldan, E. Miranda, J. Suñe, K. L. Pey, X. Wu, N. Raghavan, E. Wu, W. D. Lu, G. Navarro, W. Zhang, H. Wu, R. Li, A. Holleitner, U. Wurstbauer, M. C. Lemme, M. Liu, S. Long, Q. Liu, H. Lv, A. Padovani, P. Pavan, I. Valov, X. Jing, T. Han, K. Zhu, S. Chen, F. Hui, Y. Shi, *Adv. Electron. Mater.* **2019**, *5*, 1800143.

[12] T. W. Hickmott, *J. Appl. Phys.* **1962**, *33*, 2669–2682.

[13] M. Song, J. Kang, X. Zhang, W. Ji, A. Ascoli, I. Messaris, A. S. Demirkol, B. Dong, S. Aggarwal, W. Wan, S. Hong, S. G. Cardwell, I. Boybat, J. Seo, J. Lee, M. Lanza, H. Yeon, M. Onen, J. Li, B. Yildiz, J. A. del Alamo, S. Kim, S. Choi, G. Milano, C. Ricciardi, L. Alff, Y. Chai, Z. Wang, H. Bhaskaran, M. C. Hersam, D. Strukov, H.-S. P. Wong, I. Valov, B. Gao, H. Wu, R. Tetzlaff, A. Sebastian, W. Lu, L. Chua, J. J. Yang, J. Kim, *ACS Nano* **2023**, *17*, 11994–12039.

[14] Y. Liu, X. Li, H. Zheng, N. Chen, X. Wang, X. Zhang, H. Sun, S. Zhang, *Adv. Funct. Mater.* **2021**, *31*, 2009803.

[15] S. Han, Y. Zhou, V. A. L. Roy, *Adv. Mater.* **2013**, *25*, 5425–5449.

[16] A. Sebastian, M. Le Gallo, R. Khaddam-Aljameh, E. Eleftheriou, *Nat. Nanotechnol.* **2020**, *15*, 529–544.

[17] Y. Yang, P. Gao, L. Li, X. Pan, S. Tappertzhofen, S. Choi, R. Waser, I. Valov, W. D. Lu, *Nat. Commun.* **2014**, *5*, 4232.

[18] C. Y. Chen, L. Goux, A. Fantini, S. Clima, R. Degraeve, A. Redolfi, Y. Y. Chen, G. Groeseneken, M. Jurczak, *Appl. Phys. Lett.* **2015**, *106*, 053501.

[19] Y. Lin, F. Meng, T. Zeng, Q. Zhang, Z. Wang, Y. Cheng, X. Zhao, L. Gu, H. Xu, Y. Liu, *Adv. Funct. Mater.* **2023**, *33*, 2302787.

[20] R. Marquardt, F. Zahari, J. Carstensen, G. Popkirov, O. Gronenberg, G. Kolhatkar, H. Kohlstedt, M. Ziegler, *Adv. Electron. Mater.* **2023**, *9*, 2201227.

[21] Y. Abbas, S. M. Ansari, I. Taha, H. Abunahla, M. U. Khan, M. Rezeq, H. M. Aldosari, B. Mohammad, *Adv. Funct. Mater.* **2024**, *34*, 2214615.

[22] M. D. Tran, H. Kim, J. S. Kim, M. H. Doan, T. K. Chau, Q. A. Vu, J. Kim, Y. H. Lee, *Adv. Mater.* **2019**, *31*, 1807075.

[23] S. Batool, M. Idrees, S.-R. Zhang, S.-T. Han, Y. Zhou, *Nanoscale Horizons* **2022**, *7*, 480–507.

[24] S. P. Rath, D. Thompson, S. Goswami, S. Goswami, *Adv. Mater.* **2023**, *35*, 2204551.

[25] E. J. Yoo, M. Lyu, J.-H. Yun, C. J. Kang, Y. J. Choi, L. Wang, *Adv. Mater.* **2015**, *27*, 6170–6175.

[26] J. H. Heo, D. H. Shin, S. H. Moon, M. H. Lee, D. H. Kim, S. H. Oh, W. Jo, S. H. Im, *Sci. Rep.* **2017**, *7*, 16586.

[27] Y. Lin, X. Zhang, X. Shan, T. Zeng, X. Zhao, Z. Wang, Z. Kang, H. Xu, Y. Liu, *J. Mater. Chem. C* **2020**, *8*, 14789–14795.

[28] C. Li, L. Han, H. Jiang, M.-H. Jang, P. Lin, Q. Wu, M. Barnell, J. J. Yang, H. L. Xin, Q. Xia, *Nat. Commun.* **2017**, *8*, 15666.

[29] H. Yeon, P. Lin, C. Choi, S. H. Tan, Y. Park, D. Lee, J. Lee, F. Xu, B. Gao, H. Wu, H. Qian, Y. Nie, S. Kim, J. Kim, *Nat. Nanotechnol.* **2020**, *15*, 574–579.

[30] C. Chen, Y. C. Yang, F. Zeng, F. Pan, *Appl. Phys. Lett.* **2010**, *97*, 083502.

[31] H.-D. Kim, H.-M. An, S. M. Hong, T. G. Kim, *Phys. status solidi* **2013**, *210*, 1822–1827.

[32] A. Sood, A. D. Poletayev, D. A. Cogswell, P. M. Csernica, J. T. Mefford, D. Fraggedakis, M. F. Toney, A. M. Lindenberg, M. Z. Bazant, W. C. Chueh, *Nat. Rev. Mater.* **2021**, *6*, 847–867.

[33] X. Zhao, Z. Wang, Y. Xie, H. Xu, J. Zhu, X. Zhang, W. Liu, G. Yang, J. Ma, Y. Liu, *Small* **2018**, *14*, 1801325.

[34] H. Abunahla, B. Mohammad, in *Cham, Switz. Springer Int. Publ.*, **2018**.

[35] N. Casa Branca, J. Deuermeier, J. Martins, E. Carlos, M. Pereira, R. Martins, E. Fortunato, A. Kiazadeh, *Adv. Electron. Mater.* **2020**, *6*, 1900958.

[36] H. Hu, A. Scholz, Y. Liu, Y. Tang, G. C. Marques, J. Aghassi-Hagmann, *IEEE Trans. Electron Devices* **2023**, *70*, 3051–3056.

[37] C. Ye, J. Wu, G. He, J. Zhang, T. Deng, P. He, H. Wang, *J. Mater. Sci. Technol.* **2016**, *32*, 1–11.

[38] Z. Zhang, Z. Wang, T. Shi, C. Bi, F. Rao, Y. Cai, Q. Liu, H. Wu, P. Zhou, *InfoMat* **2020**, *2*, 261–290.

[39] J. C. Gonzalez-Rosillo, M. Balaish, Z. D. Hood, N. Nadkarni, D. Fraggedakis, K. J. Kim, K. M. Mullin, R. Pfenninger, M. Z. Bazant, J. L. M. Rupp, *Adv. Mater.* **2020**, *32*, 1907465.

[40] D. Ielmini, R. Bruchhaus, R. Waser, *Phase Transitions* **2011**, *84*, 570–602.

[41] H. Tian, M. Z. Bazant, *Nano Lett.* **2022**, *22*, 5866–5873.

[42] Q. Hu, R. Li, X. Zhang, Q. Gao, M. Wang, H. Shi, Z. Xiao, P. K. Chu, A. Huang, *Sci. Rep.* **2019**, *9*, 5081.

[43] D. A. Cogswell, M. Z. Bazant, *ACS Nano* **2012**, *6*, 2215–2225.

[44] H. Yi, R. Qin, S. Ding, Y. Wang, S. Li, Q. Zhao, F. Pan, *Adv. Funct. Mater.* **2021**, *31*, 2006970.

[45] X. Song, S. Song, D. Wang, H. Zhang, *Small Methods* **2021**, *5*, 2001000.

[46] J. Qian, C. Wu, Y. Cao, Z. Ma, Y. Huang, X. Ai, H. Yang, *Adv. Energy Mater.* **2018**, *8*, 1702619.

[47] Y. Tang, W. Li, P. Feng, M. Zhou, K. Wang, Y. Wang, K. Zaghib, K. Jiang, *Adv. Funct. Mater.* **2020**, *30*, 1908754.

[48] W. J. Li, C. Han, G. Cheng, S. L. Chou, H. K. Liu, S. X. Dou, *Small* **2019**, *15*, 1900470.

[49] T. Shibata, Y. Moritomo, *Chem. Commun.* **2014**, *50*, 12941–12943.

[50] M. Takachi, Y. Fukuzumi, Y. Moritomo, *Dalt. Trans.* **2016**, *45*, 458–461.

[51] Y. Kang, S. Wang, K. S. Hui, H.-F. Li, F. Liang, X.-L. Wu, Q. Zhang, W. Zhou, L. Chen, F. Chen, K. N. Hui, *Mater. Today Energy* **2021**, *20*, 100572.

[52] C. Deng, K. H. Wu, J. Scott, S. Zhu, X. Zheng, R. Amal, D. W. Wang, *ACS Appl. Mater. Interfaces* **2019**, *11*, 9925–9933.

[53] K. W. Chapman, P. D. Southon, C. L. Weeks, C. J. Kepert, *Chem. Commun.* **2005**, 3322–3324.

[54] S. Wu, H. Min, W. Shi, P. Cheng, *Adv. Mater.* **2020**, *32*, 1805871.

[55] S. Ying, C. Chen, J. Wang, C. Lu, T. Liu, Y. Kong, F. Y. Yi, *Chempluschem* **2021**, *86*, 1608–1622.

[56] X. Ma, T. Zhang, X. Wang, T. Zhang, R. Zhang, Z. Xu, M. Ma, Y. Ma, F. Shi, *ACS Appl. Nano Mater.* **2023**, *6*, 22568–22593.

[57] Y. You, X. Wu, Y. Yin, Y. Guo, *Energy Environ. Sci.* **2014**, *7*, 1643–1647.

[58] S. L. Dreyer, F. M. Maddar, A. Kondrakov, J. Janek, I. Hasa, T. Brezesinski, *Batter. Supercaps* **2024**, *7*, e202300595.

[59] H. Pang, Y. Zhang, T. Cheng, W.-Y. Lai, W. Huang, *Nanoscale* **2015**, *7*, 16012–16019.

[60] Y. Lin, L. Zhang, Y. Xiong, T. Wei, Z. Fan, *Energy Environ. Mater.* **2020**, *3*, 323–345.

[61] J. Long, Y. Guari, C. Guérin, J. Larionova, *Dalt. Trans.* **2016**, *45*, 17581–17587.

[62] S. Li, L. Tan, X. Meng, *Adv. Funct. Mater.* **2020**, *30*, 1908924.

[63] W. Cui, T. Hu, X. Bu, *Adv. Mater.* **2020**, *32*, 1806445.

[64] J. Peng, W. Zhang, Q. Liu, J. Wang, S. Chou, H. Liu, S. Dou, *Adv. Mater.* **2022**, *34*, 2108384.

[65] X. Liu, J. Peng, W. Lai, Y. Gao, H. Zhang, L. Li, Y. Qiao, S. Chou, *Adv. Funct. Mater.* **2022**, *32*, 2108616.

[66] L. B. Avila, P. C. Serrano Arambulo, A. Dantas, E. E. Cuevas-Arizaca, D. Kumar, C. K. Müller, *Nanomaterials* **2022**, *12*, 2881.

[67] F. L. Faita, L. B. Avila, J. P. B. Silva, M. H. Boratto, C. C. P. Cid, C. F. O. Graeff, M. J. M. Gomes, C. K. Müller, A. A. Pasa, *J. Alloys Compd.* **2022**, *896*, 162971.

[68] L. Jiang, Y. Lu, C. Zhao, L. Liu, J. Zhang, Q. Zhang, X. Shen, J. Zhao, X. Yu, H. Li, X. Huang, L. Chen, Y. S. Hu, *Nat. Energy* **2019**, *4*, 495–503.

[69] B. Shyam, M. Guo, Y. Wang, L. A. Wray, W. Yang, *J. Mater. Chem. A* **2016**, *4*, 4211–4223.

[70] D. Yang, J. Xu, X. Liao, Y. He, H. Liu, Z. Ma, *Chem. Commun.* **2014**, *50*, 13377–13380.

[71] J. Song, L. Wang, Y. Lu, J. Liu, B. Guo, P. Xiao, J. J. Lee, X. Q. Yang, G. Henkelman, J. B. Goodenough, *J. Am. Chem. Soc.* **2015**, *137*, 2658–2664.

[72] Y. Xu, J. Wan, L. Huang, M. Ou, C. Fan, P. Wei, J. Peng, Y. Liu, Y. Qiu, X. Sun, C. Fang, Q. Li, J. Han, Y. Huang, J. A. Alonso, Y. Zhao, *Adv. Energy Mater.* **2019**, *9*, 1803158.

[73] L. Deng, J. Qu, X. Niu, J. Liu, J. Zhang, Y. Hong, M. Feng, J. Wang, M. Hu, L. Zeng, Q. Zhang, L. Guo, Y. Zhu, *Nat. Commun.* **2021**, *12*, 2167.

[74] Y. Shang, X. Li, J. Song, S. Huang, Z. Yang, Z. J. Xu, H. Y. Yang, *Chem* **2020**, *6*, 1804–1818.

[75] Y. Ma, Y. Ma, S. L. Dreyer, Q. Wang, K. Wang, D. Goonetilleke, A. Omar, D. Mikhailova, H. Hahn, B. Breitung, T. Brezesinski, *Adv. Mater.* **2021**, *33*, 2101342.

[76] J. W. Yeh, S. K. Chen, S. J. Lin, J. Y. Gan, T. S. Chin, T. T. Shun, C. H. Tsau, S. Y. Chang, *Adv. Eng. Mater.* **2004**, *6*, 299–303.

[77] B. Cantor, I. T. H. Chang, P. Knight, A. J. B. Vincent, *Mater. Sci. Eng. A* **2004**, *375–377*, 213–218.

[78] C. M. Rost, E. Sachet, T. Borman, A. Moballegh, E. C. Dickey, D. Hou, J. L. Jones, S. Curtarolo, J.-P. Maria, *Nat. Commun.* **2015**, *6*, 8485.

[79] A. Amiri, R. Shahbazian-Yassar, *J. Mater. Chem. A* **2021**, *9*, 782–823.

[80] C. Oses, C. Toher, S. Curtarolo, *Nat. Rev. Mater.* **2020**, *5*, 295–309.

[81] Y. Yao, Q. Dong, A. Brozena, J. Luo, J. Miao, M. Chi, C. Wang, I. G. Kevrekidis, Z. J. Ren, J. Greeley, G. Wang, A. Anapolsky, L. Hu, *Science.* **2022**, *376*, eabn3103.

[82] Y. Ma, Y. Ma, Q. Wang, S. Schweidler, M. Botros, T. Fu, H. Hahn, T. Brezesinski, B. Breitung, *Energy Environ. Sci.* **2021**, *14*, 2883–2905.

[83] M. C. Gao, D. B. Miracle, D. Maurice, X. Yan, Y. Zhang, J. A. Hawk, *J. Mater. Res.* **2018**, *33*, 3138–3155.

[84] X. Shi, J. Zou, Z. Chen, *Chem. Rev.* **2020**, *120*, 7399–7515.

[85] W. Xu, H. Chen, K. Jie, Z. Yang, T. Li, S. Dai, *Angew. Chem. Int. Ed.* **2019**, *58*, 5018–5022.

[86] T. A. A. Batchelor, J. K. Pedersen, S. H. Winther, I. E. Castelli, K. W. Jacobsen, J. Rossmeisl, *Joule* **2019**, *3*, 834–845.

[87] Q. Wang, A. Sarkar, D. Wang, L. Velasco, R. Azmi, S. S. Bhattacharya, T. Bergfeldt, A. Düvel, P. Heitjans, T.

Brezesinski, H. Hahn, B. Breitung, *Energy Environ. Sci.* **2019**, *12*, 2433–2442.

[88] Y. F. Ye, Q. Wang, J. Lu, C. T. Liu, Y. Yang, *Mater. Today* **2016**, *19*, 349–362.

[89] E. P. George, D. Raabe, R. O. Ritchie, *Nat. Rev. Mater.* **2019**, *4*, 515–534.

[90] X. Wang, W. Guo, Y. Fu, *J. Mater. Chem. A* **2021**, *9*, 663–701.

[91] J. Gild, Y. Zhang, T. Harrington, S. Jiang, T. Hu, M. C. Quinn, W. M. Mellor, N. Zhou, K. Vecchio, J. Luo, *Sci. Rep.* **2016**, *6*, 37946.

[92] X. Yan, L. Constantin, Y. Lu, J. Silvain, M. Nastasi, B. Cui, *J. Am. Ceram. Soc.* **2018**, *101*, 4486–4491.

[93] C. Zhao, F. Ding, Y. Lu, L. Chen, Y. S. Hu, *Angew. Chem. Int. Ed.* **2020**, *59*, 264–269.

[94] A. Sarkar, Q. Wang, A. Schiele, M. R. Chellali, S. S. Bhattacharya, D. Wang, T. Brezesinski, H. Hahn, L. Velasco, B. Breitung, *Adv. Mater.* **2019**, *31*, 1806236.

[95] Z. Lun, B. Ouyang, D.-H. Kwon, Y. Ha, E. E. Foley, T.-Y. Huang, Z. Cai, H. Kim, M. Balasubramanian, Y. Sun, J. Huang, Y. Tian, H. Kim, B. D. McCloskey, W. Yang, R. J. Clément, H. Ji, G. Ceder, *Nat. Mater.* **2021**, *20*, 214–221.

[96] P. Sarker, T. Harrington, C. Toher, C. Oses, M. Samiee, J.-P. Maria, D. W. Brenner, K. S. Vecchio, S. Curtarolo, *Nat. Commun.* **2018**, *9*, 4980.

[97] E. Castle, T. Csanádi, S. Grasso, J. Dusza, M. Reece, *Sci. Rep.* **2018**, *8*, 8609.

[98] T. Jin, X. Sang, R. R. Unocic, R. T. Kinch, X. Liu, J. Hu, H. Liu, S. Dai, *Adv. Mater.* **2018**, *30*, 1707512.

[99] L. Lin, K. Wang, A. Sarkar, C. Njel, G. Karkera, Q. Wang, R. Azmi, M. Fichtner, H. Hahn, S. Schweidler, B. Breitung, *Adv. Energy Mater.* **2022**, *12*, 2103090.

[100] Y. Qin, J.-X. Liu, F. Li, X. Wei, H. Wu, G.-J. Zhang, *J. Adv. Ceram.* **2019**, *8*, 148–152.

[101] Y. Ma, Y. Hu, Y. Pramudya, T. Diemant, Q. Wang, D. Goonetilleke, Y. Tang, B. Zhou, H. Hahn, W. Wenzel, M. Fichtner, Y. Ma, B. Breitung, T. Brezesinski, *Adv. Funct. Mater.* **2022**, *32*, 2202372.

[102] X. Zhao, Z. Xue, W. Chen, Y. Wang, T. Mu, *ChemSusChem* **2020**, *13*, 2038–2042.

[103] M. C. Gao, J. Yeh, P. K. Liaw, Y. Zhang, *High-Entropy Alloys*, Cham: Springer International Publishing, **2016**.

[104] B. S. Murty, J. W. Yeh, S. Ranganathan, in *High Entropy Alloy.* (Eds.: B.S. Murty, J.W. Yeh, S. Ranganathan), Butterworth-Heinemann, Boston, **2014**, pp. 13–35.

[105] A. Manzoor, S. Pandey, D. Chakraborty, S. R. Phillpot, D. S. Aidhy, *npj Comput. Mater.* **2018**, *4*, 47.

[106] D. Ma, B. Grabowski, F. Körmann, J. Neugebauer, D. Raabe, *Acta Mater.* **2015**, *100*, 90–97.

[107] F. Körmann, Y. Ikeda, B. Grabowski, M. H. F. Sluiter, *npj Comput. Mater.* **2017**, *3*, 36.

[108] S. Schweidler, M. Botros, F. Strauss, Q. Wang, Y. Ma, L. Velasco, G. Cadilha Marques, A. Sarkar, C. Kübel, H. Hahn, J. Aghassi-Hagmann, T. Brezesinski, B. Breitung, *Nat. Rev. Mater.* **2024**, *9*, 266–281.

[109] J. W. Yeh, *Ann. Chim. Sci. des Mater.* **2006**, *31*, 633–648.

[110] W. Hsu, C. Tsai, A.-C. Yeh, J. Yeh, *Nat. Rev. Chem.* **2024**, DOI 10.1038/s41570-024-00602-5.

[111] S. Ranganathan, *Curr. Sci.* **2003**, *85*, 1404–1406.

[112] J. Epp, in *Mater. Charact. Using Nondestruct. Eval. Methods* (Eds.: G. Hübschen, I. Altpeter, R. Tschuncky, H.-G.B.T.-M.C.U.N.E. (NDE) M. Herrmann), Elsevier, **2016**, pp. 81–124.

[113] A. A. Bunaciu, E. gabriela Udriştioiu, H. Y. Aboul-Enein, *Crit. Rev. Anal. Chem.* **2015**, *45*, 289–299.

[114] R. E. Dinnebier, S. J. L. Billinge, *Powder Diffraction: Theory and Practice*, Royal Society Of Chemistry, **2008**.

[115] H. Khan, A. S. Yerramilli, A. D'Oliveira, T. L. Alford, D. C. Boffito, G. S. Patience, *Can. J. Chem. Eng.* **2020**, *98*, 1255–1266.

[116] B. Kvamme, *Chem. Thermodyn. Therm. Anal.* **2021**, *1*, 100004.

[117] A. K. Galwey, in *Handb. Therm. Anal. Calorim.*, **2003**, pp. 595–656.

[118] J. I. Goldstein, D. E. Newbury, J. R. Michael, N. W. M. Ritchie, J. H. J. Scott, D. C. Joy, *Scanning Electron Microscopy and X-Ray Microanalysis*, Springer, **2017**.

[119] G. E. Christidis, *Advances in the Characterization of Industrial Minerals*, The Mineralogical Society Of Great Britain And Ireland, **2011**.

[120] L. E. Franken, E. J. Boekema, M. C. A. Stuart, *Adv. Sci.* **2017**, *4*, 1600476.

[121] M. Sardela, *Practical Materials Characterization*, Springer New York, New York, NY, **2014**.

[122] J. M. Zuo, J. C. H. Spence, *Advanced Transmission Electron Microscopy*, Springer, **2017**.

[123] M. C. Biesinger, B. P. Payne, A. P. Grosvenor, L. W. M. Lau, A. R. Gerson, R. S. C. Smart, *Appl. Surf. Sci.* **2011**, *257*, 2717–2730.

[124] M. C. Biesinger, B. P. Payne, A. P. Grosvenor, L. W. M. Lau, A. R. Gerson, R. S. C. Smart, *Appl. Surf. Sci.* **2011**, *257*, 2717–2730.

[125] P. Zimmermann, S. Peredkov, P. M. Abdala, S. DeBeer, M. Tromp, C. Müller, J. A. van Bokhoven, *Coord. Chem. Rev.* **2020**, *423*, 213466.

[126] G. Peng, F. M. F. DeGroot, K. Hámáláinen, J. A. Moore, X. Wang, M. M. Crush, J. B. Hastings, D. P. Siddons, W. H. Armstrong, O. C. Mullins, S. P. Cramer, *J. Am. Chem. Soc.* **1994**, *116*, 2914–2920.

[127] E. P. Jahrman, W. M. Holden, A. S. Ditter, D. R. Mortensen, T. Gerald, T. T. Fister, S. A. Kozimor, L. F. J. Piper, J. Rana, C. Neil, M. C. Stennett, *Rev. Sci. Instrum.* **2019**, *94*, 024106.

[128] B. Ravel, M. Newville, *J. Synchrotron Radiat.* **2005**, *12*, 537–541.

[129] M. Newville, *J. Phys. Conf. Ser.* **2013**, *430*, 012007.

[130] M. Newville, P. Līviņš, Y. Yacoby, J. J. Rehr, E. A. Stern, *Phys. Rev. B* **1993**, *47*, 14126–14131.

[131] S. R. Khan, B. Sharma, P. A. Chawla, R. Bhatia, *Food Anal. Methods* **2022**, *15*, 666–688.

[132] J. W. Olesik, *Anal. Chem.* **2000**, *63*, 12A-21A.

[133] B. B. Berkes, A. Jozwiuk, H. Sommer, T. Brezesinski, J. Janek, *Electrochem. commun.* **2015**, *60*, 64–69.

[134] B. B. Berkes, A. Jozwiuk, M. Vračar, H. Sommer, T. Brezesinski, *Anal. Chem.* **2015**, *87*, 5878−5883.

[135] F. Strauss, J. H. Teo, A. Schiele, T. Bartsch, T. Hatsukade, P. Hartmann, J. Janek, T. Brezesinski, *ACS Appl. Mater. Interfaces* **2020**, *12*, 20462–20468.

[136] Z. Choi, D. Kramer, R. Mönig, *J. Power Sources* **2013**, *240*, 245–251.

[137] M. Janzen, D. Kramer, R. Mönig, *Energy Technol.* **2021**, *9*, 2000867.

[138] G. G. Stoney, *Proc. R. Soc. London. Ser. A, Contain. Pap. a Math. Phys. Character* **1909**, *82*, 172–175.

[139] G. Kresse, J. Furthmüller, *Comput. Mater. Sci.* **1996**, *6*, 15–50.

[140] J. P. Perdew, K. Burke, M. Ernzerhof, *Phys. Rev. Lett.* **1996**, *77*, 3865.

[141] J. P. Perdew, K. Burke, M. Ernzerhof, *Phys. Rev. Lett.* **1997**, *78*, 1396.

[142] P. E. Blöchl, *Phys. Rev. B* **1994**, *50*, 17953.

[143] S. L. Dudarev, G. A. Botton, S. Y. Savrasov, C. J. Humphreys, A. P. Sutton, *Phys. Rev. B* **1998**, *57*, 1505–1509.

[144] A. Jain, G. Hautier, C. J. Moore, S. Ping Ong, C. C. Fischer, T. Mueller, K. A. Persson, G. Ceder, *Comput. Mater. Sci.* **2011**, *50*, 2295–2310.

[145] A. Zunger, S.-H. Wei, L. G. Ferreira, J. E. Bernard, *Phys. Rev. Lett.* **1990**, *65*, 353–356.

[146] A. Van De Walle, M. Asta, G. Ceder, *Calphad* **2002**, *26*, 539–553.

[147] A. Van De Walle, P. Tiwary, M. M. de Jong, D. L. Olmsted, M. D. Asta, A. Dick, D. Shin, Y. Wang, L.-Q. Chen, Z.-K. Liu, *Calphad* **2013**, *42*, 13.

[148] I. Burgués-Ceballos, M. Stella, P. Lacharmoise, E. Martínez-Ferrero, *J. Mater. Chem. A* **2014**, *2*, 17711–17722.

[149] K. Yan, J. Li, L. Pan, Y. Shi, *APL Mater.* **2020**, *8*, 120705.

[150] H. Zhang, X. Ju, Y. Zhou, C. Gu, J. Pan, D. S. Ang, *ACS Appl. Mater. Interfaces* **2019**, *11*, 41490–41496.

[151] G. Ding, Y. Wang, G. Zhang, K. Zhou, K. Zeng, Z. Li, Y. Zhou, C. Zhang, X. Chen, S. T. Han, *Adv. Funct. Mater.* **2019**, *29*, 1806637.

[152] M. Ahn, Y. Park, S. H. Lee, S. Chae, J. Lee, J. T. Heron, E. Kioupakis, W. D. Lu, J. D. Phillips, *Adv. Electron. Mater.* **2021**, *7*, 2001258.

[153] A. D. Nikolov, D. T. Wasan, P. Wu, *Curr. Opin. Colloid Interface Sci.* **2021**, *51*, 101387.

[154] P. Giannozzi, O. Baseggio, P. Bonfà, D. Brunato, R. Car, I. Carnimeo, C. Cavazzoni, S. de Gironcoli, P. Delugas, F. Ferrari Ruffino, A. Ferretti, N. Marzari, I. Timrov, A. Urru, S. Baroni, *J. Chem. Phys.* **2020**, *152*, 154105.

[155] P. Giannozzi, S. Baroni, N. Bonini, M. Calandra, R. Car, C. Cavazzoni, D. Ceresoli, G. L. Chiarotti, M. Cococcioni, I. Dabo, A. Dal Corso, S. de Gironcoli, S. Fabris, G. Fratesi, R. Gebauer, U. Gerstmann, C. Gougoussis, A. Kokalj, M. Lazzeri, L. Martin-Samos, N. Marzari, F. Mauri, R. Mazzarello, S. Paolini, A. Pasquarello, L. Paulatto, C. Sbraccia, S. Scandolo, G. Sclauzero, A. P. Seitsonen, A. Smogunov, P. Umari, R. M. Wentzcovitch, *J. Phys. Condens. Matter* **2009**, *21*, 395502.

[156] J. P. Perdew, A. Ruzsinszky, G. I. Csonka, O. A. Vydrov, G. E. Scuseria, L. A. Constantin, X. Zhou, K. Burke, *Phys. Rev. Lett.* **2008**, *100*, 136406.

[157] P. M. Kowalski, Z. He, O. Cheong, *Front. Energy Res.* **2021**, *9*, 653542.

[158] Y.-Y. Ting, P. M. Kowalski, *Electrochim. Acta* **2023**, *443*, 141912.

[159] D. Vanderbilt, *Phys. Rev. B* **1990**, *41*, 7892–7895.

[160] H. J. Monkhorst, J. D. Pack, *Phys. Rev. B* **1976**, *13*, 5188–5192.

[161] J. C. Wojdeł, I. de P. R. Moreira, S. T. Bromley, F. Illas, *J. Chem. Phys.* **2008**, *128*, 044713.

[162] S. Watanabe, Y. Sawada, M. Nakaya, M. Yoshino, T. Nagasaki, T. Kameyama, T. Torimoto, Y. Inaba, H. Takahashi, K. Takeshita, J. Onoe, *J. Appl. Phys.* **2016**, *119*, 235102.

[163] E. Targholi, S. M. Mousavi-Khoshdel, M. Rahmanifara, M. Z. A. Yahya, *Chem. Phys. Lett.* **2017**, *687*, 244–249.

[164] A. van de Walle, M. Asta, G. Ceder, *Calphad* **2002**, *26*, 539–553.

[165] A. van de Walle, P. Tiwary, M. de Jong, D. L. Olmsted, M. Asta, A. Dick, D. Shin, Y. Wang, L.-Q. Chen, Z.-K. Liu, *Calphad* **2013**, *42*, 13–18.

[166] Y. He, S. L. Dreyer, Y. Ting, Y. Ma, Y. Hu, D. Goonetilleke, Y. Tang, T. Diemant, B. Zhou, P. M. Kowalski, M. Fichtner, H. Hahn, J. Aghassi-Hagmann, T. Brezesinski, B. Breitung, Y. Ma, *Angew. Chem. Int. Ed.* **2024**, *136*, e202315371.

[167] Y. He, S. L. Dreyer, T. Akçay, T. Diemant, R. Mönig, Y. Ma, Y. Tang, H. Wang, J. Lin, S. Schweidler, M. Fichtner, H. Hahn, T. Brezesinski, B. Breitung, Y. Ma, *ACS Nano* **2024**, *18*, 24441–24457.

[168] Y. He, Y. Ting, H. Hu, T. Diemant, Y. Dai, J. Lin, S. Schweidler, G. C. Marques, H. Hahn, Y. Ma, T. Brezesinski, P. M. Kowalski, B. Breitung, J. Aghassi-Hagmann, *Adv. Mater.* **2024**, 2410060.

[169] Q. Liu, Z. Hu, M. Chen, C. Zou, H. Jin, S. Wang, S. L. Chou, Y. Liu, S. X. Dou, *Adv. Funct. Mater.* **2020**, *30*, 1909530.

[170] W. Li, C. Han, W. Wang, Q. Xia, S. Chou, Q. Gu, B. Johannessen, H. K. Liu, S. Dou, *Adv. Energy Mater.* **2020**, *10*, 1903006.

[171] L. Wang, J. Song, R. Qiao, L. A. Wray, M. A. Hossain, Y. De Chuang, W. Yang, Y. Lu, D. Evans, J. J. Lee, S. Vail, X. Zhao, M. Nishijima, S. Kakimoto, J. B. Goodenough, *J. Am. Chem. Soc.* **2015**, *137*, 2548–2554.

[172] Z. Shen, S. Guo, C. Liu, Y. Sun, Z. Chen, J. Tu, S. Liu, J. Cheng, J. Xie, G. Cao, X. Zhao, *ACS Sustain. Chem. Eng.* **2018**, *6*, 16121–16129.

[173] V. Renman, D. O. Ojwang, C. Pay Gómez, T. Gustafsson, K. Edström, G. Svensson, M. Valvo, *J. Phys. Chem. C* **2019**, *123*, 22040–22049.

[174] K. Hurlbutt, S. Wheeler, I. Capone, M. Pasta, *Joule* **2018**, *2*, 1950–1960.

[175] M. Oliver-Tolentino, M. González M., H. Osiry, G. Ramos-Sánchez, I. González, *Dalt. Trans.* **2018**, *47*, 16492–16501.

[176] F. Maddar, A. Menon, K. Gonos, J. Compton, D. Atkinson, L. F. J. Piper, M. Copley, I. Hasa, *ECS Meet. Abstr.* **2022**, *MA2022-02*, 500–500.

[177] W. Wang, Y. Gang, J. Peng, Z. Hu, Z. Yan, W. Lai, Y. Zhu, D. Appadoo, M. Ye, Y. Cao, Q. Gu, H. Liu, S. Dou, S. Chou, *Adv. Funct. Mater.* **2022**, *32*, 2111727.

[178] L. Hartmann, J. Deshmukh, L. Zhang, S. Buchele, M. Metzger, *ECS Meet. Abstr.* **2022**, *MA2022-02*, 459–459.

[179] B. S. Murty, J.-W. Yeh, R. Srikanth, P. P. Bhattacharjee, *High-Entropy Alloys*, Elsevier, **2019**.

[180] M. Giorgetti, M. Berrettoni, *Inorg. Chem.* **2008**, *47*, 6001–6008.

[181] D. Wardecki, D. O. Ojwang, J. Grins, G. Svensson, *Cryst. Growth Des.* **2017**, *17*, 1285–1292.

[182] Y. Liu, D. He, R. Han, G. Wei, Y. Qiao, *Chem. Commun.* **2017**, *53*, 5569–5572.

[183] D. Jiang, Z. Sun, H. Jia, D. Lu, P. Du, *J. Mater. Chem. A* **2016**, *4*, 675–683.

[184] Z. Yan, X. Yu, A. Han, P. Xu, P. Du, *J. Phys. Chem. C* **2014**, *118*, 22896–22903.

[185] X. Zhang, M. Xia, T. Liu, N. Peng, H. Yu, R. Zheng, L. Zhang, M. Shui, J. Shu, *Chem. Eng. J.* **2021**, *421*, 127767.

[186] Y. Huang, M. Xie, J. Zhang, Z. Wang, Y. Jiang, G. Xiao, S. Li, L. Li, F. Wu, R. Chen, *Nano Energy* **2017**, *39*, 273–283.

[187] I. Sarhid, I. Lampre, D. Dragoe, P. Beaunier, B. Palpant, H. Remita, *Materials (Basel).* **2019**, *12*, 3012.

[188] M. Giorgetti, S. Della Longa, M. Benfatto, *J. Phys. Conf. Ser.* **2009**, *190*, 012145.

[189] M. Giorgetti, L. Guadagnini, D. Tonelli, M. Minicucci, G. Aquilanti, *Phys. Chem. Chem. Phys.* **2012**, *14*, 5527.

[190] C. A. Chatzidimitriou-Dreismann, T. Abdul-Redah, B. Kolaric, I. Juranic, *Phys. Rev. Lett.* **2000**, *84*, 5237.

[191] J. Sottmann, F. L. M. Bernal, K. V. Yusenko, M. Herrmann, H. Emerich, D. S. Wragg, S. Margadonna, *Electrochim. Acta* **2016**, *200*, 305–313.

[192] Y. Moritomo, M. Takachi, Y. Kurihara, T. Matsuda, *Adv. Mater. Sci. Eng.* **2013**, *2013*, 967285.

[193] S. Lafuerza, A. Carlantuono, M. Retegan, P. Glatzel, *Inorg. Chem.* **2020**, *59*, 12518–12535.

[194] C. J. Pollock, M. U. Delgado-Jaime, M. Atanasov, F. Neese, S. Debeer, *J. Am. Chem. Soc.* **2014**, *136*, 9453–9463.

[195] U. Bergmann, M. M. Grush, C. R. Horne, P. Demarois, C. F. Yocum, D. W. Wright, C. E. Dube, W. H. Armstrong, G. Christou, H. J. Eppley, S. P. Cramer, *J. Phys. Chem. B* **1998**, *5647*, 8350–8352.

[196] M. A. Beckwith, M. Roemelt, C. Duboc, T. Weng, U. Bergmann, P. Glatzel, F. Neese, S. Debeer, *Inorg. Chem.*

2011, *50*, 8397–8409.

[197] X. Huang, C. Yang, Y. You, *ACS Appl. Energy Mater.* **2022**, *5*, 8123–8131.

[198] X. Bie, K. Kubota, T. Hosaka, K. Chihara, S. Komaba, *J. Power Sources* **2018**, *378*, 322–330.

[199] L. Wang, Y. Lu, J. Liu, M. Xu, J. Cheng, D. Zhang, J. B. Goodenough, *Angew. Chem.* **2013**, *125*, 2018–2021.

[200] D. Yang, J. Xu, X. Z. Liao, Y. S. He, H. Liu, Z. F. Ma, *Chem. Commun.* **2014**, *50*, 13377–13380.

[201] M. Xie, M. Xu, Y. Huang, R. Chen, X. Zhang, L. Li, F. Wu, *Electrochem. Commun.* **2015**, *59*, 91–94.

[202] Z. Wang, Y. Huang, R. Luo, F. Wu, L. Li, M. Xie, J. Huang, R. Chen, *J. Power Sources* **2019**, *436*, 226868.

[203] H. Fu, C. Liu, C. Zhang, W. Ma, K. Wang, Z. Li, X. Lu, G. Cao, *J. Mater. Chem. A* **2017**, *5*, 9604–9610.

[204] S. Yu, Y. Li, Y. Lu, B. Xu, Q. Wang, M. Yan, Y. Jiang, *J. Power Sources* **2015**, *275*, 45–49.

[205] W. Wang, Y. Gang, Z. Hu, Z. Yan, W. Li, Y. Li, Q.-F. Gu, Z. Wang, S.-L. Chou, H.-K. Liu, S.-X. Dou, *Nat. Commun.* **2020**, *11*, 980.

[206] B. Rowden, N. Garcia-Araez, *Energy Reports* **2020**, *6*, 10–18.

[207] S. L. Dreyer, A. Kondrakov, J. Janek, T. Brezesinski, *J. Mater. Res.* **2022**, *37*, 3146–3168.

[208] M. Metzger, B. Strehle, S. Solchenbach, H. A. Gasteiger, *J. Electrochem. Soc.* **2016**, *163*, A1219–A1225.

[209] Y. Yang, E. Liu, X. Yan, C. Ma, W. Wen, X.-Z. Liao, Z.-F. Ma, *J. Electrochem. Soc.* **2016**, *163*, A2117–A2123.

[210] S. G. Patnaik, P. Adelhelm, in *Sodium-Ion Batter.*, Wiley, **2022**, pp. 167–187.

[211] R. Jung, M. Metzger, F. Maglia, C. Stinner, H. A. Gasteiger, *J. Phys. Chem. Lett.* **2017**, *8*, 4820–4825.

[212] T. Hatsukade, A. Schiele, P. Hartmann, T. Brezesinski, J. Janek, *ACS Appl. Mater. Interfaces* **2018**, *10*, 38892–38899.

[213] M. Metzger, B. Strehle, S. Solchenbach, H. A. Gasteiger, *J. Electrochem. Soc.* **2016**, *163*, A798–A809.

[214] K. U. Schwenke, S. Solchenbach, J. Demeaux, B. L. Lucht, H. A. Gasteiger, *J. Electrochem. Soc.* **2019**, *166*, A2035–A2047.

[215] J. Wang, S. L. Dreyer, K. Wang, Z. Ding, T. Diemant, G. Karkera, Y. Ma, A. Sarkar, B. Zhou, M. V Gorbunov, A. Omar, D. Mikhailova, V. Presser, M. Fichtner, H. Hahn, T. Brezesinski, B. Breitung, Q. Wang, *Mater. Futur.* **2022**, *1*, 035104.

[216] Z. Li, M. Dadsetan, J. Gao, S. Zhang, L. Cai, A. Naseri, M. E. Jimenez-Castaneda, T. Filley, J. T. Miller, M. J. Thomson, V. G. Pol, *Adv. Energy Mater.* **2021**, *11*, 2101764.

[217] D. O. Ojwang, L. Häggström, T. Ericsson, J. Ångström, W. R. Brant, *Dalt. Trans.* **2020**, *49*, 3570–3579.

[218] D. Streich, C. Erk, A. Guéguen, P. Müller, F. Chesneau, E. J. Berg, *J. Phys. Chem.* **2017**, *121*, 13481–13486.

[219] A. T. S. Freiberg, J. Sicklinger, S. Solchenbach, H. A. Gasteiger, *Electrochim. Acta* **2020**, *346*, 136271.

[220] L. A. Kaufman, B. D. McCloskey, *Chem. Mater.* **2021**, *33*, 4170–4176.

[221] F. Strauss, S. Payandeh, A. Kondrakov, T. Brezesinski, *Mater. Futur.* **2022**, *1*, 023501.

[222] D. O. Ojwang, M. Svensson, C. Njel, R. Mogensen, A. S. Menon, T. Ericsson, L. Häggström, J. Maibach, W. R. Brant, *ACS Appl. Mater. Interfaces* **2021**, *13*, 10054–10063.

[223] J. Peng, B. Zhang, W. Hua, Y. Liang, W. Zhang, Y. Du, G. Peleckis, S. Indris, Q. Gu, Z. Cheng, J. Wang, H. Liu, S. Dou, S. Chou, *Angew. Chem. Int. Ed.* **2023**, *62*, e202215865.

[224] J. C. Pramudita, S. Schmid, T. Godfrey, T. Whittle, M. Alam, T. Hanley, H. E. A. Brand, N. Sharma, *Phys. Chem. Chem. Phys.* **2014**, *16*, 24178–24187.

[225] M. Oliver-Tolentino, M. González, H. Osiry, G. Ramos-Sánchez, I. González, *Dalt. Trans.* **2018**, *47*, 16492–16501.

[226] Mettler Toledo, *METTLER TOLEDO DSC823* **2005**.

[227] J. Yin, Y. Shen, C. Li, C. Fan, S. Sun, Y. Liu, J. Peng, L. Qing, J. Han, *ChemSusChem* **2019**, *12*, 4786–4790.

[228] F. Fu, X. Liu, X. Fu, H. Chen, L. Huang, J. Fan, J. Le, Q. Wang, W. Yang, Y. Ren, K. Amine, S.-G. Sun, G.-L. Xu, *Nat. Commun.* **2022**, *13*, 2826.

[229] Y. Yue, N. Li, L. Li, E. E. Foley, Y. Fu, V. S. Battaglia, C. Wang, W. Tong, *Chem. Mater.* **2020**, *32*, 4490−4498.

[230] S. Li, H. Chen, Q. Zhang, H. Deng, S. Chen, X. Shen, Y. Yuan, Y. Ding, Y. Cheng, H. Sun, J. Zhu, B. Lu, *Chem. Eng. J.* **2023**, *466*, 143342.

[231] R. Tian, Z. Wang, J. Liao, H. Zhang, D. Song, L. Zhu, L. Zhang, *Adv. Energy Mater.* **2023**, *13*, 2300850.

[232] J. Liang, Z. Li, J. Cheng, J. Qin, H. Liu, D. Wang, *Nano Res.* **2023**, *16*, 4987–4995.

[233] B. B. Berkes, A. Jozwiuk, M. Vračar, H. Sommer, T. Brezesinski, J. Janek, *Anal. Chem.* **2015**, *87*, 5878–5883.

[234] B. B. Berkes, A. Jozwiuk, H. Sommer, T. Brezesinski, J. Janek, *Electrochem. Commun.* **2015**, *60*, 64–69.

[235] D. Streich, C. Erk, A. Guéguen, P. Müller, F. F. Chesneau, E. J. Berg, *J. Phys. Chem. C* **2017**, *121*, 13481–13486.

[236] M. Metzger, B. Strehle, S. Solchenbach, H. A. Gasteiger, *J. Electrochem. Soc.* **2016**, *163*, A1219–A1225.

[237] R. Lundström, N. Gogoi, X. Hou, E. J. Berg, *J. Electrochem. Soc.* **2023**, *170*, 040516.

[238] L. Ge, Y. Song, P. Niu, B. Li, L. Zhou, W. Feng, C. Ma, X. Li, D. Kong, Z. Yan, Q. Xue, Y. Cui, W. Xing, *ACS Nano* **2024**, *18*, 3542–3552.

[239] W. R. Blanchard, P. J. McCarthy, H. F. Dylla, P. H. LaMarche, J. E. Simpkins, *J. Vac. Sci. Technol. A Vacuum, Surfaces, Film.* **1986**, *4*, 1715–1719.

[240] J. H. Batey, *Vacuum* **2014**, *101*, 410–415.

[241] X. Yan, Y. Yang, E. Liu, L. Sun, H. Wang, X.-Z. Liao, Y. He, Z.-F. Ma, *Electrochim. Acta* **2017**, *225*, 235–242.

[242] D. A. Robinson, M. E. Foster, C. H. Bennett, A. Bhandarkar, E. R. Webster, A. Celebi, N. Celebi, E. J. Fuller, V. Stavila, C. D. Spataru, D. S. Ashby, M. J. Marinella, R. Krishnakumar, M. D. Allendorf, A. A. Talin, *Adv. Mater.*

2023, *35*, 2207595.

[243] Y. You, X. Yu, Y. Yin, K.-W. Nam, Y.-G. Guo, *Nano Res.* **2015**, *8*, 117–128.

[244] L. Samain, B. Gilbert, F. Grandjean, G. J. Long, D. Strivay, *J. Anal. At. Spectrom.* **2013**, *28*, 524.

[245] S. M. Haight, D. T. Schwartz, M. A. Lilga, *J. Electrochem. Soc.* **1999**, *146*, 1866–1872.

[246] G. Zhang, J. Qin, Y. Zhang, G. Gong, Z. Xiong, X. Ma, Z. Lv, Y. Zhou, S. Han, *Adv. Funct. Mater.* **2023**, *33*, 2302929.

[247] R. Waser, R. Dittmann, G. Staikov, K. Szot, *Adv. Mater.* **2009**, *21*, 2632–2663.

[248] R. Waser, M. Aono, *Nat. Mater.* **2007**, *6*, 833–840.

[249] V. S. Nguyen, V. H. Mai, P. Auban Senzier, C. Pasquier, K. Wang, M. J. Rozenberg, N. Brun, K. March, F. Jomard, J. Giapintzakis, C. N. Mihailescu, E. Kyriakides, P. Nukala, T. Maroutian, G. Agnus, P. Lecoeur, S. Matzen, P. Aubert, S. Franger, R. Salot, P.-A. Albouy, D. Alamarguy, B. Dkhil, P. Chrétien, O. Schneegans, *Small* **2018**, *14*, 1801038.

[250] X. Zhu, C. S. Ong, X. Xu, B. Hu, J. Shang, H. Yang, S. Katlakunta, Y. Liu, X. Chen, L. Pan, J. Ding, R.-W. Li, *Sci. Rep.* **2013**, *3*, 1084.

[251] W. Bai, R. Huang, Y. Cai, Y. Tang, X. Zhang, Y. Wang, *IEEE Electron Device Lett.* **2013**, *34*, 223–225.

[252] C. Ye, C. Zhan, T.-M. Tsai, K.-C. Chang, M.-C. Chen, T.-C. Chang, T. Deng, H. Wang, *Appl. Phys. Express* **2014**, *7*, 034101.

[253] T.-H. Hou, K.-L. Lin, J. Shieh, J.-H. Lin, C.-T. Chou, Y.-J. Lee, *Appl. Phys. Lett.* **2011**, *98*, 103511.

[254] M. K. Kim, J. S. Lee, *ACS Appl. Mater. Interfaces* **2016**, *8*, 32918–32924.

[255] C. B. Lee, D. S. Lee, A. Benayad, S. R. Lee, M. Chang, M.-J. Lee, J. Hur, Y. B. Kim, C. J. Kim, U.-I. Chung, *IEEE Electron Device Lett.* **2011**, *32*, 399–401.

[256] G. W. Burr, R. M. Shelby, A. Sebastian, S. Kim, S. Kim, S. Sidler, K. Virwani, M. Ishii, P. Narayanan, A. Fumarola, L. L. Sanches, I. Boybat, M. Le Gallo, K. Moon, J. Woo, H. Hwang, Y. Leblebici, *Adv. Phys. X* **2017**, *2*, 89–124.

[257] A. Moradpour, O. Schneegans, S. Franger, A. Revcolevschi, R. Salot, P. Auban-Senzier, C. Pasquier, E. Svoukis, J. Giapintzakis, O. Dragos, V. C. Ciomaga, P. Chrétien, *Adv. Mater.* **2011**, *23*, 4141–4145.

[258] L. B. Avila, C. K. Müller, D. Hildebrand, F. L. Faita, B. F. Baggio, C. C. P. Cid, A. A. Pasa, *Materials.* **2020**, *13*, 5618.

[259] X. Zhu, J. Zhou, L. Chen, S. Guo, G. Liu, R. Li, W. D. Lu, *Adv. Mater.* **2016**, *28*, 7658–7665.

[260] S. Wang, W. Wang, C. Yakopcic, E. Shin, G. Subramanyam, T. M. Taha, *Microelectron. Eng.* **2017**, *168*, 37–40.

[261] C. M. Orfanidou, P. S. Ioannou, E. Kyriakides, C. Nicolaou, C. N. Mihailescu, V. S. Nguyen, V. H. Mai, O. Schneegans, J. Giapintzakis, *AIP Adv.* **2018**, *8*, 115211.

[262] C. W. Chu, J. Ouyang, J. -H. Tseng, Y. Yang, *Adv. Mater.* **2005**, *17*, 1440–1443.

[263] H. Wu, X. Li, F. Huang, A. Chen, Z. Yu, H. Qian, *Nanotechnology* **2015**, *26*, 035203.

[264] Z. Wang, W. G. Zhu, A. Y. Du, L. Wu, Z. Fang, X. A. Tran, W. J. Liu, K. L. Zhang, H. Y. Yu, *IEEE Trans. Electron Devices* **2012**, *59*, 1203–1208.

[265] C.-W. Hsu, C.-C. Wan, I.-T. Wang, M.-C. Chen, C.-L. Lo, Y.-J. Lee, W.-Y. Jang, C.-H. Lin, T.-H. Hou, in *2013 IEEE Int. Electron Devices Meet.*, IEEE, **2013**, pp. 10.4.1-10.4.4.

[266] F. Cai, J. M. Correll, S. H. Lee, Y. Lim, V. Bothra, Z. Zhang, M. P. Flynn, W. D. Lu, *Nat. Electron.* **2019**, *2*, 290–299.

[267] M. Lanza, R. Waser, D. Ielmini, J. J. Yang, L. Goux, J. Suñe, A. J. Kenyon, A. Mehonic, S. Spiga, V. Rana, S. Wiefels, S. Menzel, I. Valov, M. A. Villena, E. Miranda, X. Jing, F. Campabadal, M. B. Gonzalez, F. Aguirre, F. Palumbo, K. Zhu, J. B. Roldan, F. M. Puglisi, L. Larcher, T.-H. Hou, T. Prodromakis, Y. Yang, P. Huang, T. Wan, Y. Chai, K. L. Pey, N. Raghavan, S. Dueñas, T. Wang, Q. Xia, S. Pazos, *ACS Nano* **2021**, *15*, 17214–17231.

[268] F.-C. Chiu, *Adv. Mater. Sci. Eng.* **2014**, *2014*, 578168.

[269] C. A. Marianetti, G. Kotliar, G. Ceder, *Nat. Mater.* **2004**, *3*, 627–631.

[270] T. Motohashi, Y. Sugimoto, Y. Masubuchi, T. Sasagawa, W. Koshibae, T. Tohyama, H. Yamauchi, S. Kikkawa, *Phys. Rev. B* **2011**, *83*, 195128.

[271] Z. Wang, X. Zhang, S. Zhou, K. Edström, M. Strømme, L. Nyholm, *Adv. Funct. Mater.* **2018**, *28*, 1804038.

[272] N. Zhu, X. Mao, G. Wang, M. Zhu, H. Wang, G. Xu, M. Wu, H. K. Liu, S.-X. Dou, C. Wu, *J. Mater. Chem. A* **2021**, *9*, 13200–13208.

[273] H. Wang, Y. Wu, S. Liu, Y. Jiang, D. Shen, T. Kang, Z. Tong, D. Wu, X. Li, C. Lee, *Small Methods* **2021**, *5*, 2001050.

[274] K. Kushida, K. Kuriyama, *Solid State Commun.* **2004**, *129*, 525–528.

[275] A. Milewska, K. Świerczek, J. Tobola, F. Boudoire, Y. Hu, D. K. Bora, B. S. Mun, A. Braun, J. Molenda, *Solid State Ionics* **2014**, *263*, 110–118.

[276] E. Flores, N. Mozhzhukhina, U. Aschauer, E. J. Berg, *ACS Appl. Mater. Interfaces* **2021**, *13*, 22540–22548.

[277] M. Zea, A. Moya, M. Fritsch, E. Ramon, R. Villa, G. Gabriel, *ACS Appl. Mater. Interfaces* **2019**, *11*, 15160–15169.

[278] H. Hu, A. Scholz, C. Dolle, A. Zintler, A. Quintilla, Y. Liu, Y. Tang, B. Breitung, G. C. Marques, Y. M. Eggeler, J. Aghassi-Hagmann, *Adv. Funct. Mater.* **2024**, *34*, 2302290.

[279] X. Zhu, D. Li, X. Liang, W. D. Lu, *Nat. Mater.* **2019**, *18*, 141–148.

[280] T. George, A. V. Murugan, *ACS Appl. Mater. Interfaces* **2022**, *14*, 51066–51083.

[281] H. Abbas, Y. Abbas, G. Hassan, A. S. Sokolov, Y.-R. Jeon, B. Ku, C. J. Kang, C. Choi, *Nanoscale* **2020**, *12*, 14120–14134.

[282] W. Wang, J. Xu, H. Ma, X. Zhao, Y. Lin, C. Zhang, Z. Wang, H. Xu, Y. Liu, *ACS Appl. Nano Mater.* **2019**, *2*, 307–314.

[283] M. A. Zidan, Y. Jeong, J. Lee, B. Chen, S. Huang, M. J. Kushner, W. D. Lu, *Nat. Electron.* **2018**, *1*, 411–420.

[284] J. Guo, W. Li, Y. Liao, Y. Shen, K. Wang, C. H. Suk, X. Zhou, Y. Zhang, C. Wu, T. Guo, T. W. Kim, *Adv. Funct. Mater.* **2022**, *32*, 2207885.

[285] S. K. Nath, X. Sun, S. K. Nandi, X. Chen, Z. Wang, S. K. Das, W. Lei, L. Faraone, W. D. A. Rickard, R. G. Elliman, *Adv. Funct. Mater.* **2023**, *33*, 2306428.

[286] K. S. Woo, J. Kim, J. Han, J. M. Choi, W. Kim, C. S. Hwang, *Adv. Intell. Syst.* **2021**, *3*, 2100062.

13. Acknowledgements

First of all, I would like to sincerely thank Prof. Dr. Jasmin Aghassi-Hagmann, for giving me the opportunity to join her research group at the Institute of Nanotechnology (INT) at Karlsruhe Institute of Technology (KIT). I take this chance to also show my sincerest gratitude to Dr. Ben Breitung for mentoring me during my stay in the INT. The group provides optimal conditions and good atmosphere for scientific research, and significant opportunities for personal growth. I deeply appreciate their scientific support and trust for the batteries and memristors research.

I would like to appreciate all my coworkers during my Ph.D journey. I am very thankful to Dr. Torsten Brezesinski (INT) and Sören L. Dreyer (INT) for the DEMS measurements. Thanks to Dr. Thomas Diemant (HIU) for the XPS measurements. Thanks to Hongrong Hu (INT) for assisting in memristors work. Thanks to Yang Hu (HIU) for the XAS and XES measurements. Thanks to Tolga Akçay (IAM) for the *operando* stress measurements. Thanks to Yuting Dai (INT) and Yushu Tang (INT) for TEM characterization. Thanks to Yin-Ying Ting (RWTH Aachen University) for the DFT calculation. Thanks to Simon Schweidler (INT), Hao Liu (IAM) and Damian Goonetilleke (INT) for assisting in the Rietveld refinement analyses. Thanks to Jing Lin for the DSC measurements. Our collaboration is truly remarkable. Thanks to Bastian Weinert for his assistance with the XRF measurements. Their assistance is indispensable, and without their support, I couldn't have achieved such good results.

My special thanks goes to Prof. Yanjiao Ma, for her scientific guidance, generous help and valuable insights in the battery research. Without her help, the completion of the batteries research would have taken much more time.

Furthermore, thanks to Dr. Gabriel Cadilha Marques, Anurag Dinesh Khandelwal, Dr. Simon Schweidler, Dr. Junbo Wang, Yan Liu, Bei Zhou, Dr. Yanyan Cui, Dr. Qingshou Wang, Mohana Veerraju Kante and all other INT colleagues for support and help. I would like to thank everyone in the institute for their helpfulness on various occasions.

Finally, I would like to express my gratitude to my motherland, China. I am sincerely grateful to China Scholarship Council (CSC) for the financial support and the valuable opportunity to pursue my Ph.D study abroad. It is a wonderful journey that I have had during my doctoral studies.

14. List of publications

Peer-reviewed journal publications

During Ph.D phase

[1] Yueyue He, Sören L. Dreyer, Yin-Ying Ting, Yuan Ma, Yang Hu, Damian Goonetilleke, Yushu Tang, Thomas Diemant, Bei Zhou, Piotr M. Kowalski, Maximilian Fichtner, Horst Hahn, Jasmin Aghassi-Hagmann,Torsten Brezesinski, Ben Breitung and Yanjiao Ma, Entropy-Mediated Stable Structural Evolution of Prussian White Cathodes for Long-Life Na-Ion Batteries. **Angewandte Chemie International Edition**. 2024, 136 (7), e202315371. (Cover)

[2] Yueyue He, Sören L. Dreyer, Tolga Akçay, Thomas Diemant, Reiner Mönig, Yuan Ma, Yushu Tang, Huifeng Wang, Jing Lin, Simon Schweidler, Maximilian Fichtner, Horst Hahn, Torsten Brezesinski, Ben Breitung and Yanjiao Ma, Leveraging Entropy and Crystal Structure Engineering in Prussian Blue Analogue Cathodes for Advancing Sodium-Ion Batteries. **ACS Nano**. 2024, 18 (35), 24441-24457.

[3] Yueyue He, Yin-Ying Ting, Hongrong Hu, Thomas Diemant, Yuting Dai, Jing Lin, Gabriel Cadilha Marques, Horst Hahn, Yanjiao Ma, Torsten Brezesinski, Piotr M. Kowalski, Ben Breitung and Jasmin Aghassi-Hagmanna, Printed Memristors Based on High-Entropy Prussian Blue Analogues. **Advanced Materials**. 2024, 2410060.

During Master/Bachelor

[1] Yueyue He, Shuo Wang, Haiyan Zhang, Xin Chen, Jin Li, Huiyuan Xu, Yanhui Zhang, Kanghui Hu, Genpin Lv, Yan Meng and Wei Xiang, Identifying the Effect of Fluorination on Cation and Anion Redox Activity in Mn Based Cation-Disordered Cathode. **Journal of Colloid and Interface Science**. 2022, 607, 1333–1342.

[2] Yueyue He, Wei Xiang, Genpin Lv, YanJun Zhong, Yang Song, Kun Zhou, Zhenguo Wu, Jun Zhang, Erqiang Yang and Xiaodong Guo, Disordered Li-Rich, Ti-Based Oxyfluoride Cathode with Multiple Cation and Anion Redox Chemistry. **Chemical Engineering Journal**. 2021, 417, 128189.

[3] Yueyue He, Chao-Qiong Zhu, Kang-Hui Hu, Kun Zhou, Qing Yang, Xin-Lin Yan, Yin Liu, Er-Qiang Yang, Chaomei Yang and Nian-Cu Chen, Ni-Rich $LiNi_{0.6}Co_{0.2}Mn_{0.2}O_2$ Microrod with

Hierarchical Structure Synthesized by Template Reaction as Cathode Material for Lithium-Ion Battery. **Ionics**. 2019, 25 (11), 5277–5285.

[4] Kanghui Hu, Yueyue He, Chaoqiong Zhu, Kun Zhou, Qi Chen, Zhaomei Yang, Bingrui Wan, Erqiang Yang, Tingting Zhang, and Yuandong Qin. Insight into the Evolution of Precursor and Electrochemical Performance of Ni-Rich Cathode Modulated by Ammonia during Hydroxide Precipitation. **Journal of Alloys and Compounds**. 2019, 803, 538–45. (Co-first author)

Conference oral presentations

Yueyue He, Ben Breitung and Jasmin Aghassi-Hagmann, Entropy-Mediated Stable Structural Evolution of Prussian White Cathodes for Long-Life Na-Ion Batteries, 2024 Materials Research Society (MRS) Spring Meeting & Exhibit, Seattle, US, 2024. (Oral presentation)

15. Personal Data

Education Background

10.2021 – 01.2025	Ph. D	Karlsruhe Institute of Technology (KIT), Germany • Major: Electrical Engineering and Information Technology • Ph. D thesis: High-entropy Prussian blue analogues for sodium-ion batteries and memristor applications
09.2018 – 06.2021	Master	Chengdu University of Technology, PR China • Major: Chemical Engineering and Technology • Master thesis: The synthesis and performance research of disordered rock-salt cathode with high capacity and low cost
09.2014 – 06.2018	Bachelor	Weifang University of Science and Technology, PR China • Major: Chemical Engineering and Technology

Research Experience

10.2021 – 01.2025	• Design and synthesize novel high-entropy Prussian blue analogues for Na-ion and K-ion batteries, and study the impact of the composition disorder on the structure and performance. • Study high-temperature performance and assemble full-cell for Na-ion batteries. • Prepare electrolytes for Na-ion and K-ion batteries. • Design and synthesize novel high-entropy Prussian blue analogues for memristors, and study the conduction mechanisms. • Fabricate memristors using inkjet printing and microplotting.	INT, KIT Prof. Jasmin Aghassi Hagmann Dr. Ben Breitung
09.2018-06.2021	• Synthesize Ni-rich $LiNi_{0.6}Co_{0.2}Mn_{0.2}O_2$ cathode with hierarchical structure by a stepwise oxalate co-precipitation method. • Design and synthesize Ti based oxyfluorides	Sichuan University Prof. Benhe Zhong

$Li_2Ti_{1/3}Ni_{1/3}M_{1/3}O_2F$ (M=Mn, Fe) cathode and study the electrochemical mechanisms.	Prof. Xiaodong Guo
• Design and synthesize cationic disordered cathodes ($Li_{1.25}Mn_{0.25}Ti_{0.25}Nb_{0.25}O_2$, $Li_{1.25}Mn_{0.25}Ti_{0.5}O_{1.75}F_{0.25}$) and study the effect of fluorine substitution on structure and electrochemical performance.	Dr. Zhenguo Wu Dr. Wei Xiang

Research Interests/ Material Science Skills

Research interests	Secondary batteries (Na-ion batteries; K-ion batteries; Solid state batteries; Pouch bag cells) Printed technologies for memristors or transistors
Synthesis methods	Co-precipitation; Mechanochemical synthesis (ball-milling); Sol-gel synthesis
Instrumental operation	X-ray diffraction (Cu and Ga source); Scanning electron microscopy; Atomic force microscope; Laser (Laser ablation); Inkjet printer; Microplotter; BioLogic potentiostat
Characterization	Transmission electron microscopy; X-ray photoelectron spectroscopy; X-ray absorption spectroscopy; *Operando* X-ray diffraction; Electrochemical impedance spectroscopy; Differential electrochemical mass spectrometry；DFT calculation
Software	Vesta; Diamond3; GSAS Refinement; Jade; Xpspeak; 3Dmax; ZView; DigitalMicrograp; HighScore; NanoScope Analysis; Spyder